1991

Finite element study of ultrasonic imaging

Zhongqing You
Iowa State University

Order Number 9126275

Finite element study of ultrasonic imaging

You, Zhongqing, Ph.D.

Iowa State University, 1991

U·M·I
300 N. Zeeb Rd.
Ann Arbor, MI 48106

Finite element study of ultrasonic imaging

by

Zhongqing You

A Dissertation Submitted to the

Graduate Faculty in Partial Fulfillment of the

Requirements for the Degree of

DOCTOR OF PHILOSOPHY

Department: Electrical Engineering and Computer Engineering
Major: Electrical Engineering (Electromagnetics)

Approved:

Signature was redacted for privacy.

In Charge of Major Work

Signature was redacted for privacy.

For the Major Department

Signature was redacted for privacy.

For the Graduate College

Members of the Committee:

Signature was redacted for privacy.

Iowa State University
Ames, Iowa
1991

TABLE OF CONTENTS

LIST OF TABLES

LIST OF FIGURES

ACKNOWLEDGEMENTS

I would like to express my sincere gratitude to my advisor, Dr. William Lord, for providing the opportunity for me to pursue a PhD degree. He has always been supportive and encouraging throughout this research. His professional and personal guidance will be beneficial to me for a life time.

I would like to extend my appreciation to Dr. Reinhold Ludwig, who has contributed numerous useful ideas and suggestions to push this research towards completion. I am also indebted to Dr. Satish Upda for his valuable insights and suggestions on determining the theme of this dissertation.

I would also like to thank Dr. John P. Basart, Dr. Alvin A. Read, Dr. Lester W. Schmerr Jr. and Dr. Thomas Rudolphi for willfully taking the time to serve on my committee.

Many thanks are also owed to the graduate students working in the NDT laboratory whose advice, thoughts, expertise and friendship throughout the course of this research are extremely useful.

This dissertation is dedicated to my parents who sacrificed so much to make my dreams come true.

CHAPTER 1. INTRODUCTION

Nondestructive testing (NDT) techniques have been used extensively in the testing of critical components in the aerospace, transportation and nuclear industries, since failures in these areas cannot be tolerated. Even though many different NDT methods are used in industry, ultrasonic NDT has always played a key role and is likely to be as important in the future. There are several distinctive advantages in using elastic waves which makes ultrasonic NDT unique. For instance, elastic waves will propagate in solids, liquids and gases, so the whole range of technological materials are accessible. A large excitation frequency range from about 10^5 to 10^8 Hz makes the detectable flaw dimension cover a wide range from millimeters down to microns. Ultrasonic NDT is also economical.

With the attention restricted to ultrasonic NDT, this chapter explains why a forward model is important and provides a brief review of some techniques available for solving forward problems. This is then followed by an overview of the relationships between a series of inverse algorithms. Finally, the major objective of the dissertation is outlined as the development of finite element modeling and its application to studying inverse algorithms.

Forward Problem and Model Review

A firm understanding of the basic physics of energy/defect interaction is very important to NDT. The selection of appropriate testing procedures for ultrasonic NDT depends on the understanding of the way in which elastic waves propagate in solids and interact with internal features of materials such as defects, inhomogeneities, interfaces and boundaries. Even the choice of a suitable wavelength is no trivial task. In-depth understanding is based on either the models by which the testing process can be accurately simulated or the detailed, well-controlled experiments. A good forward model is not only very useful in transducer design, but also provide solutions to defect characterization problems. There would be no inverse procedure without an appropriate forward model. This relationship is presented in different ways. The direct inversion of the forward model could result in a powerful inverse formulation such as, for example, the Inverse Born Approximation (IBA) and the Inverse Kirchhoff Approximation. Some inverse algorithms require an accurate forward model to produce the scattered field as the algorithm iterates for a better description of the scatterer. Moreover, a good forward model can always serve as a test bed to study the sensitivity of certain inverse procedures.

Even though exact solutions are most desirable, not all problems can be solved analytically. Separation of variables in certain coordinate systems gives a solution in the form of an eigenfunction (special function) expansion for problems with simple penny-shaped cracks [1], cylindrical [2,3] or spherical [4,5] inclusions in an infinite full or an infinite half space. Semi-numerical techniques also predict elastic wave propagation for isotropic [6,7] or transversely isotropic [8,9] materials. Quite often, the low-frequency expansions of these exact solutions are useful. However, these

approaches have proved incapable of being extended to the general problem of arbitrarily shaped defects in an arbitrary part. Subsequently, several approximations have been investigated.

The Born approximation [10] and the quasi-static approximation are both low-frequency theories. The Born technique is particularly interesting because it results in an explicit inverse scheme [11]. Based on the assumption of a weak and/or small scatterer which assumes that the scattered field is negligible in comparison with the incident field inside the scatterer, the Born approximation provides a simple way of calculating the scattered displacement field outside the scatterer. It does not, however, predict several key aspects of coupled wave phenomena. For high frequency problems, or equivalently, the situation with large crack size in comparison with wavelength, the Kirchhoff approximation [12,13] is applicable if the incident angle is in a restricted range. The basic assumptions involved in the approximation are that the incident field reflects at each point on the defect as though the defect were an infinite plane and the wavefield is zero on the dark side of the crack. Based on ray-theory [14], the geometrical theory of diffraction (GTD) [15] is best established for large defects (size of 3 wavelengths or greater). This treatment assumes that the diffracted field propagates along curves called rays according to the ray theory which then makes use of geometrical rules.

The difficulty, however, arises if one works in the region where the size of the scatterer is comparable with the wavelength as in many NDT problems. Neither the Born, nor the Kirchhoff approximation is applicable. More elaborate procedures, such as numerical techniques, are necessary to understand the scattering field in this range. The methods suitable for this region are the Transition Matrix (t-matrix)

theories, boundary element, finite difference and finite element methods.

The t-matrix method [16,17] expands both the incident and scattered fields in terms of complete infinite sets of suitable basis functions. The boundary conditions on the crack are then used to obtain a formula in which the unknown coefficients of the series representing the scattered field are given by multiplying the coefficients of the incident field by a matrix called the t-matrix. This matrix relation can then be truncated at a suitable point and evaluated numerically. The validity of this method depends on the choice of basis functions and the geometry of the scatterer. At present level of computer resources, the t-matrix method can probably handle a wider range of scatterer geometries than the finite difference and finite element method. It is, however, a single-frequency method which has difficulty in modeling short pulses.

The boundary element method (BEM) [18,19] starts also from the same integral equation as in the t-matrix method. The surface of the scatterer now is discretized into a number of boundary elements. A set of matrix equations with the nodal displacement and/or tractions as unknowns are formed after numerically evaluating the surface integrations over the elements. Recently, BEM has been exploited extensively by the NDT community [20,21]. However, it has not yet been used so far for general anisotropic materials because of the difficulty in evaluating Green's functions.

Finite difference (FD) [22] is conceptually straightforward. The application of FD involves a uniform discretization of the space and the approximation of the partial derivatives in the wave equation, to a given accuracy. This is achieved by a Taylor series expansion of the functions in the grid. This process results in a set of algebraic equations with the field values of all grid points at a particular instant of time, as the unknowns. Time stepping is carried out through the approximation of a time

derivative term by the accelerated Taylor expansion of the field value in the time axis. Bond [23,24], Bond et al. [25], Harker[26], Harumi [27,28] and Harumi et al. [29] have applied FD to NDT-related ultrasonic wave studies.

Even though FD is a powerful tool for predicting elastic wave propagation in NDT applications, it is somewhat restricted by its uniform mesh. In order to simulate a real ultrasonic inspection, a good forward model should be able to handle complicated geometries and even material properties such as anisotropy and attenuation. This model should also be combined with appropriate transmitter and receiver models. The finite element model was, therefore, developed under this motivation [30].

The finite element method (FEM) is based on two fundamental ideas: 1) the weak formulation of a boundary value problem; and 2) the domain decomposition, i.e., the decomposition of the domain into smaller subdomains, called elements. Both these ideas are closely related to basic concepts of solid mechanics. Indeed the first systematic and large scale utilizations of FEM occurred in solid mechanics [31,32]. The weak formulation of a boundary value problem coincides with the virtual work theorems and energy principles in the statics of solids. Domain decomposition is also an extrapolation of the natural approach in structural mechanics in which a large structure is represented as a number of smaller substructures that are properly connected or assembled. The study of the large structure is then reduced to that of the elementary structures and their connections. Application of FEM to wave propagation problems was introduced by Lysmer and Drake [33] for seismology in 1972. Smith [34] then described finite element analysis for body wave propagation in 1975. The time-dependent FE formulation was not developed until 1976 by Bazant et

al. [35] with application to diffraction by a crack tip. Tsao, et al. [36], have proposed a hybrid finite element and wave expansion technique for subsurface flaws which was also used by Datta and Shah [37] in conjunction with an analytical technique for the far field. The application of FEM to ultrasonic NDT was introduced only recently by Ludwig [30], Ludwig and Lord [38-40]. They extended the modeling work on electromagnetic NDT problems [41] to handle the ultrasonic case. The early results are promising and in agreement with exact theory and with experiment. However, the model is still in the early stages of development and only considers isotropic materials in 2-dimensional geometries [38]. Further refinements are needed in order to consider more complicated geometries, such as axi-symmetric and 3-dimensional cases, and general anisotropy must be included before using this model in more realistic NDT applications.

Overview of Applied Inverse Problem

Recent developments in nondestructive testing include the improvement of instrumentation, and beyond mere detection, the identification of what is observed by the testing procedures. The ultimate goal of NDT is to provide accurate information about the flaw location, size and shape from the detected signals. An *object function* can be introduced to describe the scatterer as a function of space. It is defined as unit value inside the scatterer and zero elsewhere. The inverse process is more difficult than the forward problem because the inversion is in general unstable, ill-posed and nonlinear. The instability can be observed from the fact that no real solution to the inverse problem can be obtained if noise dominates the detected signals. The nature of an inversion problem intimates that the inversion in general is nonunique [42]. To

make things worse, nonlinearity of the inversion furthermore implies that there is no linear relationship between the scattered field and the scatterer properties including its geometry and material parameters.

Under some assumptions, or a priori information, the inversion process does give a unique solution. The *Golden Rule* [43] describing the condition of obtaining a unique solution states that the dimensionality of the data must exceed or equal the dimensionality of the unknown. An analysis of the dimensionality of the observed (measured) data structure and the scattering sources (for inverse source problems) or the scatterer (for inverse scattering problems) proves the observation of nonuniqueness. For most problems of interest, however, the material parameters are assumed to be independent of frequency or time. The dimensionality of the scatterer will be the same as that of the measured data. Therefore, under the assumption of a weak scatterer, a transient experiment which records the scattered data in a certain period of time would possess a unique solution to the inverse scattering problem [44]. Multiple angle experiments also generate a unique solution in a similar manner.

There are a number of inverse techniques operating in the nondestructive inspection of materials, seismic prospecting, ultrasonic imaging of biologic tissue, astronomy, etc. It is, however, appropriate to categorize all the techniques to two groups: linearized inverse scattering and exact (hence, nonlinear) inversion. The first group for scalar waves can be derived within a general framework as the diffraction expansion of computer tomography [45,46]. Significantly different approaches are possible for the second group , such as an optimization procedure [47-49], a quantitative nonlinear theory toward a set of self-consistent equations [50,51], artificial intelligence [52,53], etc. These nonlinear inversions need very accurate forward models to produce

the scattered data field during the iteration towards the better reconstructions of the scatterer, which supports the argument stated earlier on the necessity of developing forward models. All these nonlinear inversions, however, require tremendous computing time which makes them hard to implement in real time. Therefore, the focus here is on the linearized inversion.

Even though NDT problems are basically inverse scattering problems, they can be converted to inverse source problems by relating the scatterer parameters to an equivalent secondary source. The reconstruction, therefore, recovers the source resulted from the related scatterer. Linearization is done through simplifications on the representation of the secondary sources.

For a penetrable scatterer, the weak scatterer or Born approximation postulates zero scattered field inside the scatterer which holds for relatively low wavenumber and flaw/host contrast. For perfect scatterers we put the scattered field on the illuminated side of the surface and set the scattered field to be zero on the shadow side. This is the physical optics (PO) or Kirchhoff approximation holding for high frequencies and convex surface. After posing these assumptions, the secondary sources depend only on the parameters (geometry and material parameters) of the scatterer. Further utilization of the information on the frequency range over which the technique operates and of the experimental setup clarifies the categories of the imaging techniques.

Computer tomography [54] is the solution of an inverse scattering problem where diffraction effects do not play a significant role, which is the Radon transform [55]. This is the case for very high frequencies such as with an X-ray source. The *object function* can be recovered from the projection either via the algorithm of filtered

backprojection [56] or utilizing the Fourier slice theorem [44,56,57], which allows the recovering of projection data in the spatial frequency domain of the object function.

In the intermediate frequency range of most ultrasonic and microwave NDT, an appropriate diffraction tomography has to be developed in order to consider the diffraction effect. This means that Huygens-type data representation has to be inverted. For a far-field measurement surface, the Born approximation immediately yields the algorithm of the far-field Fourier inversion either in angular or frequency diversity, the time domain counterpart of the latter algorithm exhibiting the structure of a backprojection scheme [45]. If the far-field approximation does not hold, a generalized holography [44,58] is introduced. The back-propagation principle of generalized holography then yields the Porter-Bojarski integral equation [59,60] with an image output of minimal energy sources revealing the properties of the scatterer on an Ewald sphere [44,58]. The integration of minimal energy output with regard to a diversity variable (angle or frequency) results in either an angular diversity or a frequency diversity generalized filtered back-propagation algorithm under the weak scatterer approximation [44,46]. For a planar measurement, the Porter-Bojarski integral equation reduces to the Fourier diffraction slice theorem [61,62] which is considered as an extension of the Fourier slice theorem. The generalized filtered backpropagation counterpart of the Fourier diffraction slice theorem results in two versions of diffraction tomography in terms of angular diversity or frequency diversity [63-66]. The frequency diversity diffraction tomography, furthermore, is amenable to a transformation into the time domain, where the introduction of a *slight* far-field approximation results in the synthetic aperture focusing technique (SAFT) algorithm [67,68], an algorithm used intensively in astronomy and NDT.

This brief outline of inversion techniques reveals that the concept of generalized holography with the direct result of the Porter-Bojarski integral equation can in fact be considered as the basis of a general framework of linearized inversions which includes most techniques operating at present in different applications. Of all the linearized inverse algorithms, diffraction tomography results directly from the reduction of the Porter-Bojarski integral equation to a planar measurement and the superposition over the diversity variable. Therefore, diffraction tomography can be chosen as a representative to study the effects of approximations on the linearized inverse techniques. The applications of diffraction tomography can be found widely in geophysics, medical diagnostics, ultrasonic NDE and microwave imaging.

Much has been reported in the past concerning the formulation and applications of ultrasonic imaging by diffraction tomography. Besides the Born approximation, there is another approximation called the Rytov approximation [69] which is used widely. However, there has been little work reported that has focused on the treatment of the approximation errors when the diffraction methods are applied to solve inverse problem. Soumekh and Kaveh [70] demonstrate the sensitivity of the model approximation errors to a measure of the magnitude of the disturbance based on a Fourier representation of the Born and Rytov function. Their theoretical model analyzes the severity of degradation and interprets the error appearing in the reconstructed images of simulated cylindrical test objects. The model, however, does not take into account any practical factors of the experiments. A more detailed study of the sensitivity is needed which can simulate real NDT conditions. The application of a forward model as a test bed provides the only means for this purpose.

Objective of Dissertation

The major objective of this dissertation work is to develop further the finite element modeling of elastic wave propagation phenomena such that diffraction tomographic type of inverse algorithms can be studied by using the finite element model as a test bed.

With regard to a forward model, this dissertation carries on the development of finite element modeling of an ultrasonic inspection system. Special attention is paid to the treatment of anisotropy and attenuation, formulation and verification in general 3-D and axi-symmetric geometries, mass lumping techniques and the integration scheme. Viscous boundary conditions are also introduced to restrict the size of geometries. Due to the flexibility of the finite element method, the achievement of this dissertation on the forward problem is expected to develop an accurate, flexible model which inherently incorporates mode conversion, attenuation, beam focusing and defocusing, beam skewing, and the ability to model arbitrarily shaped defects. With careful programming and incorporating mass lumping and viscous boundary, the final code should be able to simulate most NDT geometries in 2-D and axi-symmetric cases on a workstation without extensive memory requirements.

The study of diffraction tomography by the finite element model, on the other hand, aims at the sensitivity characterization with respect to different factors. A measure of the degradation of the reconstructed image is based on the comparison with the original geometry (image).

The dissertation is organized as follows. Chapter 2 is devoted to a generic finite element formulation in 3-D geometries with full anisotropy, inhomogeneity and attenuation by viscous damping carried through the formulation. Chapter 3 discusses

the special considerations of the integration scheme to carry out time-stepping and mass lumping techniques which avoids the matrix inversion. Stability and accuracy of the formulations are also analyzed in this chapter. Due to the restriction of the computer resources, 2-D and axi-symmetric formulations are particularly useful for many NDT situations. Chapter 4, therefore, discusses these special cases. Chapter 5 introduces special absorbing boundary conditions to eliminate the unwanted reflections from artificial boundaries. These artificial boundaries are very useful in modeling large geometry problems. Results are presented in Chapter 6 in various considerations and applications. The validity of the formulation is proven through the comparison of finite element results with analytic and experimental data. From Chapter 7, this dissertation concentrates on the topic of the inverse problem. Chapter 7 derives a diffraction tomographic algorithm to reconstruct the object function of defects. With the raw data produced by FEM, Chapter 8 focuses on the exercises of this diffraction tomography. Its sensitivity with respect to the model approximation errors and other practical factors is measured by their effects on the quality of the reconstructed images. Conclusions in Chapter 9 ends the dissertation, with a brief outline of the future topics to be pursued on these important aspects of ultrasonic NDT system.

CHAPTER 2. FINITE ELEMENT ANALYSIS

This chapter, first of all, examines the underlying physics of ultrasonic wave propagation and derives the governing equations. The energy functional of the system is then introduced for the purpose of deriving finite element formulations. After space is discretized into a series of elements, the minimization of the energy functional results in the desired finite element formulation which forms the foundation of the finite element simulation of ultrasonic NDT phenomena.

Governing Equations

For all ultrasonic NDT testing situations, the general description of the whole process is no more than a solid material subjected to some special driving forces and/or boundary conditions. Without losing generality, an elastic body with volume Ω enclosed by a surface $\Gamma = \Gamma_t \cup \Gamma_u$, where Γ_t and Γ_u are the traction and kinematic boundaries, respectively, and satisfy $\Gamma_t \cap \Gamma_u = 0$, is considered throughout the rest of the thesis. Attenuation of the elastic wave propagation is caused by different mechanisms[71]. However, the scattering effect of the microstructure is neglected, which then leaves only geometrical attenuation and elastic damping to be considered in this model. Even though elastic damping in materials depends on temperature as well as the frequency and type of vibrations in a rather complicated manner,

attention here is restricted to room temperature at which acoustic losses in some materials may be adequately described by the viscous damping mechanism[71]. For the case of small strains, as in most ultrasonic NDT problems, Hooke's law is applied with an extra term containing the derivative of the strain which takes into account the viscous damping effect[72]

$$T_{ij} = C_{ijkl}S_{kl} + \eta_{ijkl}\dot{S}_{kl} \tag{2.1}$$

where C_{ijkl} and η_{ijkl} are the Cartesian elastic constant and viscosity constant, respectively. Roman indices take on the integer values 1-3 implying x, y and z axes, respectively, and the summation convention over repeated indices is assumed throughout. T_{ij} and S_{kl} are stress and strain tensors, respectively, and a superposed dot denotes differentiation with respect to time. Let u_i be the displacement vector, then the strain tensor in the linear range satisfies

$$S_{kl} = \frac{1}{2}(u_{k,l} + u_{l,k}) \quad \text{in } \Omega \tag{2.2}$$

where the comma denotes partial differentiation. The elastic coefficients satisfy the symmetry conditions

$$C_{ijkl} = C_{jikl} = C_{ijlk} = C_{jilk} = C_{klij} \tag{2.3}$$

so that only 21 of them are independent. The number of elastic constants reduces as the material symmetry increases such that only two are needed for isotropic media. This symmetric consideration is also applicable to the viscosity constants.

The elastic and viscosity constants for crystalline materials are always given with respect to crystal axes. In many cases, however, the global coordinates chosen for the convenience of solving specific problem may not coincide with the crystal axes. It

is, therefore, necessary to transform the property constants to other coordinates. In order to perform this transformation, a matrix is introduced to give a new description of the same vector in different coordinates. This transformation matrix is always orthogonal. An example of such a transformation matrix is given for a clockwise rotation of the coordinate axes through an angle θ about the z axis

$$[a_{ij}] = \begin{bmatrix} \cos\theta & \sin\theta & 0 \\ -\sin\theta & \cos\theta & 0 \\ 0 & 0 & 1 \end{bmatrix}$$

The transformation matrix transforms vector or first rank tensors according to

$$u_i' = a_{ij}u_j \tag{2.4}$$

And for a second rank tensor such as stress

$$T_{kl}' = a_{ki}a_{lj}T_{ij} \tag{2.5}$$

The elastic constant tensors are fourth rank, therefore, the transformation is carried out by

$$C_{mnop}' = a_{mi}a_{nj}a_{ok}a_{pl}C_{ijkl} \tag{2.6}$$

where u_i', T_{kl}' and C_{mnop}' are the displacement vector, stress tensor and the elastic constants, in the new coordinate system, respectively.

Similarly, the viscosity constants can also be transformed to other coordinates.

In the case of our elastic body Ω. Associated with every point in Ω will be a velocity $\dot{u}_i$, while acting on the body will be surface traction t_i and body force f_i. Conservation of momentum states that the time rate of change of momentum is

equal to the total force acting on the body. Taken in the differential expression, this statement has the form

$$T_{ij,j} + f_i = \rho \ddot{u}_i \text{ in } \Omega \tag{2.7}$$

where the Green-Gaussian theorem and the relation $t_i = T_{ij} n_j$ are used to derive this equation[73] and where ρ is the material density. Neglecting the body force and substituting equation(2.1) and (2.2) into (2.7) yields the following governing equation for a general elastic wave problem in lossy media with two possible boundary conditions.

$$C_{ijkl} \; u_{k,lj} + \eta_{ijkl} \dot{u}_{k,lj} = \rho \ddot{u}_i \text{ in } \Omega \tag{2.8a}$$

$$t_i = T_{ij} n_j \text{ on } \Gamma_t \tag{2.8b}$$

$$u_i = \bar{u}_i \text{ on } \Gamma_u \tag{2.8c}$$

where t_i and $\bar{u}_i$ are the surface tractions and the displacements given on boundaries Γ_t and Γ_u, respectively. Initial conditions are also required to start the solution process

$$u_i|_{t=0} = u_i^0 \text{ in } \Omega \tag{2.9a}$$

$$\dot{u}_i|_{t=0} = v_i^0 \text{ in } \Omega \tag{2.9b}$$

Equation (2.8) and (2.9) together give a full description of the physics involved in a linear elastic wave system.

Energy Functional

Solution of the governing equation derived in the previous section by the finite element method is proven, using variational calculus, to be equivalent to finding a

state which gives a stationary value to a scalar functional. This scalar functional turns out to be related to the total energy involved in the system, and is therefore called the energy functional. Even though the formulation can be easily established by the weighted residual scheme[74], the energy functional approach gives a more physical interpretation to the finite element method.

A dynamic system contains both kinetic and potential energy, that is

$$E(u_i,t) = P(u_i,t) + K(u_i,t) \tag{2.10}$$

where $P(u_i,t)$ is the potential energy and $K(u_i,t)$ is the kinetic energy. The potential energy or strain energy can be represented as

$$P(u_i,t) = \frac{1}{2}\int_\Omega S_{ji} C_{ijkl} S_{kl} dv \tag{2.11}$$

While the kinetic energy is

$$K(u_i,t) = \frac{1}{2}\int_\Omega \rho \dot{u}_i \dot{u}_i dv \tag{2.12}$$

It can be shown that the kinetic energy is equal to the work done by the equivalent internal body force $\rho\ddot{u}_i$, that is

$$K(u_i,t) = \int_\Omega \rho \ddot{u}_i u_i dv \tag{2.13}$$

It is obvious that the energy level of the system changes as a consequence of the external forces and internal energy loss mechanisms. Energy conservation states that the time rate of the change of kinetic energy and potential energy is equal to the work done upon the body by the external forces per unit time and the sum of all other energies such as energy loss per unit time. The only energy loss considered in the

governing equation(2.8) is due to viscous damping, which therefore can be calculated by

$$W_d(u_i,t) = \int_\Omega \dot{S}_{ji}\eta_{ijkl}S_{kl}dv \tag{2.14}$$

If the system is assumed to be initially at rest, the total energy including potential energy, kinetic energy, absorbed energy and the work done by the external force have to be at the stationary level for all the time. Upon neglecting the body force, the only external force is the surface traction acting on the traction boundaries. The work done by this source can be calculated by

$$W_e(u_i,t) = \int_{\Gamma_t} t_i u_i ds \tag{2.15}$$

It is, therefore, appropriate to define the energy functional as

$$F(u_i,t) = E(u_i,t) + W_d(u_i,t) - W_e(u_i,t) \tag{2.16}$$

which satisfies the requirement of having a stationary value regardless of the external forces and time. The final expression for the energy functional is, upon substituting the expressions of the stored energies, lost energy, and the work done by the external forces

$$\begin{aligned} F(u_i,t) &= \frac{1}{2}\int_\Omega C_{ijkl}S_{kl}S_{ij}dv + \int_\Omega \eta_{ijkl}\dot{S}_{kl}S_{ij}dv + \\ &\quad + \int_\Omega u_i\rho\ddot{u}_i dv - \int_{\Gamma_t} u_i t_i ds \end{aligned} \tag{2.17}$$

Notice here the definition of potential energy is different from the one given in the form of $\frac{1}{2}\int_\Omega S_{ji}T_{ij}dv$ which includes not only the strain energy, but also half of the lost energy due to viscous damping effect.

Discretization and Interpolation

Even though the exact solution gives the minimum or a stationary value for the energy functional, it is difficult to find an analytical expression for the solution. The solution is usually expressed by its values at a series of discrete points in any numerical methods. With the function defined in Ω, we require a discretization of this domain into subdomains called elements whose area are denoted by Ω^e. Considering the nodal values as unknowns solved for by the numerical method, the displacement will be completely defined if it is given in each element. This is done through selecting a set of special functions called approximation or shape functions $N_I(x, y, z)$ which express the displacement u_i in an element in terms of its nodal values $U^e_{iI}(t)$ as

$$u^e_i(x, y, z; t) = N_I(x, y, z) U^e_{iI}(t) \tag{2.18}$$

where the subscript I sums over the number of nodes per element and superscript e represents a specific element. The shape function which acts as a global basis function spanning the approximation space must meet certain compatibility and completeness requirements. These requirements can be summarized as[30]

a) a shape function should be smooth on each element interior Ω^e;

b) a shape function should be continuous across each element boundary Γ^e;

c) a shape function should be complete in the sense that the element interpolation gives complete polynomials to the degree permitted by the number of nodes.

The choice of the shape function depends on the type of element used for the discretization. With the choice of isoparametric element, the shape function can be

easily derived as a polynomial from a standard local element coordinate system. The mapping of the local element to a particular shape and location of real elements is carried out also by the shape function, which suggests the name of the element.

After the discretization, the energy functional can be evaluated element by element. That is

$$F(u_i,t) = F^e(u_i,t) \tag{2.19}$$

where e sums over all elements

$$\begin{aligned} F^e(u_i,t) &= \frac{1}{2}\int_{\Omega^e} C_{ijkl}S_{kl}S_{ij}dv + \int_{\Omega^e}\eta_{ijkl}\dot{S}_{kl}S_{ij}dv + \\ &+ \int_{\Omega^e} u_i\rho\ddot{u}_i dv - \int_{\Gamma_t^e} u_i t_i ds \end{aligned} \tag{2.20}$$

represents the energy functional in one element and where Γ_t^e is that part of the traction boundary on which the element e is located. Obviously, the last term vanishes if the element is an interior element or is located on the kinematic boundary.

Minimization of the total energy functional is done through the minimization of the elemental energy functional as discussed in the next section.

Minimization

As stated before, the solution of the elastic wave equation gives the stationary point for the energy functional. Therefore, the solution can be obtained by the process of minimizing the energy functional. Setting variation of the energy functional δF^e with respect to a small variation of the displacement δu_i to be zero produces

$$\begin{aligned} &\int_{\Omega^e}\delta u_{i,j}C_{ijkl}u_{k,l}dv + \int_{\Omega^e}\delta u_{i,j}\eta_{ijkl}\dot{u}_{k,l}dv + \\ &+ \int_{\Omega^e}\delta u_i\rho\ddot{u}_i dv - \int_{\Gamma_t^e}\delta u_i t_i ds = 0 \end{aligned} \tag{2.21}$$

Substituting the interpolation relation (2.17) into this equation gives

$$\delta U^e_{iI}\{M^e_{ik}(I,J)\ddot{U}^e_{kJ} + D^e_{ik}(I,J)\dot{U}^e_{kJ} + K^e_{ik}(I,J)U^e_{kJ} - R^e_{iI}\} = 0 \qquad (2.22)$$

where

$$M^e_{ik}(I,J) = \begin{cases} \int_{\Omega^e} \rho N_I N_J dv & \text{if } i = k \\ 0 & \text{if } i \neq k \end{cases} \qquad (2.23a)$$

$$D^e_{ik}(I,J) = \int_{\Omega^e} N_{I,j}\eta_{ijkl}N_{J,l}dv \qquad (2.23b)$$

$$K^e_{ik}(I,J) = \int_{\Omega^e} N_{I,j}C_{ijkl}N_{J,l}dv \qquad (2.23c)$$

$$R^e_{iI} = \int_{\Gamma^e_t} N_I t_i ds \qquad (2.23d)$$

with $I, J = 1, 2, ..., N_e$ (the number of nodes per element). Now the indices can be rearranged such that the matrices and vectors are ordered in the way that all degrees of freedom for each node are grouped together by defining the new indices as

$$I = (I-1)N_d + i$$
$$J = (J-1)N_d + k$$

where N_d is the degree of freedom per node. Let

$$\{U^e_I\} = \begin{Bmatrix} U^e_{xI} \\ U^e_{yI} \\ U^e_{zI} \end{Bmatrix}, \quad \{R^e_I\} = \begin{Bmatrix} R^e_{xI} \\ R^e_{yI} \\ R^e_{zI} \end{Bmatrix}$$

$$[M^e_{IJ}] = \begin{bmatrix} M^e_{xx}(I,J) & 0 & 0 \\ 0 & M^e_{yy}(I,J) & 0 \\ 0 & 0 & M^e_{zz}(I,J) \end{bmatrix}$$

$$[D^e_{IJ}] = \begin{bmatrix} D^e_{xx}(I,J) & D^e_{xy}(I,J) & D^e_{xz}(I,J) \\ D^e_{yx}(I,J) & D^e_{yy}(I,J) & D^e_{yz}(I,J) \\ D^e_{zx}(I,J) & D^e_{zy}(I,J) & D^e_{zz}(I,J) \end{bmatrix}$$

$$[K^e_{IJ}] = \begin{bmatrix} K^e_{xx}(I,J) & K^e_{xy}(I,J) & K^e_{xz}(I,J) \\ K^e_{yx}(I,J) & K^e_{yy}(I,J) & K^e_{yz}(I,J) \\ K^e_{zx}(I,J) & K^e_{zy}(I,J) & K^e_{zz}(I,J) \end{bmatrix}$$

Equation(2.21) then can be rewritten in the following form

$$\delta U^e_I (M^e_{IJ}\ddot{U}^e_J + D^e_{IJ}\dot{U}^e_J + K^e_{IJ}U^e_J - R^e_I) = 0 \tag{2.24}$$

The I, J now count over the number of unknowns per element. M^e_{IJ}, D^e_{IJ} and K^e_{IJ} are called elemental mass, damping and stiffness matrices, respectively. R^e_{iI} is the discretized loading from the surface traction which exists only if the element is located on the traction boundary. The symmetry of all matrices can be seen from equation (2.23). It can be shown that M^e_{IJ} is positive definite. While D^e_{IJ} and K^e_{IJ} are only positive semi-definite. M^e_{IJ} can also be seen to be a block diagonal matrix where nonzero elements exist only among the unknowns of the same direction. This nondiagonal mass matrix is usually called a consistent mass matrix. Of particular interest, numerical evaluation shows that mass matrices are always highly dominated by the diagonal terms and that no negative element exists. These properties are very useful when a diagonalization is made on the mass matrix in the next chapter.

Since δU_I^e is an arbitrary variation, eq. (2.24) implies the following elemental matrix equation

$$M_{IJ}^e \ddot{U}_J^e + D_{IJ}^e \dot{U}_J^e + K_{IJ}^e U_J^e = R_I^e \tag{2.25}$$

This equation can be considered as an analog to a damped mass-spring oscillator system with matrices M_{IJ}^e, D_{IJ}^e and K_{IJ}^e representing the elemental mass, damping and stiffness matrices, respectively.

The total energy of the entire region Ω consists of the energy in all elements. The minimization of the total energy then is equivalent to assembling the minimized results for each element. This assembly is achieved through two steps. First of all, the ranges of indices on matrices $M_{IJ}^e, D_{IJ}^e, K_{IJ}^e$ and vector R_I^e are effectively expanded to the total number of unknowns in the connected mesh by identifying the local element indices with the appropriate nodal numbers in the connected finite element mesh. Algebraically, this is equivalent to adding rows and columns of zeros in $M_{IJ}^e, D_{IJ}^e, K_{IJ}^e$ and vector R_I^e for all nodes not contained in the element e. The assembly of the global matrices and load vector is accomplished by the summation of element contributions. The final result can be expressed as

$$M\ddot{U}_t + D\dot{U}_t + KU_t = R_t \tag{2.26}$$

where the superscript e is dropped because of the global vectors containing all nodal values and global matrices instead of elemental ones in this equation, and subscript t is added to clarify the fact that this equation holds at a particular instant of time t. The mass matrix M is called the consistent mass matrix. In essence, equation(2.26) can be likened to a damped mass spring system in which the collection of all elements into the

global matrix form represents the solid as an arrangement of masses interconnected to one another by damped springs.

This formulation is in a general form and models any anisotropy by the direct presence of the elastic constant throughout the formulation. The inhomogeneity of the materials can be specified by the different values of ρ, C_{ijkl} and η_{ijkl} for different elements. The viscosity constants η_{ijkl} account for the attenuation of the ultrasonic wave propagation in lossy media.

CHAPTER 3. TIME INTEGRATION AND MASS LUMPING

Discretization in space and the utilization of the finite element approximation have resulted in an ordinary differential equation(2.26) which is called a semi-discretization formula because the time axis has not been discretized yet. In order to obtain a fully discrete approximation, the behavior of $u_i(t)$ in time is approximated through direct time integration. Implementation of the finite element formulation usually involves a matrix inversion which is often computer resource intensive. The matrix inversion can be avoided by using a mass-lumping technique and an appropriate choice of integration scheme.

Time Integration

Time integration can be categorized as either implicit or explicit. A typical implicit scheme is the Newmark integration [75] in which a linear acceleration relationship between time steps t and $t + \Delta t$ is assumed

$$U_{t+\Delta t} = U_t + \Delta t \dot{U}_t + \frac{\Delta t^2}{2}[(1-2\alpha)\ddot{U}_t + 2\alpha\ddot{U}_{t+\Delta t}] \tag{3.1}$$

$$\dot{U}_{t+\Delta t} = \dot{U}_t + \Delta t[(1-\beta)\ddot{U}_t + \beta\ddot{U}_{t+\Delta t}] \tag{3.2}$$

where α is an acceleration factor and β is the damping. The stability and accuracy of this algorithm can be controlled by properly adjusting the parameters α and β.

Rewriting eq. (3.1) as

$$\ddot{U}_{t+\Delta t} = \frac{1}{\alpha \Delta t^2}(U_{t+\Delta t} - U_t) - \frac{1}{\alpha \Delta t}\dot{U}_t - (\frac{1}{2\alpha} - 1)\ddot{U}_t \tag{3.3}$$

Substituting eqs. (3.2) and (3.3) into eq. (2.26) at time step $t + \Delta t$ yields

$$\begin{aligned}(K + \frac{\beta}{\alpha \Delta t}D + \frac{1}{\alpha \Delta t^2}M)U_{t+\Delta t} = R_{t+\Delta t} + (\frac{\beta}{\alpha \Delta t}D + \frac{1}{\alpha \Delta t^2}M)U_t + \\ +[(\frac{\beta}{\alpha} - 1)D + \frac{1}{\alpha \Delta t}M]\dot{U}_t + [(\frac{\beta}{2\alpha} - 1)\Delta t D + (\frac{1}{2\alpha} - 1)M]\ddot{U}_t \end{aligned} \tag{3.4}$$

where

$$\ddot{U}_t = \frac{1}{\alpha \Delta t^2}(U_t - U_{t-\Delta t}) - \frac{1}{\alpha \Delta t}\dot{U}_{t-\Delta t} - (\frac{1}{2\alpha} - 1)\ddot{U}_{t-\Delta t} \tag{3.5}$$

$$\dot{U}_t = \dot{U}_{t-\Delta t} + \Delta t(1 - \beta)\ddot{U}_{t-\Delta t} + \Delta t \beta \ddot{U}_t \tag{3.6}$$

The coefficient matrix of the left hand side in eq. (3.4) involves the stiffness matrix K and the damping matrix D. As pointed out in Chapter 2, the elemental stiffness matrix K^e and damping matrix D^e are positive semi-definite full matrices and are formed by the integration of the partial derivatives of the shape functions.. They cannot be diagonalized as this would completely change the underlying physics described by the governing equation. The solution of eq. (3.4) then requires an inversion of the matrix $(K + \frac{\beta}{\alpha \Delta t}D + \frac{1}{\alpha \Delta t^2}M)$. This is the main shortcoming of the implicit scheme; the memory requirement and the operations involved in the matrix inversion restrict the applications of this finite element model in large geometry problems. Advantages of an implicit integration scheme are associated with better numerical stability and accuracy which may result in a larger time step size. Discussions on the stability conditions later in the chapter reveal, however, that this advantage is not necessarily true for high frequency cases. Therefore, the dissertation utilizes explicit approaches.

The time integration used in the explicit model is a combination of the central difference approximation for the second order time derivative and the backward difference approximation for the first order time derivative.

$$\ddot{U}_t = \frac{1}{\Delta t^2}(U_{t-\Delta t} - 2U_t + U_{t+\Delta t}) \tag{3.7}$$

$$\dot{U}_t = \frac{1}{\Delta t}(U_t - U_{t-\Delta t}) \tag{3.8}$$

Substituting (3.7) and (3.8) into (2.25) yields

$$\frac{1}{\Delta t^2}MU_{t+\Delta t} = R_t - (K + \frac{1}{\Delta t}D - \frac{2}{\Delta t^2}M)U_t + (\frac{1}{\Delta t}D - \frac{2}{\Delta t^2}M)U_{t-\Delta t} \tag{3.9}$$

where only the mass matrix is presented in the left hand side. It should be noticed that only this particular choice of difference approximation preserves this property. The coefficient matrix of the left hand side involves the damping matrix if the forward or central difference approximation is chosen for the first time derivative term. This then requires additional inverse procedures for the damping matrix. When solved by the finite difference method, the governing equation(2.25) leads to a very similar system [23] as eq. (3.9). The coefficient matrix M, however, is diagonal in the usual finite difference method, which normally iterates the solution explicitly without solving the associated sparse matrix equation. Encouraged by the success of the finite difference formulation and the fact that the consistent matrix is dominated by its diagonal terms as pointed out in Chapter 2, the mass matrix is lumped to a diagonal one in practice through the techniques described in the following section.

Mass Lumping Techniques

With the fully discretized finite element formula (3.9), lumping is introduced to approximate the system by diagonalizing the consistent matrix such that the matrix

inversion process is avoided when solving for the displacement field. For a material of constant mass density, the consistent matrix is the inner product of the shape functions or the basis of finite element space as shown in eq. (2.23a). Diagonalization of the mass matrix is then similar to approximating the basis by an orthogonal set (restricted to the mass matrix only) which obviously violates the convergence requirements of the shape function. Nevertheless, the diagonalized mass matrix is often employed, despite the fact that the consistent matrix leads to optimal error estimates, due to the extremely low computer cost of lumped mass. There are several ways of going about the construction of lumped mass matrices. A nodal quadrature mass matrix [76] is convergent and retains full order of accuracy under some conditions. However, it tends to generate zero and negative masses which is unacceptable in practice because they produce nonphysical behavior such as unbounded solutions. Therefore, the nodal quadrature is not always an effective tool for producing useful lumped-mass matrices.

In the row-sum technique, the elements of the consistent matrix are summed in each row and the result is lumped on the diagonal, that is

$$M_{II}^{diag} = \sum_{J} M_{JI}^{e} \tag{3.10}$$

This method eliminates the problem of zero masses at nodes along the z-axis in problems of axisymmetry. However, the row-sum technique sometimes produces negative masses.

An additional technique for mass lumping is called the special lumping technique [77]. The idea is to set the entries of the lumped mass matrix proportional to the diagonal entries of the consistent mass. This produces necessarily positive lumped masses. The constant of proportionality is selected to conserve the total element

mass. The formula is

$$M_{IJ}^{diag} = \begin{cases} \alpha M_{IJ} & \text{if } I = J \\ 0 & \text{if } I \neq J \end{cases} \tag{3.11}$$

where

$$\alpha = \frac{\sum_I \sum_J M_{IJ}}{\sum_I M_{II}} \tag{3.12}$$

Even though this technique lacks mathematical support, it is the only method that can be recommended for arbitrary elements and has been reported to work well on structural and solid mechanics problems. This dissertation, therefore, adopts this method.

It should be pointed out that, for simple elements, the lumping procedures described above tend to produce similar if not identical masses. For the bilinear quadrilateral element, for example, the lumped mass matrices resulting from different techniques are identical.

Physical interpretations of lumping can be viewed clearly through considering an example of a vibrating string of mass per unit length ρ. Using linear approximation on an element and a uniform mesh, the general row I of the consistent mass matrix corresponding to an interior node I has nonzero tridiagonal entries, so that the typical row I is

$$M_{IJ} = \frac{\rho h}{6}[\ 0\ \ \ldots\ \ 0\ 1\ 4\ 1\ 0\ \ \ldots\ \ 0\ ] \tag{3.13}$$

where h is the length of the element and the nonzero entries are in columns $I - 1$, I, $I + 1$, respectively. The lumping proceeds by adding the off-diagonal terms to the diagonal location and then zeroing the off-diagonals. This can be interpreted

physically as replacing the continuous string by a massless string with the distributed mass now concentrated as "beads" at the nodes.

After diagonalization, the inversion of M^{diag} is trivial and eq. (3.8) can be rewritten explicitly for $U_{t+\Delta t}$ as

$$\begin{aligned} U_{t+\Delta t} &= \Delta t^2 (M^{diag})^{-1} R_t - (K + \frac{1}{\Delta t} D)\Delta t^2 (M^{diag})^{-1} U_t + \\ &\quad + 2U_t + \Delta t (M^{diag})^{-1} D U_{t-\Delta t} - U_{t-\Delta t} \end{aligned} \tag{3.14}$$

Accuracy

Accuracy of the finite element formulation can be considered in two aspects. Standard error estimation provides the proof of the convergence of the algorithm. That is, as the size of the elements in the discretization approaches zero, the finite element solution should converge to the exact solution. For finite element users in practice, however, the requirements of the discretization such as the number of the elements, the element type, etc., are more important to know before discretization. Therefore, the number of the elements needed per wavelength is discussed following the error estimation.

Due to the fact that the viscous damping increases the stability of the algorithm and exponentially attenuates the amplitude of field quantities, the error estimates will follow the analysis of Carey and Oden [78] for the fully discrete approximation of a second-order hyperbolic problem in which finite elements are used for spatial approximation and central differences are used to approximate the temporal behavior of the solution. Assume

1. Finite element approximations of the spatial dependence of the solution are

made using conforming piecewise polynomials of degree k.

2. The time interval $[0,T]$ is partitioned into N equal subintervals with time step size Δt

   $0 = t_0 < t_1 < \ \ldots \ < t_N = T,\ \Delta t = t_{n+1} - t_n.$

3. The time derivatives of the solution are approximated by backward or central difference quotients

$$\dot{u}_i \approx \delta_t^{-1/2} u^n = \frac{u^n - u^{n-1}}{\Delta t} \tag{3.15}$$

$$\ddot{u}_i \approx \delta_t^2 u^n = \frac{u^{n+1} - 2u^n + u^{n-1}}{\Delta t^2} \tag{3.16}$$

   where $u^n = u_i(n\Delta t)$.

If the solution u_i is sufficiently regular that

$$\frac{\partial u_i}{\partial t} \in L^\infty(0,T;\ H^{k+1}(\Omega)) \tag{3.17}$$

$$\frac{\partial^2 u_i}{\partial t^2} \in L^2(0,T;\ H^{k+1}(\Omega)) \tag{3.18}$$

$$\frac{\partial^4 u_i}{\partial t^4} \in L^2(0,T;\ L^2(\Omega)) \tag{3.19}$$

where $L^p(\Omega)$ is the linear space on which the measurable function u_i satisfies

$$\int_\Omega |u_i(t;\ x_i)|^p dv < \infty \tag{3.20}$$

An approximate norm can be associated with it

$$||u_i||_{L^p(\Omega)} = (\int_\Omega |u_i(t;\ x_i)|^p dv)^{1/p} \tag{3.21}$$

which then turns in the space to a Banach or Hilbert space. $H^k(\Omega)$ is a space on which a function u_i satisfies that its derivatives of order k and less are square-integrable

over Ω, that is

$$\int_\Omega [(\frac{\partial^k u_i}{\partial x_i^k})^2 + \quad ... \quad + (\frac{\partial u_i}{\partial x_i})^2 + u_i^2] dv \quad < \quad \infty \tag{3.22}$$

Assume the time step Δt and the maximum element size h are chosen so that the condition for numerical stability, which is discussed in the next section, is satisfied. Let u_h^n represent the discretized version of u^n, then the error

$$e_h^n = u^n - u_h^n \tag{3.23}$$

in the fully discrete approximation satisfies the inequality

$$\begin{aligned} &||\delta_t e_h^n||_{l^\infty(L^2(\Omega))} + C_1 ||e_h^n||_{l^\infty(L^2(\Omega))} \\ &\leq C_2 [||e_h^0||_1 + ||e_h^1||_1 + ||\delta_t \dot{e}_h^{1/2}||_0] + C_3 h^{k+1} [||u||_{L^\infty(H^{k+1}(\Omega))} + \\ &+ ||u_t||_{L^\infty(H^{k+1}(\Omega))} + ||u||_{L^2(H^{k+1}(\Omega))} + \Delta t^2 ||u_{tttt}||_{L^2(L^2(\Omega))}] \end{aligned} \tag{3.24}$$

where

$$\begin{aligned} ||\Delta_t e_h^n||_{l^\infty(L^2(\Omega))} &= = sup_n ||\Delta_t e_h^n||'_{L^2(\Omega)} \\ L^\infty(L^2(\Omega)) &= L^\infty(0,T;\ L^2(\Omega)),, \qquad etc., \end{aligned}$$

and C_1, C_2 and C_3 are constants independent of h and Δt. When $h \rightarrow 0$, the stability condition requires $\Delta t \rightarrow 0$, it is obvious that the terms involving $C_3 h^{k+1}$ approach to zero. The terms with C_2 represent initial errors which can be shown to be zero as $h \rightarrow 0$ from the error estimation of the semi-discrete formula [31]. Therefore, both e_h^n and $\delta_t e_h^n$ converge to zero as $h \rightarrow 0$, which implies that both u_h^n and $\delta_t u_h^n$ converge to the exact solution u_i and $\dot{u}_i$, respectively.

It has been pointed out by Strang and Fix [79] that the lumped mass implicitly uses elements of low degree, such as piecewise constants, in dealing with terms which

are not differentiated with respect to spatial variables. There is no loss in accuracy if a consistent mass matrix is replaced by a diagonal one through a suitable lumping process provided that the elements used are low degree.

With regard to the requirement on the number of elements per wavelength needed for discretization, a numerical example is chosen in a 2-D geometry to illustrate the effects caused by coarse grids.

Consider a 10 cm x 5 cm aluminum block shown in Fig. 3-1a with a density $\rho = 2700\ kg/m^3$, a longitudinal velocity $v_l = 6300\ m/s$ and a shear velocity $v_s = 3100\ m/s$. This block is excited by a line source of raised cosine function whose waveform is shown in Fig. 3-1b. Using the formulation of the 2-D plane strain approximation to be discussed in detail in Chapter 4, we compute the displacement field under different discretizations. Results are shown in Fig. 3-2 where the wavefronts on a half of the block are displaced. By comparison with classical analysis [73] one can conclude that at least eight nodes per shortest wavelength are required in order to produce all the artifacts associated with such a situation. If more accurate results are required for better consistency of the wave form, twelve nodes per shortest wavelength are recommended [80].

Stability

An integration scheme is called stable if the error in the system measured under a certain norm does not become unbounded as time increases. The stability consideration, therefore, governs both system responses and the choice of the time step size.

Due to the fact that the central difference scheme can be considered as a member

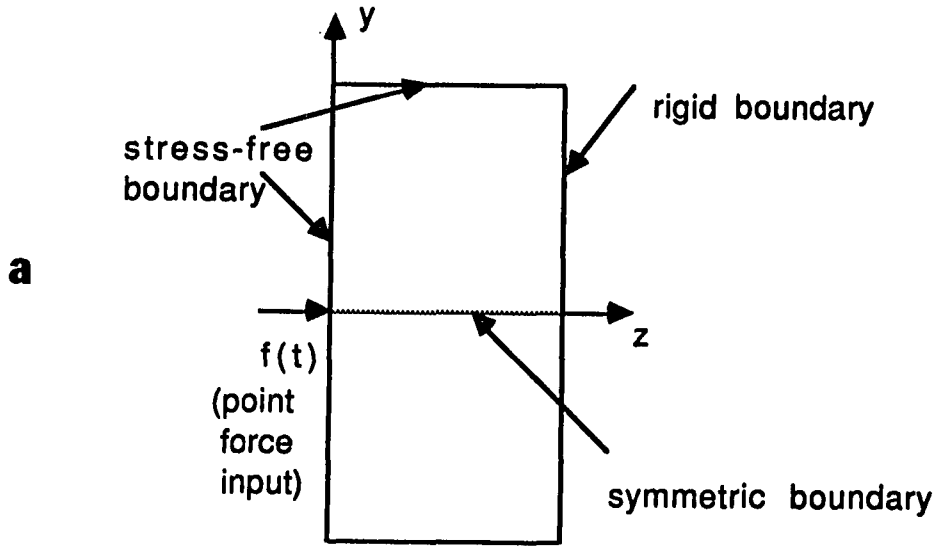

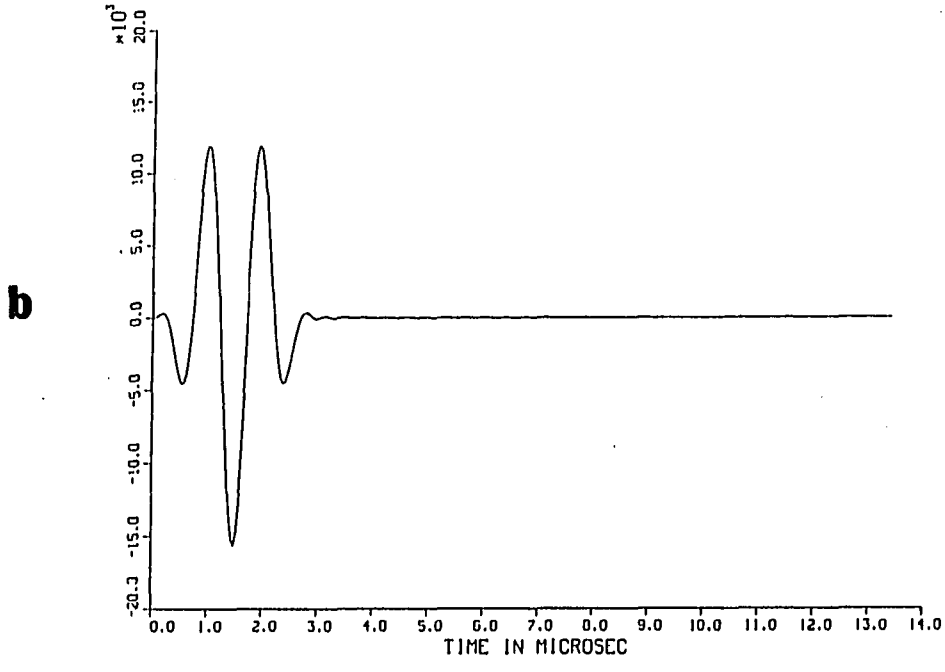

Figure 3.1: A typical 2-D geometry and waveform used for finite element study: a) Geometry; b) Input waveform

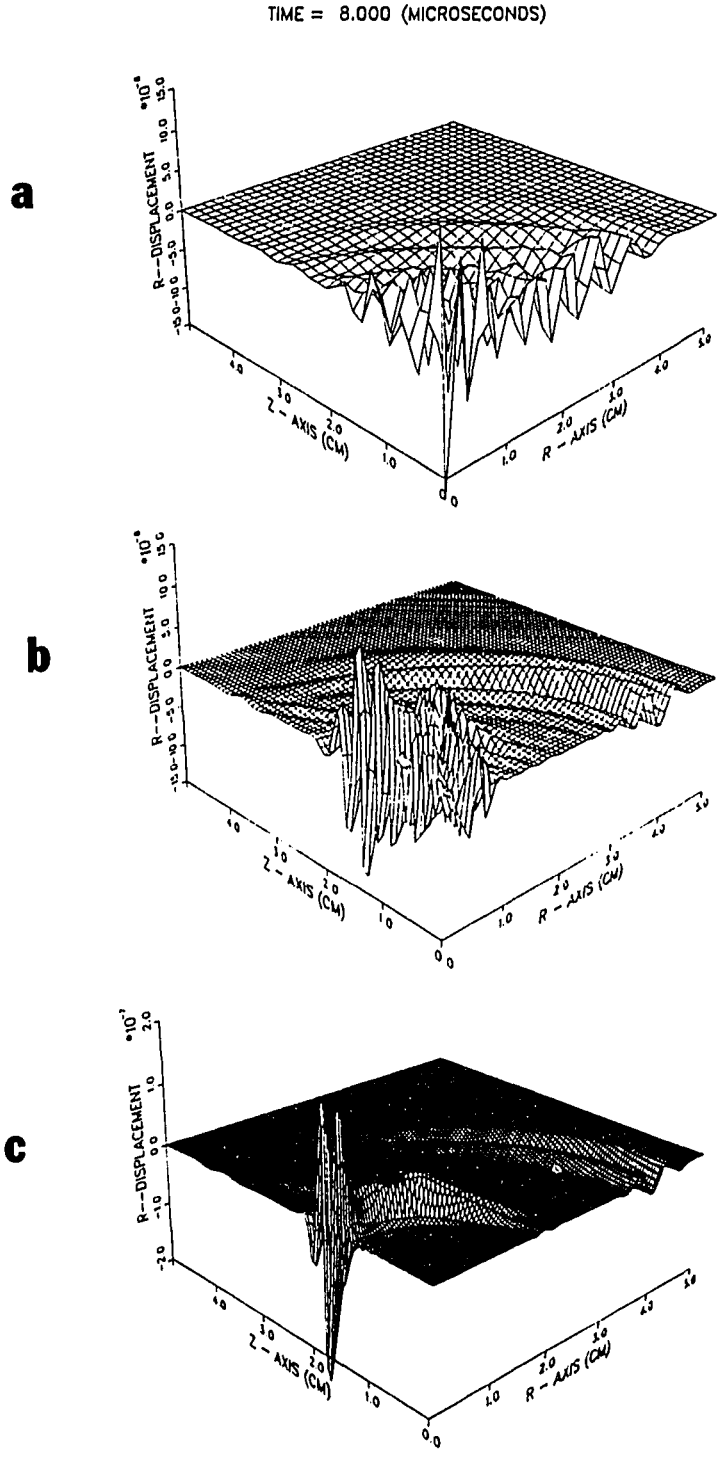

Figure 3.2: Wavefront comparison at different discretization levels: a) 2 nodes per shear wavelength; b) 4 nodes per shear wavelength; c) 8 nodes per shear wavelength

of the Newmark family of methods with the choice of $\alpha = 0, \beta = \frac{1}{2}$, the following analysis is concentrated on the Newmark family.

For simplicity, we assume the damping matrix in eq. (2.26) is in the form of Rayleigh damping, i.e.,

$$D = aM + bK \tag{3.25}$$

which then defines a parameter called damping ratio as

$$\xi = \frac{1}{2}(\frac{a}{\omega} + b\omega) \tag{3.26}$$

where a and b are constants, ω is the frequency of the mode under consideration. The convergence analysis of the Newmark family of methods for eq. (2.26) concludes a summary of stability conditions as given in [31]

Unconditional

$$2\alpha \geq \beta \geq \frac{1}{2} \tag{3.27}$$

Conditional

$$\beta \geq \frac{1}{2} \tag{3.28}$$

$$\alpha < \frac{\beta}{2} \tag{3.29}$$

$$\omega^h \Delta t \leq \Omega_{crit} \tag{3.30}$$

where

$$\Omega_{crit} = \frac{\xi(\beta - \frac{1}{2}) + [\frac{\beta}{2} - \alpha + \xi^2(\beta - \frac{1}{2})^2]^{1/2}}{(\frac{\beta}{2} - \alpha)} \tag{3.31}$$

which is called the critical sampling frequency; ω^h is the natural frequency of elements. It is obvious that if $\beta = \frac{1}{2}$ viscous damping has no effect on stability. The

trapezoidal rule of $\alpha = \frac{1}{4}$ and $\beta = \frac{1}{2}$ results in an unconditionally stable scheme. If the effect of viscous damping is neglected, the stability of the algorithm used in the thesis is the same as that of the central difference scheme. The critical sampling frequency then is given as [31]

$$\Omega^{cf}_{crit} = 2 \tag{3.32}$$

The stability conditions stated above must be satisfied for each mode in the system. Consequently, a maximum natural frequency ω^h_{max} is critical and therefore must satisfy eq. (3.30). For the bilinear quadrilateral elements in 2-D or hexahedral elements in 3-D, Flanagan and Belytschko [81] obtain the following maximum element frequency

$$\omega^h_{max} \leq v_l g^{1/2} \tag{3.33}$$

where v_l is the longitudinal wave velocity and g is a geometric parameter. For example, in the case of the quadrilateral element, g is defined as

$$g = \frac{4}{A^2} \sum_{i=1}^{2} \sum_{I=1}^{4} B^2_{iI} \tag{3.34}$$

where

$$[B_{iI}] = \frac{1}{2} \begin{bmatrix} (y_2 - y_4) & (y_3 - y_1) & (y_4 - y_2) & (y_1 - y_3) \\ (x_4 - x_2) & (x_1 - x_3) & (x_2 - x_4) & (x_3 - x_1) \end{bmatrix} \tag{3.35}$$

where x_I and y_I are the coordinates of node I and A is the area. For the central difference scheme, this results in a sufficient condition for the stability

$$\Delta t \leq \frac{2}{v_l g^{1/2}} \tag{3.36}$$

As an explicit example, a rectangular element with side lengths h_1 and h_2 is considered. Its geometric parameter is

$$g = 4(\frac{1}{h_1^2} + \frac{1}{h_2^2}) \tag{3.37}$$

which then gives the stability condition

$$\Delta t \leq \frac{1}{v_l(\frac{1}{h_1^2} + \frac{1}{h_2^2})^{1/2}} \tag{3.38}$$

This is, however, a sufficient condition, which may not be necessary. Numerical examples of a square element of side length h has resulted in the stability condition [80]

$$\Delta t < \frac{h}{v_l} \tag{3.39}$$

which is larger than the analytical one ($\Delta t \leq \frac{h}{\sqrt{2}V_l}$). Equation (3.39) means that the time step should be less than the transit time for the longitudinal wave traveling to traverse the shortest distance across the element.

Even though the implicit Newmark scheme with the choice of $\alpha = \frac{1}{4}, \beta = \frac{1}{2}$ is unconditionally stable, the time step size can not be unlimited. The semi-discretized finite element formulation assumes implicitly that the wave travels less than the shortest distance among nodes in one time step. The time step size should be chosen such that this assumption is not violated. Severe accumulations of error would otherwise occur from the formulation which would invalidate the whole result. Fig. 3-3 shows precisely what would happen if the time step goes beyond this limit where the geometry in Fig. 3-1 is used. The time step size is varied under a fixed spatial discretization. It can be seen that when $\frac{\Delta t v_l}{h} = 0.84$, the solution is stable

as illustrated in Fig. 3-3a. However, the accumulated error dominates the solution when $\frac{\Delta t v_l}{h} = 1.008$ as plotted in Fig. 3-3b and the solution diverges rapidly toward infinity. Therefore, one requirement regardless of the integration schemes is

$$\Delta t < \frac{h}{v_l} \tag{3.40}$$

which coincides with the stability requirement of the central difference scheme. The implicit Newmark scheme then loses the claimed advantage of using a larger time step than the central difference scheme.

It is interesting to note, as pointed out by Hughes [31], that reducing the size of the time step while holding the mesh length fixed can only worsen the results. It converges to the exact solution of the spatially discrete, temporally continuous system rather then the exact solution. It is generally believed advantageous to compute at a time step as close to critical as possible.

Stability analysis shows also that the diagonalization of the mass matrix tends to yield a larger critical step than the consistent mass matrix. For example, the stability condition for the vibrating string discussed before is $\Delta/h < 1/\sqrt{3}$ for the consistent mass and $\Delta/h < 1$ for a lumped one.

Experiences in elastodynamics suggest that the matches between integration schemes and the mass matrices can improve the accuracy of the finite element formulation due to the different tendency to the solution by mass matrices (consistent or lumped) and integration schemes (implicit or explicit). The appropriate matches are the explicit central difference scheme with the lumped mass matrix, and the implicit Newmark scheme with the consistent matrix.

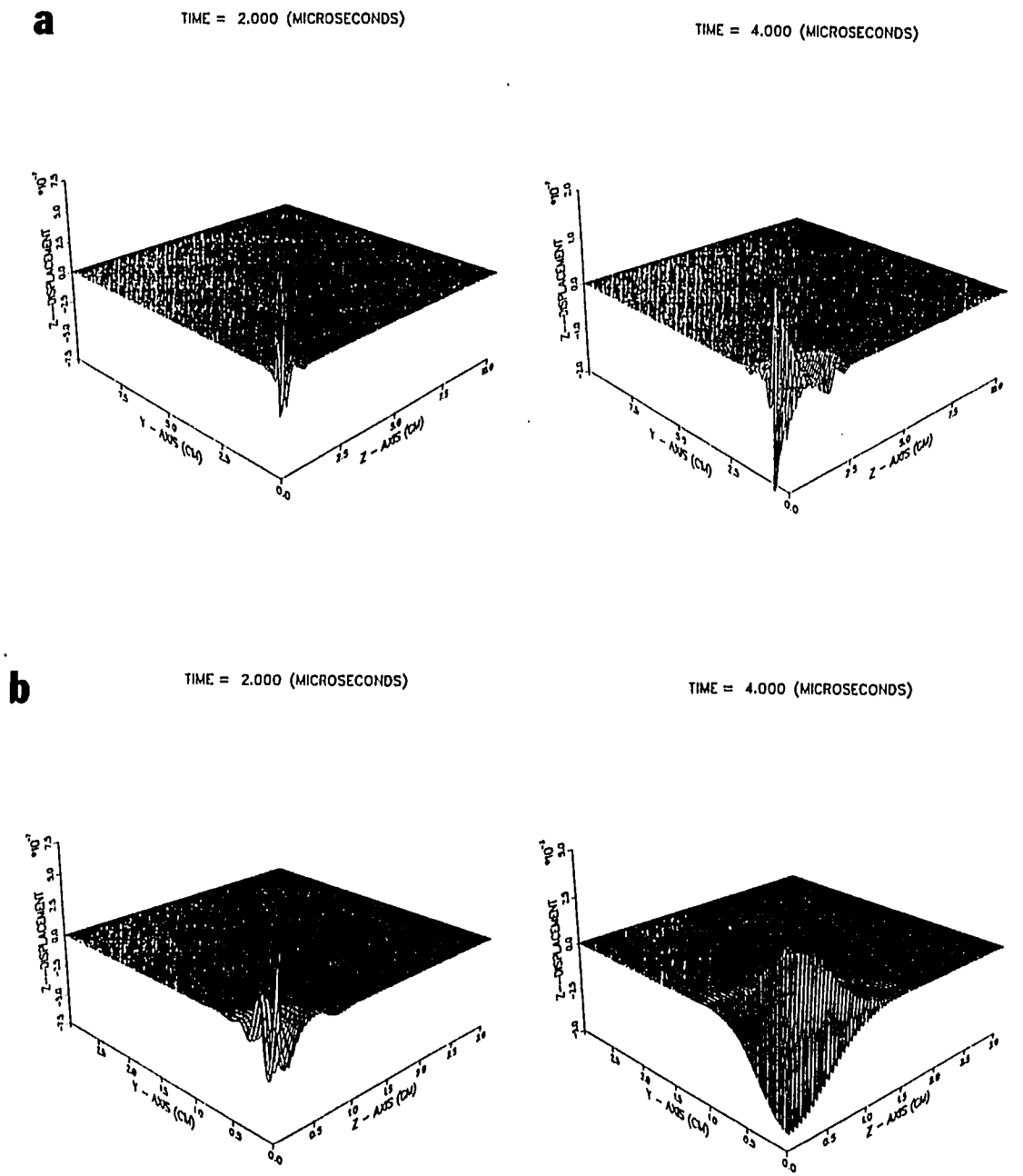

Figure 3.3: Illustration of the stability condition: a) $\frac{\Delta t v_l}{h} = 0.84 < 1$, stable; b) $\frac{\Delta t v_l}{h} = 1.008 > 1$, unstable

CHAPTER 4. TWO-DIMENSIONAL AND AXISYMMETRIC CONSIDERATIONS

Although a full three-dimensional formulation is most desirable, its implementation is restricted to simple geometries due to limited computer resources. For many engineering problems, a simplified formulation may be more suitable if it provides dependable solutions within reasonable costs. An obvious simplification is to reduce one dimension to a 2-D or an axisymmetric formulation depending upon the geometry. It has been shown in various areas that a 2-D or an axisymmetric finite element formulation is amazingly useful, even though it is only an approximation to a true 3-D geometry. This chapter, therefore, concerns the 2-D and axisymmetric conditions as well as their formulations. Special considerations are given to the treatment of elastic anisotropy.

Two-Dimensional Formulation

A fully three-dimensional situation reduces to a two-dimensional problem if all quantities are independent of one of the coordinate directions, assumed to be the z-axis. Futhermore, for a planar condition to exist, all body forces and surface tractions acting on the solid must act in the xy plane only, i.e., there should be no z components. In addition, if the normal strain or the displacement in the z direction is

zero then a plane strain condition is said to exist. In this case, the only nonzero stress components are the in-plane components T_{xx}, T_{yy}, T_{xy} and the through thickness stress T_{zz}. All equations are satisfied making this an exact formulation within the framework of three-dimensional elasticity. This condition is applicable to the problem where the thickness of the solid (in the z direction) is large in comparison with the representative x and y dimensions.

The other commonly used condition is that of plane stress by which normal stress in the z direction is assumed to be zero. In this case, the in-plane stress components T_{xx}, T_{yy} and T_{xy} are again nonzero together with the normal strain component. This is an approximation mainly for the case of a thin body (small dimension in z in comparison with the representative x and y dimensions) without surface forces acting on the end surface.

It is obvious that the plane strain condition should be chosen because the geometries considered in this thesis are mainly thick bodies (large in z dimension). Under this assumption, the displacement u_z vanishes, and the displacements u_x, u_y are functions of the coordinates x and y only, i.e., all derivatives with respect to z are zero. Therefore, equation(2.8) reduces to a 2-D formula which can be written in the following operator form

$$\nabla \cdot T = \rho \underline{\ddot{u}} \tag{4.1}$$

where

$$\nabla \cdot = \begin{bmatrix} \frac{\partial}{\partial x} & 0 & \frac{\partial}{\partial y} \\ 0 & \frac{\partial}{\partial y} & \frac{\partial}{\partial x} \end{bmatrix} \tag{4.2}$$

$$T = \begin{bmatrix} T_{xx} \\ T_{yy} \\ T_{xy} \end{bmatrix} = C'S + \eta\dot{S} \tag{4.3}$$

$$C' = \begin{bmatrix} C_{11} & C_{12} & C_{16} \\ C_{12} & C_{22} & C_{26} \\ C_{16} & C_{26} & C_{66} \end{bmatrix} \tag{4.4}$$

where an index transformation of $xx \rightarrow 1$, $yy \rightarrow 2$, $zz \rightarrow 3$, yz (and zy) $\rightarrow 4$, xz (and zx) $\rightarrow 5$, xy (and yx) $\rightarrow 6$ is introduced and the symmetric property of the elastic constant tensor is used. And

$$\eta = \begin{bmatrix} \eta_{11} & \eta_{12} & \eta_{16} \\ \eta_{12} & \eta_{22} & \eta_{26} \\ \eta_{16} & \eta_{26} & \eta_{66} \end{bmatrix} \tag{4.5}$$

$$S = \begin{bmatrix} S_{xx} \\ S_{yy} \\ 2S_{xy} \end{bmatrix} = \begin{bmatrix} \frac{\partial}{\partial x} & 0 \\ 0 & \frac{\partial}{\partial y} \\ \frac{\partial}{\partial y} & \frac{\partial}{\partial x} \end{bmatrix} \begin{bmatrix} u_x \\ u_y \end{bmatrix} = A\underline{u} \tag{4.6}$$

where the viscosity constant tensor is assumed to have the same symmetry as that of the elastic constants. Notice also that a nonzero normal stress exists. For an isotropic material, for instance, it can be calculated by

$$T_{zz} = -\nu(T_{xx} + T_{yy}) \tag{4.7}$$

where ν is the Poisson ratio.

In order to solve the 2-D elastic wave equation(4.1) by the finite element method, similar procedures to those described in Chapter 2 must be followed. With the

operator representation, the resulting elemental matrices (equation(2.23)) in 2-D now can be written as

$$M^e = \int\int \rho N^T N dx dy \tag{4.8a}$$

$$K^e = \int\int (AN)^T C AN dx dy \tag{4.8b}$$

$$D^e = \int\int (AN)^T \eta AN dx dy \tag{4.8c}$$

$$R^e = \int_{\Gamma_t^e} N^T \underline{t} ds \tag{4.8d}$$

where

$$N = \begin{bmatrix} N_1 & N_2 & \dots & N_{Ne} \\ N_1 & N_2 & \dots & N_{Ne} \end{bmatrix} \tag{4.9}$$

is a matrix of shape functions defined for a 2-D element and A is the operator defined in eq. (4.6). The rest of the process is the same as described in Chapter 2 and 3.

For an isotropic material with Lame constants λ and μ, the elastic constant tensor can be expressed as

$$C = \begin{bmatrix} \lambda + 2\mu & \lambda & 0 \\ \lambda & \lambda + 2\mu & 0 \\ 0 & 0 & \mu \end{bmatrix}$$

Longitudinal and shear velocities are related to Lame constants through

$$v_l^2 = \frac{\lambda + 2\mu}{\rho} \quad \text{and} \quad v_s^2 = \frac{\mu}{\rho}$$

It can be shown that the property transformation always gives the same values for the isotropic elastic constants. Notice that there are still the same two independent

parameters in the 2-D equation which produce two wavefronts as does the 3-D equation. The main restriction for the 2-D approximation, therefore, is that the source is modeled as a line source or strip-like transducer, which then results in cylindrical types of wavefronts. A real 3-D model, on the other hand, can simulate point sources and finite aperture transducers which produce spherical types of wavefronts. Ludwig [30] presents many results for 2-D isotropic cases and compares them extensively with experimental results as an approximation. A comparison of finite element results subjected to a line source excitation with corresponding analytical solutions can be found in [7]. Results of wave interactions with defects in 2-D geometries are illustrated in the next Chapter.

For anisotropic media, the testing situations are more complicated. In general, there are three wavefronts associated with a 3-D geometry, while only two wavefronts can be modeled in a 2-D formulation. Moreover, the reduction to 2-D from a 3-D equation generally excludes some of the independent elastic (and viscosity) constants. For example, an orthorhombic material has 9 independent constants in 3-D. Only four of them are used in the 2-D equation as.

$$C = \begin{bmatrix} C_{11} & C_{12} & 0 \\ C_{12} & C_{22} & 0 \\ 0 & 0 & C_{66} \end{bmatrix}$$

where $C_{33}, C_{13}, C_{23}, C_{44}$ and C_{55} are deleted from the formulation. The 2-D results would be accurate if the plane strain condition is well satisfied. In many cases, however, the 2-D condition is only an approximation. The reliability of the solutions for 2-D anisotropic problems is obviously less than that for an isotropic material because more information is missed in the anisotropic cases.

The property transformation for anisotropic media usually gives a set of new values. An example of the property transformation for the orthorhombic material gives

$$C' = \begin{bmatrix} C'_{11} & C'_{12} & C'_{16} \\ C'_{12} & C'_{22} & C'_{26} \\ C'_{16} & C'_{26} & C'_{66} \end{bmatrix}$$

where

$$C'_{11} = a_{11}^4 C_{11} + 2a_{11}^2 a_{12}^2 C_{12} + a_{12}^4 C_{22} + 4a_{11}^2 a_{12}^2 C_{66} \quad (4.10a)$$

$$C'_{22} = a_{21}^4 C_{11} + 2a_{21}^2 a_{22}^2 C_{12} + a_{22}^4 C_{22} + 4a_{21}^2 a_{22}^2 C_{66} \quad (4.10b)$$

$$C'_{12} = a_{11}^2 a_{21}^2 C_{11} + a_{11}^2 a_{22}^2 C_{12} + 4a_{11} a_{12} a_{21} a_{22} C_{66} + \\ + a_{12}^2 a_{21}^2 C_{12} + a_{12}^2 a_{22}^2 C_{22} \quad (4.10c)$$

$$C'_{16} = a_{11}^3 a_{21} C_{11} + a_{11}^2 a_{12} a_{22} C_{12} + a_{12}^2 a_{11} a_{21} C_{12} + \\ + a_{12}^3 a_{22} C_{22} + 2a_{11}^2 a_{12} a_{22} C_{66} + 2a_{11} a_{12}^2 a_{21} C_{66} \quad (4.10d)$$

$$C'_{26} = a_{21}^3 a_{11} C_{11} + a_{21}^2 a_{12} a_{22} C_{12} + a_{22}^2 a_{11} a_{21} C_{12} + \\ + a_{22}^3 a_{12} C_{22} + 2a_{21}^2 a_{22} a_{11} C_{66} + 2a_{21} a_{22}^2 a_{12} C_{66} \quad (4.10e)$$

$$C'_{66} = a_{11}^2 a_{21}^2 C_{11} + 2a_{11} a_{12} a_{21} a_{22} C_{12} + a_{12}^2 a_{22}^2 C_{22} + \\ + a_{11}^2 a_{22}^2 C_{66} + a_{12}^2 a_{12}^2 C_{66} + 2a_{11} a_{12} a_{21} a_{22} C_{66} \quad (4.10f)$$

and $a_{11}, a_{12}, a_{21}, a_{22}$ are the elements of the transformation matrix which, for a counterclockwise rotation of angle θ, are of the form:

$$[a] = \begin{bmatrix} a_{11} & a_{12} \\ a_{21} & a_{22} \end{bmatrix} = \begin{bmatrix} \cos\theta & \sin\theta \\ -\sin\theta & \cos\theta \end{bmatrix} \quad (4.11)$$

For example, when $\theta = 90^o$, the property transformation results in

$$C' = \begin{bmatrix} C_{22} & C_{12} & 0 \\ C_{12} & C_{11} & 0 \\ 0 & 0 & C_{66} \end{bmatrix}$$

which can be seen intuitively.

The zero constants may apparently become nonzero after the transformation. However, the number of independent constants for a given material does not change with the transformation.

It should also be noticed that if a different 2-D plane, for example, the yz plane, is considered, the elastic constant tensor then is correspondingly chosen to be

$$C = \begin{bmatrix} C_{22} & C_{23} & C_{24} \\ C_{23} & C_{33} & C_{34} \\ C_{24} & C_{34} & C_{44} \end{bmatrix}$$

In some cases, it may be necessary to perform the property transformation in 3-D before reducing the 3-D equation to 2-D.

Even though the waves of a general anisotropic material described by a 2-D equation are different from those resulting from the 3-D equation, anomalous phenomena due to the anisotropy are predicted qualitatively by the 2-D model. Fig. 4-1 shows the wavefront for an orthorhombic block with the geometry shown in Fig. 3-1 and paramters:

$$C_{11} = 9.313 \times 10^{10}\ N/m^2 \qquad C_{22} = 3.722 \times 10^{10}\ N/m^2$$

$$C_{66} = 2.670 \times 10^{10}\ N/m^2 \qquad C_{12} = 1.130 \times 10^{10}\ N/m^2$$

$$\rho = 2983\ kg/m^3$$

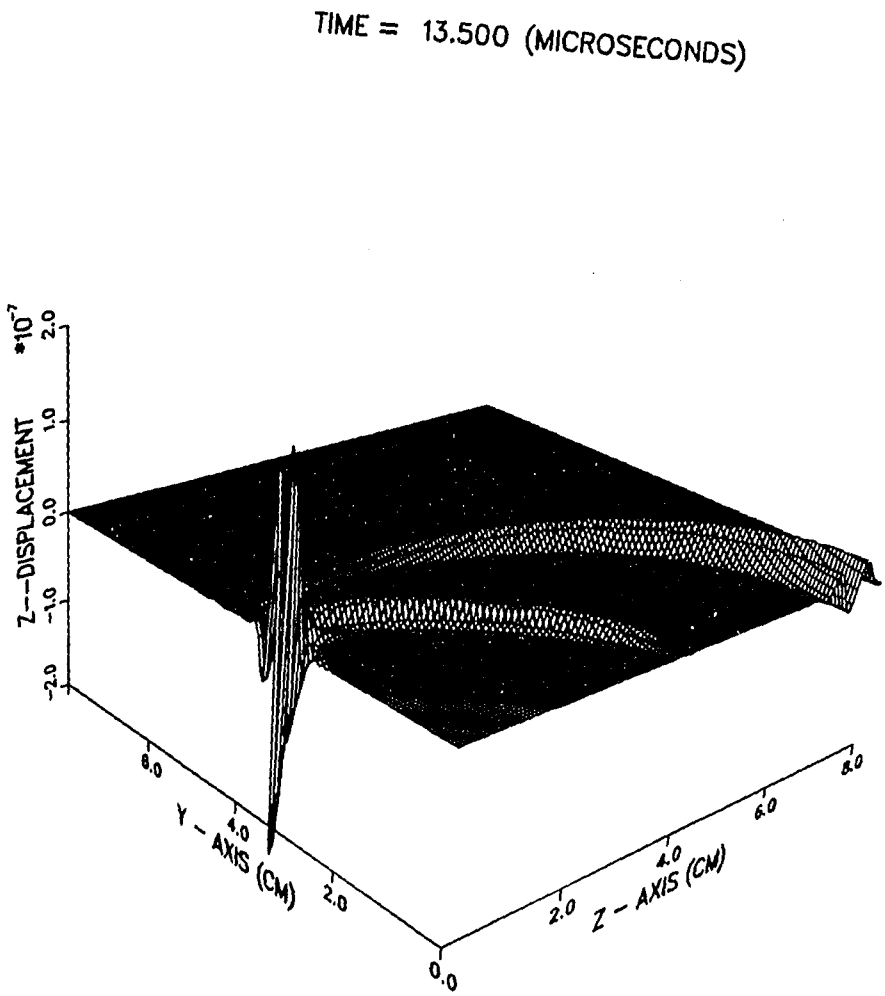

Figure 4.1: 2-D anisotropic wavefront illustration

at 5 μs upon the action of a line source (2-D point source), given by $\cos(\omega t)[1 - \cos(\omega t/3)]$, which can obviously be compared with the velocity surface obtained by inverting the slowness surface resulted from the solution of the Christoffel equation [72]. The basic shape of the wavefronts shows the anisotropic nature. In addition, all other relevant waves are also clearly presented, including the shear wave, the head wave and the surface wave, because only a half space (finite block) is modeled.

Using a finite aperture model in which a uniform energy distribution over the aperture area ($1/2''$ diameter) is assumed, the effects of focusing, defocusing and skewing [82] are successfully predicted for the afore mentioned orthorhombic material of geometry shown in Fig. 4-2. The displacement distribution in this material at different time are shown in Fig. 4-3 when the grain axis parallel to the direction of phase velocity. The source signal is still taken in the form of a triple cosine function. The similar results for the situations with the grain axis perpendicular and at a 45^o angle to the direction of phase velocity are illustrated in Figs. 4-4 and 4-5. The defocusing effect in Fig. 4-4 can be seen clearly in comparison with the focusing effect shown in Fig. 4-3. The skewing phenomenon depicted in Fig. 4-5 are due to the different directions of the group velocity and phase velocity. In order to give an overall comparison, these three effects are summarized in Fig. 4-6.

Axisymmetric Formulation

Reconsider the wave equation(2.8). Axisymmetric conditions assume that both the geometry and boundary conditions are symmetric with respect to the z-axis which implies that the stresses, strain, and displacements are independent of the θ-coordinate. Therefore, all derivatives with respect to θ vanish. In addition, the

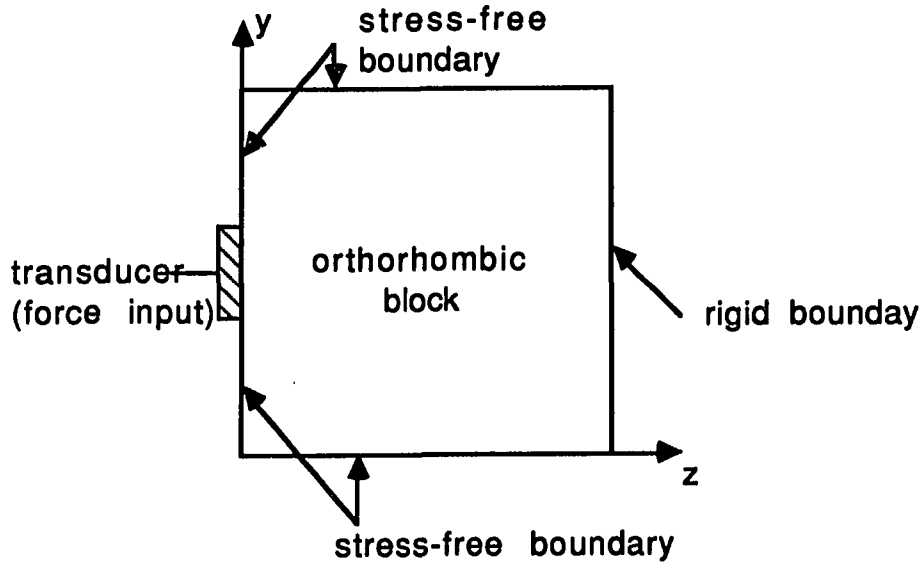

Figure 4.2: Illustration of the geometry used for predicting anomalous phenomena of wave propagation in the orthorhombic material

displacement component u_θ (tangent to the θ direction), the shear strain $S_{r\theta}, S_{\theta z}$ and the shear stresses $T_{r\theta}, T_{\theta z}$ are all zero. Introducing the operator

$$\nabla\cdot = \begin{bmatrix} (\frac{\partial}{\partial r} + \frac{1}{r}) & 0 & \frac{\partial}{\partial z} & -\frac{1}{r} \\ 0 & \frac{\partial}{\partial z} & (\frac{\partial}{\partial r} + \frac{1}{r}) & 0 \end{bmatrix} \tag{4.12}$$

gives the governing equation for axisymmetric geometries in the form of eq. (4.2) with

$$T = \begin{bmatrix} T_{rr} \\ T_{zz} \\ T_{rz} \\ T_{\theta\theta} \end{bmatrix} = CS + \eta\dot{S} \tag{4.13}$$

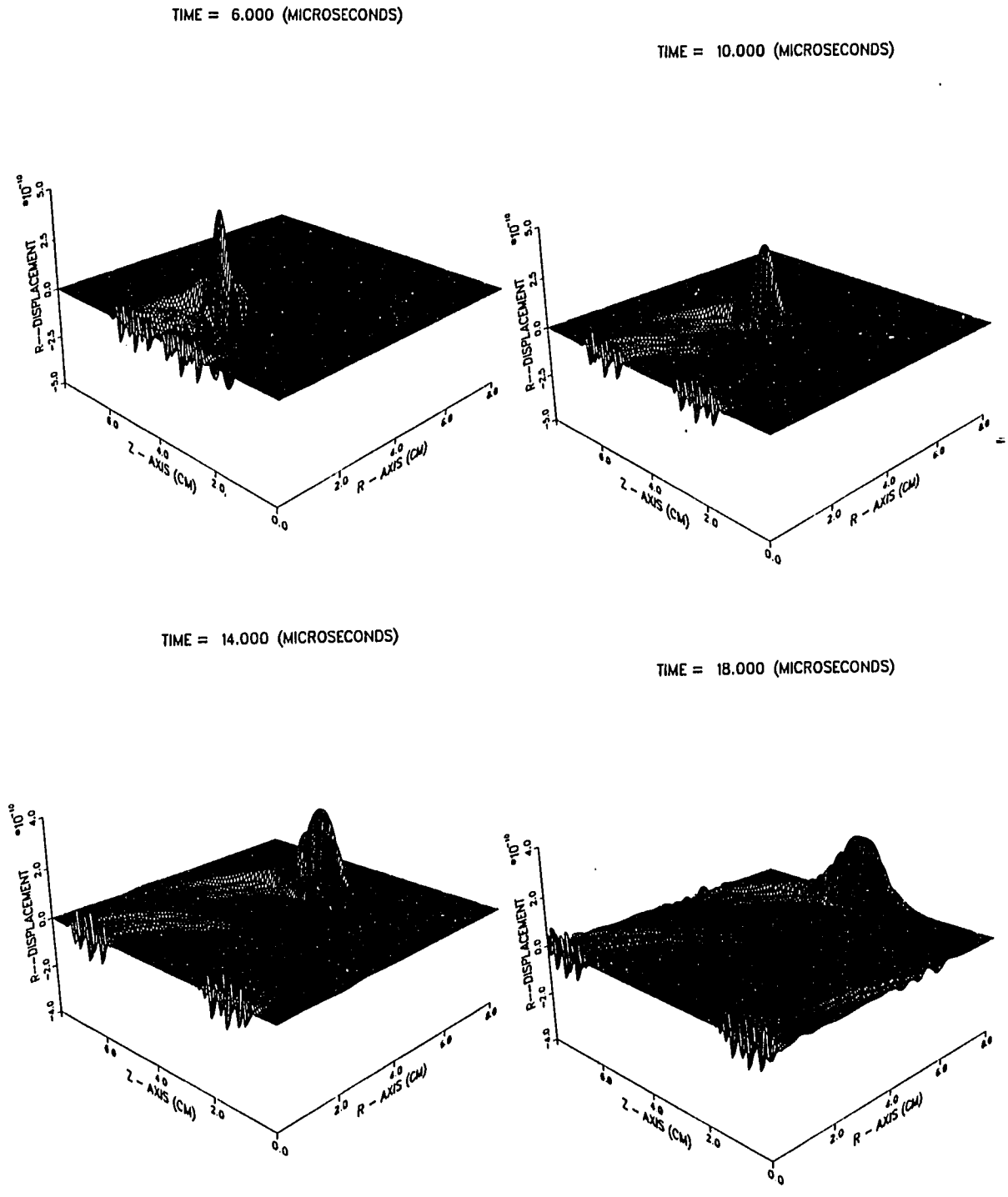

Figure 4.3: Wave propagation along the grain orientation

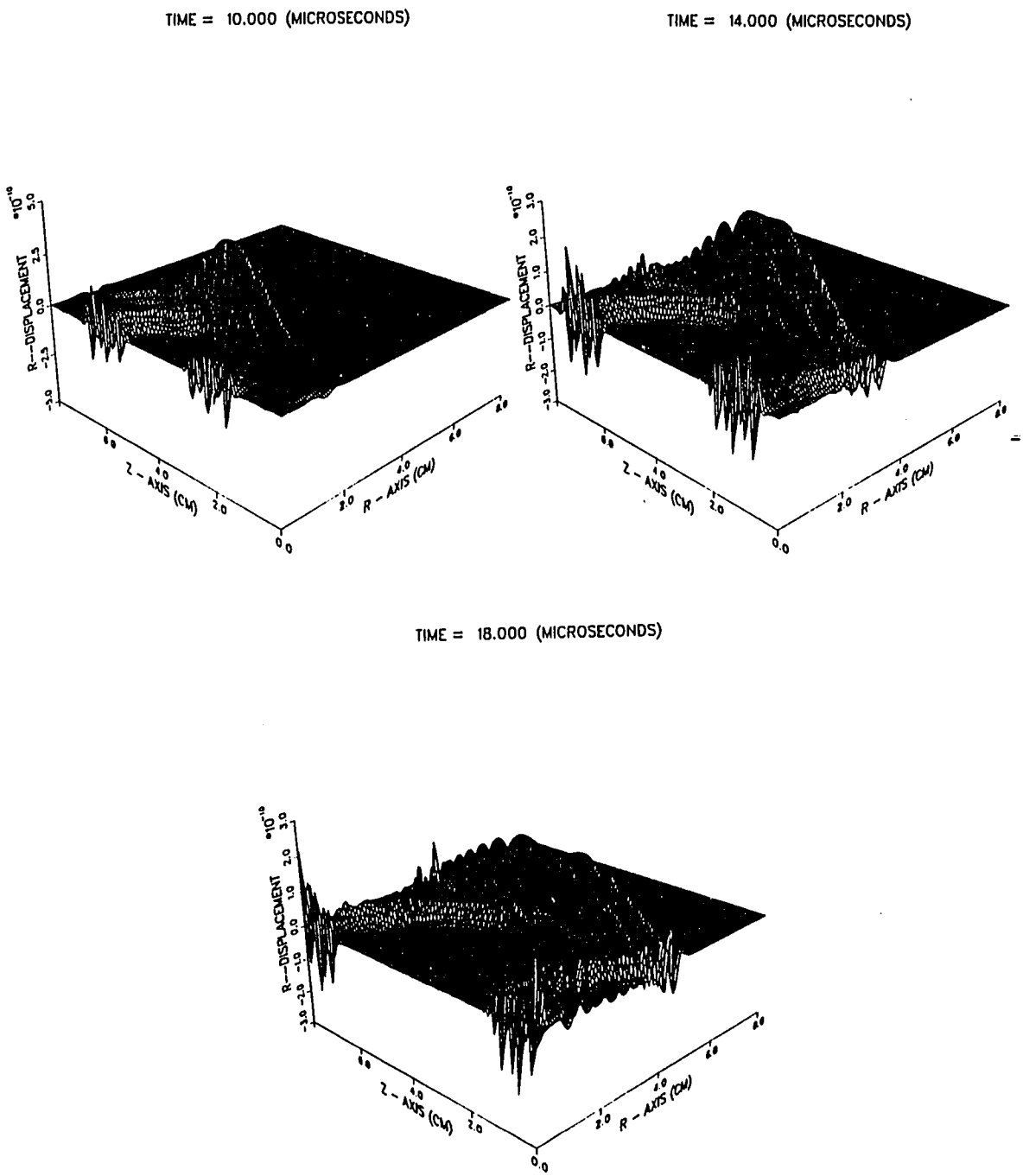

Figure 4.4: Wave propagation along the perpendicular direction of the grain orientation

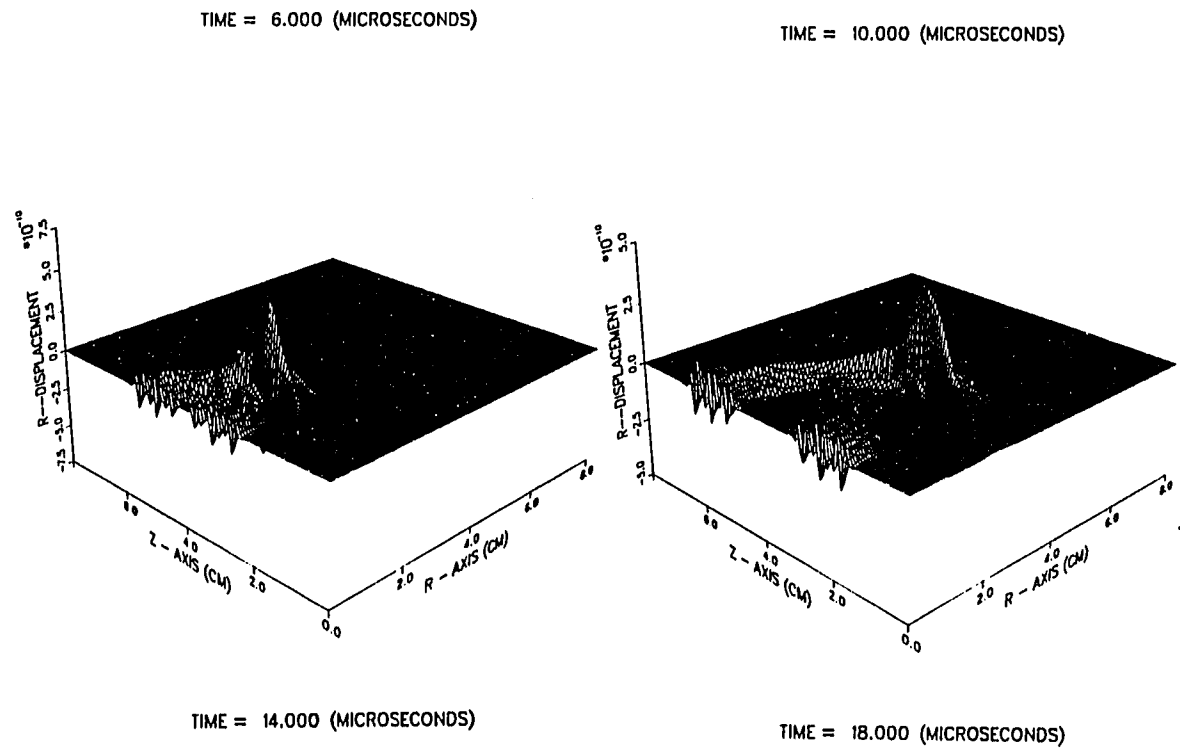

Figure 4.5: Wave propagation at the 45^{o} angle to the grain orientation

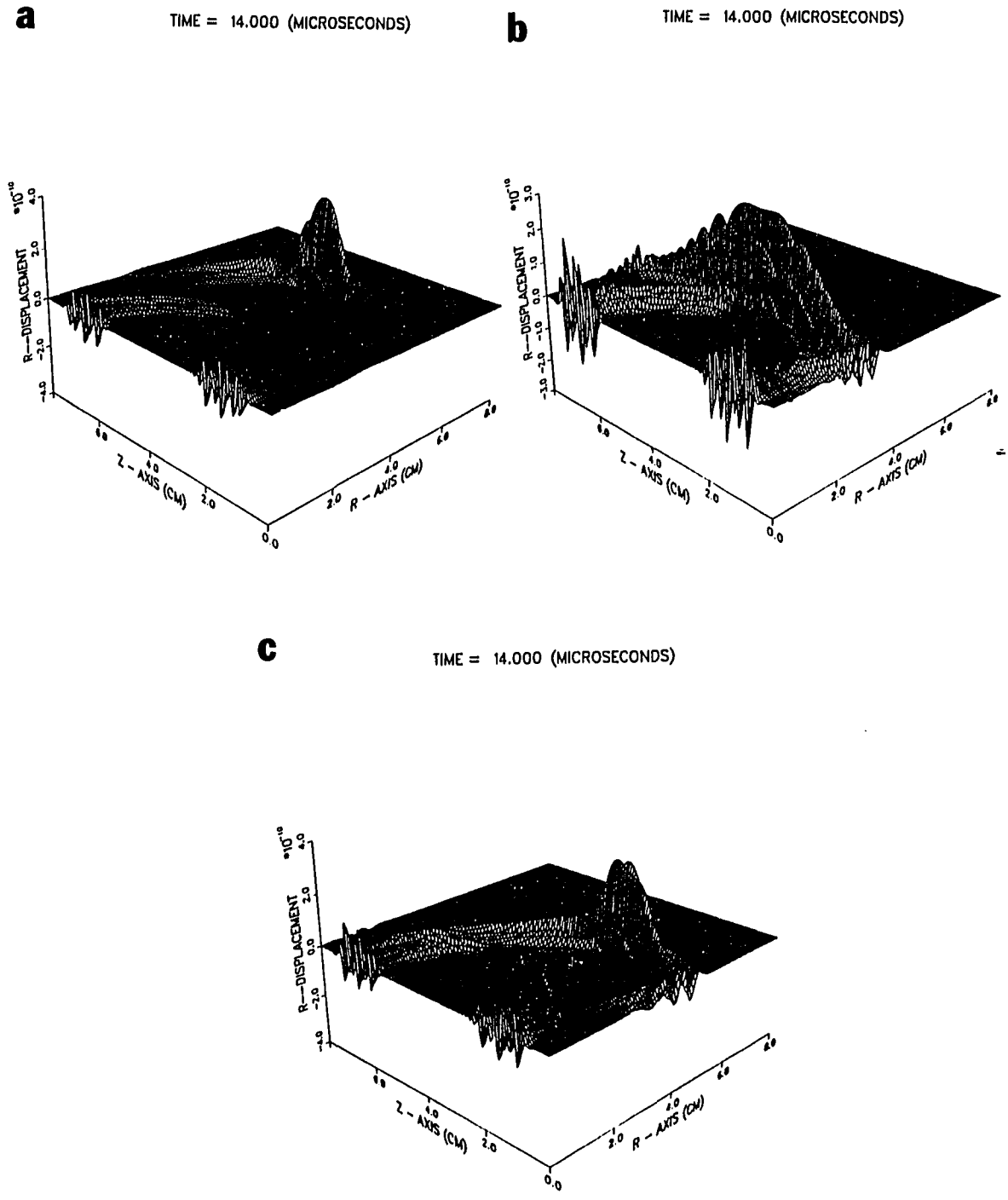

Figure 4.6: Comparisons of wave propagation phenomena associated with different propagation directions: a) Focusing; b) Defocusing; c) Skewing

where the elastic constant tensor C' is in the axisymmetric form. For an isotropic material, it can be written as

$$C' = \begin{bmatrix} \lambda+2\mu & \lambda & 0 & \lambda \\ \lambda & \lambda+2\mu & 0 & \lambda \\ 0 & 0 & \mu & 0 \\ \lambda & \lambda & 0 & \lambda+2\mu \end{bmatrix} \tag{4.14}$$

and once again, the symmetry of the viscosity constant tensor is assumed to be the same as that of the elastic constants, i.e.

$$\eta = \begin{bmatrix} \eta_{11} & \eta_{12} & 0 & \eta_{12} \\ \eta_{12} & \eta_{11} & 0 & \eta_{12} \\ 0 & 0 & \eta_{44} & 0 \\ \eta_{12} & \eta_{12} & 0 & \eta_{11} \end{bmatrix} \tag{4.15}$$

where $\eta_{44} = \frac{1}{2}(\eta_{11} - \eta_{12})$.

The axisymmetric strain tensor is defined by

$$S = \begin{bmatrix} S_{rr} \\ S_{zz} \\ 2S_{rz} \\ S_{\theta\theta} \end{bmatrix} = \begin{bmatrix} \frac{\partial}{\partial r} & 0 \\ 0 & \frac{\partial}{\partial z} \\ \frac{\partial}{\partial z} & \frac{\partial}{\partial r} \\ \frac{1}{r} & 0 \end{bmatrix} \begin{bmatrix} u_r \\ u_z \end{bmatrix} = A\underline{u} \tag{4.16}$$

If, for a transversely isotropic (hexagonal) material, the z-axis of the coordinates is chosen to be coincident with the normal of the isotropic plane, the corresponding

3-D elastic wave equation can also be reduced to an axisymmetric form provided that the boundary conditions and geometry are all axisymmetric. The resulting elastic constant tensor, as introduced in eq. (4.13), now becomes

$$C = \begin{bmatrix} C_{11} & C_{13} & 0 & C_{12} \\ C_{13} & C_{33} & 0 & C_{13} \\ 0 & 0 & C_{44} & 0 \\ C_{12} & C_{13} & 0 & C_{11} \end{bmatrix} \tag{4.17}$$

where all five independent parameters of an hexagonal medium in full 3-D geometries are involved.

It should be noted that, from the symmetry of the material structure, only isotropic and transversely isotropic materials possess an axisymmetric property because of the parameter relationship $C_{66} = \frac{1}{2}(C_{11} - C_{12})$ for hexagonal and $C_{44} = \frac{1}{2}(C_{11} - C_{12})$ for isotropic materials. This implies that only these two types of materials can possibly be modeled in an axisymmetric system. An explanation to this phenomenon is that the shear component $(\frac{\partial u_y}{\partial x} - \frac{\partial u_x}{\partial y})$ is independent of the other displacements for isotropic and transversely isotropic materials [83], which is also the reason that the equation of the slowness surface for these two kinds of materials can be factorized. The separated wave front can be described by u_θ and is neglected in the axisymmetric geometry.

The elemental matrices for axisymmetric formulations can be written in a similar form as eq. (4.8)

$$M^e = 2\pi \int\int \rho N^T N r dr dz \tag{4.18a}$$

$$K^e = 2\pi \int\int (AN)^T C A N r dr dz \tag{4.18b}$$

$$D^e = 2\pi \int\int (AN)^T \eta AN r dr dz \tag{4.18c}$$

$$R^e = \int_{\Gamma_t^e} N^T \underline{t} ds \tag{4.18d}$$

The implementation of this formulation involves also the time integration and mass lumping as does the general 3-D or a 2-D finite element model. Comparisons of axisymmetric results with analytical solutions are discussed in the next chapter. In order to confirm the axisymmetric code, this model is utilized to generate attenuation profiles due to geometric dispersion [71] or beam spreading for both isotropic (aluminum) and transversely isotropic (cobalt and apatite) materials. The first two data sets are for the aluminum block under two types of excitation. These were subsequently compared to experimental data. The anisotropic results mainly show the qualitative agreement between the axisymmetric finite element results with other theories.

The first case models a normal point source as an approximation to an ideal Huygen radiator. As pointed out in the literature [73], a spherically radiating source is characterized by a geometric attenuation proportional to the distance from the source. The normal point source dispersion should thus approximate such behavior. An attenuation profile of the L-wave is shown in Fig. 4-7, where it is compared with a plot of the idealized $1/r$ far field displacement behavior along the acoustical axis. The excellent agreement between the $1/r$ curve and the finite element result proves the accuracy of the numerical model. The plotted results are normalized to a point some distance away from the source to avoid the coupled field from shear, head and surface waves in the near field.

The second case considers an excitation sources of finite aperture. In order to

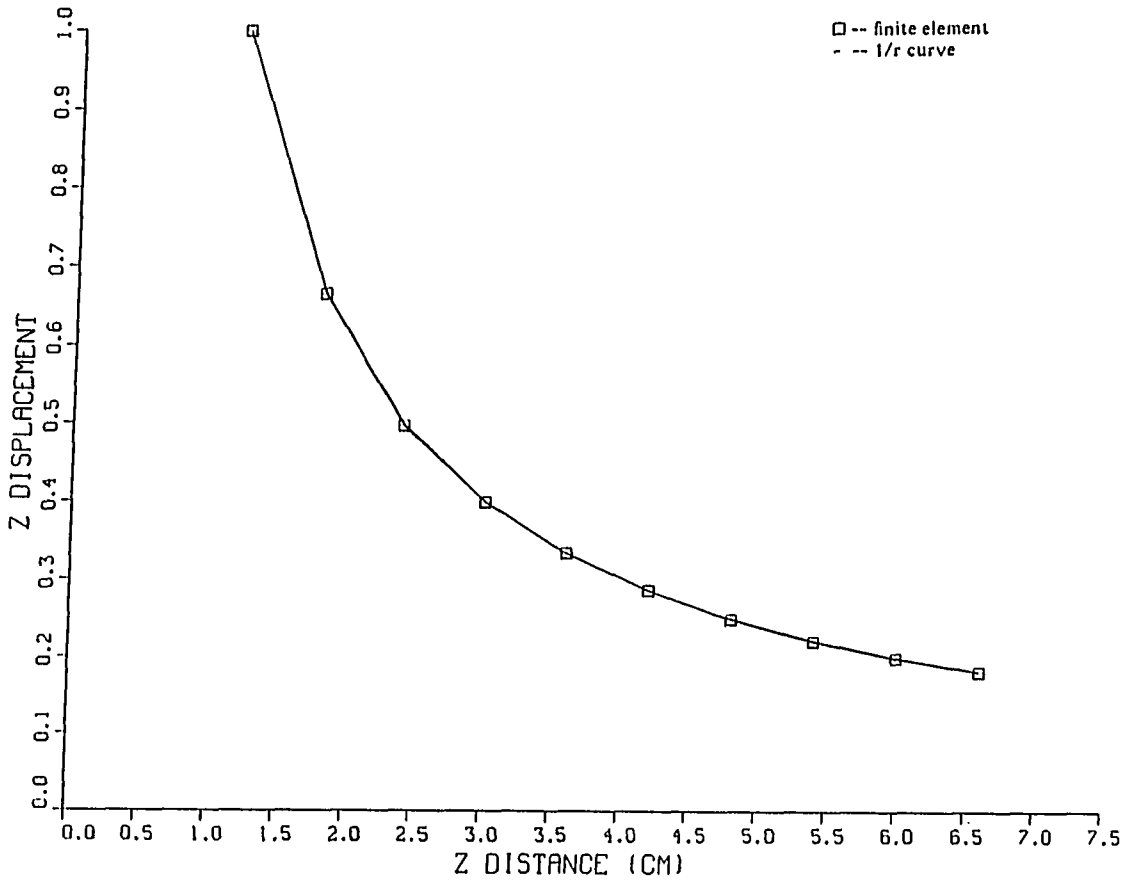

Figure 4.7: Comparison of the numerical predictions with theoretical $(1/r)$ curve for point source excitation in an isotropic solid

make an accurate comparison with experimental measurements, the through-signal data were subjected to a spatial averaging over the aperture area (1/2" diameter). The resulting dispersion profile is compared with experimental decay data which are produced by averaging ten sets of independent experimental data as illustrated in Fig. 4-8. The experimental set-up is shown in Fig. 4-9. The deviation is within ten percents.

The agreement is quite good and indicates that the amplitude decay in the aluminum blocks is characterized primarily by geometric dispersion. This is by no means a new conclusion but implies that the physical process associated with ultrasonic material interrogation for this type of material can be accurately modeled by elastic wave propagation, and that the finite element method is an effective tool to predict the geometric attenuation.

Two transversely isotropic materials with different slowness and wave surfaces are chosen to see how the finite element algorithm reproduces the wave surface as well as the precise amplitude distribution as the wave propagates. Fig. 4-10 shows the displacement at $t = 10\ \mu s$ after a point force is applied to the cobalt with parameters

$$C_{11} = 30.70 \times 10^{10}\ N/m^2 \qquad C_{12} = 16.50 \times 10^{10}\ N/m^2$$
$$C_{13} = 10.27 \times 10^{10}\ N/m^2 \qquad C_{33} = 35.81 \times 10^{10}\ N/m^2$$
$$C_{44} = 7.510 \times 10^{10}\ N/m^2 \qquad \rho = 8900\ kg/m^3$$

along the symmetric axis. As observed in Fig. 4-10, the wavefronts exhibit spatially nonuniform propagation patterns in terms of both the velocity and amplitude. The behaviors are, within limits, comparable to the time harmonic solution of the Christoffel equation in terms of the group velocity (energy) surface in Fig. 4-11

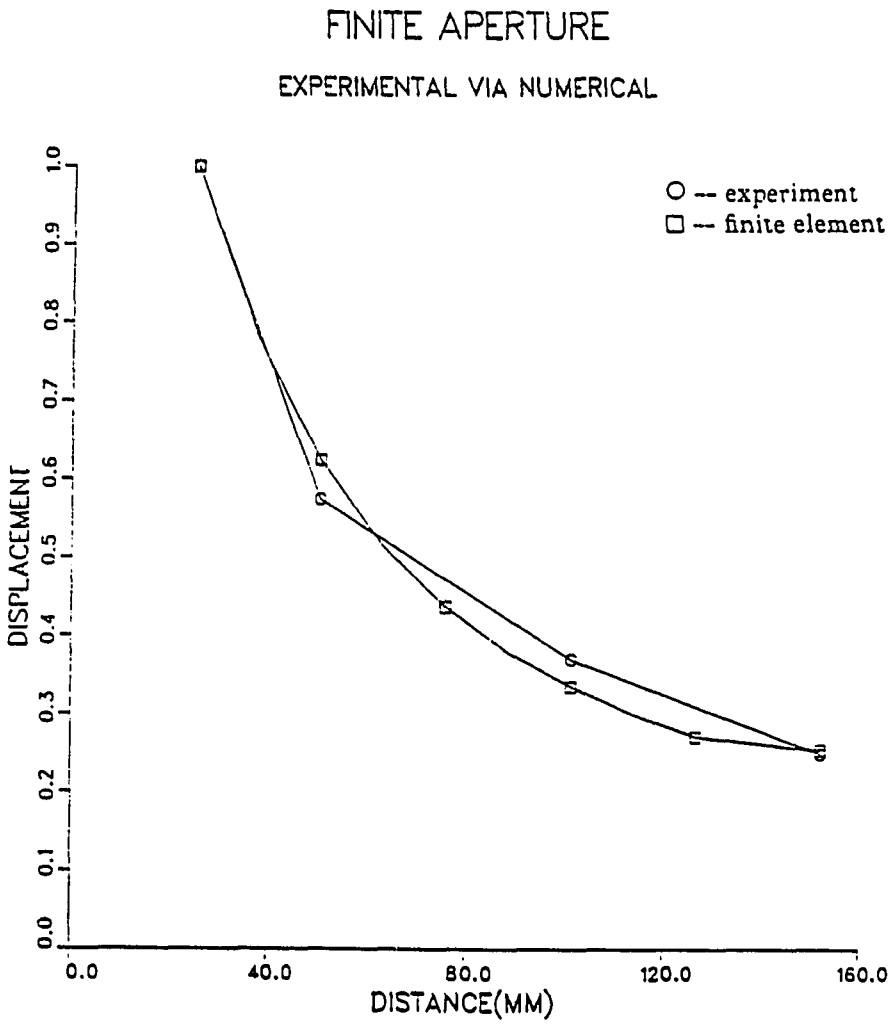

Figure 4.8: Comparison of numerical and experimental results with finite aperture transducer

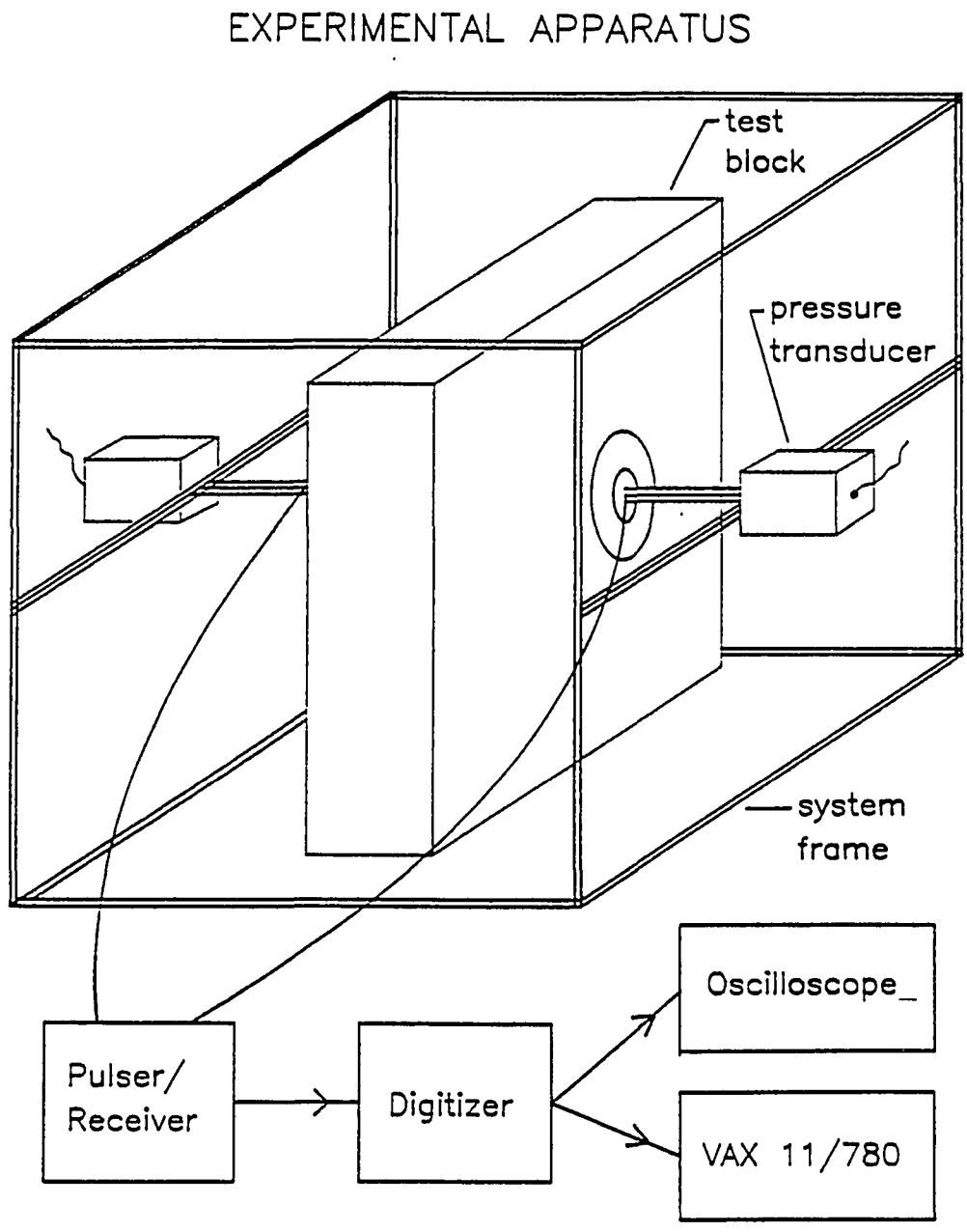

Figure 4.9: Illustration of the experimental set-up

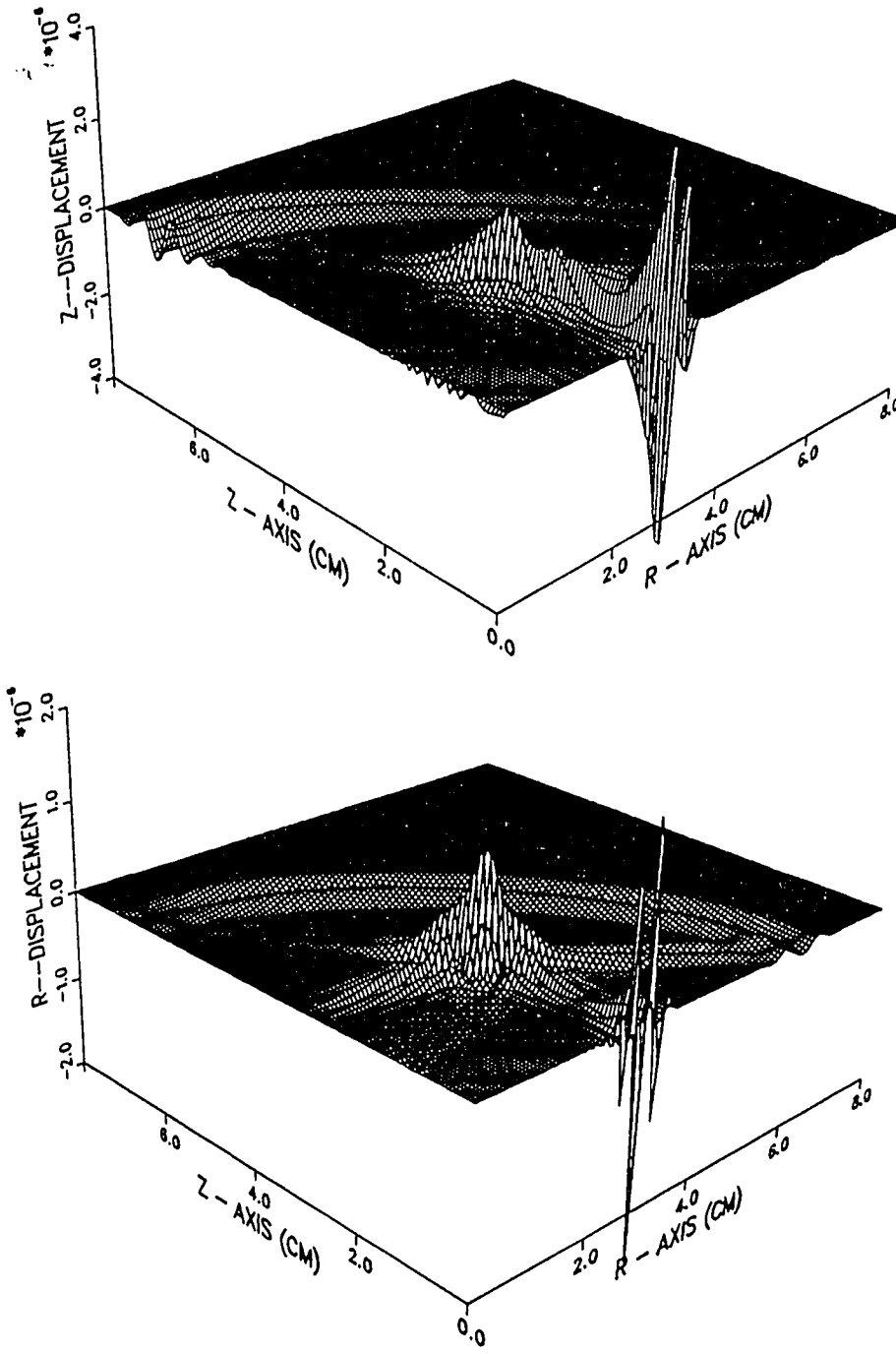

Figure 4.10: Displacement predictions of cobalt from finite element solution due to a point source

where the group velocity surface is plotted for both longitudinal and shear wave-fronts. Since the Christoffel equation is solved in an infinite full space, no head and surface waves are involved as in the case of the half-space considered in the numerical approach. The amplitude of the displacement along the symmetric axis is plotted in Fig. 4-12 in comparison with a $1/r$ curve as a function of the distance from the source. It can be seen that the geometric dispersion in anisotropic media is much more complicated than that in the isotropic media. For example, the amplitude along the z-axis for cobalt is lower than the $1/r$ curve as shown in Fig. 4-12. This may be partially because of the existence of the cuspidal edge in the slowness surface where the energy decays slower (proportional to $r^{-5/6}$). The wave front is particularly complicated in the cuspidal area which is around $\theta = 45^o (= \tan(z/r))$ for cobalt and at $\theta = 0^o$ and $\theta = 90^o$ for apatite, whose slowness and wave surfaces are shown in Fig. 4-13. The parameters for apatite are

$$C_{11} = 16.67 \times 10^{10}\ N/m^2 \qquad C_{12} = 1.31 \times 10^{10}\ N/m^2$$
$$C_{13} = 6.55 \times 10^{10}\ N/m^2 \qquad C_{33} = 13.96 \times 10^{10}\ N/m^2$$
$$C_{44} = 6.33 \times 10^{10}\ N/m^2 \qquad \rho = 3140\ kg/m^3$$

The anomalous wave front for apatite from the finite element algorithm at $t = 8\mu s$ is shown in Fig. 4-14. The shear (quasi-shear) wave along the z-axis is particularly strong due to the conical point of the wave front on the z-axis which contributes to the singularity behavior of the displacement prediction in analytical solutions. The amplitude of the displacement along the z-axis of the corresponding shear wave is plotted in Fig. 4-15 in comparison with the theoretical $1/\sqrt{r}$ far field curve given by Buckwald [83]. The good agreement shows that the axisymmetric finite element algo-

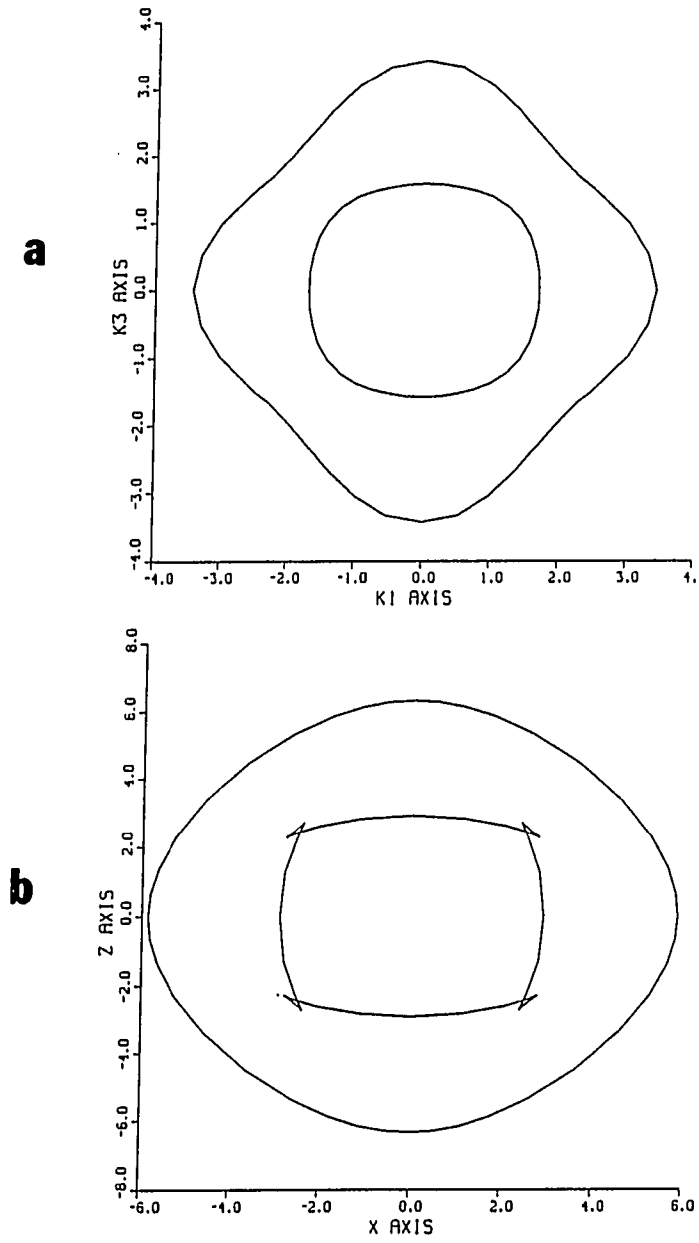

Figure 4.11: a) Slowness surface; b) Velocity surface of cobalt

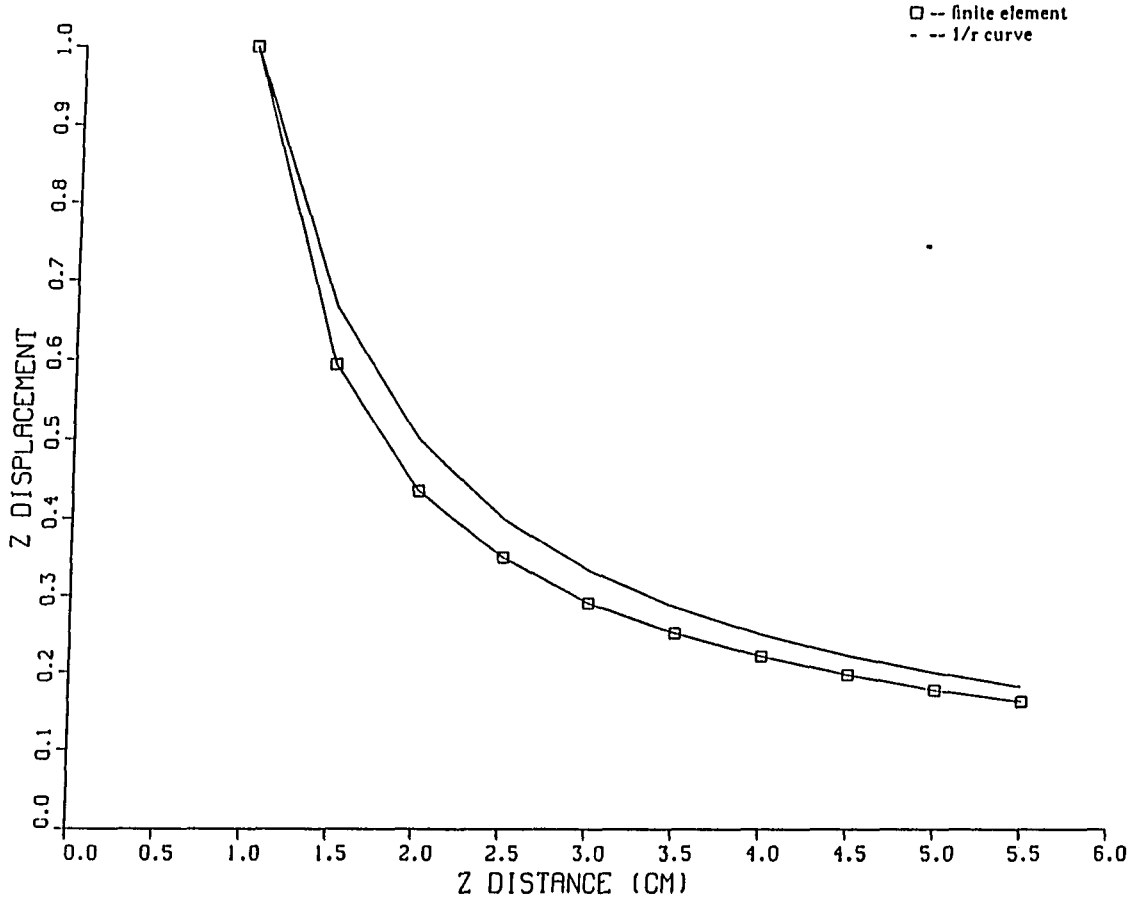

Figure 4.12: Comparison of the finite element result with 1/r curve for cobalt

a

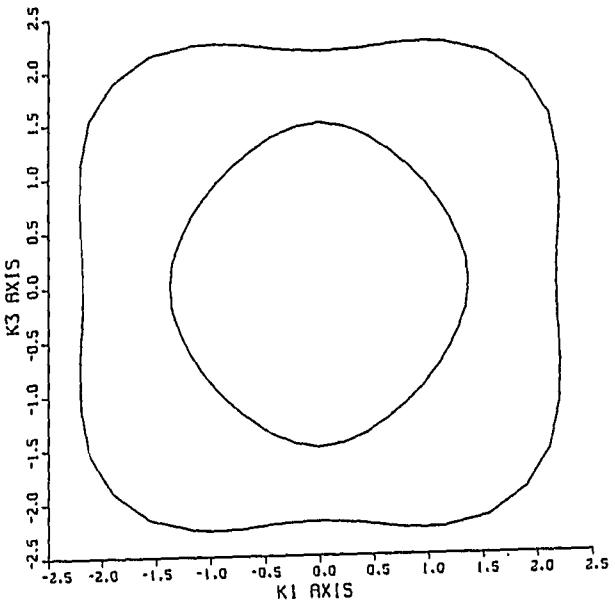

b

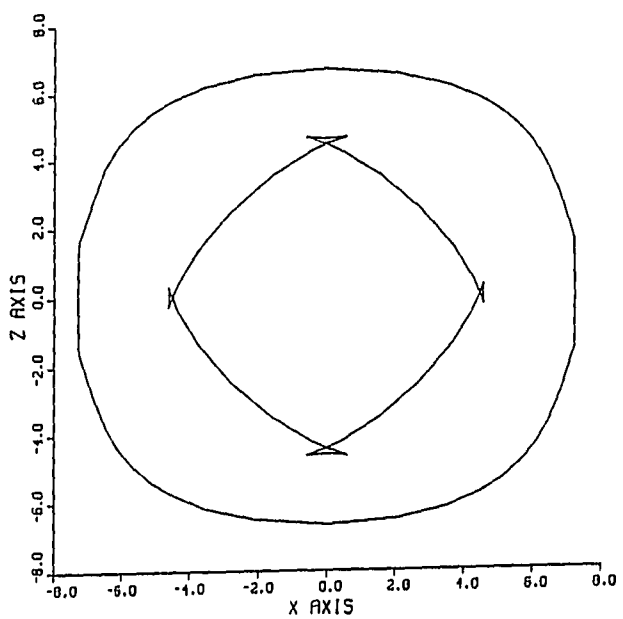

Figure 4.13: a) Slowness surface; b) Wave surfave of apatite

rithm can provide reliable insight to the physics of wave propagation in transversely isotropic media.

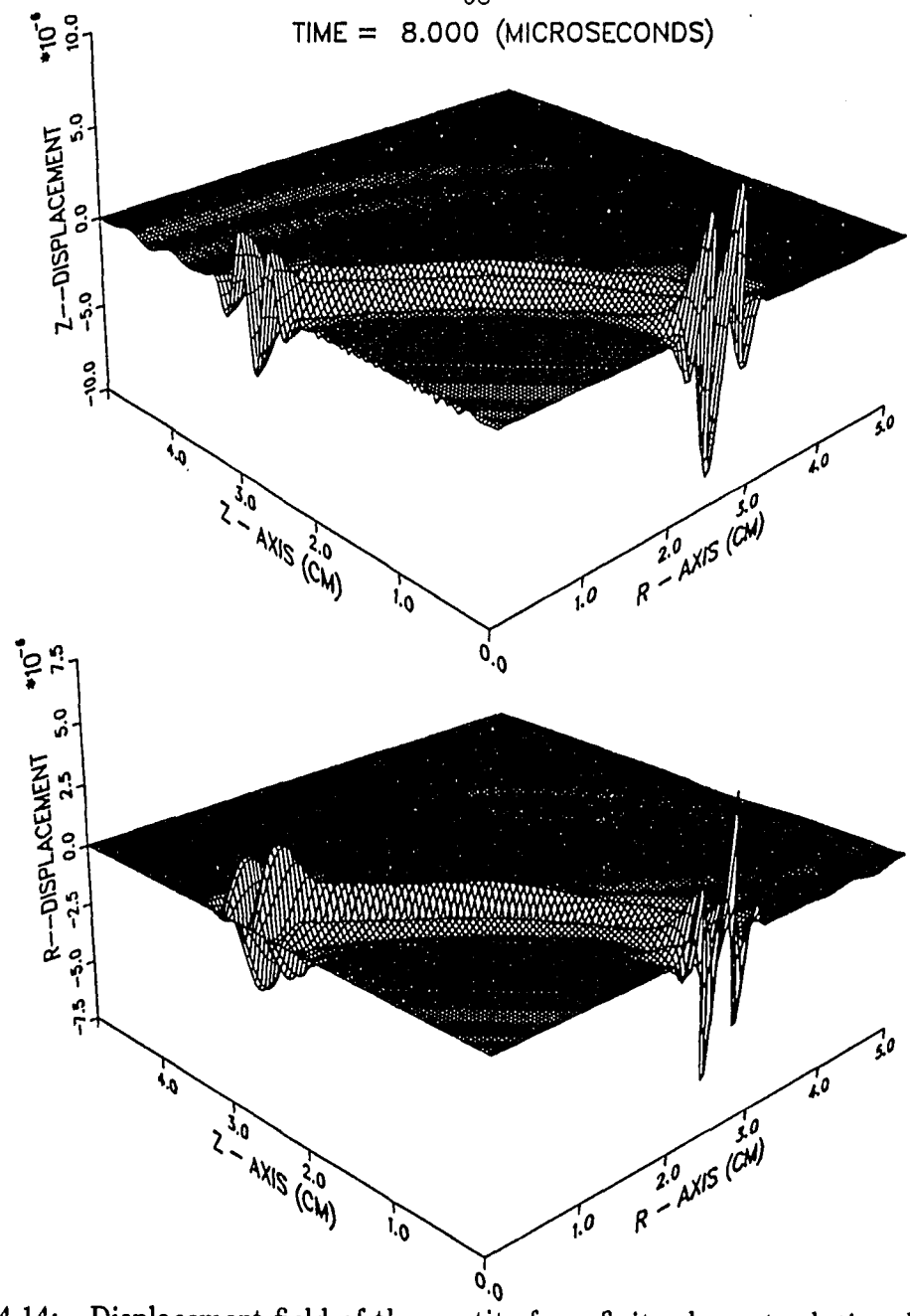

Figure 4.14: Displacement field of the apatite from finite element solution due to a point force excitation

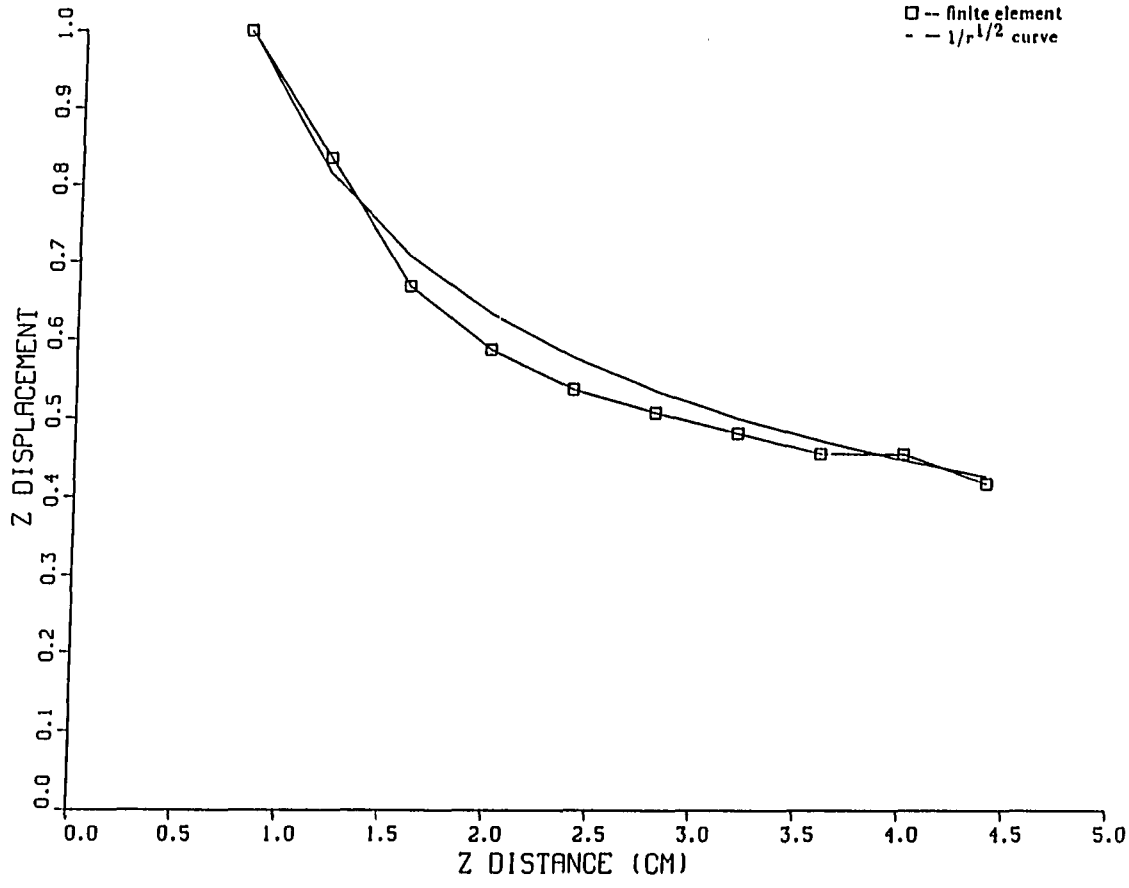

Figure 4.15: Comparison of the finite element prediction with $1/r^{1/2}$ curve at the conical point

CHAPTER 5. ABSORBING BOUNDARY CONDITIONS

For most of the large geometries encountered in ultrasonic NDE applications, finite element solutions of the elastic wave equation, as presented in the previous chapters, are usually limited to a small part of the real system because of the spatial discretization required for accuracy. This means that artificial boundaries must be introduced to limit the spatial dimensions of a given problem. An obvious problem associated with the introduction of artificial boundaries is that they can cause unwanted reflections which corrupt the desired responses from the defect. The simplest approach to this problem is to ensure that the region is large enough for the unwanted reflections to be separated from the desired signal in the time domain. For many applications, however, this may become very expensive in terms of computer resources. 3-D problems are typical examples of such applications. Techniques for avoiding all the spurious echos from the artificial boundaries, which model infinite media, therefore, are very important for numerical modeling in 3-D and even in many practical 2-D applications. The goal of all these techniques is to account for the constraining effect (stiffness) of the missing medium while preventing or minimizing the unwanted reflections at the artificial boundaries. After a review of the underlying theory and some applications of these techniques, this chapter ultimately recommends a combined approach to achieve better accuracy and efficient computer utilization.

Review of the Models for Infinite Media

Waves in infinite media can be modeled by special elements or special boundary conditions referred to as infinite elements and energy-absorbing boundaries. Infinite elements or consistent boundaries [84,85] can be categorized into two groups. In the first group, the finite element domain is extended to infinity in one or more directions, the finite element shape function is multiplied by a decay function, and a special integration rule for an infinite range is used. In the second group, a finite to infinite mapping is used which enables shape functions of a finite element to be used in the infinite element. The integration rule used will often contain a second mapping. The combination of these two methods, i.e., a shape function in an infinite domain and a mapping integration rule, is also used [86]. Even though an infinite element may constitute perfect absorbers for all wave types, it is not applicable to time domain finite element solutions because it can only be used in the frequency domain. A perfect absorber can also be accomplished by the consistent boundaries which were originally proposed by Lysmer and Waas [84] for layered rock involving antiplane loads. This concept was later extended by Waas for in-plane motion in layered soils and generalized to three dimensional models with cylindrical geometries [87]. More general consistent boundaries for 3-D geometries and 2-D geometries with arbitrary loading can be constructed using the boundary integral method to handle the infinite region. This is referred to as the hybrid approach of finite element and boundary element methods. However, the application of this hybrid approach in the time domain has not yet been reported. Therefore, this dissertation turns to the energy absorbing boundaries.

There are different approaches to define a local boundary condition by which the energy arriving at the boundary will be absorbed. Clayton and Engquist [88] derive a family of boundary conditions for numerical wave simulations based on paraxial approximations of the scalar and elastic wave equations. These boundary conditions can be implemented with varying degrees of accuracy. Higher order approximations have substantially better accuracy but involve progressively more points near the boundary. The equations, however, are more suited to finite difference formulations and are not readily implemented in the finite element approach. Ang and Newmark [89], on the other hand, develop local boundary conditions for the time domain finite difference method using the somewhat heuristic concept of the "transmittal of the D'Alembert force". These equations are again not easily applicable to our finite element model.

For time domain finite element simulations of ultrasonic NDT phenomena in infinite media, it is easiest to use viscous boundary conditions [90]. In essence, these conditions can be interpreted as dashpots connected to the boundary points whose constants are a function of the material properties at that location. A review and application of this technique is given in the next section.

All of the local boundaries, which are characterized by their spatial and temporal natures, are based on physical (e.g. viscous boundary) or mathematical (e.g. paraxial) approximations. In many NDT applications the wanted signals are so weak that they are about the same order of magnitude as the small reflections from the artificial boundaries. A perfect absorber or non-reflecting boundary, therefore, is particularly desirable. Smith [91] proposes an approach to eliminate the reflection without approximations. With this approach, the simulations are done at least twice

with different boundary conditions, and the results are summed to cancel the reflections as described in Section 5.3.

A detailed review and comparison of different techniques for numerical simulation of wave propagation problems in infinite media can be found in reference [92]. This Chapter is primarily concerned with the application of these techniques to finite element modeling of ultrasonic NDT phenomena.

Viscous Boundary

The viscous boundary conditions in 2-D geometries are defined as

$$t_n = a\rho V_l \dot{u}_n \tag{5.1}$$

$$t_t = b\rho V_s \dot{u}_t \tag{5.2}$$

where

$\dot{u}_n, \dot{u}_t$ = normal and tangential components of the velocity on the surface;

t_n, t_t = normal and tangential component of the surface tractions;

ρ = material density;

V_l, V_s = longitudinal and shear velocities;

a, b = constants

For isotropic media, the displacement can be described by two potentials, ϕ and $\bar{\psi}$, through Helmholtz decomposition.

$$\bar{u} = \nabla\phi + \nabla \times \bar{\psi} \tag{5.3}$$

In the case of 2-D geometries with plane strain constraints, $\bar{\psi}$ is simplified to be a scalar. Then the decomposition can be expressed as

$$u_x = \frac{\partial \phi}{\partial x} - \frac{\partial \psi}{\partial z} \tag{5.4}$$

$$u_z = \frac{\partial \phi}{\partial z} + \frac{\partial \psi}{\partial x} \tag{5.5}$$

where the 2-D plane is chosen to be the xz plane.

Assume a plane incident L-wave with incident angle θ as shown in Fig. 5-1, then the two potentials can be expressed as

$$\phi = e^{ik_l(V_l t + z\cos\theta - x\sin\theta)} + Ae^{ik_l(V_l t - z\cos\theta - x\sin\theta)} \tag{5.6}$$

$$\psi = Be^{ik_s(V_s t - z\cos\nu - x\sin\nu)} \tag{5.7}$$

where

$$k_l = \frac{\omega}{V_l}, \quad k_s = \frac{\omega}{V_s}$$

A and B are the amplitudes of the reflected L-waves and mode converted S-waves, respectively, and ν is the angle of the mode-converted S-wave.

Following Fig. 5-1, the surface normal is along the z-axis. $t_i = T_{ij}n_j$ then produces

$$t_n = T_{zz} \quad \text{and} \quad t_t = T_{xz}$$

Hookes's law and the strain-displacement relationship (eq. (4.6)) together give

$$t_n = \rho(V_l^2 - V_s^2)\frac{\partial u_x}{\partial x} + \rho V_l^2 \frac{\partial u_z}{\partial z} \tag{5.8}$$

$$t_t = \frac{1}{2}\rho V_s^2\left(\frac{\partial u_z}{\partial x} + \frac{\partial u_x}{\partial z}\right) \tag{5.9}$$

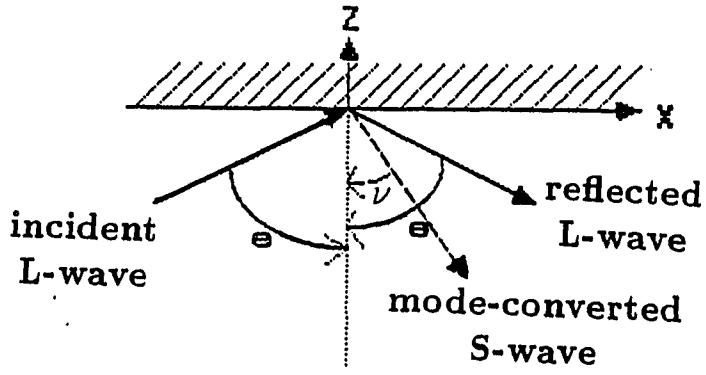

Figure 5.1: Incident L-wave at a boundary

Substituting eqs. (5.3) through (5.8) into eqs. (5.1) and (5.2) yields

$$(1 - 2S^2 \sin^2\theta + a\cos\theta)A + (\sin 2\nu + a\sin\theta)B = 2S^2 \sin^2\theta - 1 + a\cos\theta \quad (5.10)$$

$$(b\sin\nu + S^2 \sin 2\theta)A - (\cos 2\nu + b\cos\theta)B = S^2 \sin 2\theta - b\sin\nu \quad (5.11)$$

where

$$S = \frac{V_s}{V_l}$$

$$\frac{\sin\theta}{V_l} = \frac{\sin\nu}{V_s}$$

Letting $A = B = 0$ yields:

$$a = \frac{1 - 2S^2 \sin^2\theta}{\cos\theta} \quad (5.12)$$

$$b = \frac{S^2 \sin 2\theta}{\sin\nu} \quad (5.13)$$

These are the conditions for the perfect absorber.

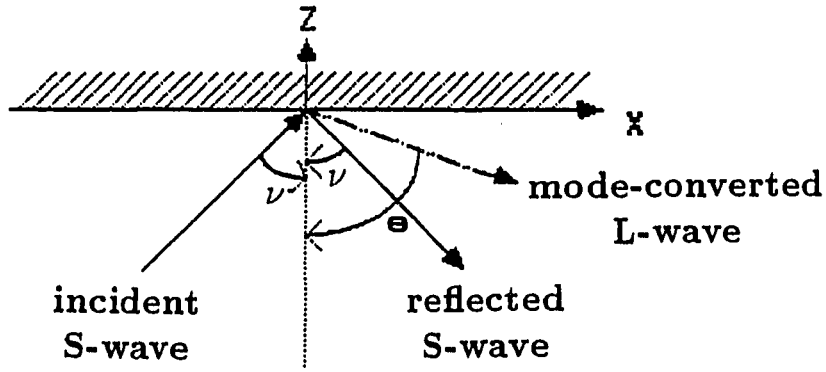

Figure 5.2: Incident shear wave at a boundary

For an incident S-wave with incident angle ν, a similar derivation yields the condition for the perfect absorber:

$$a = \frac{\sin 2\nu}{\sin \theta} \tag{5.14}$$

$$b = \frac{\cos 2\nu}{\cos \nu} \tag{5.15}$$

provided that the incident angle ν is not greater than the critical angle. And θ is the angle of the mode-converted L-wave as shown in Fig. 5-2.

It should be noted that a and b are all independent of frequency, which implies that they can be used in the time domain.

For surface waves, Lysmer and Kuhlemeyer [90] derive an expression for a and b which is dependent on the frequency. Therefore, no perfect absorber can be obtained for a surface wave in the time domain.

The implementation of the perfect absorbing boundary requires a priori information of the incident angle, which is not available in most cases. The standard absorbing boundary defined by $a = b = 1$, therefore, is recommended by Lysmer and Kuhlemeyer [90]. From eqs. (5.11) through (5.14), the standard viscous boundary is a perfect absorber only when $V_s = \frac{1}{2}V_l$ and the incident wave is normal to the surface. As a test example, a half-space problem is considered where a point excitation force is applied normal to the surface. Artificial boundaries are introduced as shown in Fig. 5-3. Vibration velocities are calculated by the backward difference formula. The results are shown in Fig. 5-4. It can be seen that the L-wave reflection is smaller than the S-wave reflection, even though both are very weak. As for the Rayleigh wave, however, the standard absorbing boundary reflects about 12.5% of the displacement amplitude.

White et al. [93] present a unified boundary condition on the basis of a systematic formulation that is applicable to anisotropic materials. For isotropic media, the first approximation for the constants a and b can be evaluated as

$$a = \frac{8}{15\pi}(5 + 2S - 2S^2) \tag{5.16}$$

$$b = \frac{8}{15\pi}(3 + 2S) \tag{5.17}$$

which are independent of both frequency and incident angle. The final values of a and b are optimized by maximizing the efficiency of the viscous boundary, which is defined as a weighted mean ratio of the absorbed energy to the energy arriving on the boundary. Using these a and b values, the example in Fig. 5-3 is recalculated with the results shown in Fig. 5-5. It can be seen that the reflections (especially the Rayleigh wave reflection) are much smaller than for the standard viscous boundary.

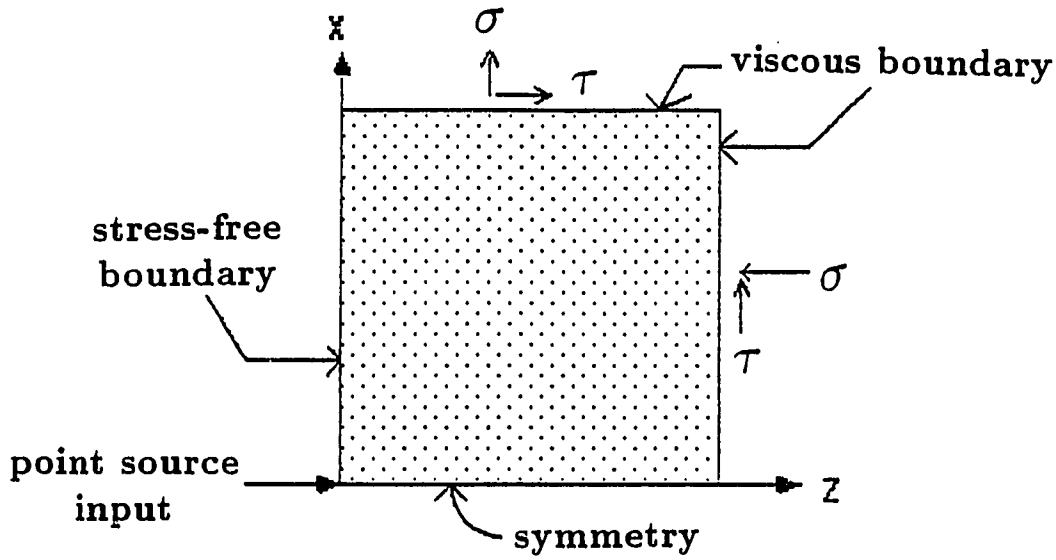

Figure 5.3: Geometry of a half-space problem with artificial boundaries

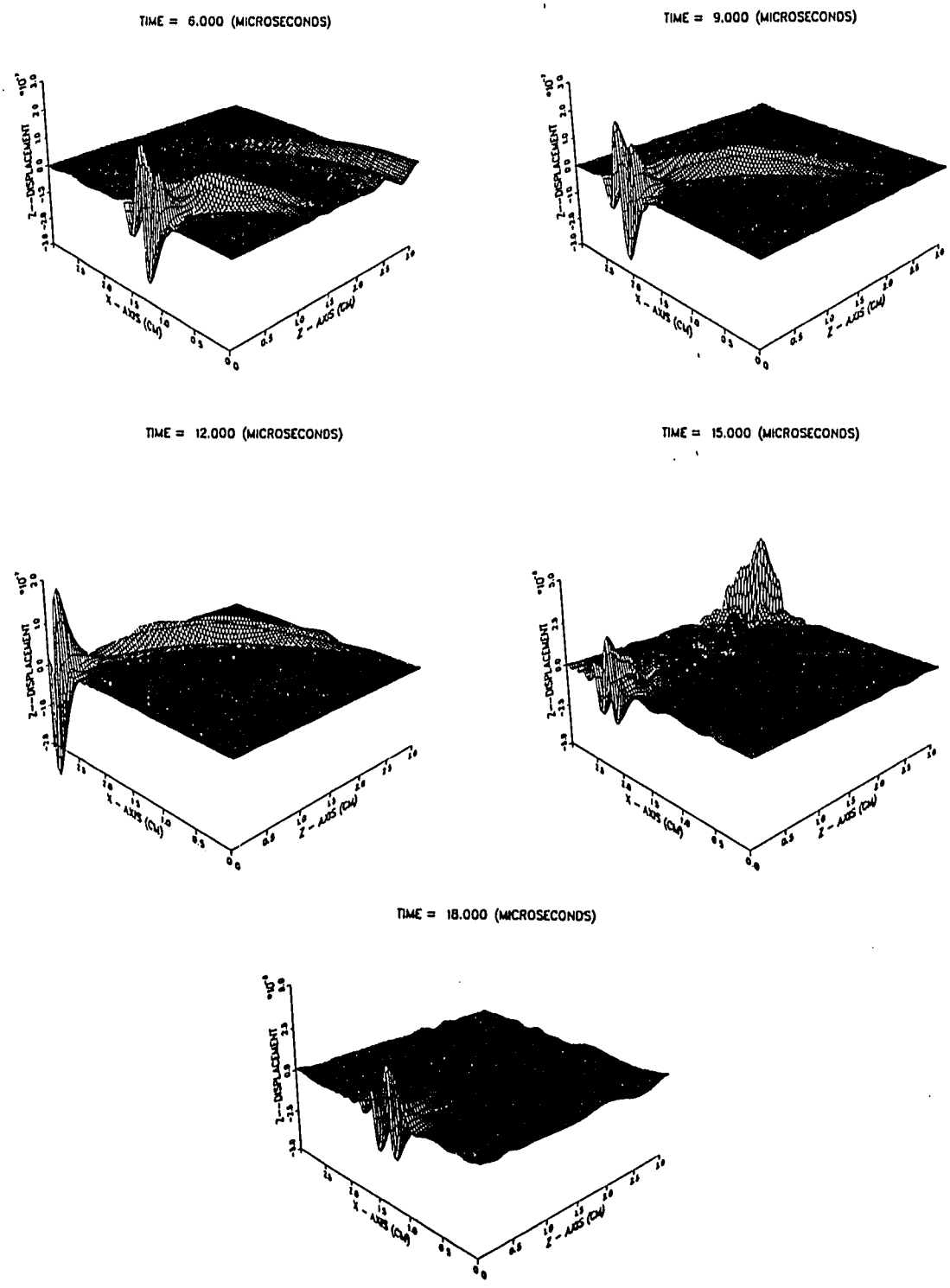

Figure 5.4: Displacement plots of the wave interaction with a standard viscous boundary

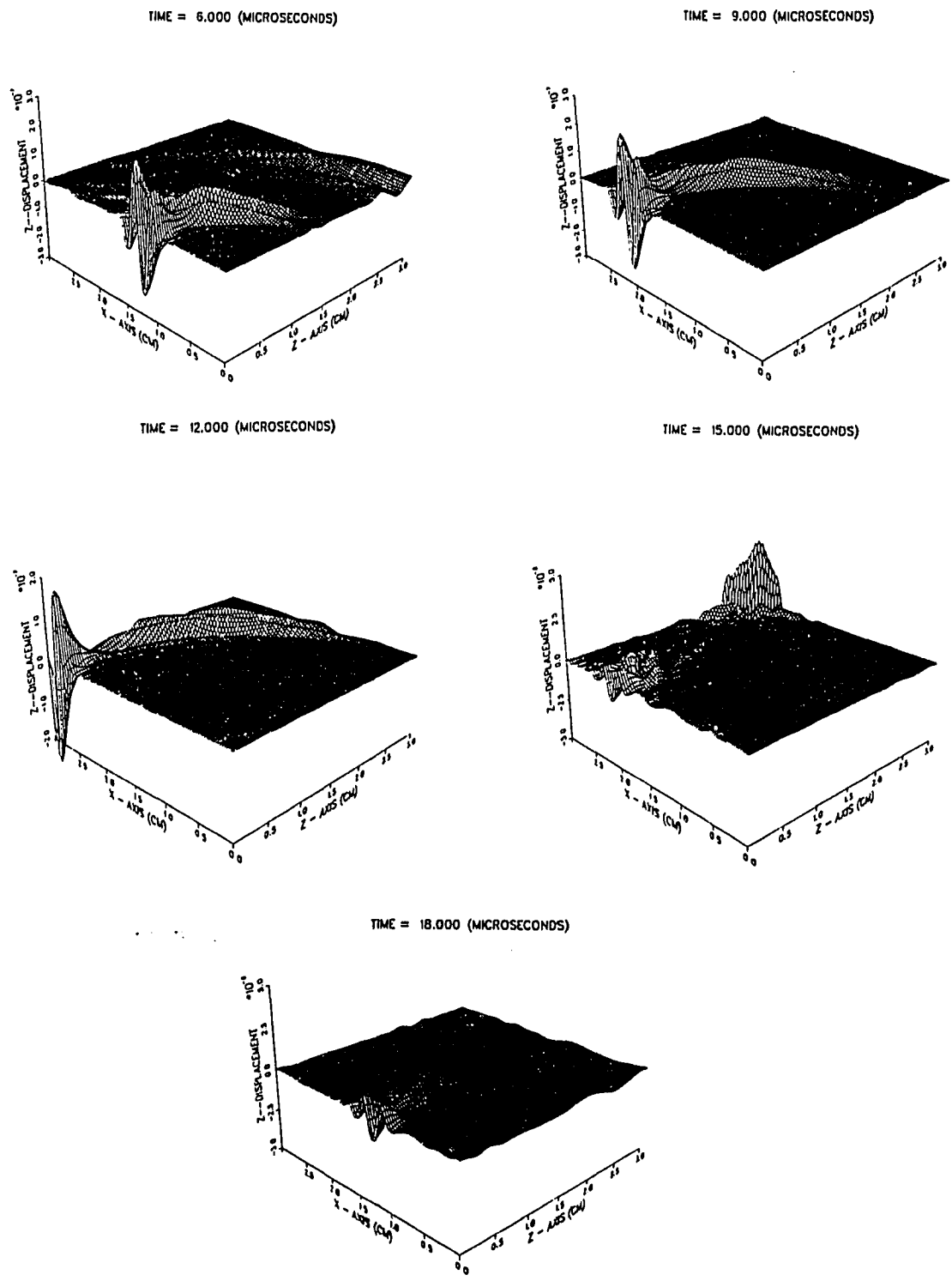

Figure 5.5: Wave interactions with an unified viscous boundary

In 3-D geometries, there are two tangential components associated with the surface traction. Consider a surface with normal along the z-axis. The surface traction has components

$$t_n = T_{zz} \tag{5.18}$$

$$t_{tx} = T_{xz} \tag{5.19}$$

$$t_{ty} = T_{yz} \tag{5.20}$$

Then the viscous boundary conditions can be similarly defined as

$$t_n = T_{zz} = a\rho v_l \dot{u_z} \tag{5.21}$$

$$t_{tx} = T_{xz} = b\rho v_s \dot{u_x} \tag{5.22}$$

$$t_{ty} = T_{yz} = c\rho v_s \dot{u_y} \tag{5.23}$$

Assume again that the constants a, b and c are of unit value.

Viscous boundaries are easy to implement and are not costly in terms of CPU-time and memory. They are not, however, very effective in absorbing Rayleigh and shear waves. If a time-gate can distinguish the reflected shear and Rayleigh waves from the wanted signals, then this method could be very useful.

Non-Reflecting Boundary

Reflections can be completely eliminated by the superposition of solutions from the different boundary conditions [91]. This section is devoted to both analytical and numerical verification of this phenomenon and the application to NDT geometries.

Following the notations in the previous section, consider the incident L-wave as

shown in Fig. 5-1. Imposing the boundary condition

$$u_z = 0, \quad \frac{\partial u_x}{\partial z} = 0 \quad \text{at} \quad z = 0$$

results in $A = 1, B = 0$, while the boundary condition

$$u_x = 0, \quad \frac{\partial u_z}{\partial z} = 0 \quad \text{at} \quad z = 0$$

gives $A = -1, B = 0$. Addition of these two solutions exactly cancels the reflection.

The reflection cancellation is also true for shear and Rayleigh waves [91]. This is particularly useful because the viscous boundary cannot handle these types of waves efficiently.

For multiple reflection boundaries, the number of solutions needed to cancel all reflections is 2^n, where n is the number of the multiple reflection boundaries. For the 2-D corner, $n = 2$, while n should be 3 for a 3-D corner if all of the planes in the corner are artificial boundaries.

Two testing problems are used to evaluate this model. The first one is a common NDE example as shown in Fig. 5-6. Two boundary value problems are solved with boundary conditions given as

$$\underline{\text{Boundary Value Problem 1}}: \quad u_x^1 = 0, \frac{\partial u_z^1}{\partial x} = 0, u_x^2 = 0, \frac{\partial u_z^2}{\partial x} = 0$$

$$\underline{\text{Boundary Value Problem 2}}: \quad u_z^1 = 0, \frac{\partial u_x^1}{\partial x} = 0, u_z^2 = 0, \frac{\partial u_x^2}{\partial x} = 0$$

where the superscript 1 and 2 represent the artificial boundary number. Addition of these two solutions is shown in Fig. 5-7 where the reflections from the artificial boundaries are completely eliminated in a time interval. The high order reflections, however, show up delayed in time depending on the geometry. Numerical results

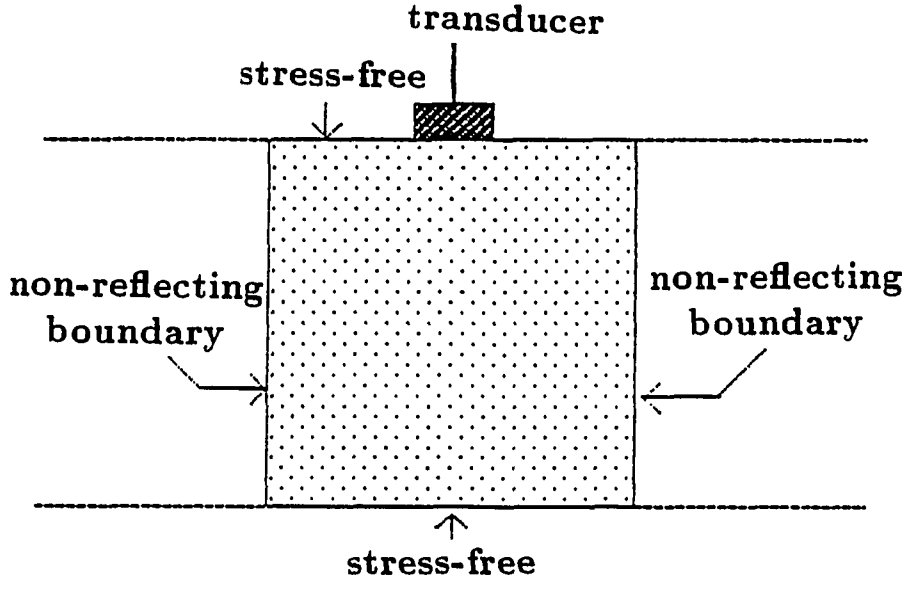

Figure 5.6: Large plate inspected by using a strip-like transducer

reveal that one non-reflecting boundary actually doubles the space in the direction of the surface normal.

The second example is again the geometry in Fig. 5-3 where four solutions are required to cancel the reflections. Fig. 5-8 shows the results after the addition of those four solutions. It should be noted that the complete elimination of all waves reflected from the artificial boundaries, including surface, shear and longitudinal components, is only obtained in certain time periods.

The non-reflecting boundary can also be applied to anisotropic materials. None of the other absorbing boundaries are suitable for this. Fig. 5-9 illustrates the wave absorptions on the boundaries of an uranium block. Even though the non-reflecting boundary is expensive to use, it provides exact solutions for all types of incident waves. Therefore, it is recommended the cases where high accuracy is a major consideration.

A Combined Approach

Since a viscous boundary can absorb the body waves quite effectively and does not cost extra computer time, the combination of a non-reflecting boundary with a viscous boundary gives a useful approach to eliminate the unwanted reflection. In this combined approach, the non-reflecting boundary is mainly used for the surface wave which cannot be effectively absorbed by the viscous boundary but which can absorb the body waves. As an example, the geometry in Fig. 5-3 is re-calculated with a non-reflecting boundary placed on the top. The results are plotted in Fig. 5-10 showing much better accuracy in comparison with the results of the pure viscous boundary in Fig. 5-4. Even though this combined approach costs more in terms of computer resources than pure viscous boundary because two solutions are superposed

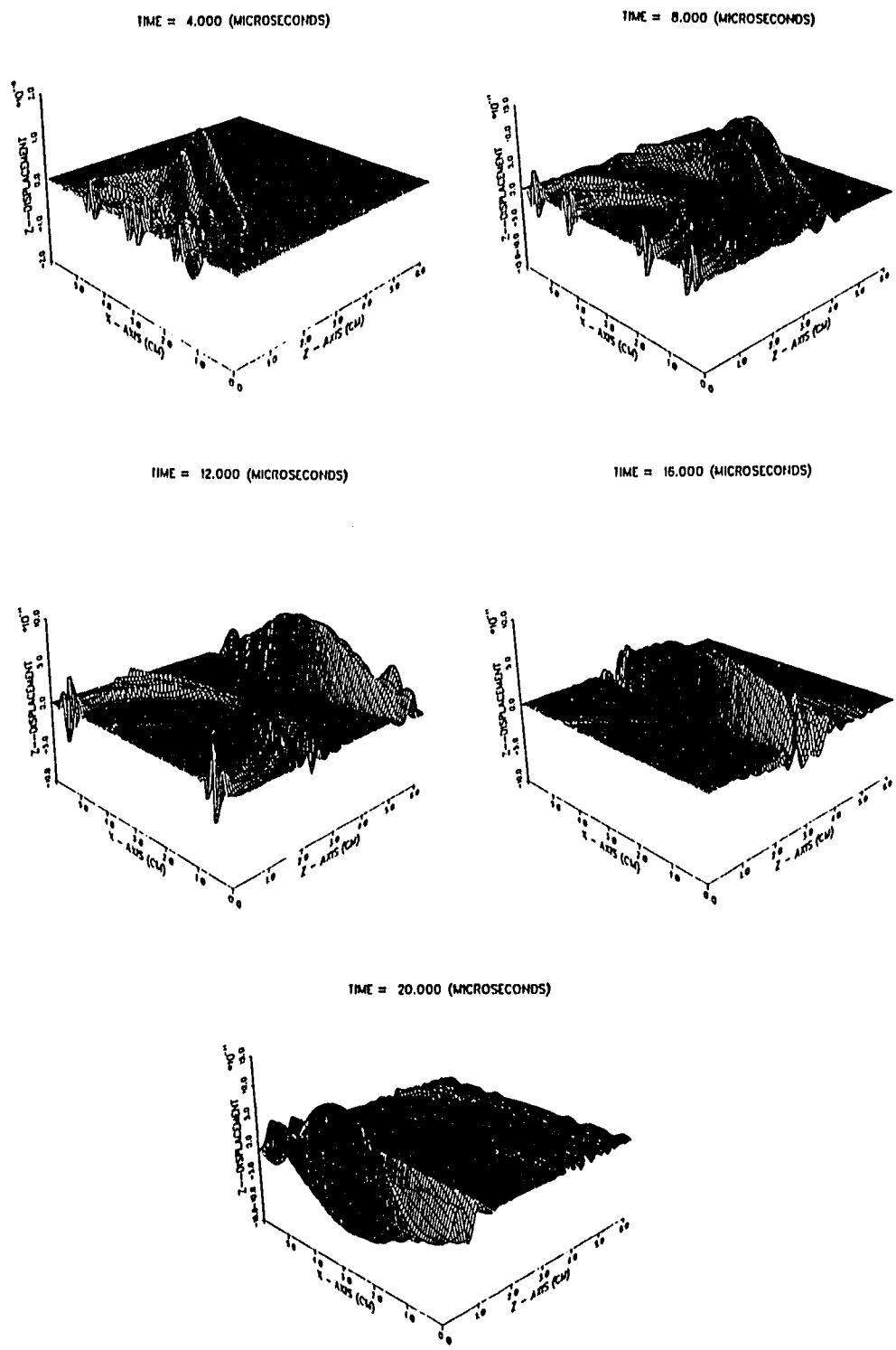

Figure 5.7: Superposition of two solutions for the plate inspection problem as shown in Fig. 5-6

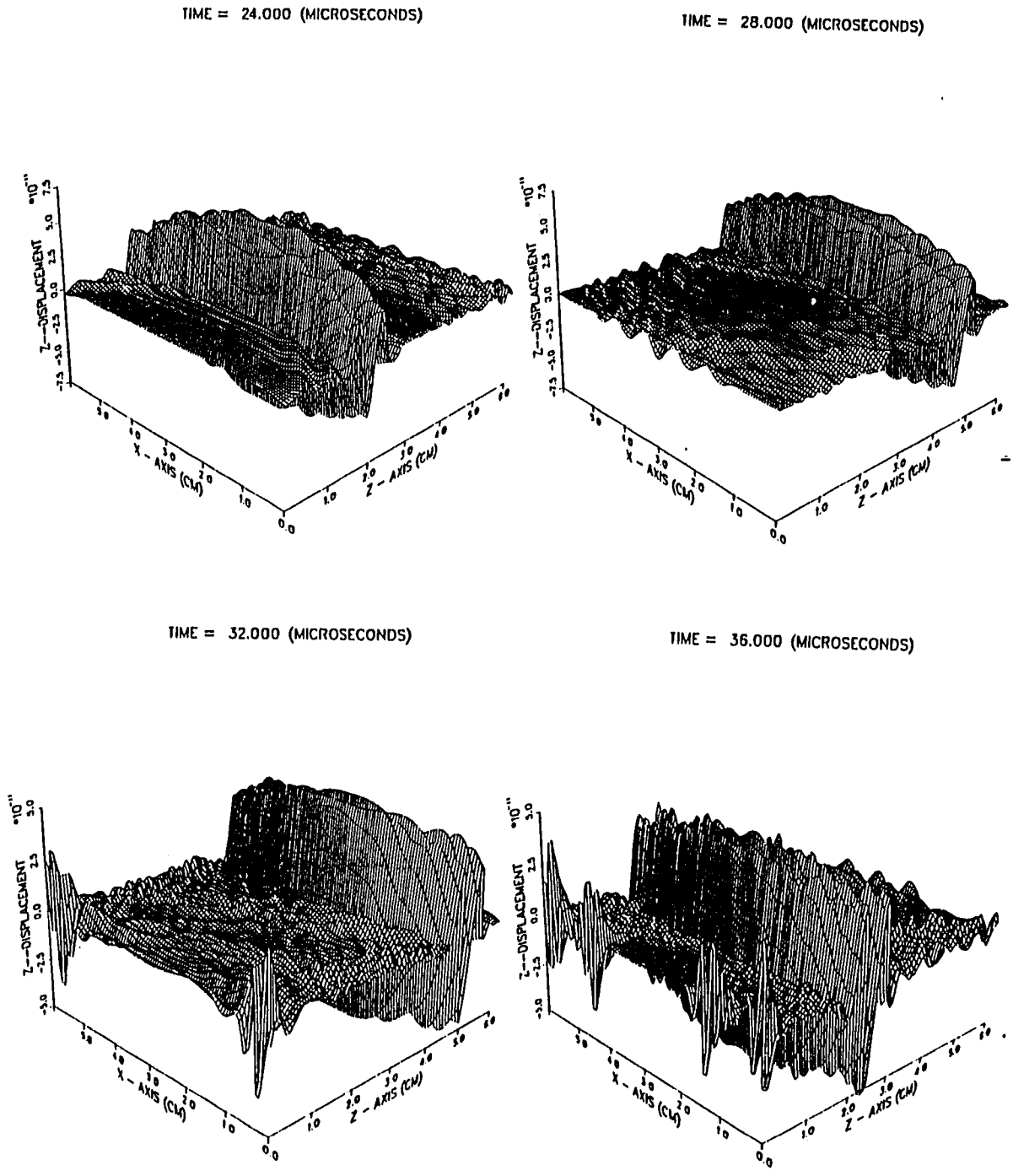

Figure 5.7 (Continued)

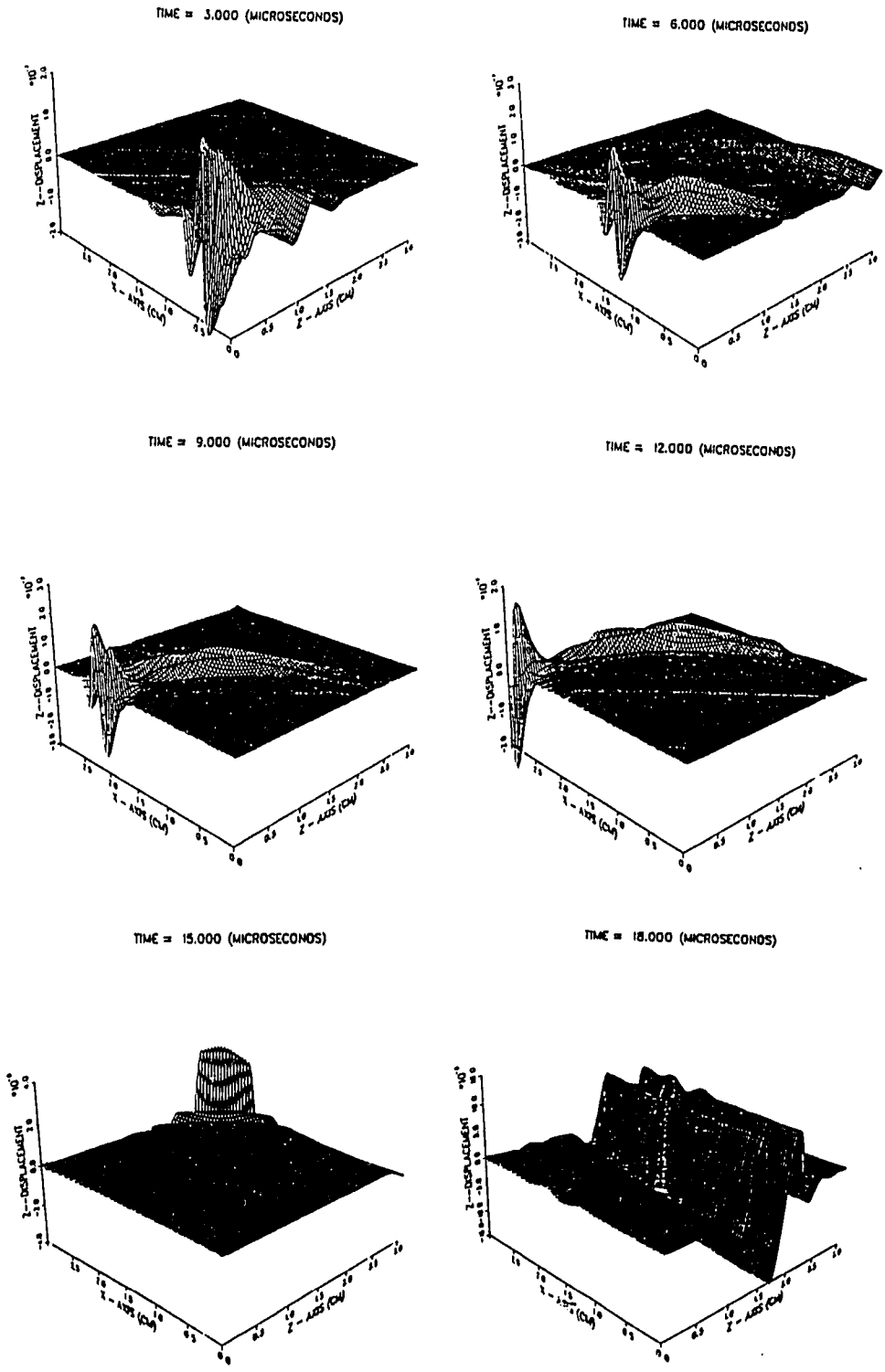

Figure 5.8: Superposition of four solutions for the half-space problem

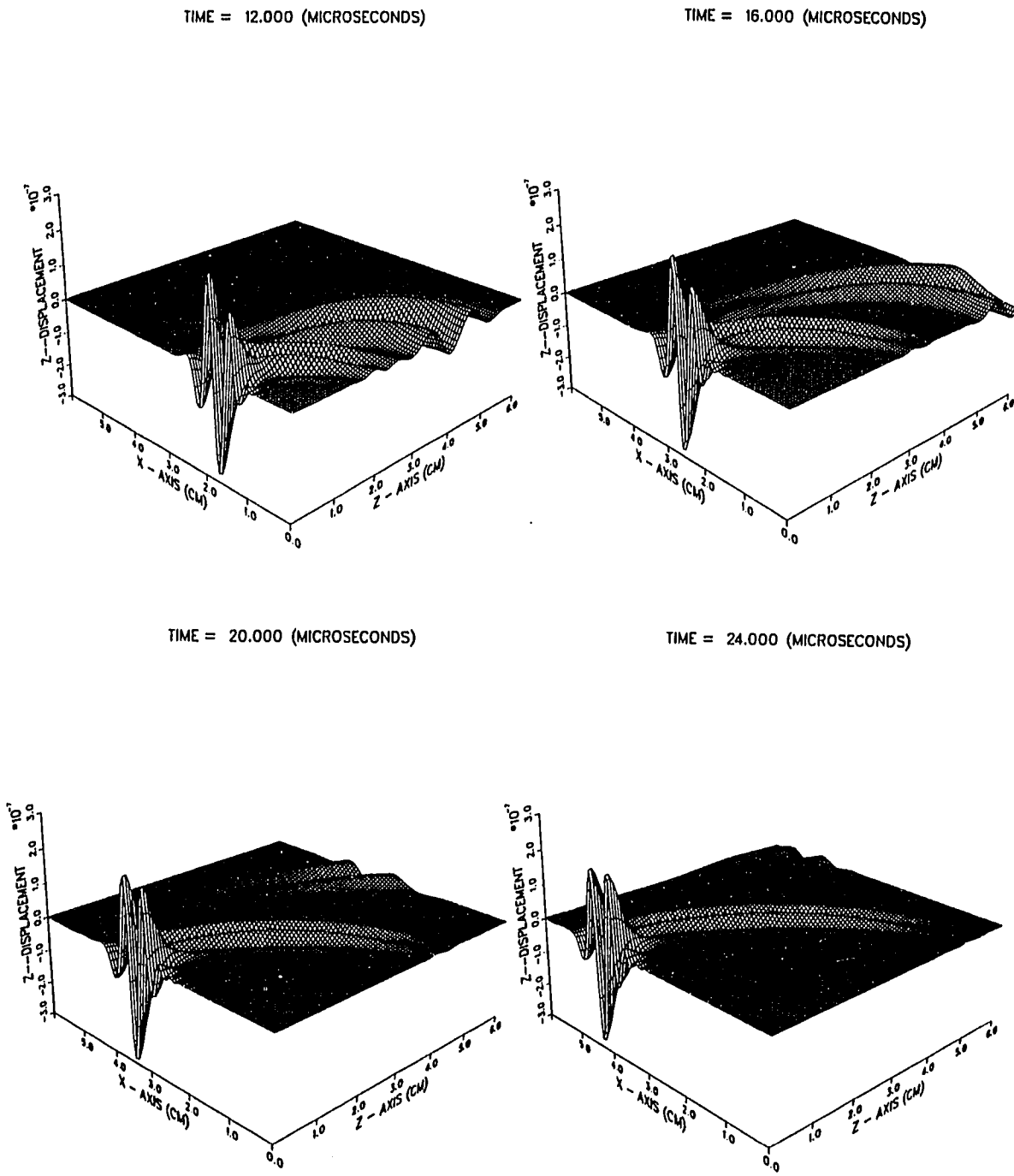

Figure 5.9: Application of the non-reflection boundary to an anisotropic material

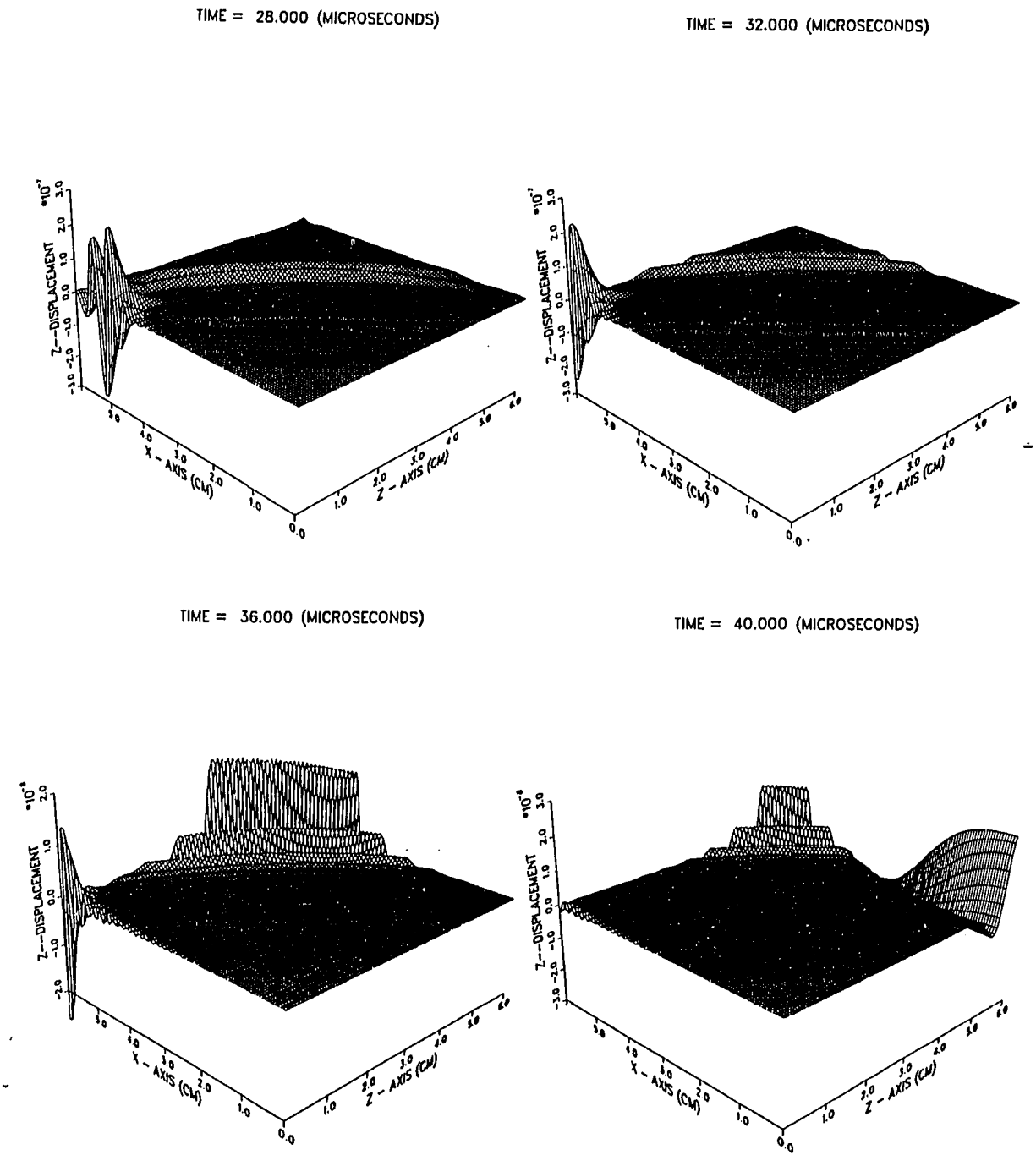

Figure 5.9 (Continued)

to get the results of Fig. 5-10, it still saves in comparison with the pure non-reflecting boundary by which four solutions are needed to produce Fig. 5-8.

The non-reflecting boundary is not widely used because of the high cost in CPU time. The combined approach, however, proves that it can be very useful if used wisely. A simple rule is to use the non-reflecting boundary only for those artificial boundaries connected directly to the real boundary.

Another advantage of this combined approach is that the higher order reflections come back at a much later time because the high speed L-wave is absorbed mainly by the viscous boundary.

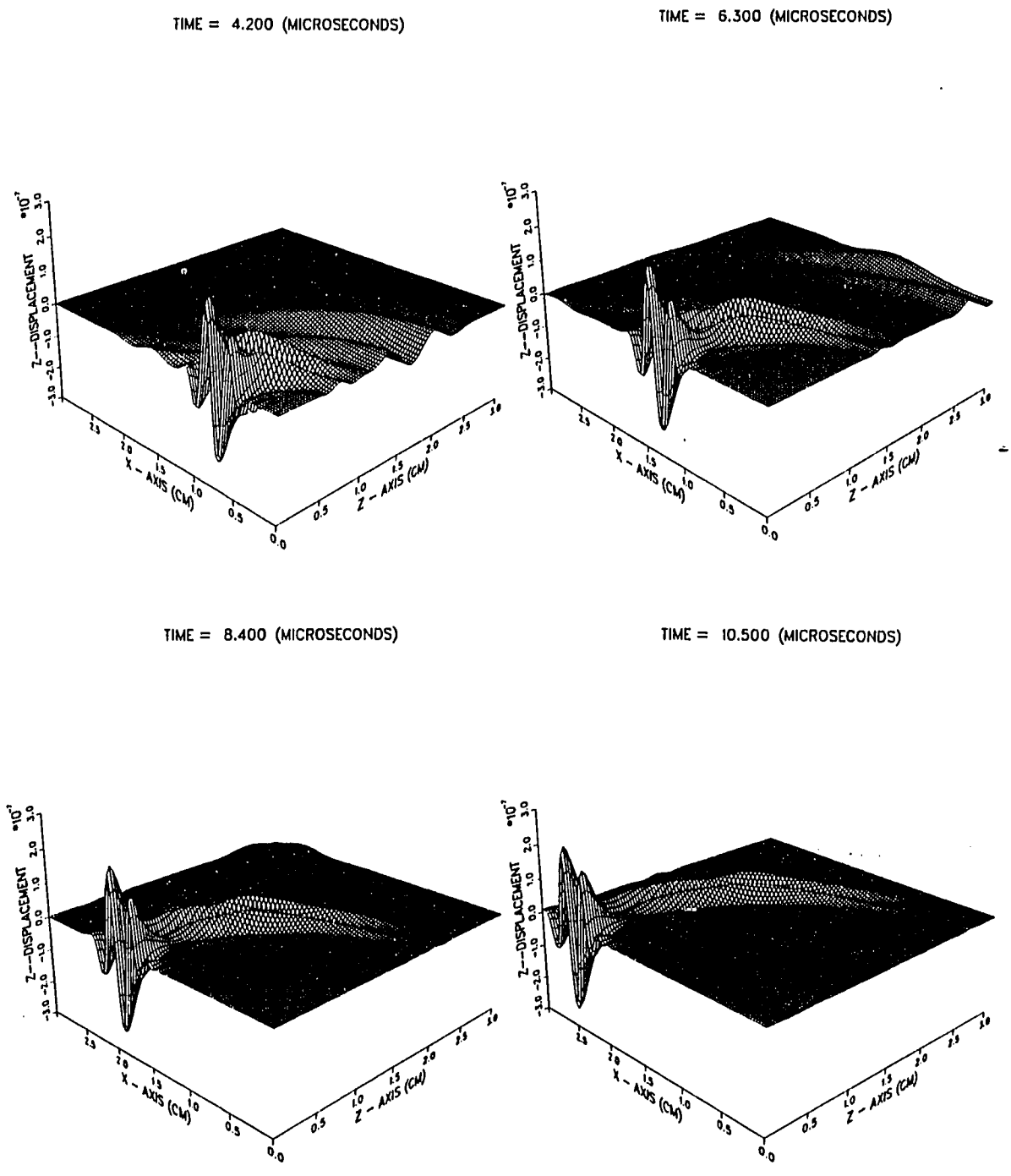

Figure 5.10: Recalculation of the half-space problem by using the combined approach

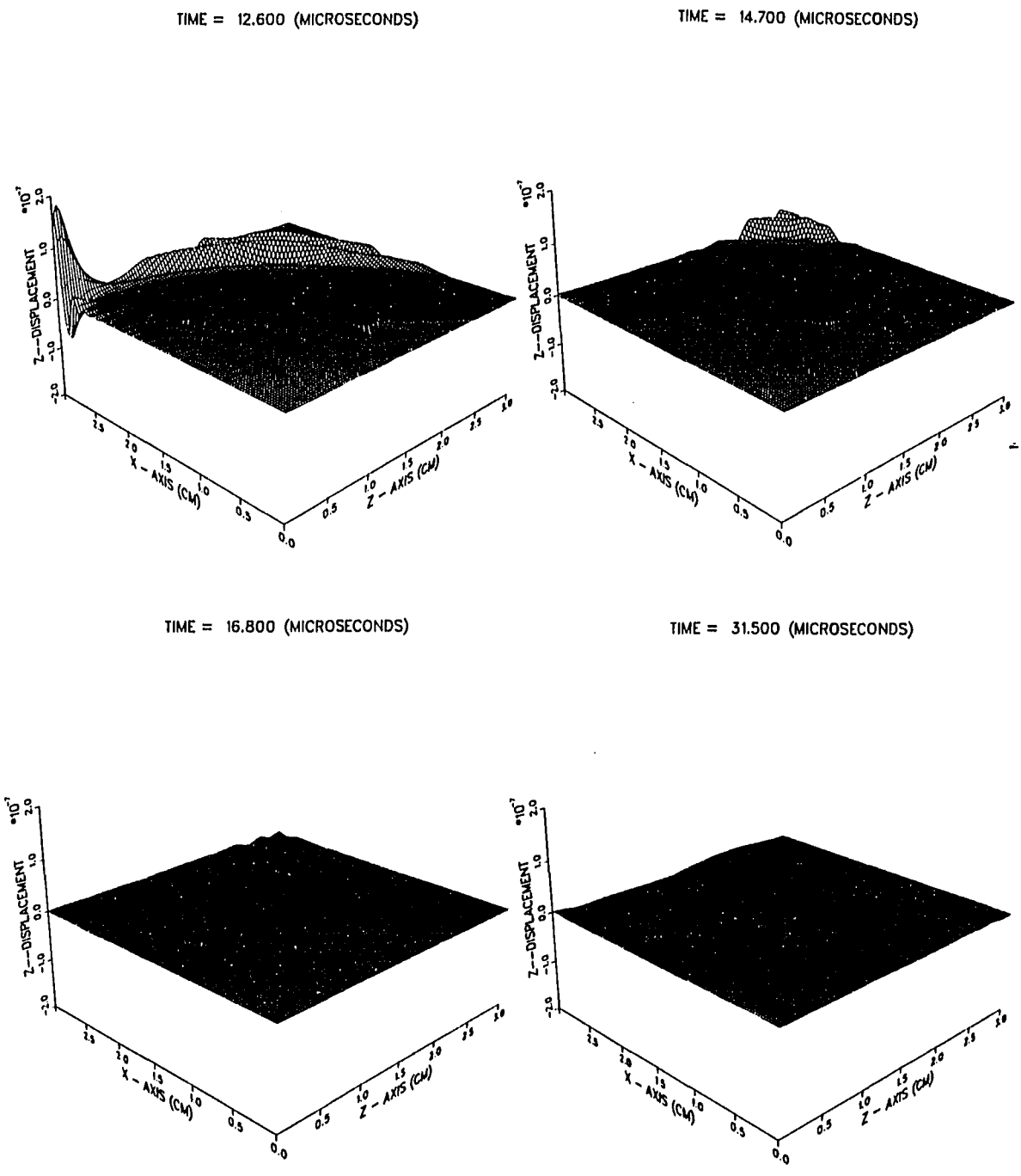

Figure 5.10 (Continued)

CHAPTER 6. COMPARISONS AND APPLICATIONS

The main purpose of this chapter pertains to the verification and application of the finite element formulation presented in the previous chapters. Due to the fact that many problems cannot be solved analytically, confirmation of the finite element model is obtained only through examples of simple geometries such as the half-space problem. As long as the model is proven to be correct and accurate, it can be used to study more complicated situations. In this chapter, comparisons are presented for an 1-D bar which has an analytical solution in series form, a 2-D point source or 3-D line source excitation half space problem, and a 3-D point source excitation on an elastic half space which can be solved by the Cagniard-de Hoop technique [7]. Applications of the finite element model include predictions of 2-D wave/defect interactions and a study of 3-D wave propagation in anisotropic media.

Transient 1-D Bar Analysis

For comparison with the 1-D series solutions presented by Dewey, et al [94], the problem to be considered is the determination of displacements in a long bar of rectangular cross section having symmetric (zero normal displacement) lateral surfaces, subject to the conditions that a uniform normal stress with a step-function time dependence is applied to the end, and that the shear stresses applied to this end

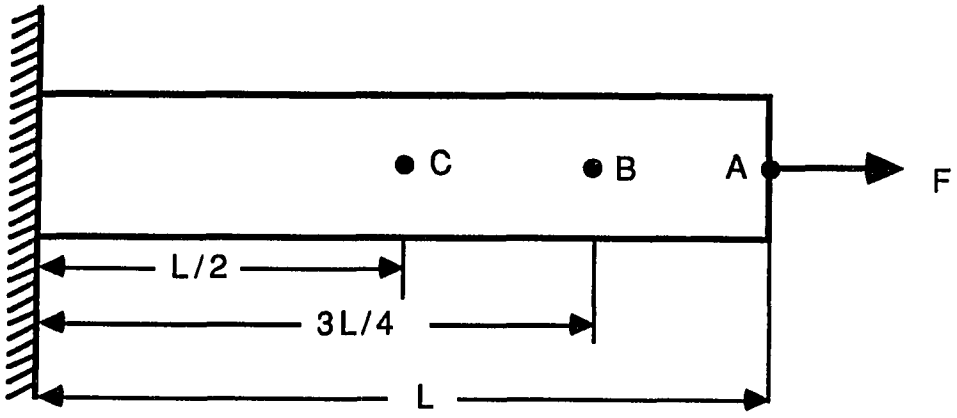

Figure 6.1: An 1-D bar subjected to a step force

are zero. The other end is laterally constrained. The geometry (on the yz-plane) is shown in Fig. 6-1. Assume that the bar is made of a homogeneous, isotropic, linearly elastic material. Only one component of the displacement exists and satisfies the 1-D wave equation with a series solution form expressed as

$$u_z(z,t) = \frac{4P_0}{\rho V_l^2 \pi} \sum_{n=1,3,\ldots} \frac{(-1)^{\frac{n-1}{2}}}{n\beta_n} [1 - \cos(\beta_n z)] \sin \omega_n t \tag{6.1}$$

where ρ, V_l are the density and longitudinal velocity of the bar, respectively. P_0 is the amplitude of the step force. $\beta_n = \frac{n\pi}{2L}$, $\omega_n = \frac{n\pi V_l}{L}$ with L the length of the bar.

In this example, an aluminum bar is chosen with parameters $\rho = 2700\ kg/m^3$, $V_l = 6300\ m/s$ and $L = 20\ mm$. A total of 3x3x100=900 elements are used for the 3-D numerical computation. Three points are selected for comparison: point A at $z = L$, point B at $z = \frac{3}{4}L$ and point C at $z = \frac{1}{2}L$. The results are plotted

in Fig. 6-2 . It can be seen that there is overall agreement between the numerical and the analytical solutions. Only small time differences and shape distortions are observed in the numerical solutions due to the step force input. The infinite frequency spectrum of a step function makes it impossible for the discretization to satisfy the discretization requirements discussed in Chapter 4.

Line Source Comparisons

To validate the finite element model further, a plane-strain problem is considered where the third dimension of the block is much larger than the dimensions of the rectangular cross-section. When a line force is applied, the plane-strain constraint simplifies the problem to a 2-D geometry. With a 3-D code, this situation can be modeled by considering only one layer with the symmetrical condition on both ends. Therefore, both 2-D and 3-D finite element codes can be used for this case. Due to the fact that analytical approaches have difficulty handling the finite boundaries, a 2-D half space Lamb's problem is considered. Its solution can be obtained from the line integration of the point source solution as discussed by Ludwig, et al [7]. It is obvious that the comparisons can give a good validation for the numerical model if the reflections from boundaries are separated from the forward propagating waves.

The 2-D problem considered in this case is a 16 cm x 8 cm aluminum block subjected to a point force (line source in 3-D) input with a raised cosine waveform

$$f(t) = \begin{cases} [1 - \cos(\omega_0 t/3)]\cos\omega_0 t, & 0 \le \omega_0 t \le 6\pi \\ 0, & \omega_0 t \ge 6\pi \end{cases} \tag{6.2}$$

where $\omega_0 = 2\pi f_0$, with the central frequency $f_0 = 1\ MHz$. The elastic parameters of this block are specified as $V_l = 6300\ m/s, V_s = 3100\ m/s, \rho = 2700\ kg/m^3$. Using

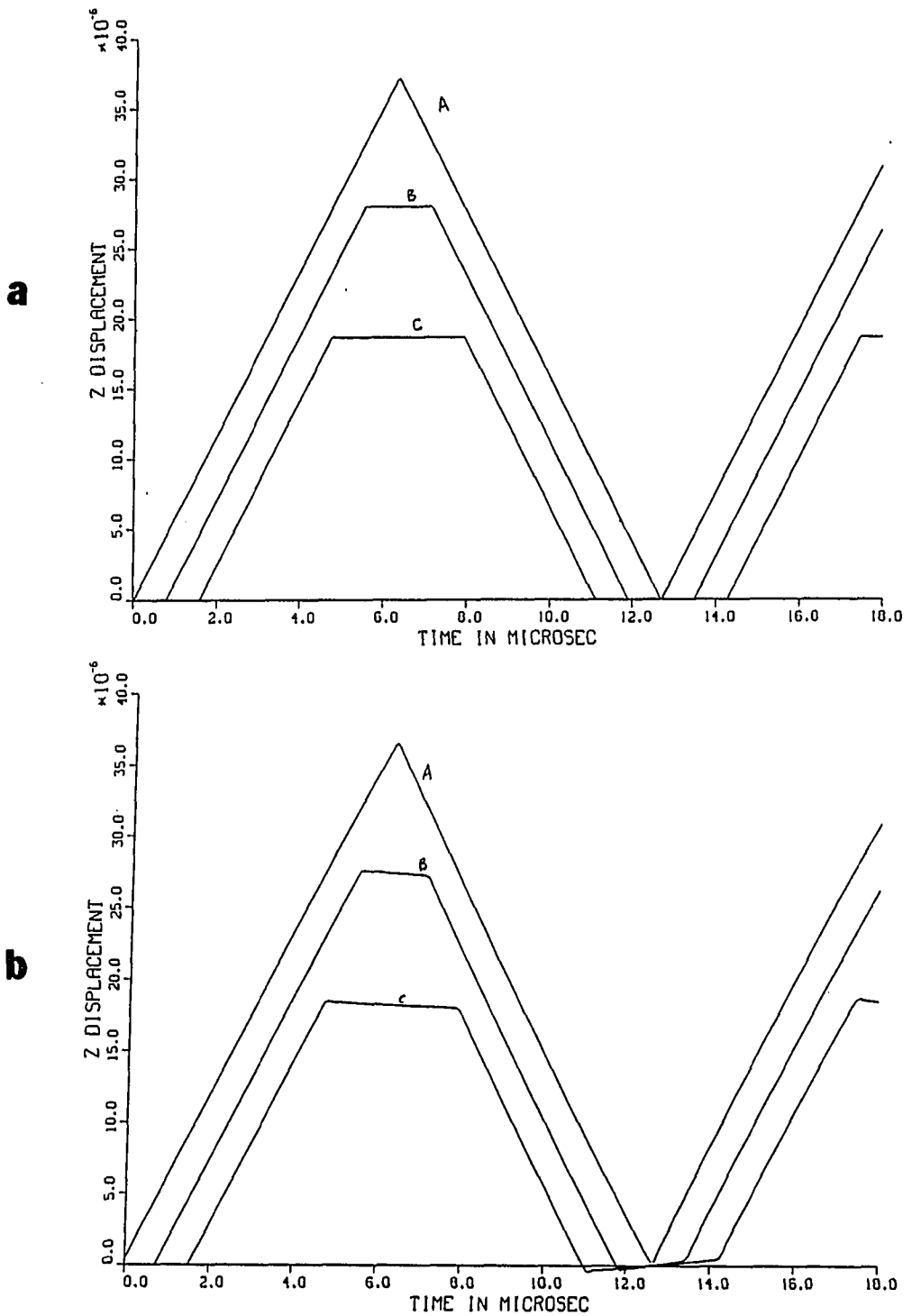

Figure 6.2: Comparisons of the displacement from finite element prediction and series solution. a) Analytic; b) Finite element

the symmetric condition, only one half of the block is discretized into 254x254 = 64,416 rectangular elements. The discretization gives about 10 elements per shear wavelength. Similarly, the 3-D situation has 254x254x1 = 64516 brick elements and 255x255x2 = 130,050 nodes. Time step size is chosen to be 40 ns which results in the Courant number of 0.82. Comparisons among 2-D finite element, 3-D finite element, and analytical results are shown in Figs. 6-3 to 6-10 for four different locations in the block. The results are almost identical, suggesting the validity and the accuracy of the finite element model for this particular situation.

Point Source Comparisons

3-D confirmation can be made through analytical and axisymmetric solutions if the geometry and the source satisfy the axisymmetric conditions. In this example, a point force input to a half-space Lamb's problem is considered. The numerical model of course, cannot handle the infinite boundary. As a matter of fact, only a small 3-D block can be modeled with the present computer power. In this example, a 3 cm x 3 cm x 3 cm aluminum block is considered and discretized into 100x100x100 = 1,000,000 elements. The total number of unknowns is 3,090,903. Time step size is chosen to be 40 ns and the time duration is 12 μs (300 steps). Correspondingly, the axisymmetric geometry is a 5 cm x 5 cm region and is discretized into 254x254 = 64,516 elements. The excitation signal is the same as equation(6.2). Five typical locations in the block are chosen for the comparisons and the results are plotted in Figs. 6-11 to 6-20. It can be noticed that the A-scan data from analytical solutions and from the axisymmetric predictions are almost identical. The error range is within 5 percent. However, reflections are presented in the 3-D results due to the limited

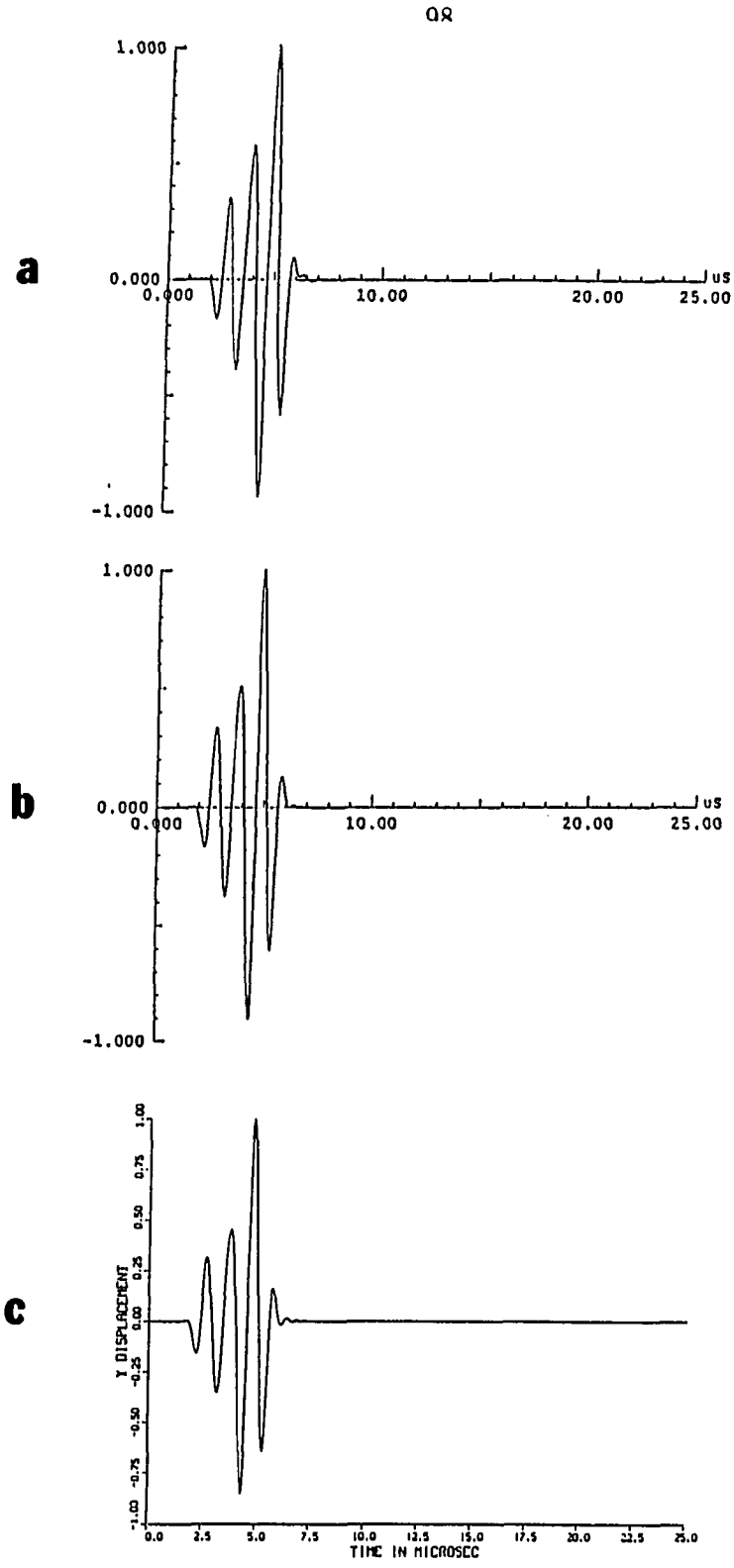

Figure 6.3: The y-component of the displacement at y = 3.4 mm, z = 9.4 mm. a) Analytic; b) 2-D finite element; c) 3-D finite element

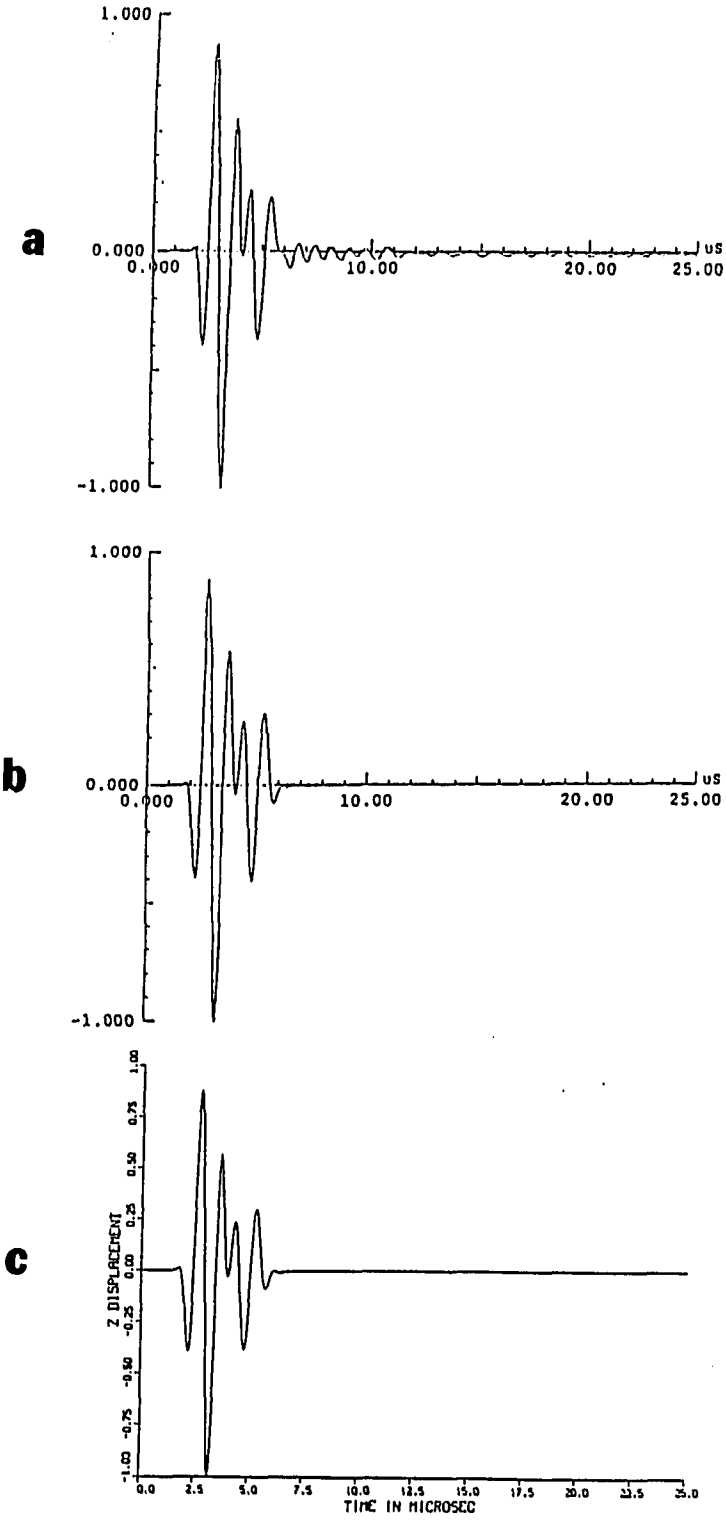

Figure 6.4: The z-component of the displacement at y = 3.4 mm, z = 9.4 mm. a) Analytic; b) 2-D finite element; c) 3-D finite element

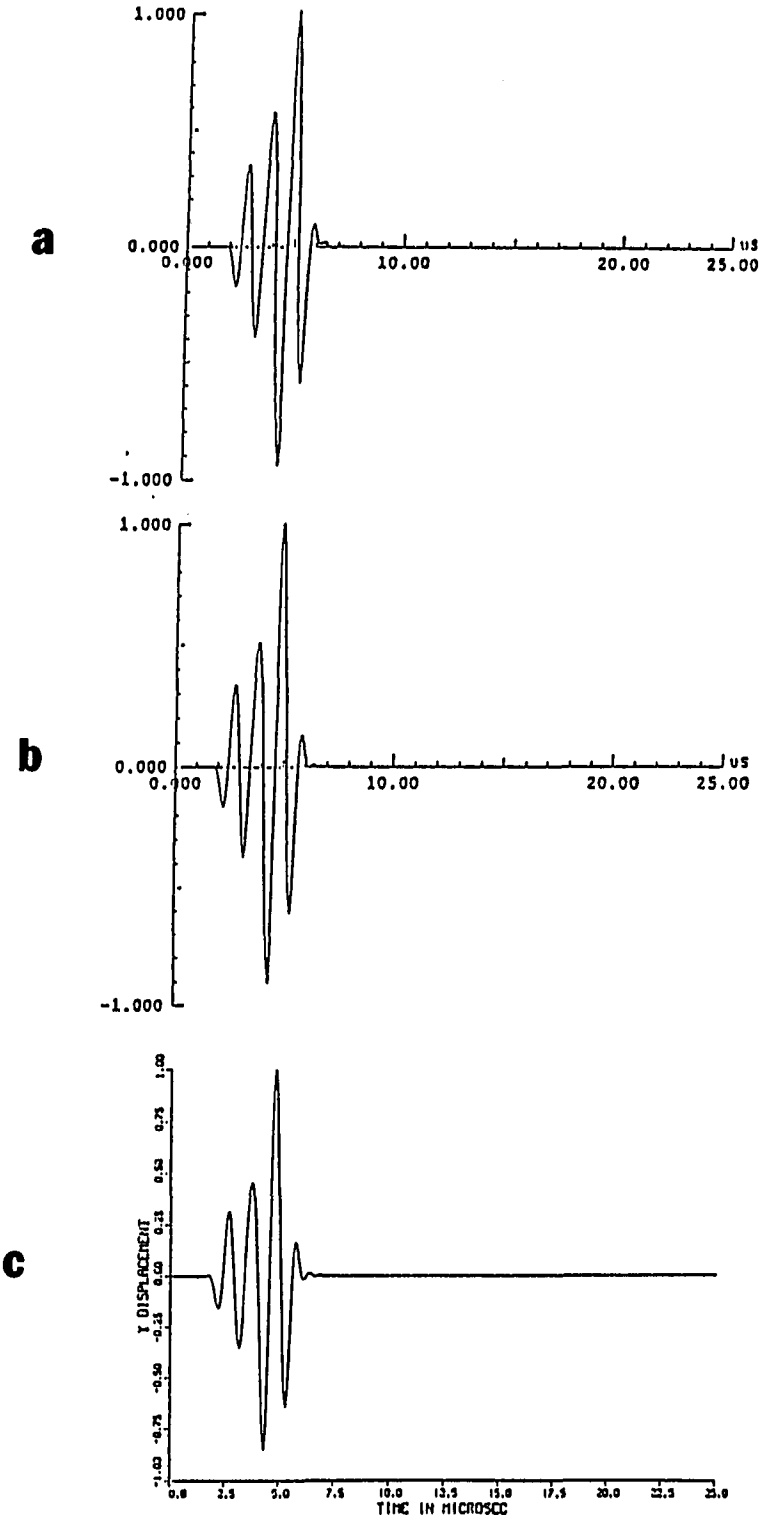

Figure 6.5: The y-component of the displacement at y = 5 mm, z = 8.6 mm. a) Analytic; b) 2-D finite element; c) 3-D finite element

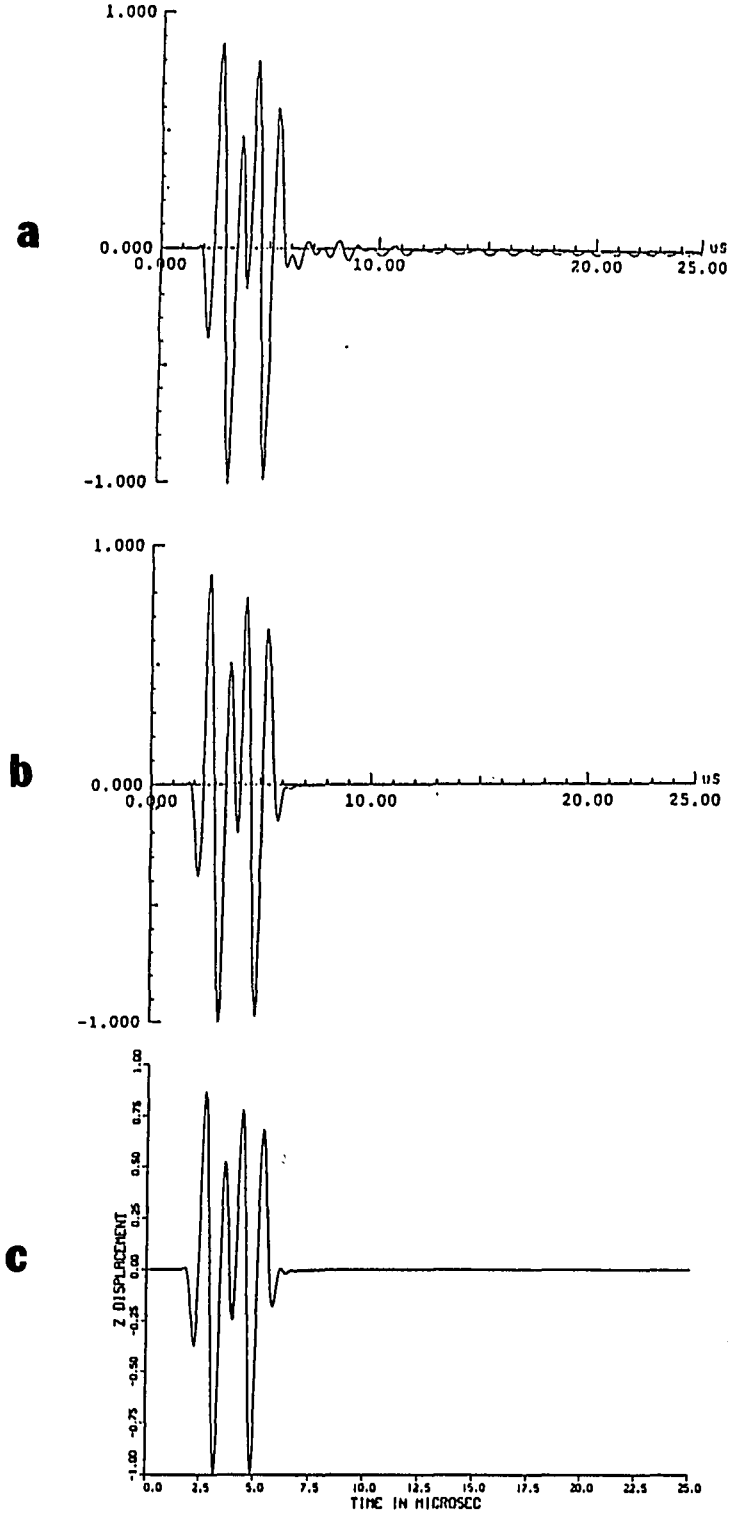

Figure 6.6: The z-component of the displacement at y = 5 mm, z = 8.6 mm. a) Analytic; b) 2-D finite element; c) 3-D finite element

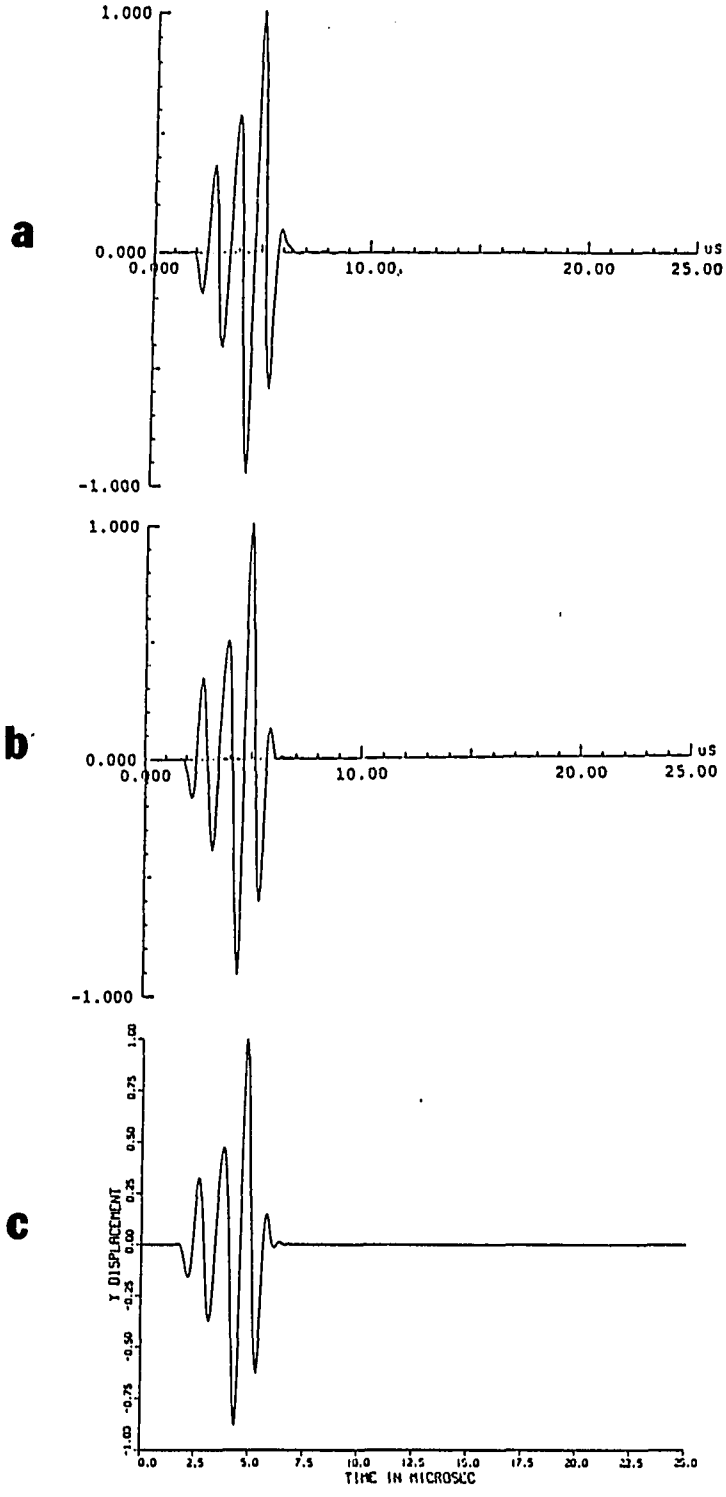

Figure 6.7: The y-component of the displacement at y = 6.4 mm, z = 7.6 mm. a) Analytic; b) 2-D finite element; c) 3-D finite element

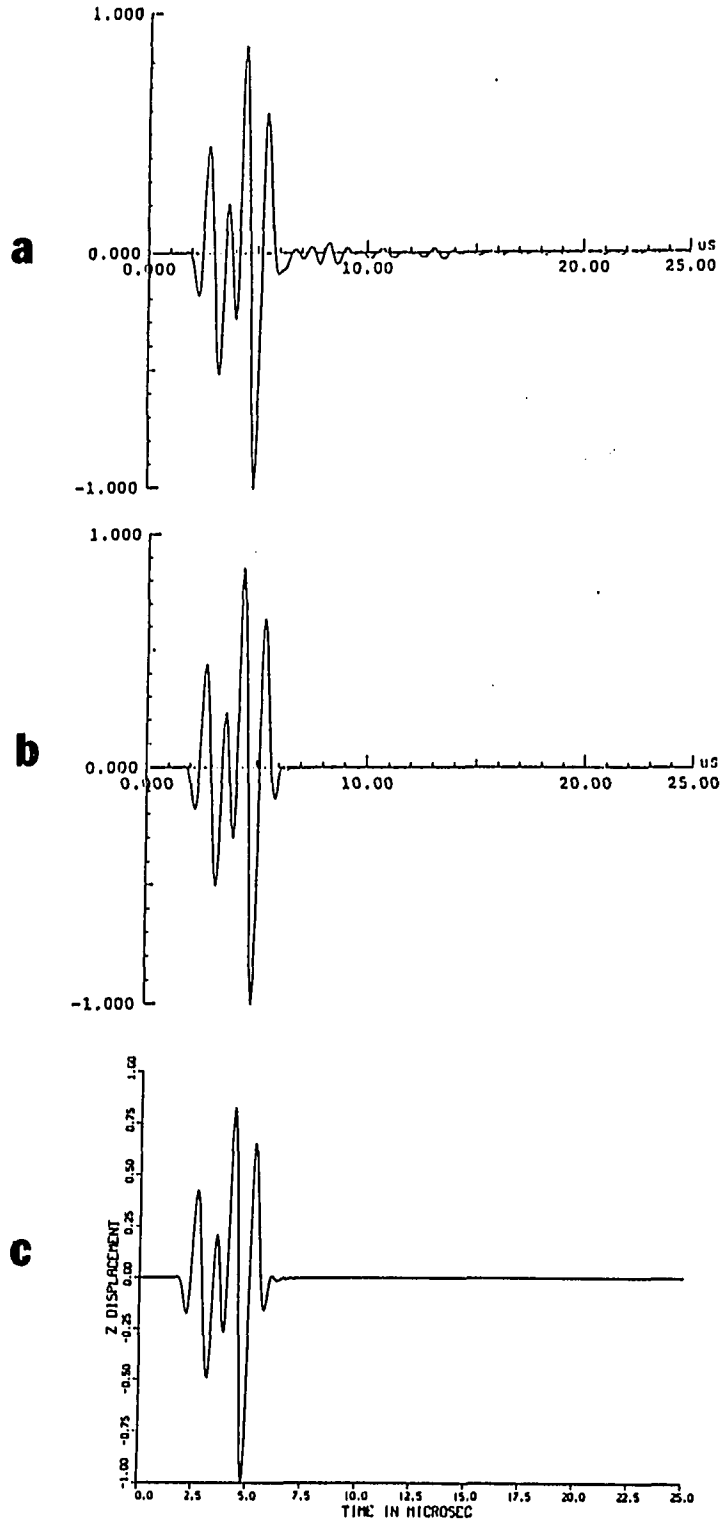

Figure 6.8: The z-component of the displacement at y = 6.4 mm, z = 7.6 mm. a) Analytic; b) 2-D finite element; c) 3-D finite element

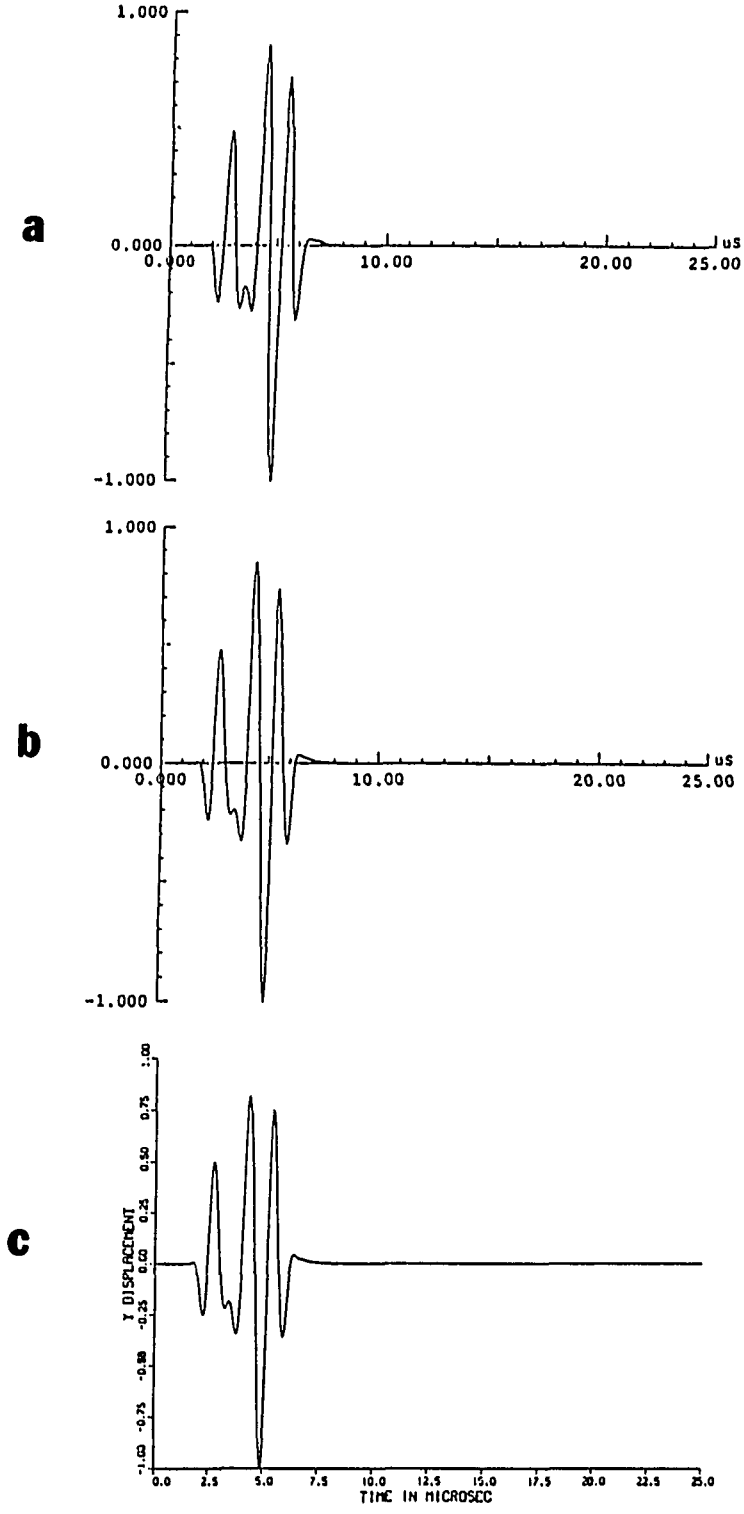

Figure 6.9: The y-component of the displacement at y = 1.8 mm, z = 9.8 mm. a) Analytic; b) 2-D finite element; c) 3-D finite element

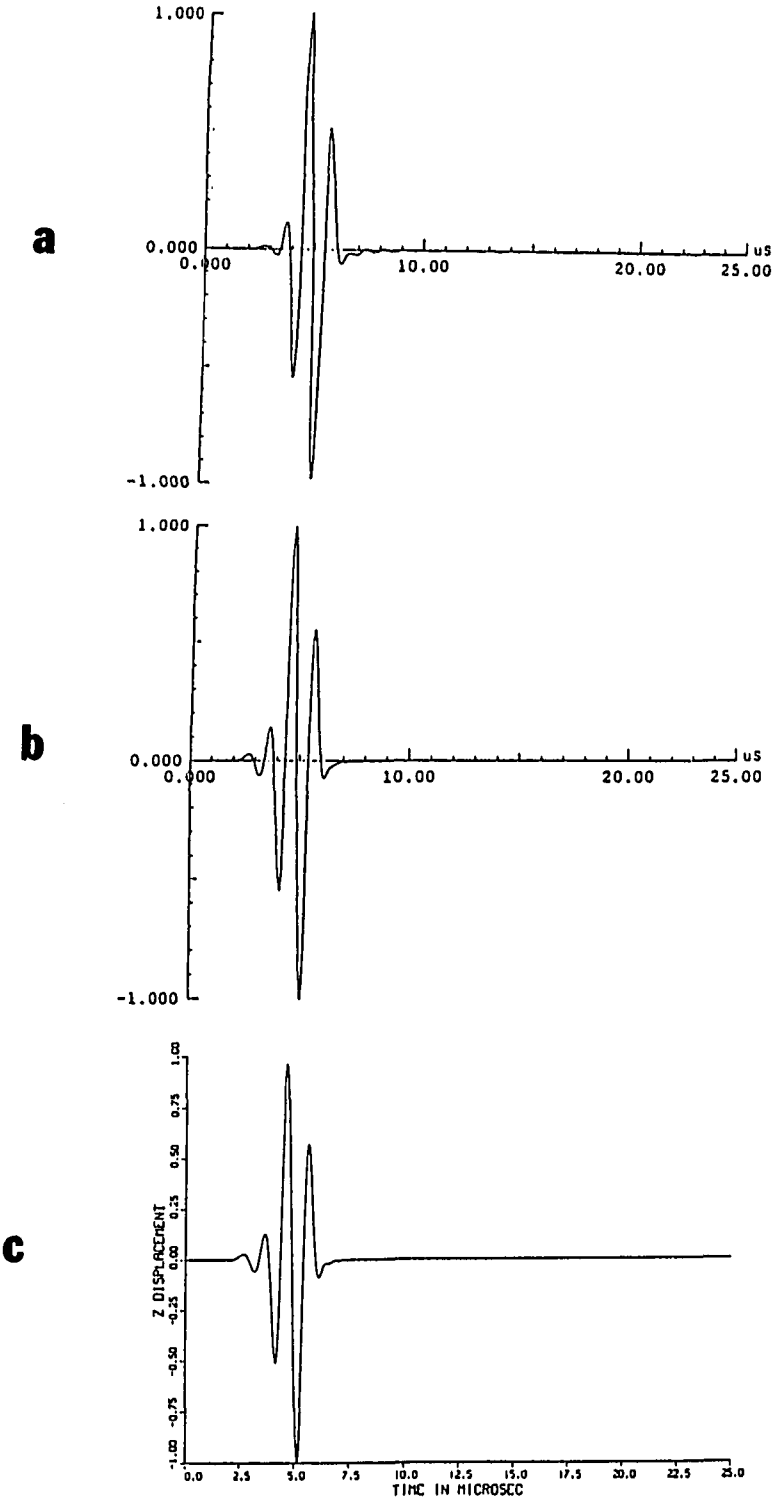

Figure 6.10: The z-component of the displacement at y = 1.8 mm, z = 9.8 mm. a) Analytic; b) 2-D finite element; c) 3-D finite element

mesh size in the 3-D model. The agreement among the longitudinal waves from different solutions are much better than that of shear waves. This is mainly due to the fact that the discretization gives only 10 elements per shear wavelength but 21 elements per longitudinal wavelength. In the axisymmetric case, however, the number of elements per shear wavelength is 15, the accuracy, therefore, is much better. In addition, the amplitudes of the three cases in Figs. 6-15 to 6-20 are different. The 3-D results are about twice the amplitude of the other two because the 3-D results are for a point on the boundary whereas an interior node is used for the axisymmetric and analytic cases. It must be pointed out that the locations of the comparison points are not exactly the same due to the fact that the discretizations are different in the 3-D and axisymmetric cases. Also, the fact that the integration involved in carrying out the analytical solutions is singular on the surface and on the symmetric axis making it more difficult to choose the points for comparison. Nevertheless, the results reveal that the finite element model is valid and accurate provided that the discretization gives at least 10 elements per shear wavelength.

It should be pointed out that even if we choose the same grid spacing Δx in both 2-D and 3-D, the effective discretization is different. The maximum spacing between nodes in 2-D is $\sqrt{2}\Delta x$. In 3-D, however, the maximum node spacing is $\sqrt{3}\Delta x$. Therefore, the discretization in 3-D should have smaller grid spacing in order to achieve the same accuracy as that in a 2-D situation.

The 3-D model is, in general, computationally intensive. Table 6.1 summarizes typical memory requirements and CPU-time consumptions. It can be seen that the 3-D model is restricted due to the present computer power. However, as computer technology improves, this model will become more and more practical.

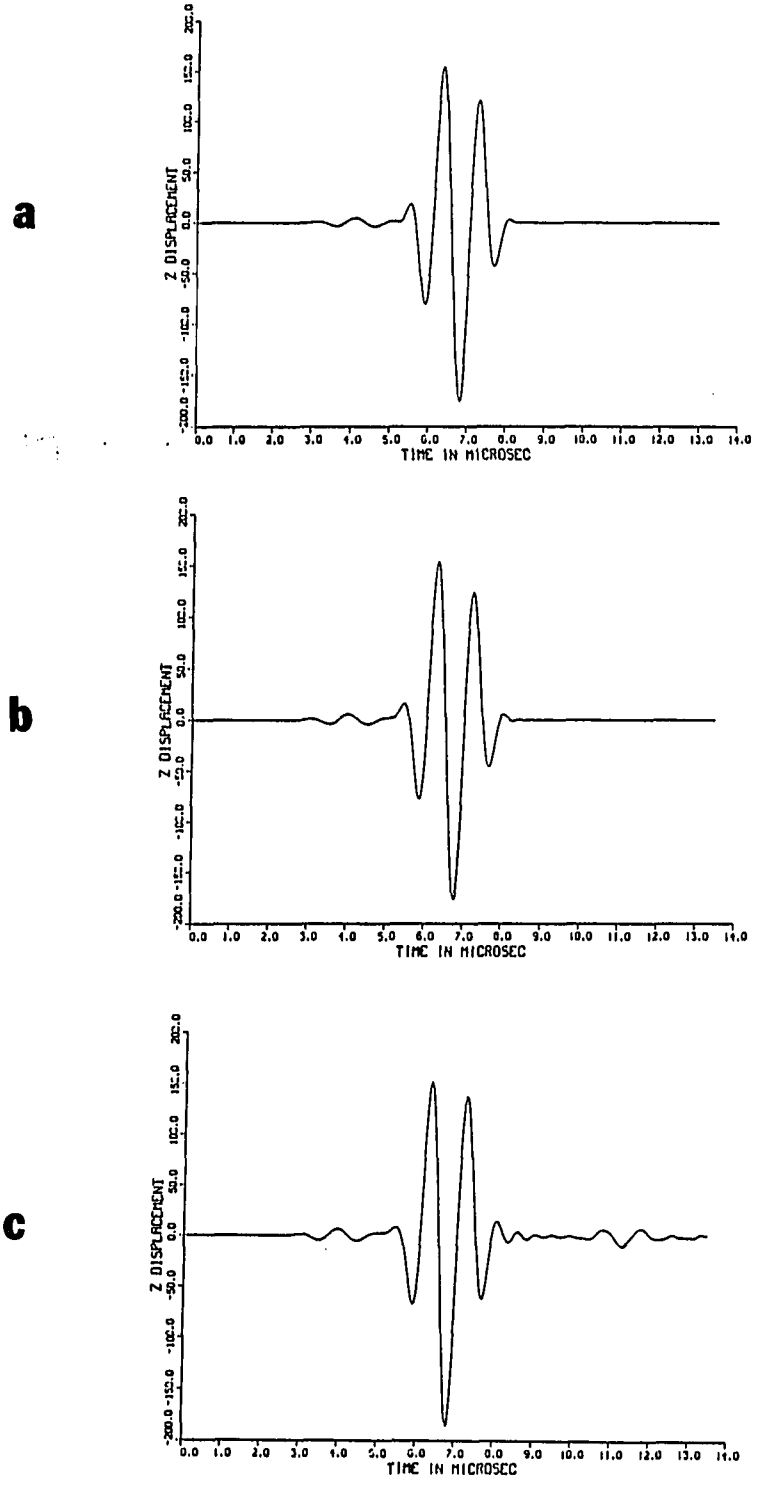

Figure 6.11: The z-component of the displacement at x = 15 mm, y = 0 mm, z = 0.3 mm. a) Analytic; b) Axisymmetric finite element; c) 3-D finite element

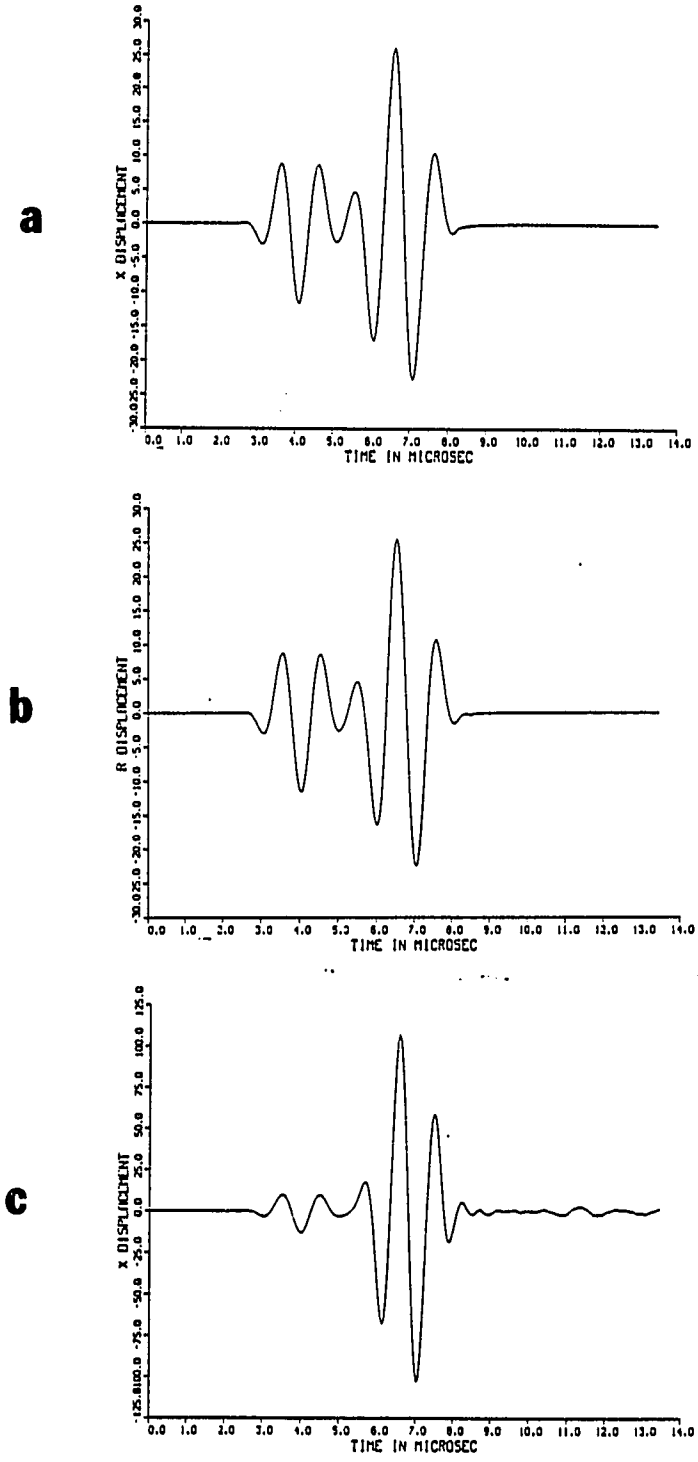

Figure 6.12: The x-component of the displacement at x = 15 mm, y = 0 mm, z = 0.3 mm. a) Analytic; b) Axisymmetric finite element; c) 3-D finite element

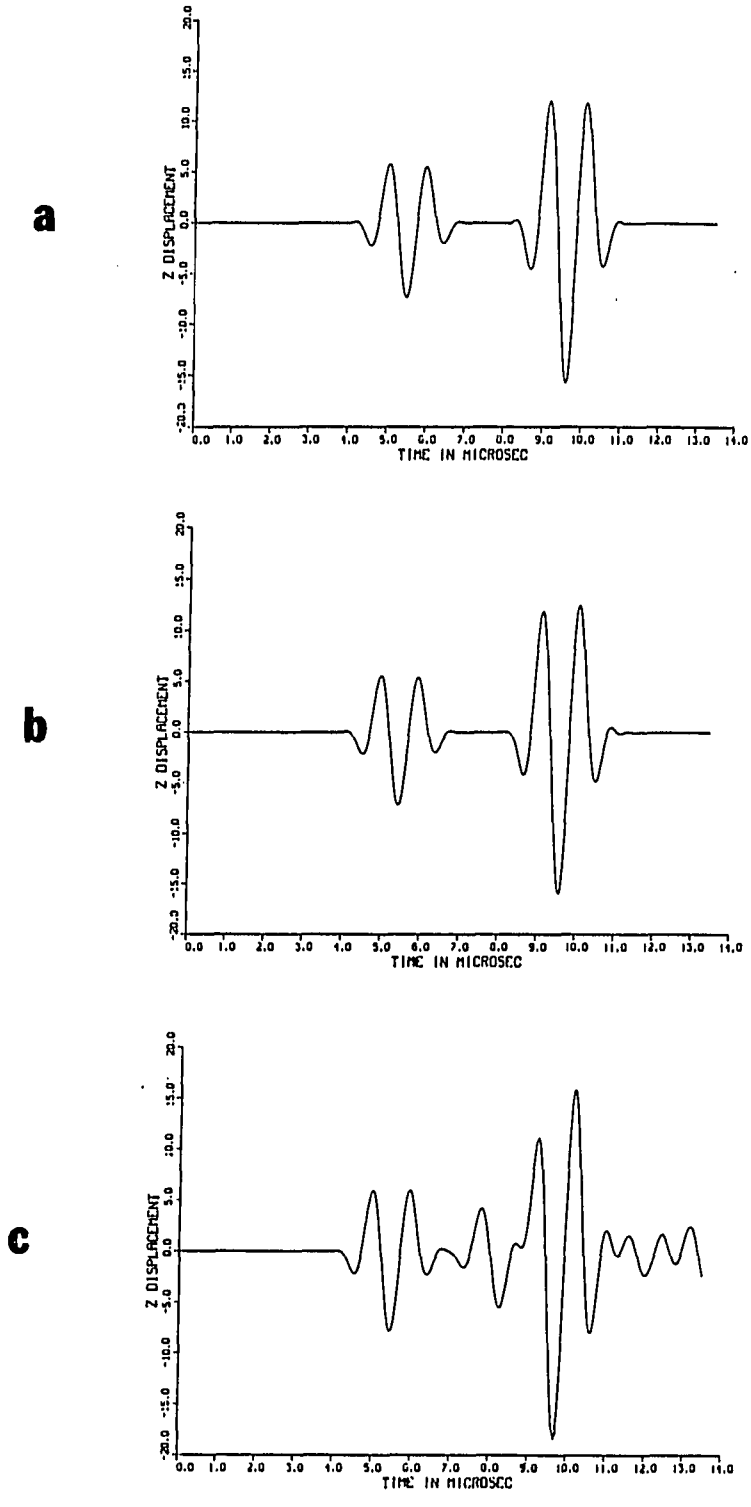

Figure 6.13: The z-component of the displacement at x = 15 mm, y = 0 mm, z = 20 mm. a) Analytic; b) Axisymmetric finite element; c) 3-D finite element

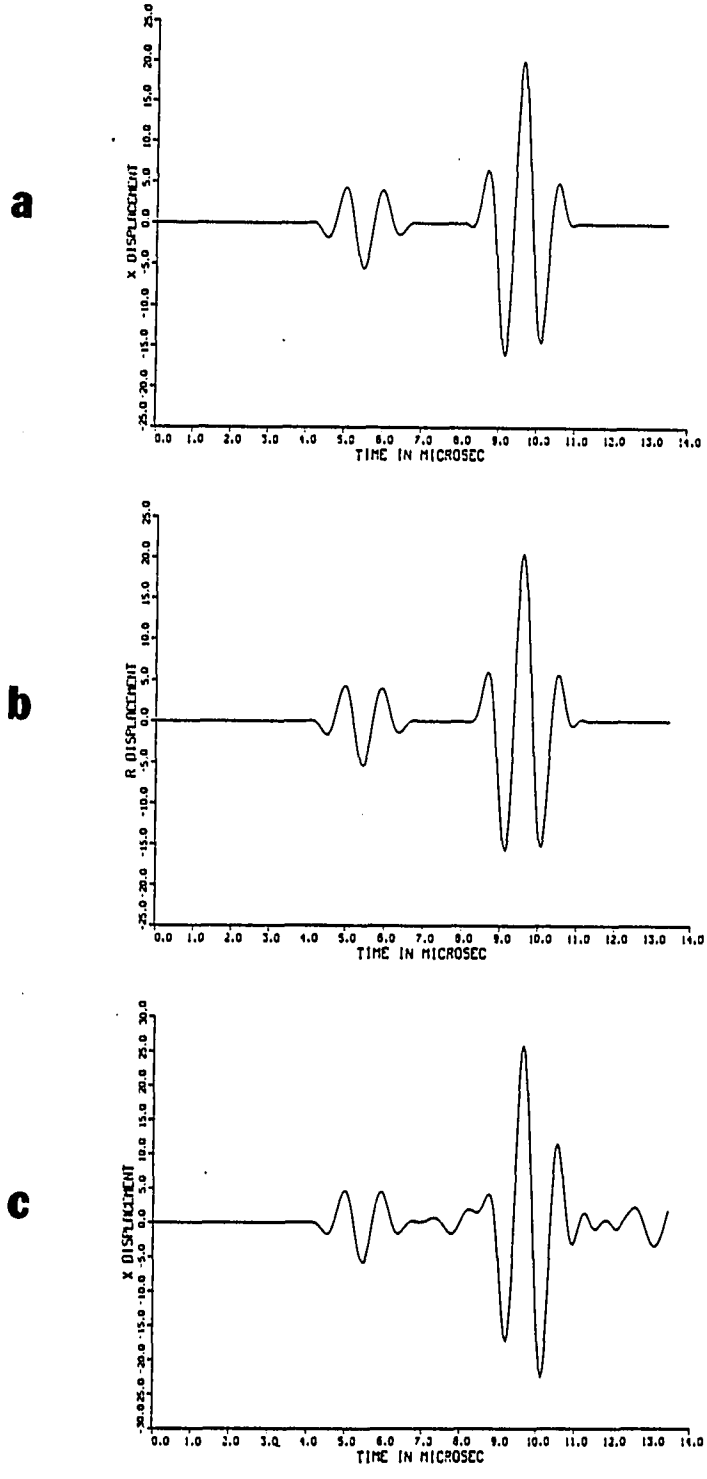

Figure 6.14: The x-component of the displacement at x = 15 mm, y = 0 mm, z = 20 mm. a) Analytic; b) Axisymmetric finite element; c) 3-D finite element

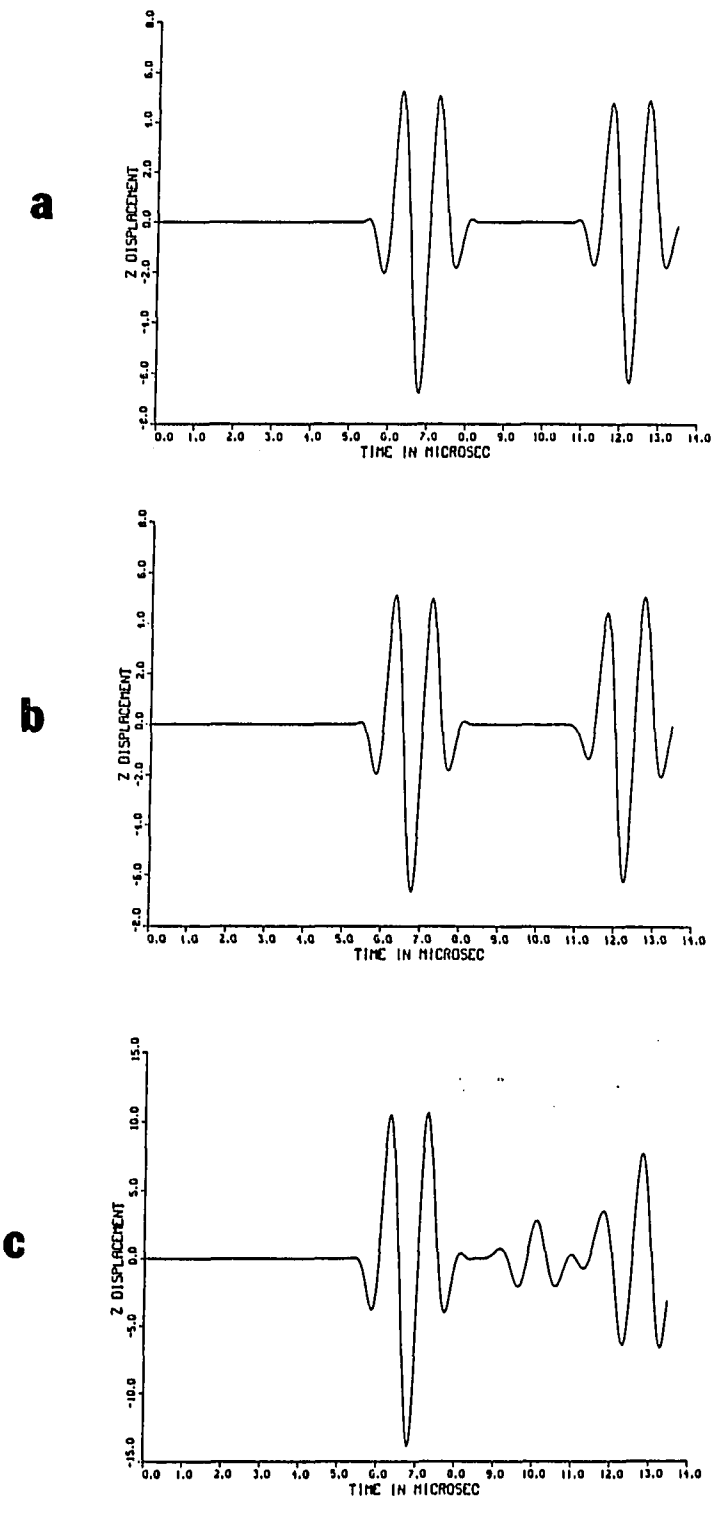

Figure 6.15: The z-component of the displacement at x = 15 mm, y = 0 mm, z = 29.7 mm. a) Analytic; b) Axisymmetric finite element; c) 3-D finite element

a

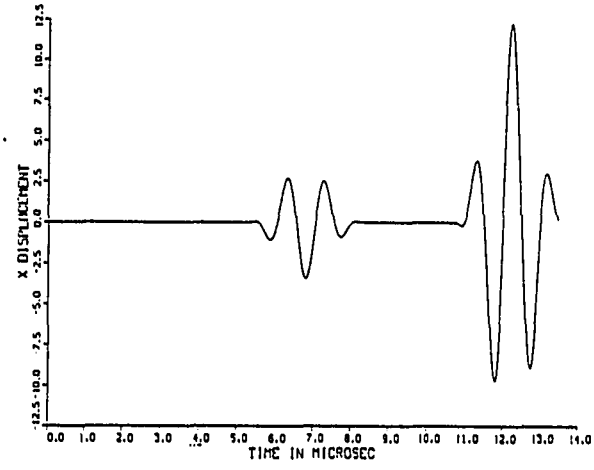

b

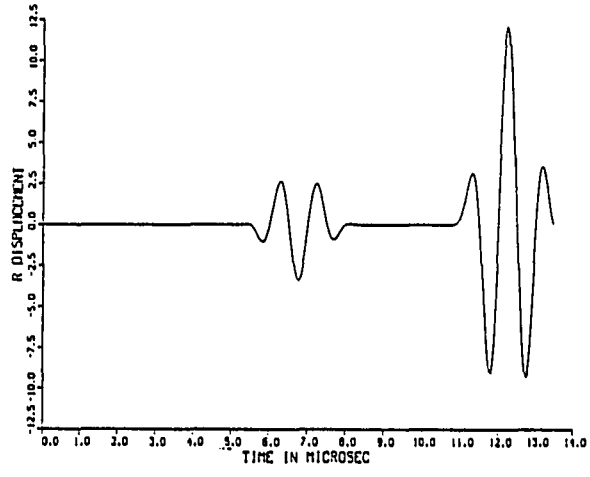

c

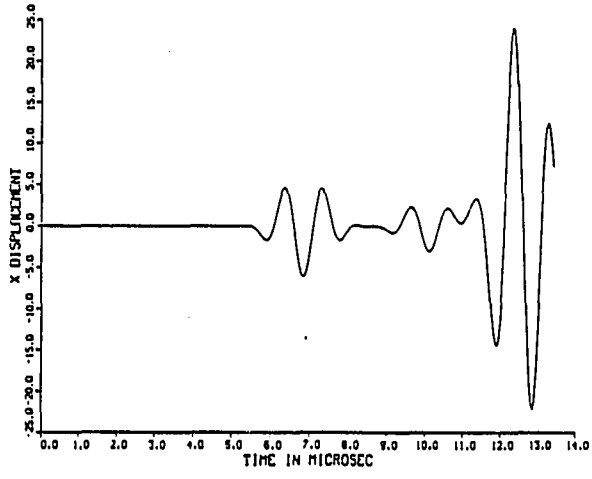

Figure 6.16: The x-component of the displacement at x = 15 mm, y = 0 mm, z = 29.7 mm. a) Analytic; b) Axisymmetric finite element; c) 3-D finite element

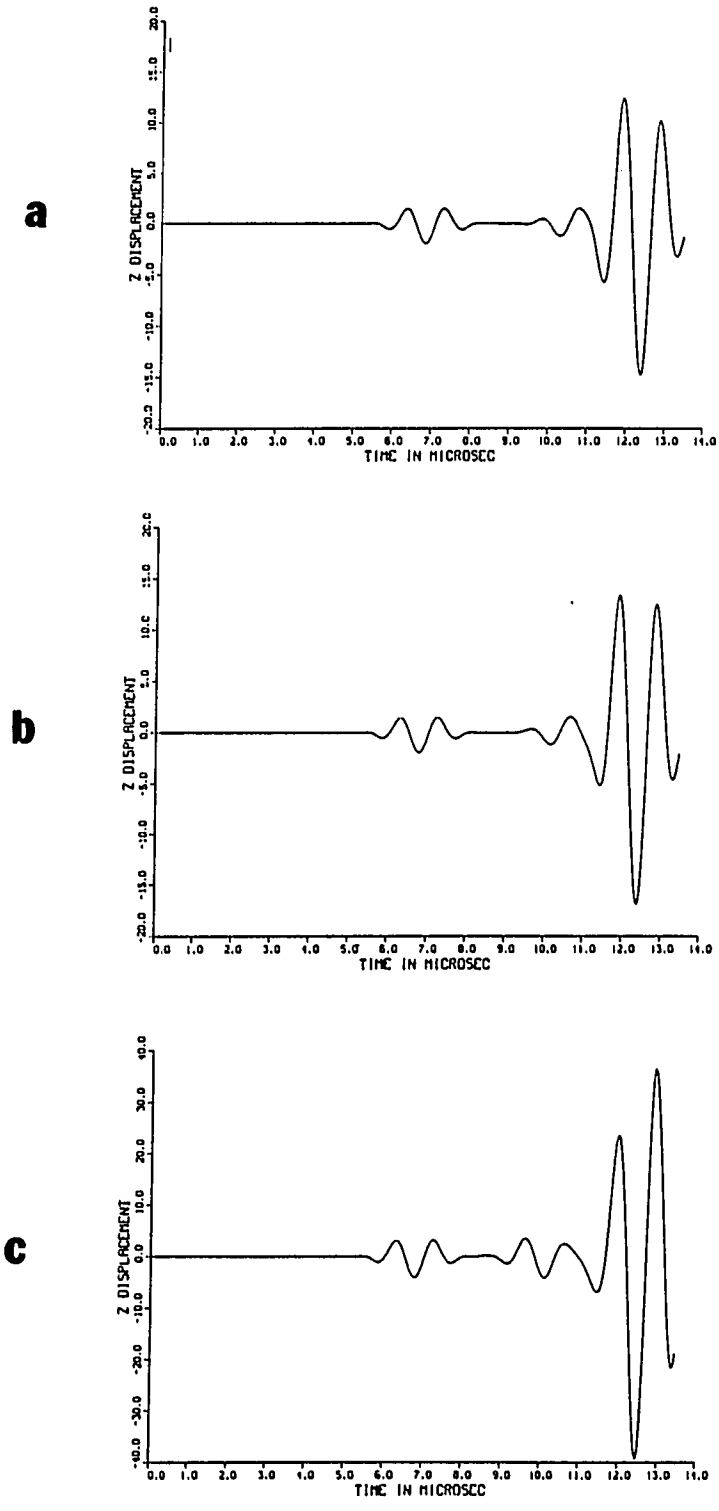

Figure 6.17: The z-component of the displacement at x = 30 mm, y = 0 mm, z = 15 mm. a) Analytic; b) Axisymmetric finite element; c) 3-D finite element

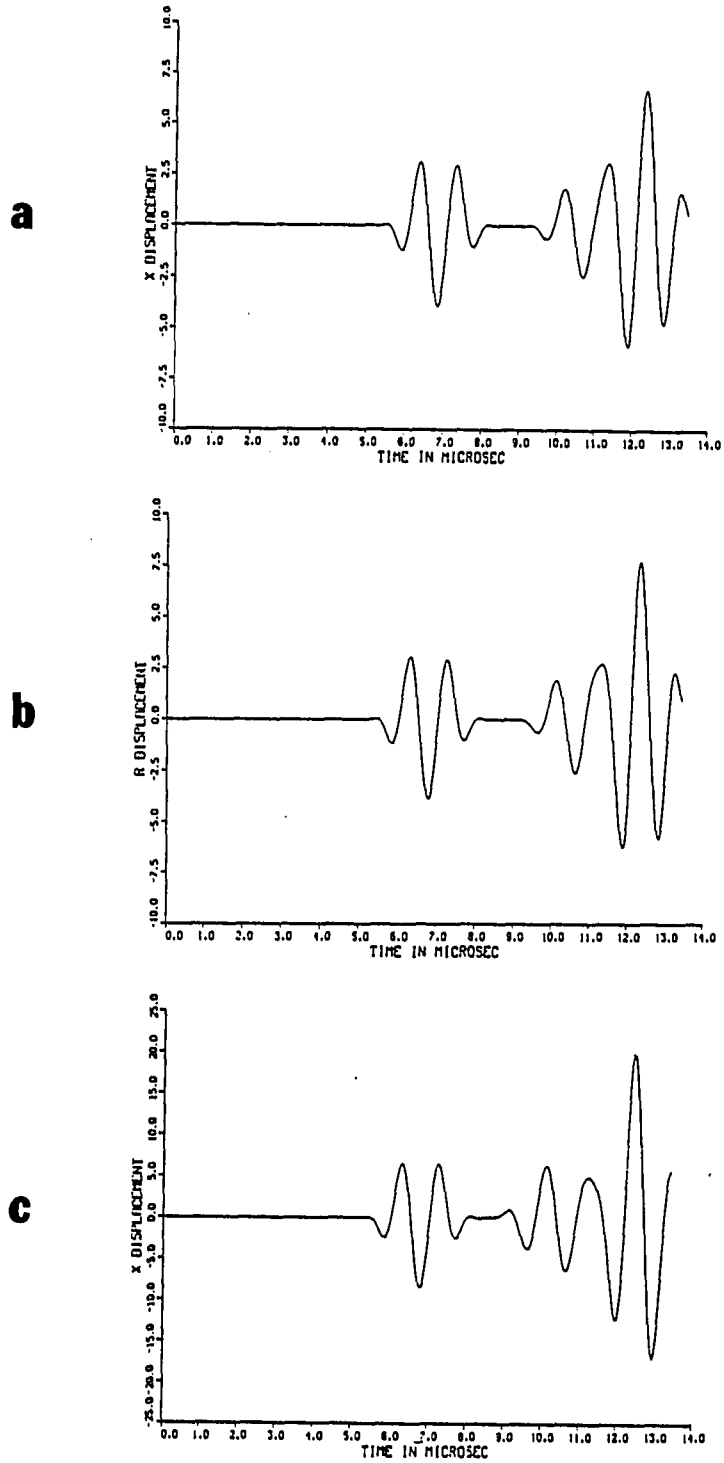

Figure 6.18: The x-component of the displacement at x = 30 mm, y = 0 mm, z = 15 mm. a) Analytic; b) Axisymmetric finite element; c) 3-D finite element

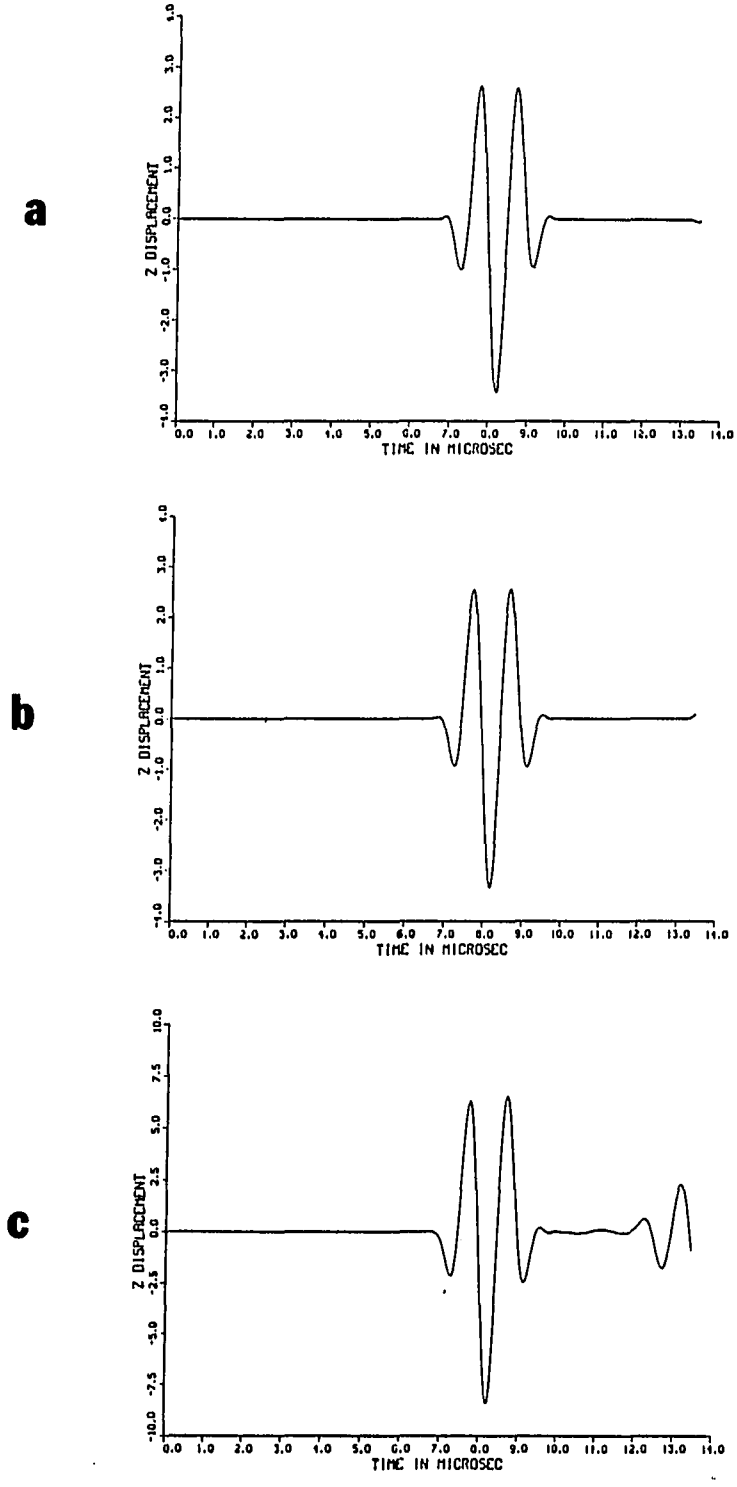

Figure 6.19: The z-component of the displacement at x = 30 mm, y = 0 mm, z = 29.7mm. a) Analytic; b) Axisymmetric finite element; c) 3-D finite element

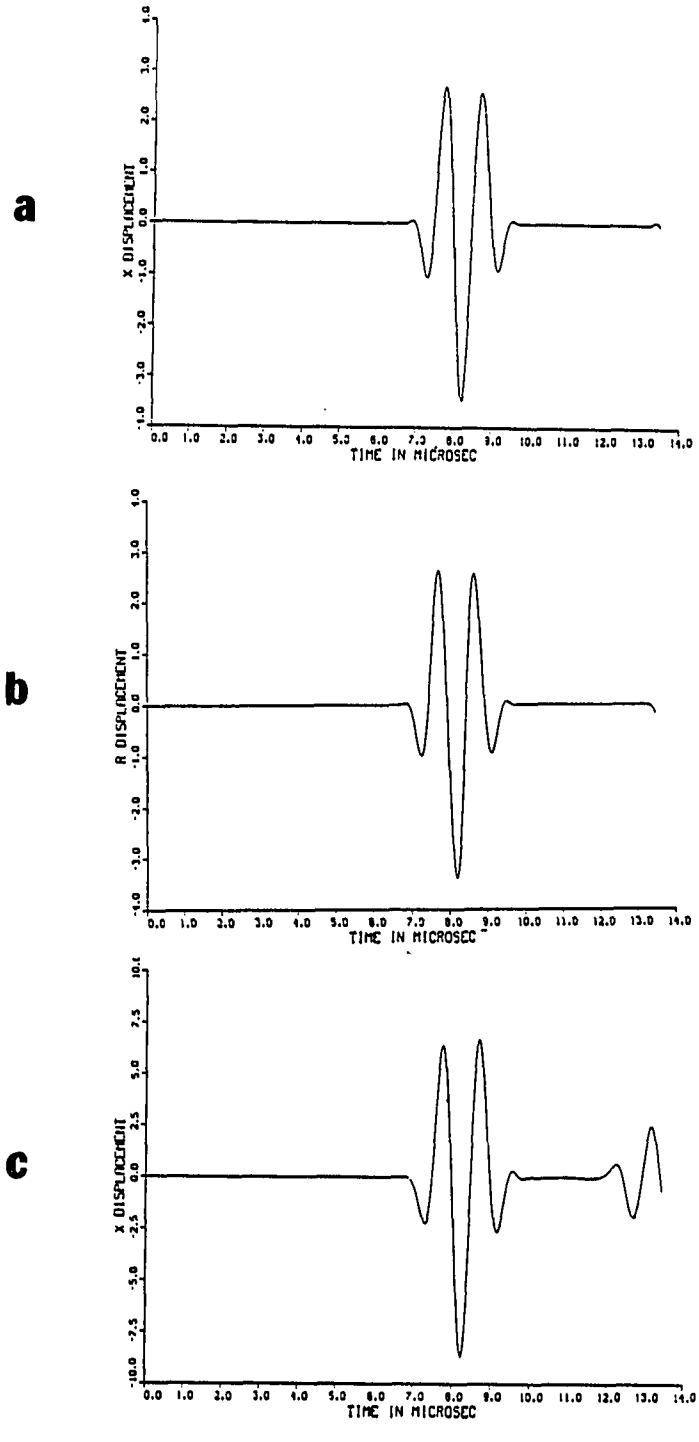

Figure 6.20: The x-component of the displacement at x = 30 mm, y = 0 mm, z = 29.7mm. a) Analytic; b) Axisymmetric finite element; c) 3-D finite element

Table 6.1: Summary of CPU-time and memory requirements of the finite element model

2-D and Axisymmetric			3-D		
# of elements	memory (MByte)	CPU-time (sec./step)	# of elements	memory (MByte)	CPU-time (sec./step)
10,000	0.36	1.4	125,000	6.88	91.8
64,516	2.13	8.10	1,000,000	49.9	672

* All the computations are performed on a Stardent GS2000 computer (128 Mbytes, 80 MFlops)

Wave/Defect Interactions

The comparisons presented in previous sections shown the validity of this finite element model. It can therefore be used to study situations where analytical solutions are not available. As a matter of fact, this is the main goal of developing numerical techniques.

For NDE applications, the type of signals that can be received from a defect are always important. The interactions of ultrasonic waves with defects, therefore, are of great interest.

Due to the high computational cost of the 3-D code, this study is restricted to 2-D geometries only. The first example is a 20 cm x 10 cm block with a rectangular slot of dimensions 8 mm x 0.4 mm in the center, subject to a point source input with an input waveform expressed in equation (6.2). The geometry is shown in Fig. 6-21. Only one half of the block is discretized because of the symmetric condition along the centerline. There are a total of 250x250 = 62,500 rectangular elements. The wave fronts are plotted in Fig. 6-22 at particular time steps. From these plots, it can be observed that the longitudinal, shear, surface, and head waves all originate from the same line source, and separate as they travel further into the material because

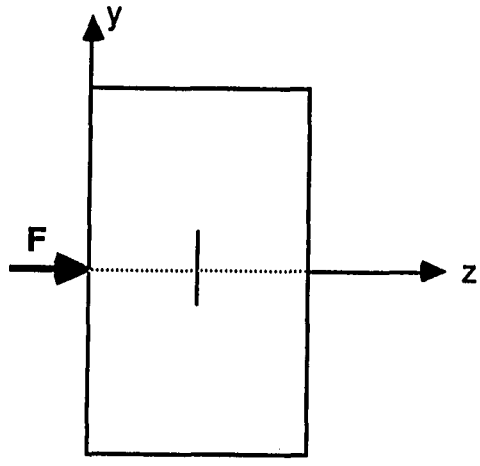

Figure 6.21: Geometry detail of the example used for studying L-wave/defect interactions

of the different traveling velocity. At about 10 μs, the longitudinal wave arrives at the defect and forms a strong reflection which can be detected on the surface. The main L-wave is distorted and acts as the transmission part of the input which travels further to the back surface of the block and can be used as the raw data for the transmission mode inverse algorithms discussed in later chapters. A more interesting phenomenon may be the two rings which travel with shear velocity and are formed through the mode conversion of the L-wave/defect interaction at the two tips of the crack. Detection of these two edge waves could help to determine the crack tip locations and therefore the size the crack. A similar study with a finite aperture transducer is presented in Fig. 6-23 where a $1''$ diameter transducer with the same waveform of equation (6.2) is used. The main difference is that both the edge waves and the shear wave are much smaller in comparison with the surface wave and the

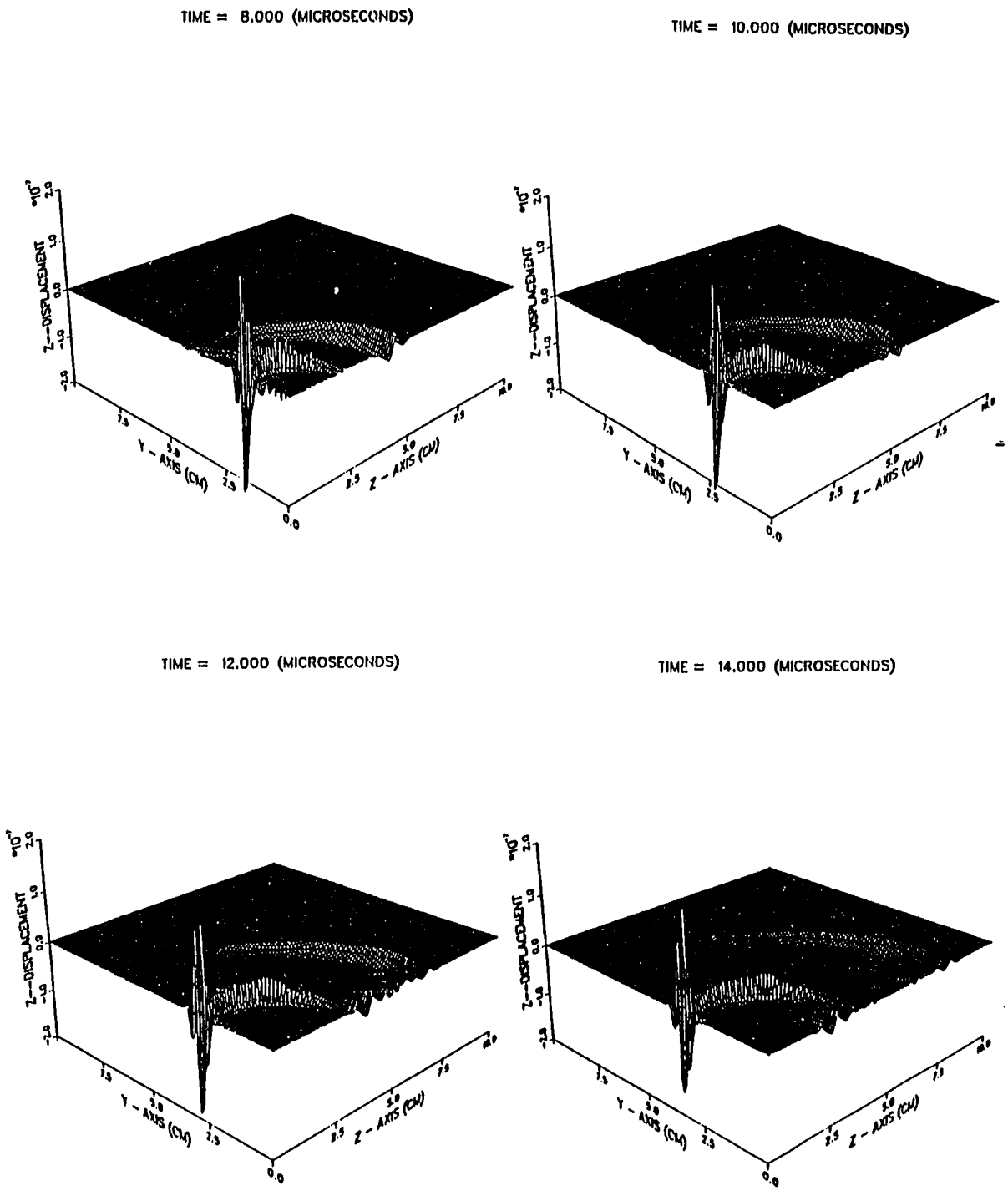

Figure 6.22: Displacement plots of the L-wave/defect interactions

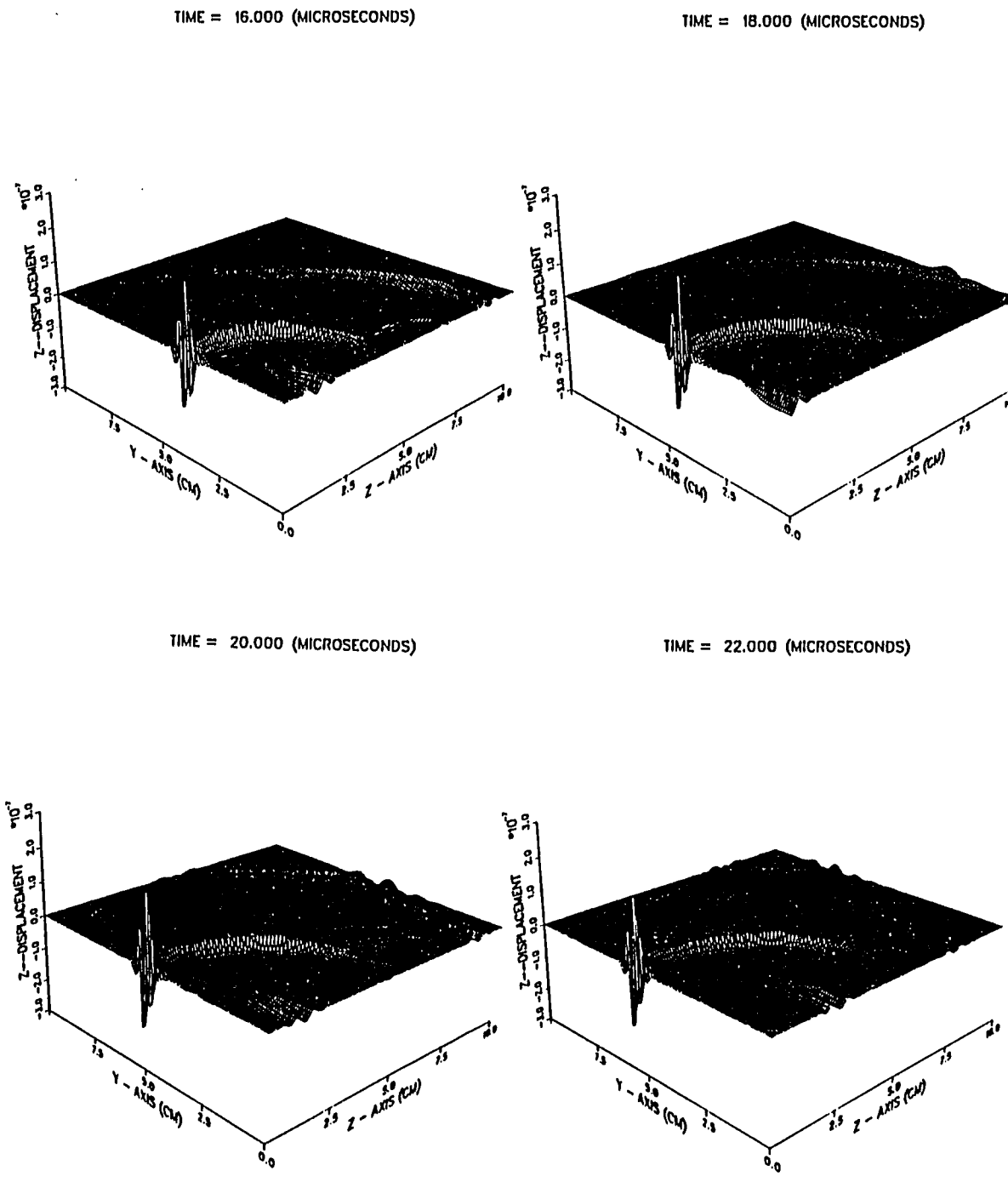

Figure 6.22 (Continued)

shear wave resulting from a point source. However, the L-wave reflections are similar. This phenomenon is referred to in Chapter 8 when the finite aperture effects of the defect image reconstruction are studied.

Since most of the point or line source energy goes with the surface wave, as illustrated in Fig. 6-23, a point source can be utilized to launch a surface wave and to detect a surface breaking crack. The second example, therefore, considers the interaction of surface waves with a surface breaking crack. The geometry is shown in Fig. 6-24 where two cracks of dimensions 4 mm x 0.4 mm are located symmetrically with respect to the y-axis. With a point source acting at the center between the two cracks, the symmetric conditions hold on the centerline of this aluminum block. Applying a similar wave form as shown in equation (6.2), results in the displacement distribution at different time steps are plotted in Fig. 6-25. Only one quarter of the geometry is shown in order to achieve better resolution for the details around the crack. It can be seen that a fairly strong reflection is formed at the first corner and the rest of the surface wave is transmitted along the crack edge going down towards the tip. A dramatic change can be noticed at the tip where the main portion of the transmitted surface wave on the edge is converted into a shear wave which is launched into the material. Only a very small part of the incident surface wave is transmitted beyond the crack.

The amplitude of the transmitted surface wave depends, to a certain extent, on the depth of the crack, as does the amplitude of the reflected wave. The displacement plots with different depths are compared in Figs. 6-26 and 6-27. It can be seen that, when the crack depth is smaller than the surface wave length (3 mm in this case), the amplitude of the transmitted wave mainly depends on the depth. However, when the

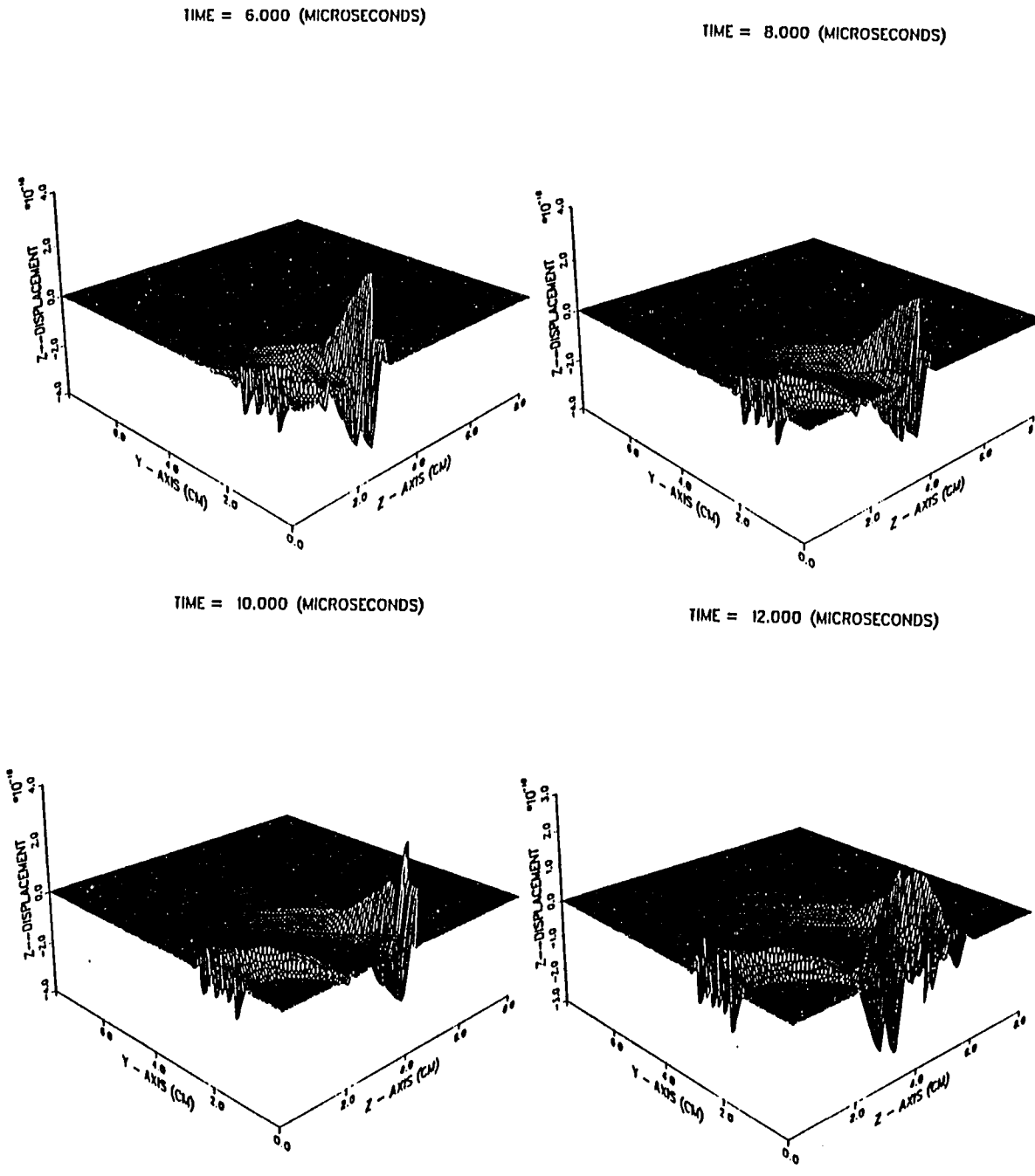

Figure 6.23: Interactions of L-wave from a finite aperture transducer with a subsurface defect

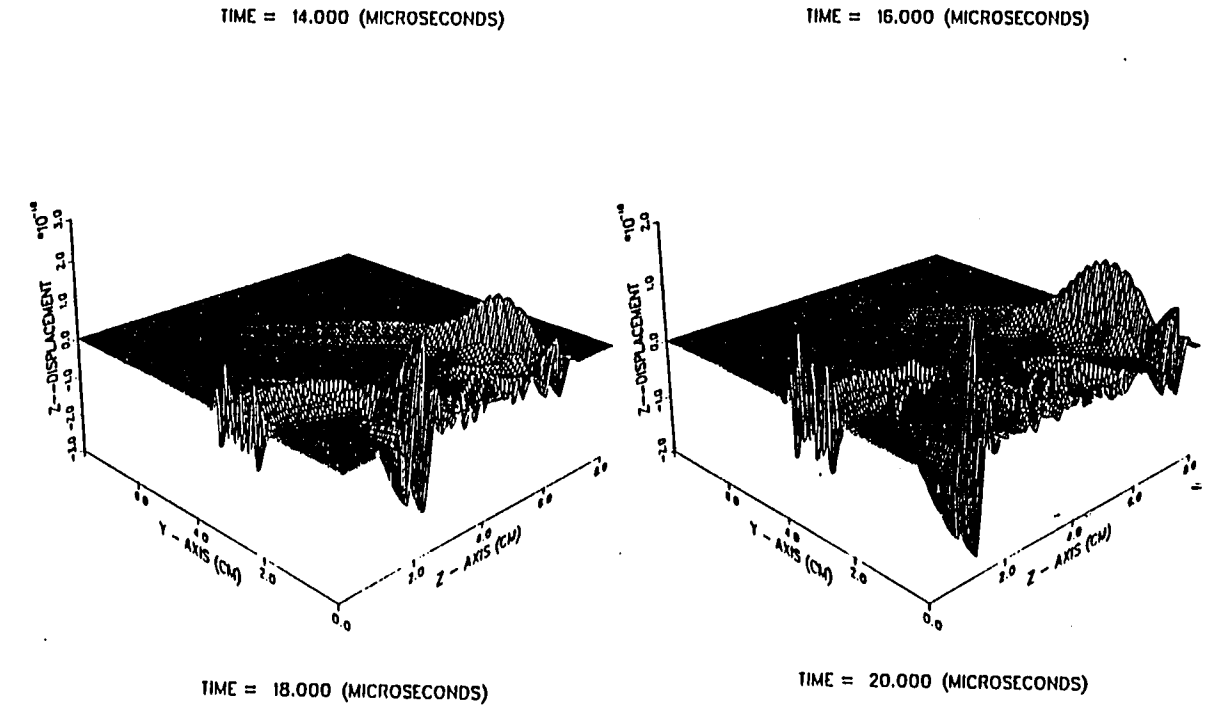

Figure 6.23 (Continued)

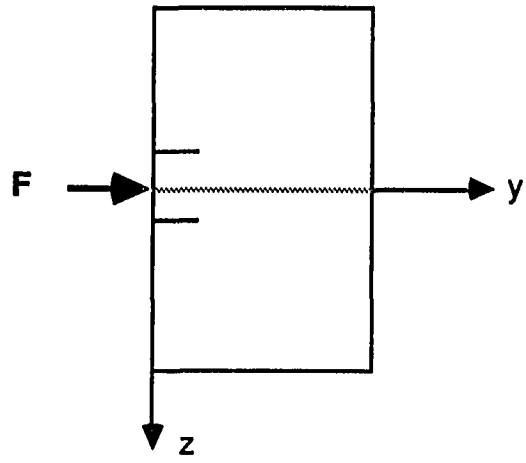

Figure 6.24: Geometry detail for studying the surface wave/defect interactions

depth becomes larger, the amplitude becomes independent of the depth. In the latter cases, the depth is related to the traveling time of the transmitted surface wave.

Even though this study is on a 2-D geometry, the phenomena associated with surface wave interaction with defects are vividly illustrated. Due to the fact that the point source in 2-D implies a line source in 3-D, the propagation of the surface wave in 2-D is different than that of the 3-D point source. For example, there is no geometry attenuation with the 2-D surface wave, while the 3-D surface wave decays according to $1/\ln r$ (point source). Nevertheless, the 2-D numerical model does give a vivid illustration of the wave/defect interactions.

Anisotropy

In chapter 4, the wave propagation phenomena in anisotropic materials are successfully modeled for both 2-D and axisymmetric cases. Significant differences, how-

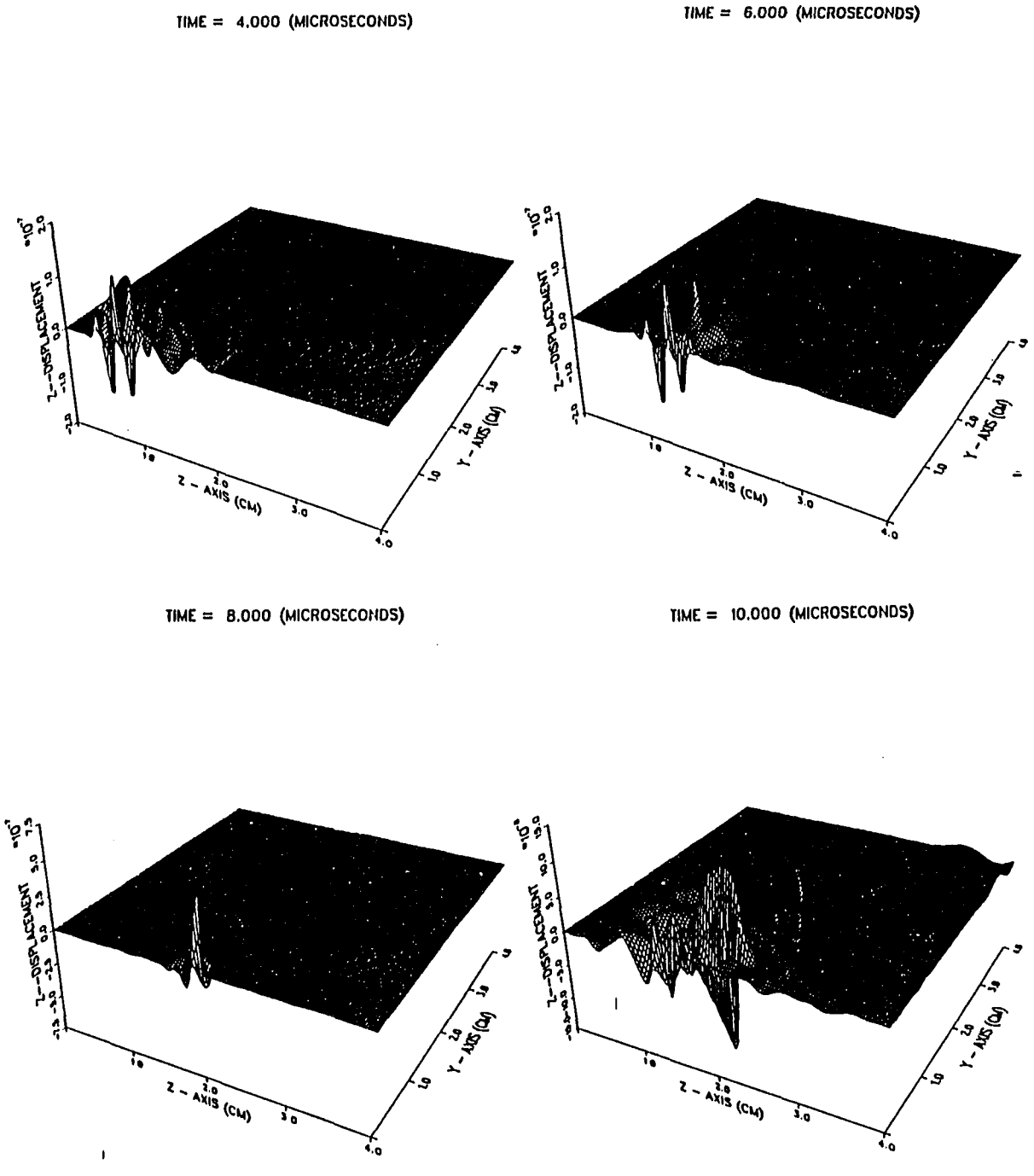

Figure 6.25: Displacement plots showing the interactions of a 2-D surface wave with a defect of 3.2mm depth

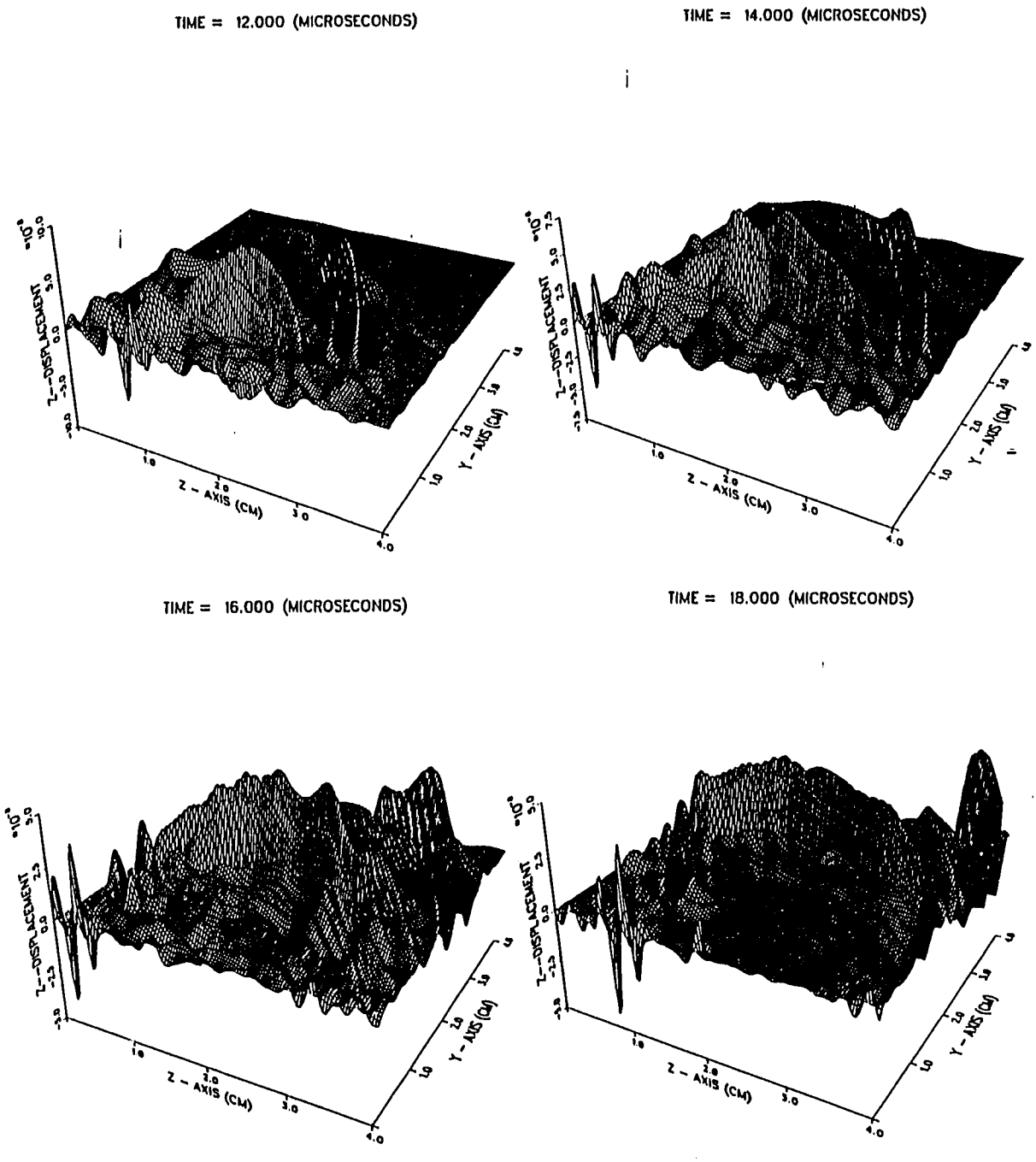

Figure 6.25 (Continued)

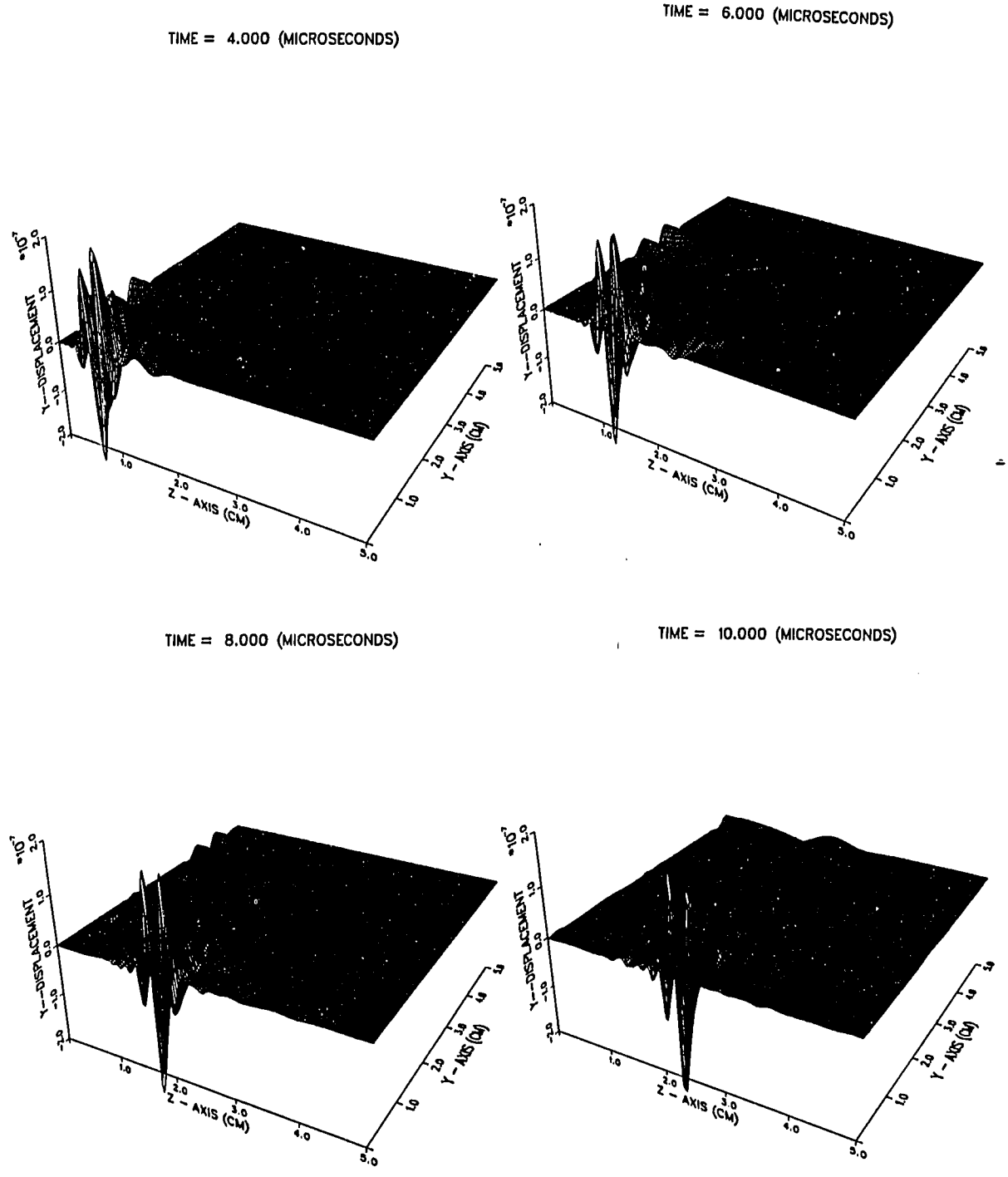

Figure 6.26: A 2-D surface wave interacts with a defect of depth 4.8mm

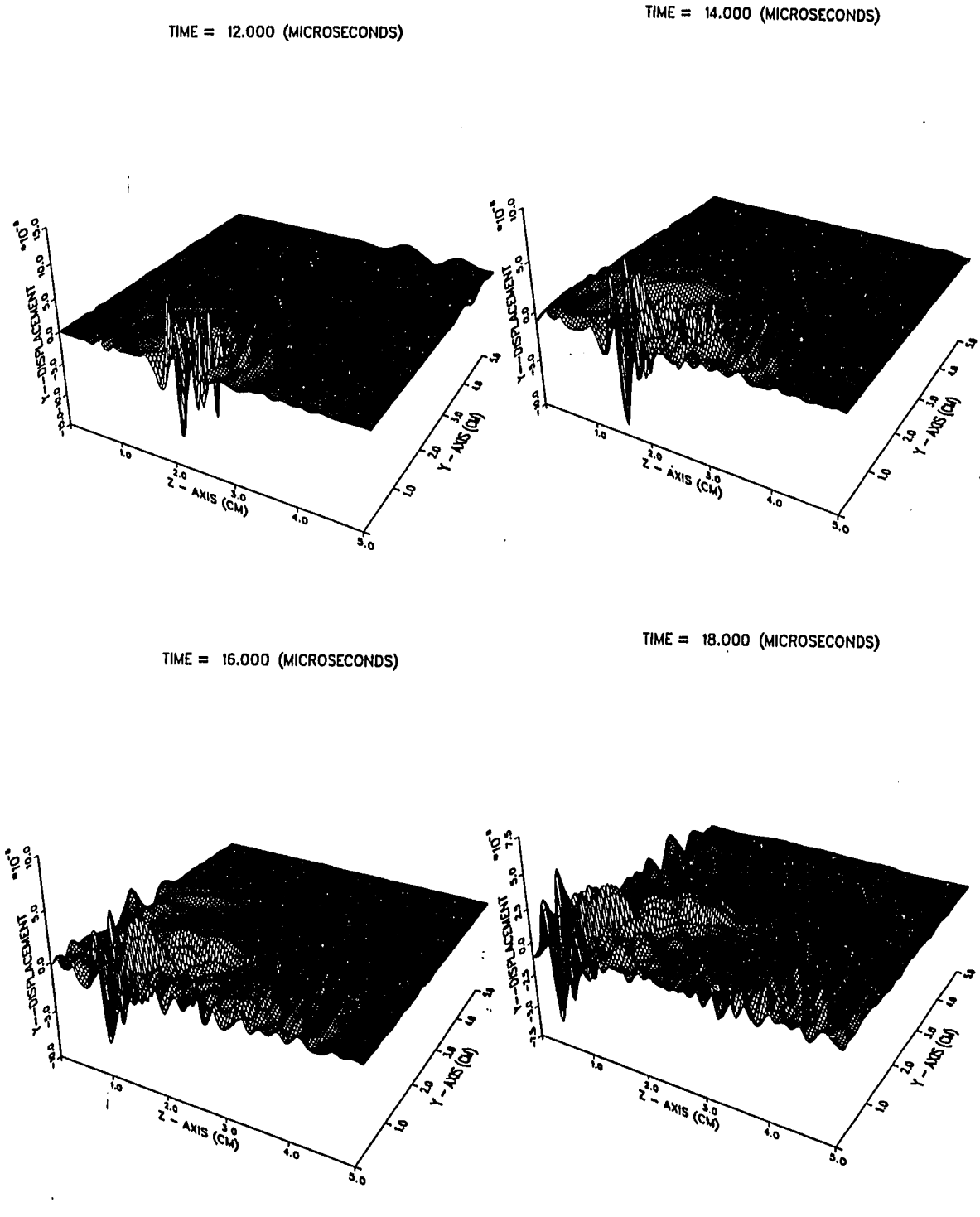

Figure 6.26 (Continued)

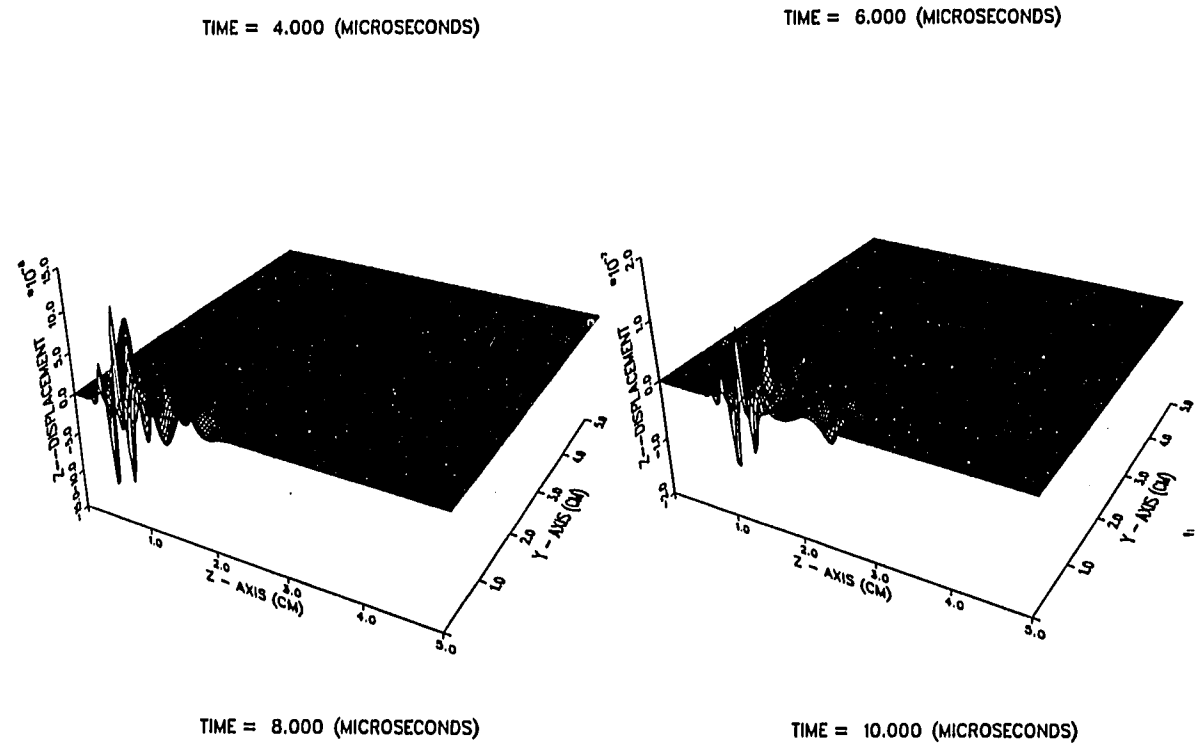

Figure 6.27: A 2-D surface wave interacts with a defect of depth 2mm

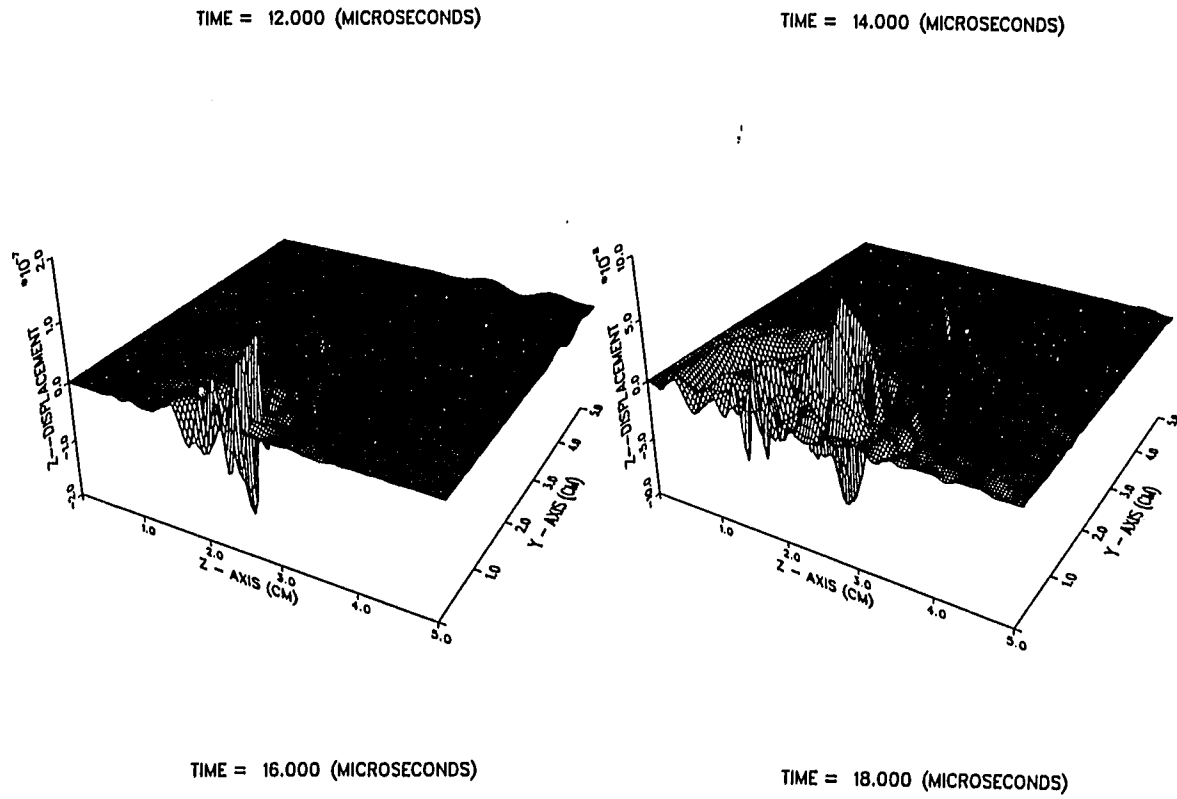

Figure 6.27 (Continued)

ever, may be observed in the full 3-D cases. This section considers an orthorhombic material in a 3-D geometry. The material properties are

$$C_{11} = 21.47 \times 10^{10}\ N/m^2 \qquad C_{22} = 19.46 \times 10^{10}\ N/m^2$$
$$C_{33} = 26.71 \times 10^{10}\ N/m^2 \qquad C_{44} = 12.44 \times 10^{10}\ N/m^2$$
$$C_{55} = 7.342 \times 10^{10}\ N/m^2 \qquad C_{66} = 7.433 \times 10^{10}\ N/m^2$$
$$C_{12} = 4.694 \times 10^{10}\ N/m^2 \qquad C_{13} = 2.177 \times 10^{10}\ N/m^2$$
$$C_{23} = 10.79 \times 10^{10}\ N/m^2 \qquad \rho = 2700\ kg/m^3$$

As it is difficult to visualize a 3-D wave, the output is plotted only on the xy-plane, yz-plane and zx-plane. The A-scan data, however, can be individually plotted at any location.

The wavefront plots are shown in Figs. 6-22 to 6-24 for the three afore-mentioned planes in the block. It can be seen that the wave fronts are showing strong anisotropy. The velocity in different directions is apparently different. Also, three wavefronts are observed inside the block (Fig. 6-22 and 6-23) showing three separate body waves. On the surface, however, only one wavefront is seen because the two surface waves travel at about the same speed (notice that C_{55} and C_{66} are nearly the same).

This finite element model is used again in Chapter 8 to produce the raw data for exercising image reconstruction algorithms. Many other finite element studies have been made and confirmed experimentally. This chapter is not intended to cover all the applications however, since the fundamentals are all the same as described in the few examples given.

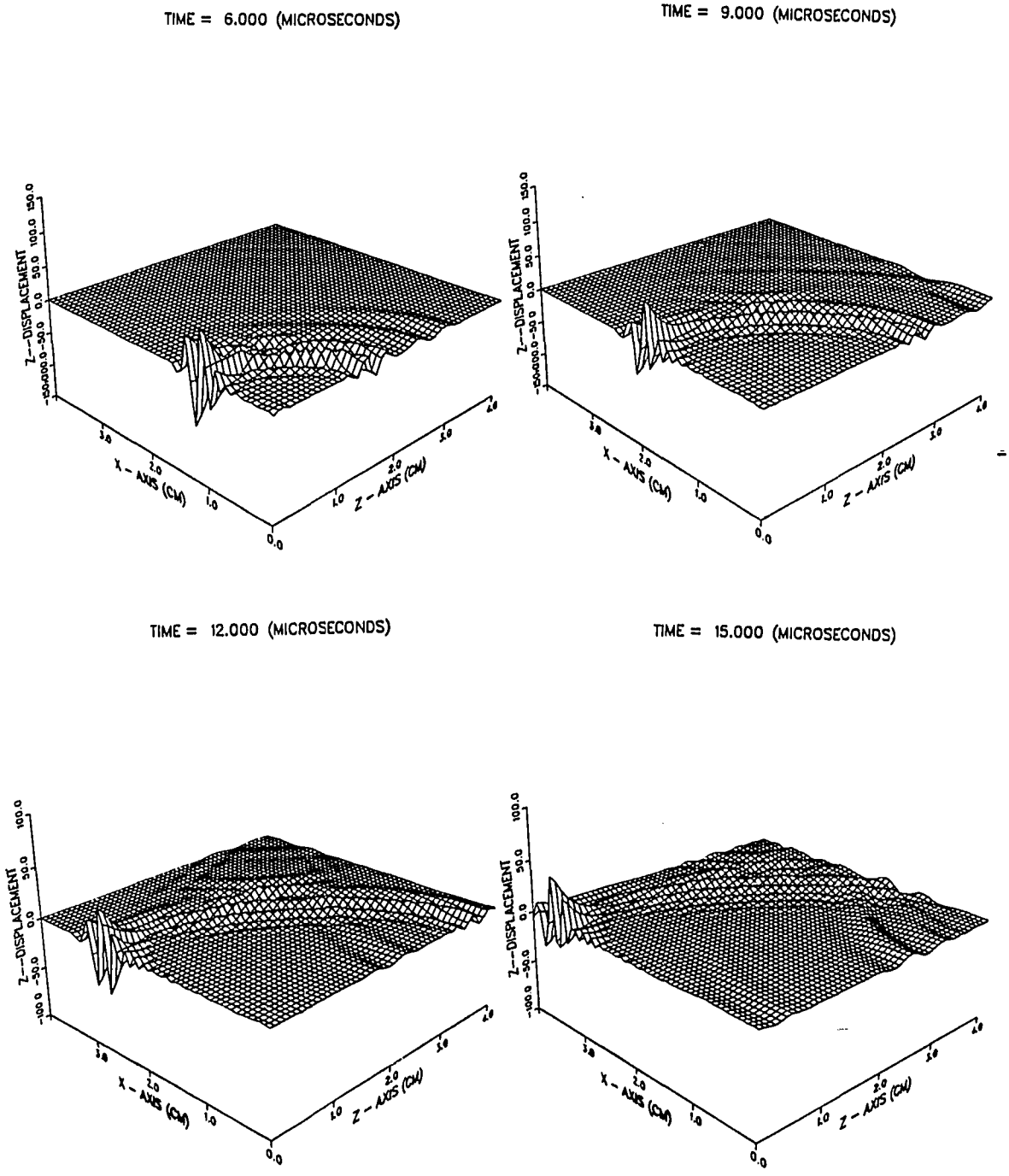

Figure 6.28: 3-D wavefronts propagating on the xz-plane

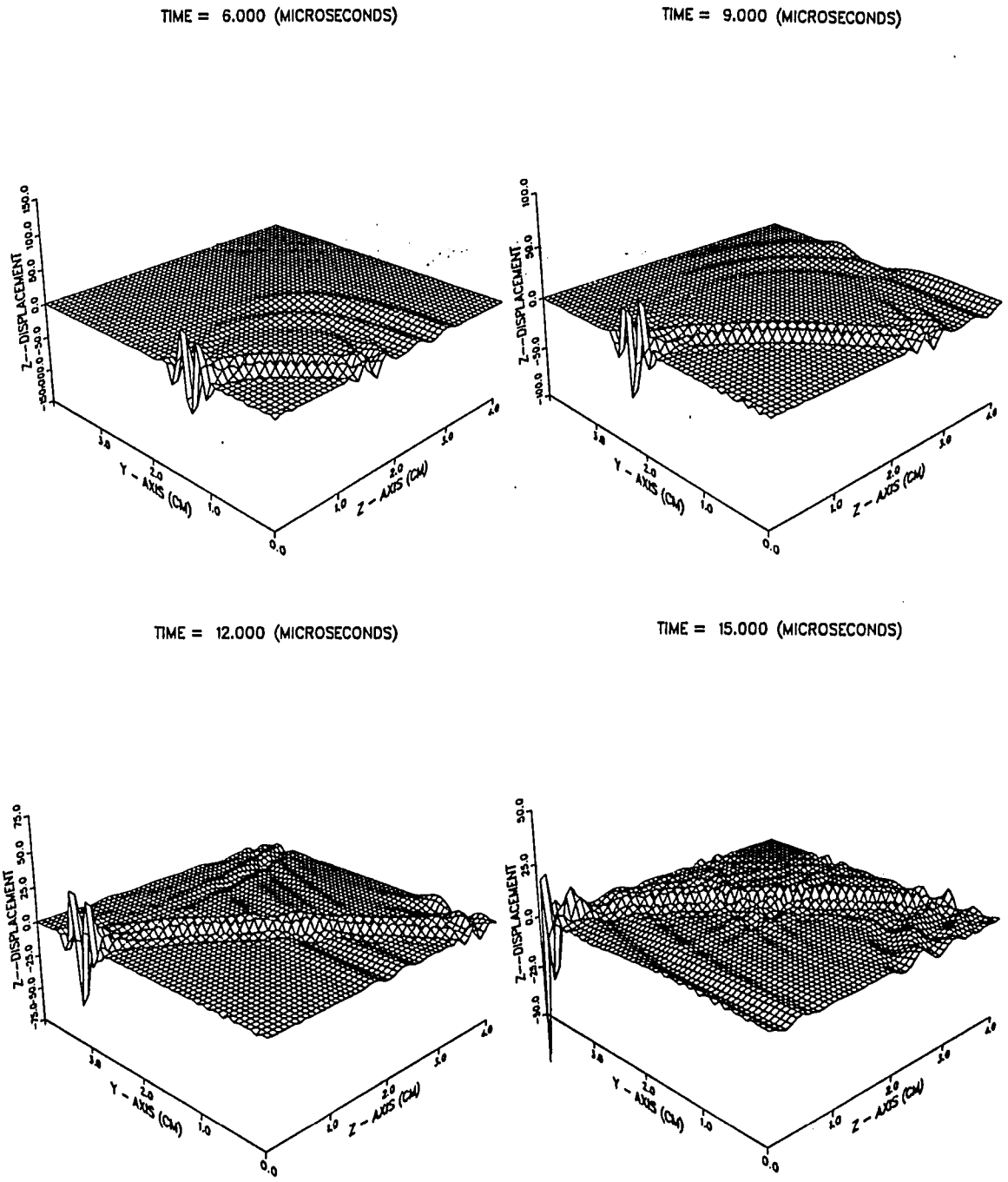

Figure 6.29: 3-D wavefronts propagating on the yz-plane

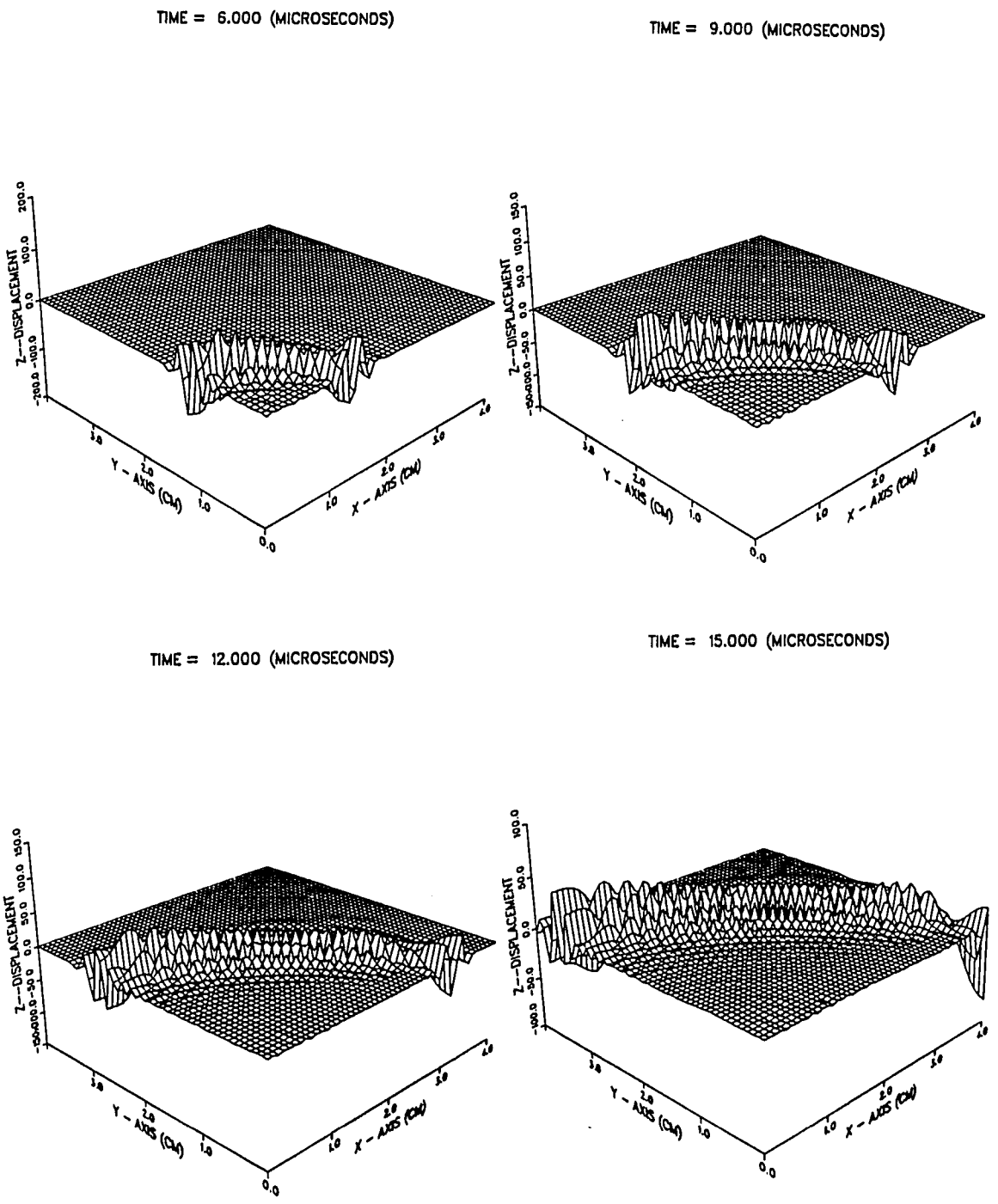

Figure 6.30: Illustration of the 3-D surface waves

CHAPTER 7. TOMOGRAPHIC RECONSTRUCTION OF DEFECT OBJECT FUNCTION

In the introduction it is stated that a successful forward model not only provides a tool to understand better the underlying physics of an NDE situation and thus help the design of the NDT experiment, but it also gives a useful means for the solution of NDE inverse problems. In this chapter, the finite element model described in the previous chapters is used as a test bed for the study of diffraction tomography, a representative of the general class of inverse algorithms.

Restricted to the scalar wave equation, this chapter explains a series of background considerations about the applied inverse problem. Tomographic forward and backward propagation is presented first to introduce the basic concepts of plane wave migration. A generalized holographic field is then introduced which accounts for the incoming wave motion toward the measurement surface and therefore relates the measurement field to its sources. The Fourier diffraction slice theorem and its counterpart, the filtered backpropagation algorithm, are finally derived using the Born approximation to linearize the relationship between the secondary sources and the scatterer.

Tomographic Forward and Backward Propagation

Consider an isotropic material free of body force where the displacement field $\underline{u}$ satisfies the following elastic wave equation

$$(\lambda + 2\mu)\nabla\nabla \cdot \underline{u} - \mu\nabla \times \nabla \times \underline{u} = \rho\ddot{\underline{u}} \tag{7.1}$$

Using the Helmholtz decomposition

$$\underline{u} = \nabla\phi + \nabla \times \underline{\psi} \tag{7.2a}$$

$$\nabla \cdot \underline{\psi} = 0 \tag{7.2b}$$

where ϕ and $\underline{\psi}$ are scalar and vector potentials, respectively, the original equation can be decomposed into two separate equations

$$\nabla^2\phi - \frac{1}{V_l^2}\ddot{\phi} = 0 \tag{7.3}$$

$$\nabla^2\underline{\psi} - \frac{1}{V_s^2}\ddot{\underline{\psi}} = 0 \tag{7.4}$$

where V_l and V_s are longitudinal and shear velocities, respectively. Considering the case of an incident L-wave and neglecting the mode converted shear wave, the vector potential can be neglected, which then leaves only the scalar wave equation as the starting point for scattering and thus inverse scattering problems.

For a sinusoidal source (incident wave), the scattered (scalar) wave satisfies the Helmholtz equation

$$\nabla^2\Phi + k^2\Phi = 0 \tag{7.5}$$

where $k = \frac{\omega}{V_l}$ is the wave number and ω is the angular frequency. It is obvious that Φ can be considered as the 1-D Fourier transform of ϕ with respect to time t if a time domain signal (pulse) is used.

Now performing a 2-D Fourier transformation with respect to x and y, the above equation becomes

$$\frac{\partial^2 \hat{\Phi}}{\partial z^2} + (k^2 - K_x^2 - K_y^2)\hat{\Phi} = 0 \tag{7.6}$$

where

$$\hat{\Phi}(K_x, K_y, z; \omega) = \int_{-\infty}^{\infty}\int_{-\infty}^{\infty} \Phi(x, y, z; \omega) e^{-jK_x x - jK_y y} dx dy \tag{7.7}$$

Equation(7.6) has a standard solution form if $k^2 \leq K_x^2 + K_y^2$

$$\begin{aligned}\hat{\Phi}(K_x, K_y, z; \omega) = \hat{A}^+(K_x, K_y, \omega) e^{j\sqrt{k^2 - K_x^2 - K_y^2}\, z} \\ + \hat{A}^-(K_x, K_y, \omega) e^{-j\sqrt{k^2 - K_x^2 - K_y^2}\, z}\end{aligned} \tag{7.8}$$

It can be seen that $\hat{\Phi}(K_x, K_y, z; \omega)$ consists of two parts which are called forward propagation and backward propagation. For $z > 0$, the first term is the forward propagation and the second term represents the backward propagation part, and vice versa for $z < 0$. At $z = 0$, the equation becomes

$$\hat{\Phi}(K_x, K_y, z = 0; \omega) = \hat{A}^+(K_x, K_y, \omega) + \hat{A}^-(K_x, K_y, \omega) \tag{7.9}$$

which means that the wave field at $z = 0$ is decomposed into two parts which then can be forward and backward propagated, respectively, to obtain the wave field at other locations. Fourier transforming eq. (7.8) with respect to z yields

$$\tilde{\Phi}(K_x, K_y, K_z; \omega) = \hat{A}^+(K_x, K_y, \omega) \int_{-\infty}^{\infty} e^{-j(K_z - \sqrt{k^2 - K_x^2 - K_y^2})z} dz +$$

$$+\hat{A}^{-}(K_x,K_y,\omega)\int_{-\infty}^{+\infty} e^{-j(K_z+\sqrt{k^2-K_x^2-K_y^2})z}dz$$

$$= 2\pi[\hat{A}^{+}(K_x,K_y,\omega)\delta(K_z-\sqrt{k^2-K_x^2-K_y^2})+$$

$$+\hat{A}^{-}(K_x,K_y,\omega)\delta(K_z+\sqrt{k^2-K_x^2-K_y^2})] \qquad (7.10)$$

It can be seen that only the Ewald-sphere values of any arbitrary spectrum $\tilde{\Phi}(\underline{K},\omega)$ represent physical wavefields. To consider this factor, the inverse Fourier transform representation of the wave field should be modified as

$$\Phi(\underline{R},\omega)=\frac{1}{(2\pi)^3}\int\int\int\tilde{\Phi}(\underline{K},\omega)e^{-j\underline{K}\cdot\underline{R}}\delta(|\underline{K}|-k)d\underline{K} \qquad (7.11)$$

Evaluating the integral with respect to K_z yields

$$\Phi(\underline{R},\omega)=\frac{1}{(2\pi)^2}\int_{-\infty}^{\infty}\int_{-\infty}^{\infty}k[\frac{\tilde{\Phi}(K_x,K_y,\sqrt{k^2-K_x^2-K_y^2};\omega)}{2\pi\sqrt{k^2-K_x^2-K_y^2}}e^{j\sqrt{k^2-K_x^2-K_y^2}z}$$

$$+\frac{\tilde{\Phi}(K_x,K_y,-\sqrt{k^2-K_x^2-K_y^2};\omega)}{2\pi\sqrt{k^2-K_x^2-K_y^2}}e^{-j\sqrt{k^2-K_x^2-K_y^2}z}]$$

$$u(k^2-k_x^2-k_y^2)e^{jK_xx+jK_yy}dK_xdK_y \qquad (7.12)$$

Comparing to (7.8), we can conclude that

$$\hat{A}^{+}(K_x,K_y,\omega) = \frac{k}{2\pi\sqrt{k^2-K_x^2-K_y^2}}\tilde{\Phi}(K_x,K_y,\sqrt{k^2-K_x^2-K_y^2};\omega)$$

$$u(k^2-K_x^2-K_y^2) \qquad (7.13a)$$

$$\hat{A}^{-}(K_x,K_y,\omega) = \frac{k}{2\pi\sqrt{k^2-K_x^2-K_y^2}}\tilde{\Phi}(K_x,K_y,-\sqrt{k^2-K_x^2-K_y^2};\omega)$$

$$u(k^2-K_x^2-K_y^2) \qquad (7.13b)$$

which means that the forward and backward propagation parts are actually the projection of the 3-D Fourier transform of the wavefield of the Ewald-half-spheres $\pm\sqrt{k^2-K_x^2-K_y^2}$ into the K_xK_y-plane.

Equation (7.12) is the migration type representation of a homogeneous time harmonic wavefield. $e^{\pm j\sqrt{k^2-K_x^2-K_y^2}z}$ are called propagators. For $k^2 < K_x^2 + K_y^2$, the propagator becomes an exponential decay representing an evanescent wave mode. Propagation does not exist in this case. Equation(7.12) excludes the evanescent waves by the unit-step function.

The above formulations also reveal that if the planar measurement at $z = 0$ can be uniquely decomposed into two parts A^+ and A^-, it can be forward and backward propagated to produce the wavefield at any plane as long as the space is homogeneous. However, the decomposition may not be available without a priori information about the field distribution.

In most cases, the measurement surface is far from the sources (primary or secondary), the amplitude corresponding to the wave travelling from each side of the surface should be one of the two parts after decomposition. Forward propagation can be carried out to all the space, but the backward propagation is valid only until it reaches the sources because the homogeneity requirement does not hold in and beyond the source region. Nevertheless, these kind of migration relationships are of tremendous importance for inverse scattering problems.

Generalized Holographic Field

Attention now is restricted to the scattering problems where a scatterer is assumed to be in an otherwise isotropic and homogeneous host material. Rewriting equation(7.5) as

$$\nabla^2\Phi + k^2\Phi = O(\underline{R})k^2\Phi \tag{7.14}$$

where k is the constant wave number of the host material and $O(\underline{R}) = 1 - \frac{k^2(\underline{R})}{k^2}$ is called the object function. It is obvious that $O(\underline{R})$ is zero outside the scatterer due to the assumption of a homogeneous host material. The right hand side of equation (7.14) is equivalent to a secondary source for the scattered wave

$$q_s = -O(\underline{R})k^2\Phi(\underline{R}) \tag{7.15}$$

Let S_M represent an arbitrary measurement surface enclosing the scatterer, Φ_i and Φ_s represent the incident and scattered wave, respectively. Applying Green's theorem to the source volume V yields

$$\Phi(\underline{R},\omega) = \Phi_i + \int\int\int_V q_s(\underline{R}',\omega)G(\underline{R}-\underline{R}',\omega)d^3\underline{R}' \tag{7.16}$$

where G is the free space Green's function given by

$$G(\underline{R}-\underline{R}',\omega) = \frac{e^{jk|\underline{R}-\underline{R}'|}}{4\pi|\underline{R}-\underline{R}'|} \tag{7.17}$$

On the other hand, Huygen's principle gives

$$\Phi(\underline{R}_{ext},\omega) = \Phi_i + \int\int_{S_M}[\Phi(\underline{R}',\omega)\frac{\partial G}{\partial n'} - G(\underline{R}_{ext}-\underline{R}',\omega)\frac{\partial\Phi}{\partial n'}]ds' \tag{7.18}$$

where $\underline{R}_{ext}$ represents the point outside the enclosed surface S_M because Huygen's principle only takes into account the forward propagation. For a point $\underline{R}_{int}$ inside the surface, the equation(7.18) becomes

$$0 = \Phi_i + \int\int_{S_M}[\Phi(\underline{R}',\omega)\frac{\partial G}{\partial n'} - G(\underline{R}_{int}-\underline{R}',\omega)\frac{\partial\Phi}{\partial n'}]ds' \tag{7.19}$$

which means that the surface integration of the measured field gives nothing but the incident field. Even though eq. (7.16) can be used elsewhere, the link between

the measured field on a surface with the wave field inside can not be established. Therefore, Huygen's radiation principle is useless for inverse scattering problems.

The fact that G accounts for the outgoing wave intuitively suggests that its complex conjugate G^* should correspond to the incoming wave toward the measurement surface. This idea was discussed by Porter, et al [58] and Bojarski [59] who define a so-called generalized holographic field for all points $\underline{R}$ inside S_M according to

$$\Phi_H(\underline{R}_{int},\omega) = -\int\int_{S_M} [\Phi_s(\underline{R}',\omega)\frac{\partial G^*}{\partial n'} - G^*(\underline{R}_{int}-\underline{R}',\omega)\frac{\partial \Phi_s}{\partial n'}]ds' \qquad (7.20)$$

which can be considered as the counterpart of the scattered wave outside S_M, expressed as the surface integration in eq. (7.18). Notice that the argument in the integration of eq. (7.20) is the scattered field while in equation(7.18) it is the total field. However, the surface integration of the incident wave for the point outside the surface in equation(7.18) is zero.

Equation(7.20) defines a generalization of the backpropagation or holographic imaging principle to arbitrary measurement surfaces and accounts for the incoming elementary spherical Huygen's waves traveling towards the measurement surface with amplitudes according to the known field values on S_M.

Now applying Green's theorem to the interior of the surface S_M to eq. (7.19) together with the relationship

$$\nabla^2\Phi_s + k^2\Phi_s = -q_s \qquad (7.21)$$

we have

$$\Phi_H(\underline{R},\omega) = \Phi_s(\underline{R},\omega) - \int\int\int_V q_s(\underline{R}',\omega)G^*(\underline{R}-\underline{R}',\omega)d^3\underline{R}' \qquad (7.22)$$

Inserting (7.16) then yields

$$\Phi_H(\underline{R},\omega) = 2j \int\int\int_V q_s(\underline{R}',\omega) G_i(\underline{R}-\underline{R}',\omega) d^3\underline{R}' \tag{7.23}$$

which is actually the Porter-Bojarski integral equation. G_i is the imaginary part of the Green's function

$$G_i(\underline{R},\omega) = \frac{1}{4\pi}\frac{\sin kR}{R} \tag{7.24}$$

The combination of eqs. (7.20) and (7.23) gives an integral equation of the first kind for the equivalent volume source q_s

$$\begin{aligned} -\int\int_{S_M} [\Phi_s(\underline{R}',\omega)\frac{\partial G^*}{\partial n'} - G^*(\underline{R}_{int}-\underline{R}',\omega)\frac{\partial \Phi_s}{\partial n'}]ds' \\ = 2j\int\int\int_V q_s(\underline{R}',\omega) G_i(\underline{R}-\underline{R}',\omega) d^3\underline{R}' \end{aligned} \tag{7.25}$$

Backpropagation of the scattered field produces the generalized holographic field or the inhomogeneity. However, the solution of the integral equation(7.25) is non-unique, therefore, this integral equation can not serve as the starting point for solving the inverse scattering problem. In order to make the solution unique, we consider only that portion of the sources which have minimal energy. A 3-D spatial Fourier transform of eq. (7.23) results in

$$\tilde{\Phi}_H(\underline{K},\omega) = 2j\tilde{q}_s(\underline{K},\omega)\tilde{G}_i(\underline{K},\omega) \tag{7.26}$$

where $\tilde{G}_i(\underline{K},\omega)$, the spatial Fourier transform of $G_i(\underline{R},\omega)$, is given by [44] as

$$\tilde{G}_i(\underline{K},\omega) = \frac{\pi}{2k}\delta(K-k) \tag{7.27}$$

Therefore

$$\tilde{\Phi}_H(\underline{K},\omega) = j\frac{\pi}{k}\tilde{q}_s(\underline{K},\omega)\delta(K-k) \tag{7.28}$$

which means that the Fourier transform of the generalized holographic field peaks on the Ewald-sphere and is zero elsewhere.

If the observation aperture is restricted to a spatial angle of 2π (the solid angle or spatial angle of the whole space is 4π) covering the half space $z \leq 0$ and the measurement surface is extended to a z =constant plane, the generalized holography reduces to the so-called Rayleigh-Sommerfeld holography. Similar steps now lead to the relationship between Fourier spectra of the minimal energy sources and the (tomographic processing) output of the Rayleigh-Sommerfeld holographic imaging scheme as

$$\tilde{\Phi}_H(\underline{K},\omega) = j\frac{\pi}{k}\tilde{q}_s(\underline{K},\omega)\delta(K-k)u(K_z) \tag{7.29}$$

where $u(K_z)$ is a unit step function. This is the key equation for the derivation of the tomographic algorithm in the later sections.

Fourier Diffraction Slice Theorem

From the Porter-Bojarski equation for the 3-D spatial Fourier transform of the backpropagated field in terms of Rayleigh-Sommerfeld holography (eq. (7.29)), we take a 1-D Fourier inverse transform with respect to K_z

$$\hat{\Phi}_H(K_x,K_y,z,\omega) = j\frac{\pi}{k}\frac{1}{2\pi}\int_{-\infty}^{\infty}\tilde{q}_s(\underline{K},\omega)\delta(K-k)u(K_z)e^{jK_zz}dK_z \tag{7.30}$$

Notice

$$\delta(K-k) = \delta(\sqrt{K_x^2+K_y^2+K_z^2}-k) \tag{7.31}$$

Utilizing a result of measure theory

$$\delta[g(x)] = \sum_i \frac{\delta(x-x_i)}{|g'(x_i)|} \tag{7.32}$$

where x_i are simple real-valued zeros of $g(x)$. Let

$$g(K_z) = \sqrt{K_x^2 + K_y^2 + K_z^2} - k$$

For $k^2 \leq K_x^2 + K_y^2$, $g(K_z) = 0$ gives

$$K_z = \pm\sqrt{k^2 - K_x^2 - K_y^2}$$

Substituting all these expressions back into eq. (7.32) gives

$$\delta(\sqrt{K_x^2 + K_y^2 + K_z^2} - k) = \frac{k}{\sqrt{k^2 - K_x^2 - K_y^2}}[\delta(K_z - \sqrt{k^2 - K_x^2 - K_y^2}) + \\ +\delta(K_z + \sqrt{k^2 - K_x^2 - K_y^2})]u(k^2 - K_x^2 - K_y^2) \quad (7.33)$$

where the step function is introduced to account for the restriction of real-valued zeros.

Inserting (7.33) into (7.30) yields

$$\hat{\Phi}_H(K_x, K_y, z, \omega) = \frac{j}{2}[\frac{\tilde{q}_s(K_x, K_y, K_z = \sqrt{k^2 - K_x^2 - K_y^2}, \omega)}{\sqrt{k^2 - K_x^2 - K_y^2}} e^{j\sqrt{k^2 - K_x^2 - K_y^2}z} + \\ + \frac{\tilde{q}_s(K_x, K_y, K_z = -\sqrt{k^2 - K_x^2 - K_y^2}, \omega)}{\sqrt{k^2 - K_x^2 - K_y^2}} e^{-j\sqrt{k^2 - K_x^2 - K_y^2}z}] \\ u(k^2 - K_x^2 - K_y^2)u(K_z) \quad (7.34)$$

The second term vanishes due to the unit step function $u(K_z)$. Assuming the measurement is done on the plane $z = d$, the backpropagation relationship gives (compare to eq. (7.8))

$$\hat{\Phi}_H(K_x, K_y, z, \omega) = \hat{\Phi}_M(K_x, K_y, z = d, \omega) e^{j(z-d)\sqrt{k^2 - K_x^2 - K_y^2}} \\ u(k^2 - K_x^2 - K_y^2) \quad (7.35)$$

where $\hat{\Phi}_M$ represents the 2-D spatial Fourier transform of the measurement field. Comparing eq. (7.34) with (7.35) yields

$$\tilde{q}_s(K_x, K_y, K_z = \sqrt{k^2 - K_x^2 - K_y^2}, \omega) u(k^2 - K_x^2 - K_y^2) u(K_z) =$$

$$\frac{2}{j}\sqrt{k^2 - K_x^2 - K_y^2}\, e^{-jd\sqrt{k^2 - K_x^2 - K_y^2}}\, \hat{\Phi}_M(K_x, K_y, d, \omega) u(k^2 - K_x^2 - K_y^2) \quad (7.36)$$

which tells us that the 2-D Fourier transform of a wavefield measured on a planar surface is explicitly related to specific K-space information about the diffraction sources on the Ewald-sphere. This is called the *Fourier diffraction slice theorem.* It is obvious from the above derivations that the Fourier diffraction slice theorem for secondary sources is nothing but the Porter-Bojarski equation for planar wavefields. It should be noted that the radius of the Ewald-half-sphere depends on the operating frequency and the orientation of the arc depends on the incident direction. Therefore, both frequency sweeping and angular diversity increase the coverage of the secondary sources in K-space.

In order to evaluate eq. (7.36) as an inverse scattering identity for the object function in terms of either angular or frequency diversity procedures, the weak scatterer or physical optics approximations are required to hold. In general, a secondary source depends upon the total field as shown in eq. (7.15), and the total field depends upon the parameters of both the scatterer and the incident field in a complicated manner. In this sense, the secondary source can be considered as a function of not only the three space variables, but also the direction (angle) and temporal frequency of the incident field. For a penetrable scatterer, for example, eq. (7.15) can be rewritten in a more explicit way as

$$q_s(\underline{R}, \theta_i, \varphi_i, \omega) = [k^2(\underline{R}) - k^2]\Phi(\underline{R}, \theta_i, \varphi_i, \omega) \quad (7.37)$$

where (θ_i, φ_i) specifies the incident direction. This equation suggests that the spatial structure of the secondary source is different for every (θ_i, φ_i) and every ω. Therefore, the information about the scatterer can not be correctly recovered even if the secondary sources are successfully reconstructed. Subsequently, weak scatterer or physical optics approximations are necessary to linearize the relationship between the scatterer and the secondary sources, thus making the inverse scattering problem solvable.

Consider a plane incidence of frequency spectrum $F(\omega)$ in the (θ_i, φ_i) direction. The Born approximation gives, upon replacing the total field in eq. (7.37) by the incident wave, the following expression for the secondary source

$$\begin{aligned} q_s(\underline{R}, \omega) &= [k^2(\underline{R}) - k^2] F(\omega) e^{j\underline{k}_i(\theta_i, \varphi_i, \omega) \cdot \underline{R}} \\ &= k^2 F(\omega) O(\underline{R}) e^{j\underline{k}_i(\theta_i, \varphi_i, \omega) \cdot \underline{R}} \end{aligned} \tag{7.38}$$

in terms of a prescribed spatially dependent phase. In this way, the secondary source and the object function are linearly related.

The Fourier transform of (7.38) into the spatial frequency domain gives

$$\tilde{q}_s(\underline{K}, \omega) = k^2 F(\omega) \tilde{O}(\underline{K} - \underline{k}_i) \tag{7.39}$$

with $\underline{k}_i$ the incident wave vector, $\tilde{O}(\underline{K})$ the K-space object function. It can be seen that the incident wave appears as a shifting operation in the spatial Fourier spectrum. Substituting (7.39) into (7.29) yields

$$\tilde{\Phi}_H(\underline{K}, \omega) = j\pi k F(\omega) \tilde{O}(\underline{K} - \underline{k}_i) \delta(K - k) u(K_z) \tag{7.40}$$

For an incidence in the (θ_i, φ_i) direction as shown in Fig. 7-1

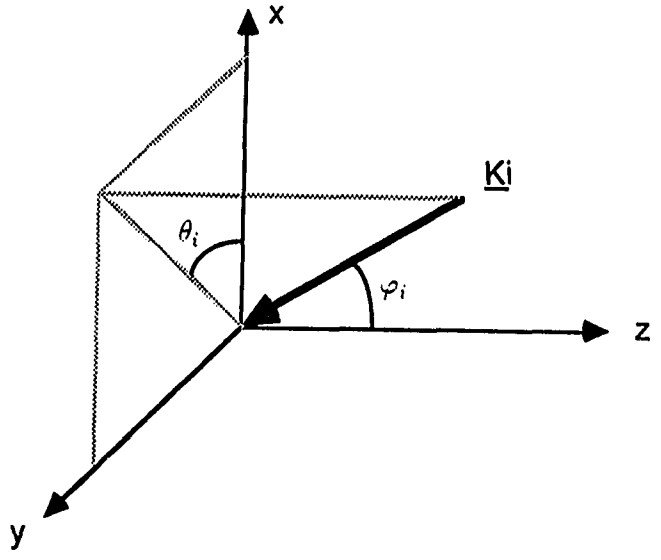

Figure 7.1: Illustration of incident direction in the observation space

$$\begin{aligned} \underline{k}_i &= k(-\cos\theta_i \sin\varphi_i, -\sin\theta_i \sin\varphi_i, -\cos\varphi_i) \\ &= k_x^i + k_y^i + k_z^i \end{aligned} \tag{7.41}$$

Then equation(7.40) can be rewritten as

$$\tilde{\Phi}_H(\underline{K} + \underline{k}_i, \omega) = -j\pi k F(\omega)\tilde{O}(\underline{K})\delta(|\underline{K} + \underline{k}_i| - k)u(K_z - k_z^i) \tag{7.42}$$

To relate the object function to the surface measurement field, we substitute (7.39) into (7.36) with $\underline{k}_i$ in (7.41)

$$\begin{aligned} k^2 F(\omega)\tilde{O}(K_x - k_x^i, K_y - k_y^i, \sqrt{k^2 - K_x^2 - K_y^2} - k_z^i)u(k^2 - K_x^2 - K_y^2) = \\ = \frac{2}{j}\sqrt{k^2 - K_x^2 - K_y^2}e^{-jd\sqrt{k^2 - K_x^2 - K_y^2}}\hat{\Phi}_M(K_x, K_y, d, \omega) \\ u(k^2 - K_x^2 - K_y^2)u(K_z) \end{aligned} \tag{7.43}$$

Let $K_x - k_x^i = K_x', K_y - k_y^i = K_y', K_z - k_z^i = K_z'$, and omit the prime in the final

form, this equation becomes

$$\tilde{O}(K_x, K_y, K_z^E - k_z^i)u((K_z^E)^2)u(K_z - k_z^i) =$$
$$= \frac{2}{jk^2F(\omega)} K_z^E e^{-jdK_z^E} \hat{\Phi}_M(K_x + k_x^i, K_y - k_y^i, d, \omega)u[(K_z^E)^2] \qquad (7.44)$$

where $K_z^E = \sqrt{k^2 - (K_x + k_x^i)^2 - (K_y - k_y^i)^2}$ defines a point on a shifted Ewald-half-sphere. This equation is the explicit representation of *Fourier diffraction slice theorem.* More detailed discussion of this equation can be illustrated in Fig. 7-2 where a surface measurement field is disposed on a shifted Ewald-half-sphere after performing a 2-D Fourier transform. The center of the Ewald-sphere is shifted to $\underline{k}_i$ which depends on the frequency and the angle of the incidence. It can be easily seen how multiple experiments could be used to increase K-space coverage in either angular or frequency diversity. Inverse Fourier transform of the recovered object function in K-space gives the object function in the observation space. It is obvious from eq. (7.44) that neither angular nor frequency diversity gives an even grid point for $\tilde{O}(\underline{K})$ in the K-space as required by the FFT algorithm. Therefore, interpolation techniques have to be utilized. To avoid this K-space operation, an alternative procedure, the filtered backpropagation algorithm, is considered in the next section.

Frequency Diversity Filtered Backpropagation

Dividing eq. (7.42) by $-j\pi k^3 F(\omega)$ and integrating with respect to k which represents the frequency diversity, we obtain

$$\tilde{O}(\underline{K})I(\underline{K}, \underline{k}_i) = \frac{j}{\pi} \int_0^\infty \frac{1}{k^3 F(\omega)} \tilde{\Phi}_H(\underline{K} + \underline{k}_i, \omega) dk \qquad (7.45)$$

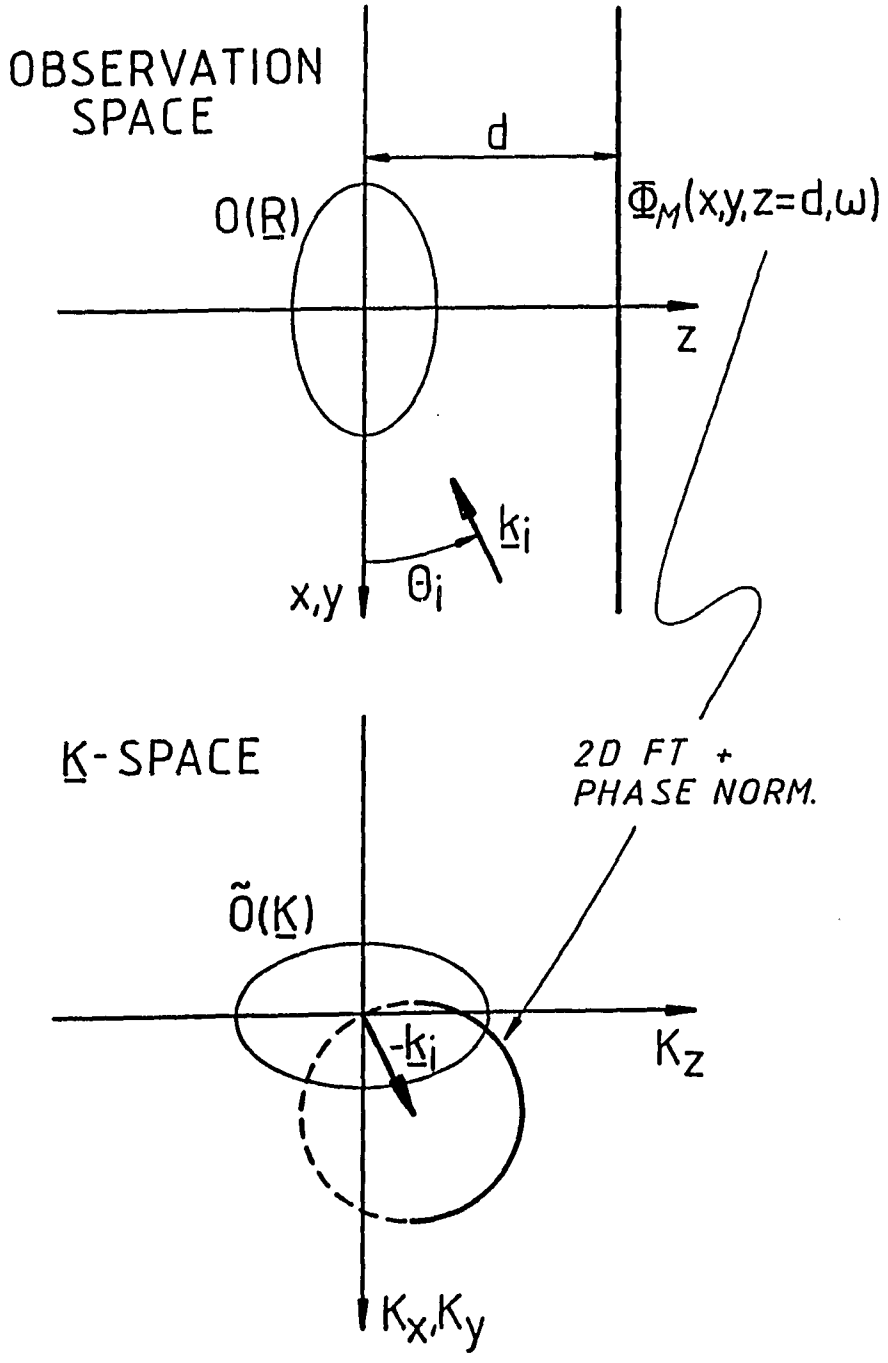

Figure 7.2: Illustration of Fourier Diffraction Slice Theorem

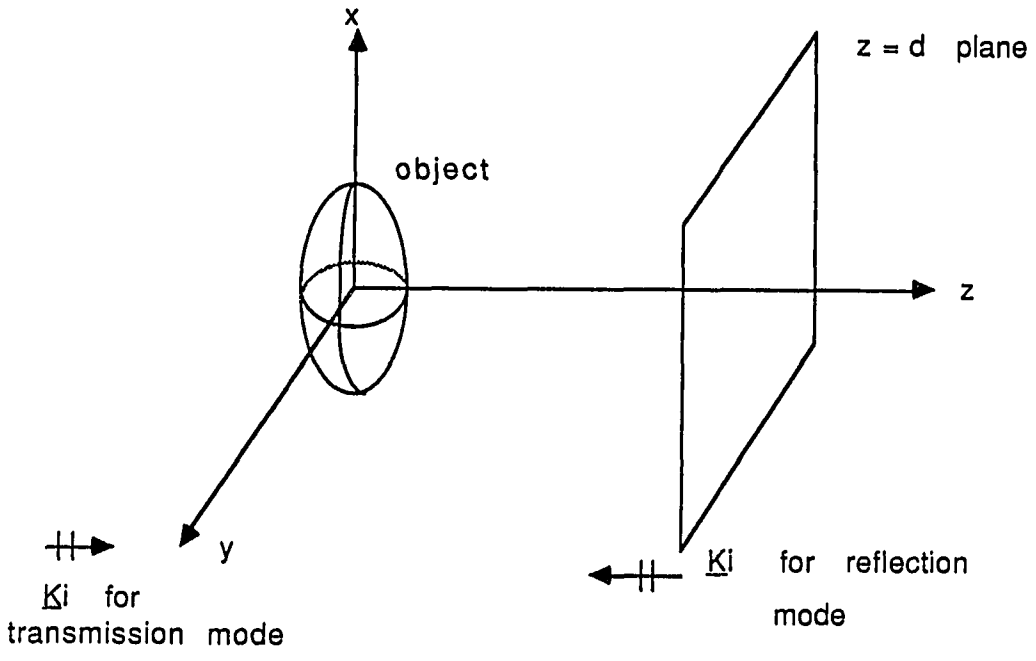

Figure 7.3: Reflection and transmission experiment setup

where

$$I(\underline{K}, \underline{k}_i) = \int_0^\infty \frac{1}{k^2} \delta(|\underline{K} + \underline{k}_i| - k) u(K_z + k_z^i) dk \tag{7.46}$$

Consider the reflection mode arrangement by putting $\underline{k}_i = k(0, 0, -1)$ (see Fig. 7-3), we have

$$\tilde{O}(\underline{K}) I(\underline{K}) = \frac{j}{\pi} \int_0^\infty \frac{1}{k^3 F(\omega)} \tilde{\Phi}_H(\underline{K} - k\underline{e}_z, \omega) dk \tag{7.47}$$

with

$$\begin{aligned} I(\underline{K}) &= \int_0^\infty \frac{1}{k^2} \delta(|\underline{K} - k\underline{e}_z| - k) u(K_z - k) dk \\ &= \sum_j \frac{u(K_z - k_j)}{k_j^2 |g'(k_j)|} \end{aligned} \tag{7.48}$$

where

$$g(k) = \sqrt{K_x^2 + K_y^2 + (K_z - k)^2} - k \tag{7.49}$$

with k_j as the simple real zero of $g(k)$ with $k_j \geq 0$. Evaluating $g(k_j) = 0$ yields

$$k_j = \frac{K^2}{2K_z} \tag{7.50}$$

which is positive if and only if $K_z > 0$

From (7.49), we have

$$g'(k_j) = -\frac{2K_z^2}{K^2} \tag{7.51}$$

Substituting (7.50) and (7.51) into (7.48) yields

$$I(\underline{K}) = \frac{2}{K^2} u(K_z) u(\frac{K_z^2 - K_x^2 - K_y^2}{2K_z}) \tag{7.52}$$

Notice $K_z > 0$, therefore, $\frac{K_z^2 - K_x^2 - K_y^2}{2K_z} > 0$ if and only if $K_z^2 > K_x^2 + K_y^2$. Equation(7.52) then can be written

$$I(\underline{K}) = \frac{2}{K^2} u(K_z) u(K_z^2 - K_x^2 - K_y^2) \tag{7.53}$$

Substituting this equation into (7.47) gives

$$\tilde{O}(\underline{K}) u(K_z) u(K_z^2 - K_x^2 - K_y^2) = \frac{j}{2\pi} \int_0^\infty \frac{K^2}{k^3 F(\omega)} \tilde{\Phi}_H(\underline{K} - k\underline{e}_z, \omega) dk \tag{7.54}$$

Notice

$$\tilde{\Phi}_H(K_x, K_y, K_z - k, \omega) = \int_{-\infty}^{\infty} \hat{\Phi}_H(K_x, K_y, z, \omega) e^{-j(K_z - k)z} dz \tag{7.55}$$

Substituting (7.35) into this equation gives

$$\begin{aligned} \tilde{\Phi}_H(K_x, K_y, K_z - k, \omega) \; &= 2\pi \hat{\Phi}_M(K_x, K_y, z = d, \omega) e^{-jd\sqrt{k^2 - K_x^2 - K_y^2}} \\ &\quad \delta(K_z - k - \sqrt{k^2 - K_x^2 - K_y^2}) \end{aligned} \tag{7.56}$$

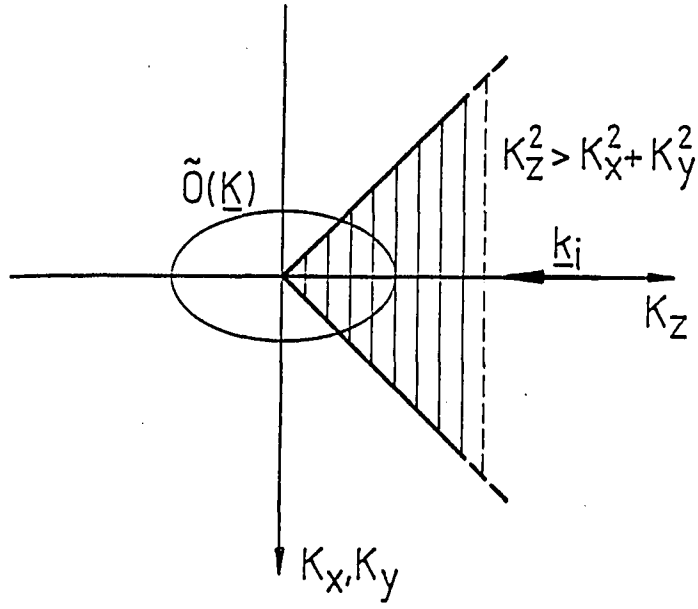

Figure 7.4: $\wedge$-shaped filter associated with the reflection mode filtered backpropagation

Upon inserting (7.56), eq. (7.54) can be expressed as

$$\tilde{O}(\underline{K})u(K_z)u(K_z^2 - K_x^2 - K_y^2) = j\int_0^\infty \frac{K^2}{k^3 F(\omega)} \hat{\Phi}_M(K_x, K_y, z = d, \omega)$$
$$e^{-jd\sqrt{k^2 - K_x^2 - K_y^2}} \quad \delta(K_z - k - \sqrt{k^2 - K_x^2 - K_y^2})dk \qquad (7.57)$$

The product of two step functions cannot be transformed into the spatial domain, therefore, only a spatially filtered object function $O_{\wedge p}(\underline{R})$ can be reconstructed after inverse Fourier transforming the right hand side of equation(7.57). The index "$\wedge$" represents the $\wedge$-shaped filter area in K-space, as shown in Fig. 7-4, introduced by the two step functions. The filtered object function now can be explicitly written as

$$O_{\wedge}P(\underline{R}) = \frac{j}{(2\pi)^3}\int_0^{\infty} dk \int_{-\infty}^{\infty}\int_{-\infty}^{\infty}\int_{-\infty}^{\infty} \frac{K^2}{k^3 F(\omega)}\hat{\Phi}_M(K_x, K_y, z=d, \omega)$$
$$e^{-jd\sqrt{k^2-K_x^2-K_y^2}}\delta(K_z - k - \sqrt{k^2-K_x^2-K_y^2})e^{jK_x x + jK_y y + jK_z z}$$
$$dK_x dK_y dK_z \quad (7.58)$$

Evaluating the integral with respect to K_z yields

$$O_{\wedge}P(\underline{R}) = \frac{j}{4\pi^3}\int_0^{\infty}\frac{dk}{k^2 F(\omega)}\int_{-\infty}^{\infty}\int_{-\infty}^{\infty}(k+\sqrt{k^2-K_x^2-K_y^2})$$
$$\hat{\Phi}_M(K_x, K_y, z=d, \omega)e^{jkz}e^{j(z-d)\sqrt{k^2-K_x^2-K_y^2}}u(k^2-K_x^2-K_y^2)$$
$$e^{jK_x x + jK_y y}dK_x dK_y \quad (7.59)$$

For a 2-D geometry (yz-plane), a similar process produces [95]

$$O_{\wedge}P(\underline{r}) = \frac{j}{2\pi^2}\int_0^{\infty}\frac{dk}{k^2 F(\omega)}\int_{-\infty}^{\infty}(k+\sqrt{k^2-K_y^2})\hat{\Phi}_M(K_y, z=d, \omega)e^{jkz}$$
$$e^{j(z-d)\sqrt{k^2-K_y^2}}u(k^2-K_y^2)e^{jK_y y}dK_y \quad (7.60)$$

where $\underline{r} = (y, z)$ representing a vector in the 2-D observation space.

For transmission mode, the incident wave vector is $\underline{k}_i = k(0,0,1)$ as illustrated in Fig. 7-3, eqs. (7.45) and (7.46) then give

$$\tilde{O}(\underline{K})I(\underline{K}) = \frac{j}{\pi}\int_0^{\infty}\frac{1}{k^3 F(\omega)}\tilde{\Phi}_H(\underline{K}+k\underline{e}_z, \omega)dk \quad (7.61)$$

with

$$I(\underline{K}) = \int_0^{\infty}\frac{1}{k^2}\delta(|\underline{K}+k\underline{e}_z| - k)u(K_z+k)dk \quad (7.62)$$

Similar derivation yields

$$\tilde{O}(\underline{K})u(-K_z)u(-K_z^2+K_x^2+K_y^2) = \frac{j}{2\pi}\int_0^{\infty}\frac{K^2}{k^3 F(\omega)}\tilde{\Phi}_H(\underline{K}+k\underline{e}_z, \omega)dk \quad (7.63)$$

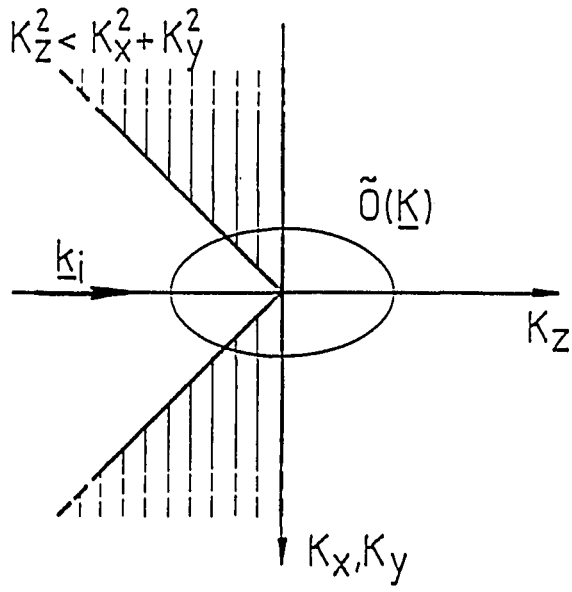

Figure 7.5: $\sum$-shaped filter associated with the transmission mode filtered back-propagation

where the two step functions act as a $\sum$-shaped filter in K-space as shown in Fig. 7-5. Transforming the right hand side to observation space and evaluating the integral with respect to K_z give

$$O_{\sum} P(\underline{R}) = \frac{j}{4\pi^3} \int_0^{\infty} \frac{dk}{k^2 F(\omega)} \int_{-\infty}^{\infty} \int_{-\infty}^{\infty} (k - \sqrt{k^2 - K_x^2 - K_y^2})$$

$$\hat{\Phi}_M(K_x, K_y, z = d, \omega) e^{-jkz} e^{j(z-d)\sqrt{k^2 - K_x^2 - K_y^2}} u(k^2 - K_x^2 - K_y^2)$$

$$e^{jK_x x + jK_y y} dK_x dK_y \quad (7.64)$$

Reducing to a 2-D object in yz-plane yields

$$O_{\sum} P(\underline{r}) = \frac{j}{2\pi^2} \int_0^{\infty} \frac{dk}{k^2 F(\omega)} \int_{-\infty}^{\infty} (k - \sqrt{k^2 - K_y^2}) \hat{\Phi}_M(K_y, z = d, \omega)$$

$$e^{-jkz} e^{j(z-d)\sqrt{k^2 - K_y^2}} u(k^2 - K_y^2) e^{jK_y y} dK_y \quad (7.65)$$

The essential difference between transmission and reflection mode is in terms of the

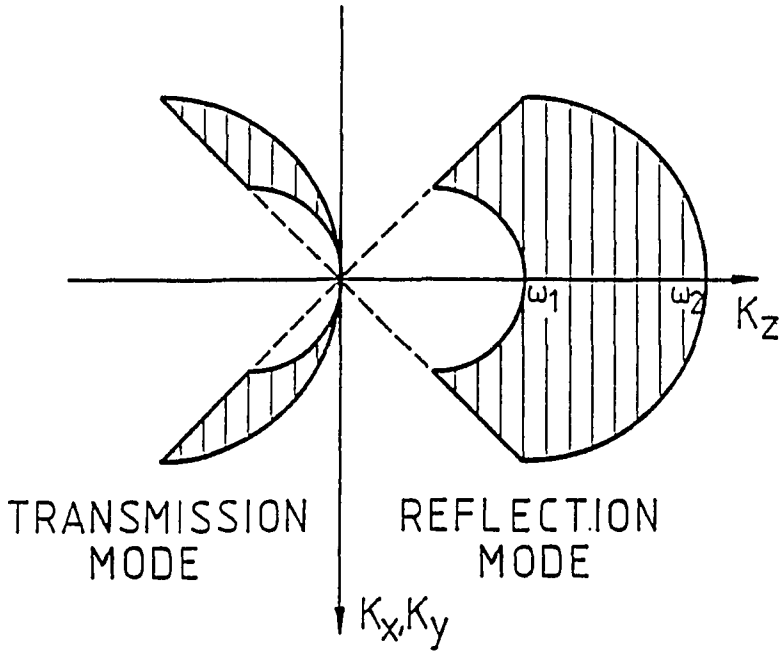

Figure 7.6: Comparison of K-space coverages of reflection and transmission mode for limited frequency apertures

spatial filter operating on $O(\underline{R})$. Due to the large K-space coverage (see Fig. 7-6) when only a limited frequency bandwidth is applied, the reflection mode offers better spatial resolution.

CHAPTER 8. SENSITIVITY STUDY

Using the finite element test bed, the tomographic algorithms derived in the previous chapter are carefully studied. The factors to be considered are the major assumptions associated with the reconstruction algorithms, including that of plane incidence, acoustic potential, isotropy and weak scattering.

Raw Data Generations

Instead of measuring experimental data, the finite element code presented in the previous chapters is used here to provide the raw data for exercising the tomographic algorithms derived in Chapter 7. As a first example, an aluminum block, having a longitudinal velocity $V_l = 6300\ m/s$, a shear velocity $V_s = 3100\ m/s$ and density $\rho = 2700\ kg/m^3$, containing a small inside crack is illuminated by a longitudinal plane wave. The reflected wave from the crack is sensed on the front wall of the block, while the transmitted wave is recorded on the back wall. A typical displacement slice at $t = 10\ \mu s$ is shown in Fig. 8-1 along with the geometry. The wave on the front surface and back wall are plotted in Fig. 8-2. Both the incident and the reflected waves are clearly shown in Fig. 8-2a, but they are separated in time. Therefore, the reflected part of the wave can be obtained from the recorded signals by time windowing out the incident wave. For the transmitted part, however, the incident

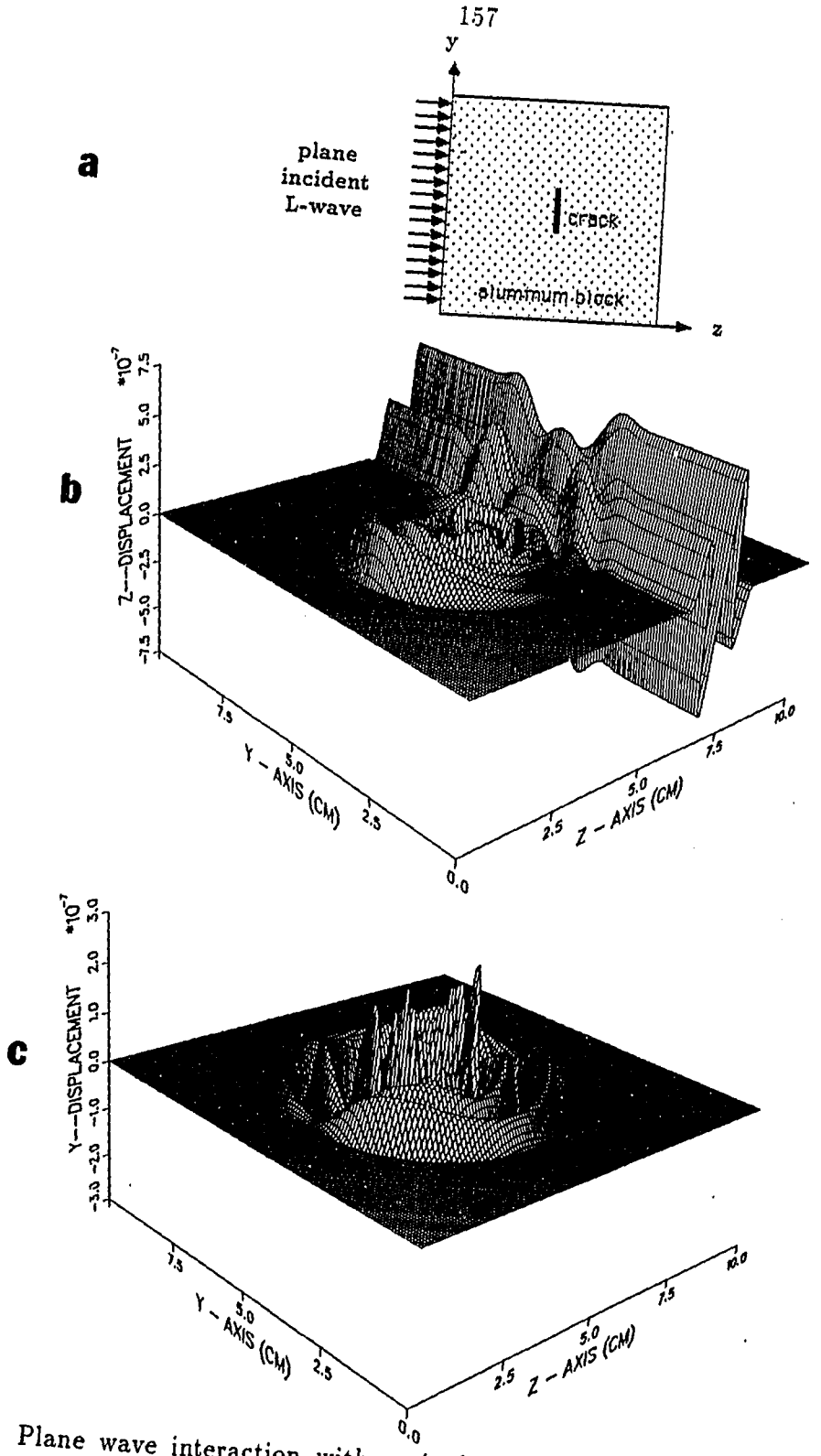

Figure 8.1: Plane wave interaction with a single crack. a) Geometry detail; b) z-displacement at $t = 10\ \mu s$; c) y-displacement at $t = 10\ \mu s$

wave is mixed up with the scattered wave. The scattered part can be obtained only by subtracting the incident field from the total field.

There are 65,025 elements used in this computation. The number of time steps is 512 with an increment of 40 ns. 128 points on both front and back surfaces are recorded. The total CPU-time required for this simulation is 28.1 minutes on the NAS AS/9160 computer system.

Similar processes are performed for the case where two rectangular cracks are located inside the block. The results are shown in Figs. 8-3 and 8-4 for displacement slices and the wave on both front and back walls, respectively.

Acoustic fields are also modeled for the purpose of comparing the potential function with normal displacement. Unlike the elastic wave equation, only the longitudinal wave is considered in acoustic models. If an acoustic potential is chosen, the governing equation is the scalar wave equation. Through a similar elemental analysis to that described in previous chapters for the elastic wave problem, the acoustic field can also be modeled in a similar fashion with the only difference being in the formation of the stiffness matrix. Therefore, the code for the elastic wave equation can be modified to model the acoustic problem. A 2-D area of the same geometry as the one considered in the elastic case is chosen. The distribution of the acoustic potential at $t = 8\ \mu s$ is plotted in Fig. 8-5 which shows a similarity to the longitudinal wave pattern in Fig. 8-1.

Reconstruction Procedures

Following the algorithms given in the last chapter, the reflected or the transmitted wave recorded on the surface is Fourier transformed with respect to time t

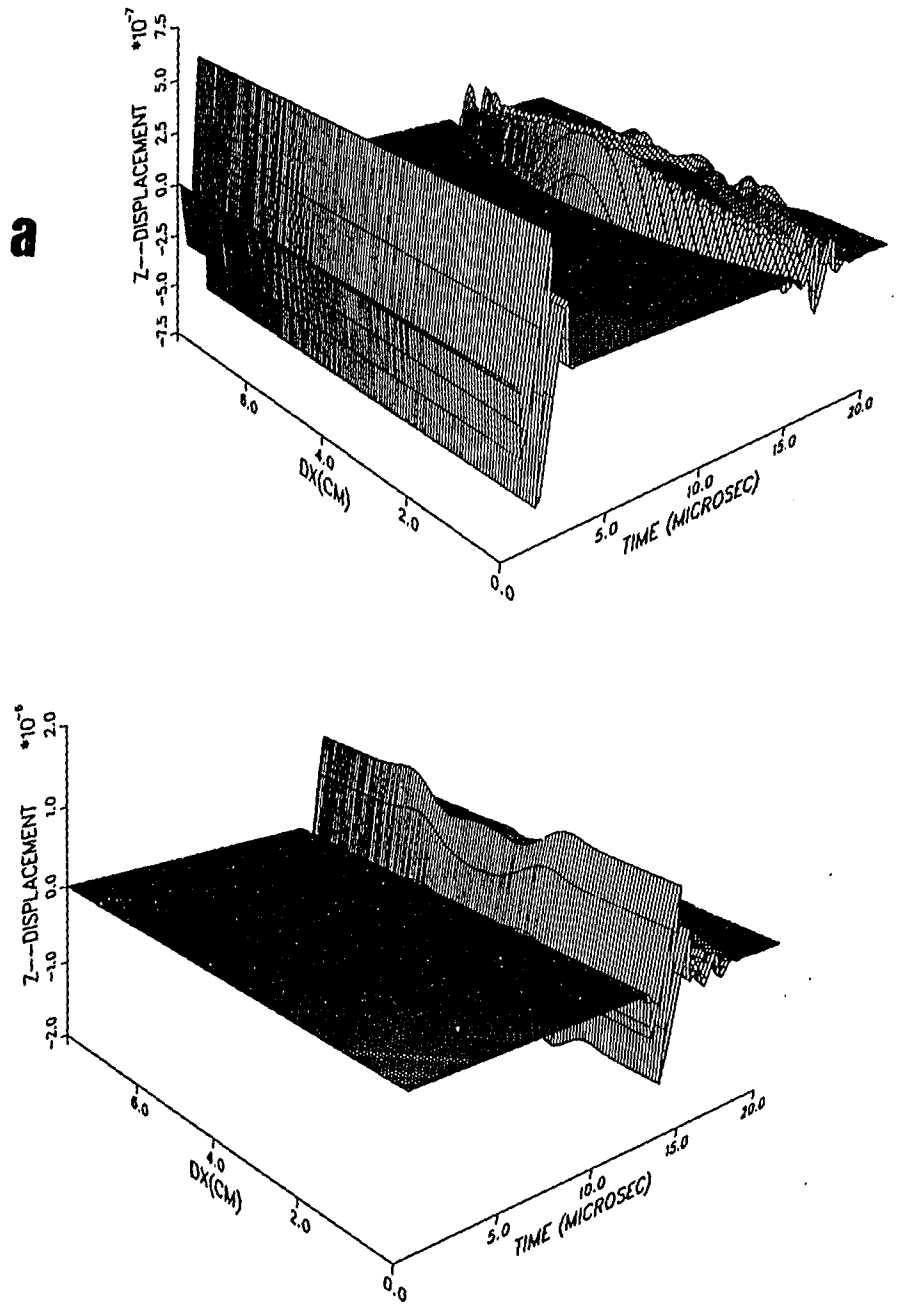

Figure 8.2: Wave recorded on the surfaces of the block. a) on the front surface; b) on the backwall.

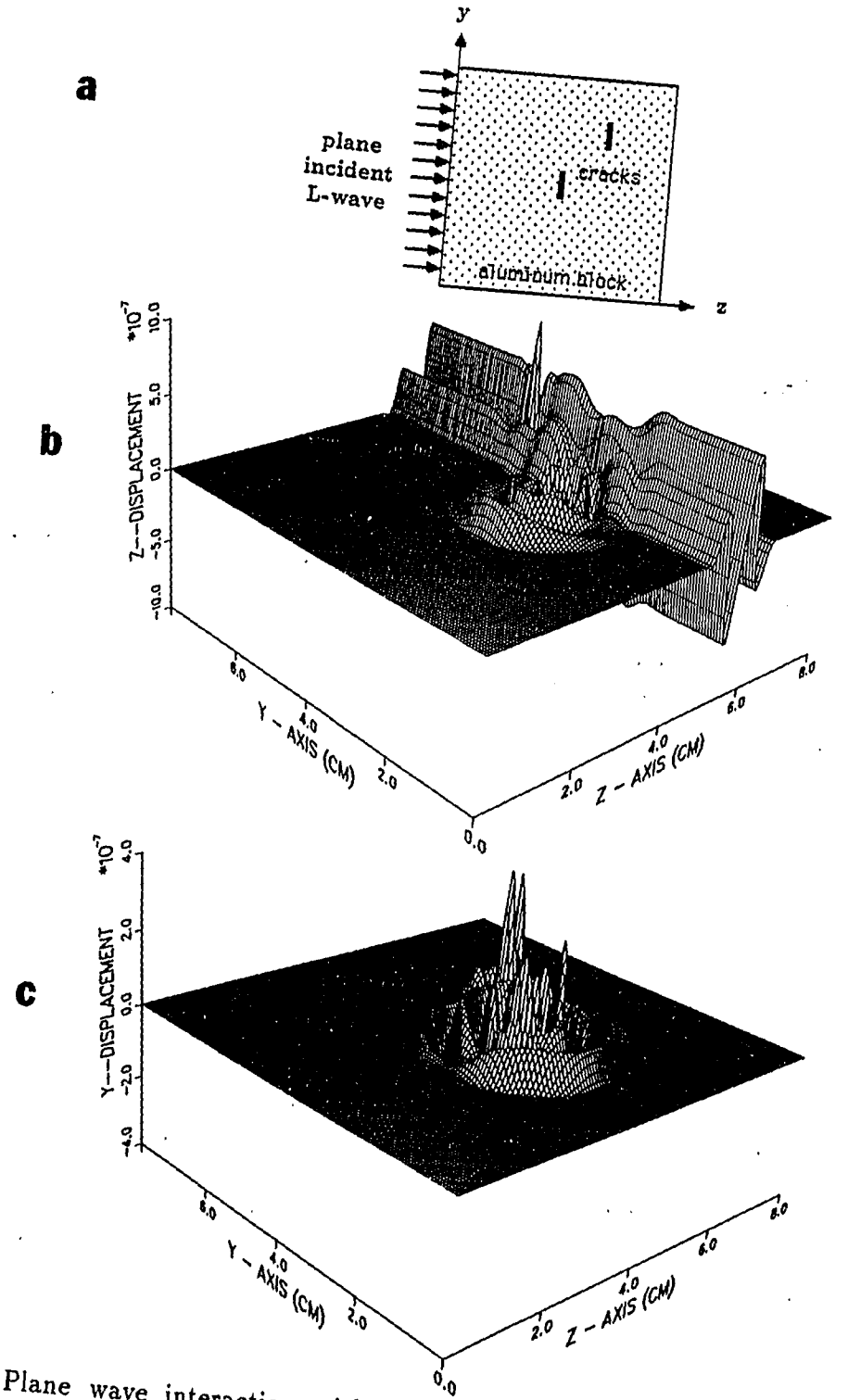

Figure 8.3: Plane wave interaction with two cracks. a) Geometry detail; b) z-displacement at $t = 10\ \mu s$; c) y-displacemnet at $t = 10\ \mu s$

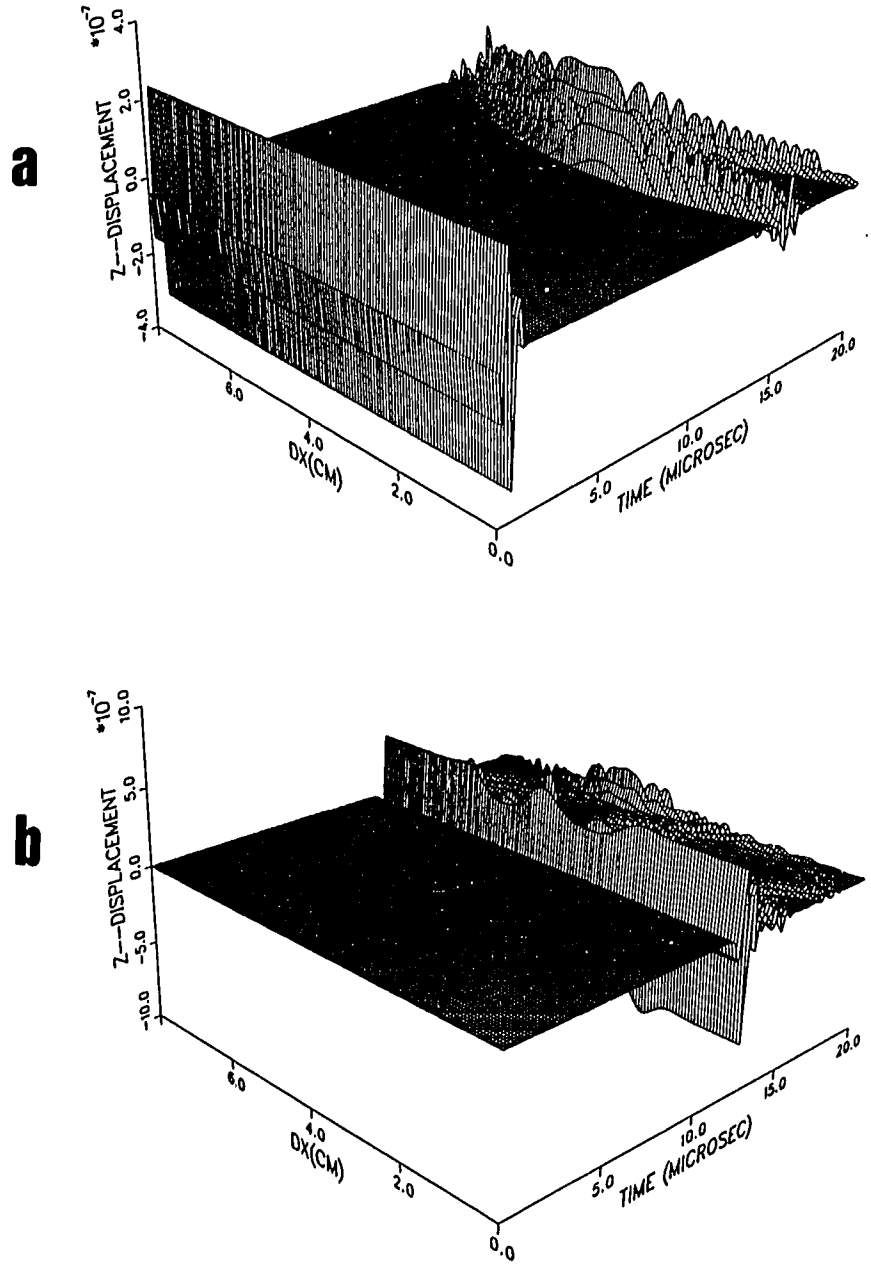

Figure 8.4: Wave recorded on the surfaces of the two-crack block. a) on the front surface; b) on the backwall

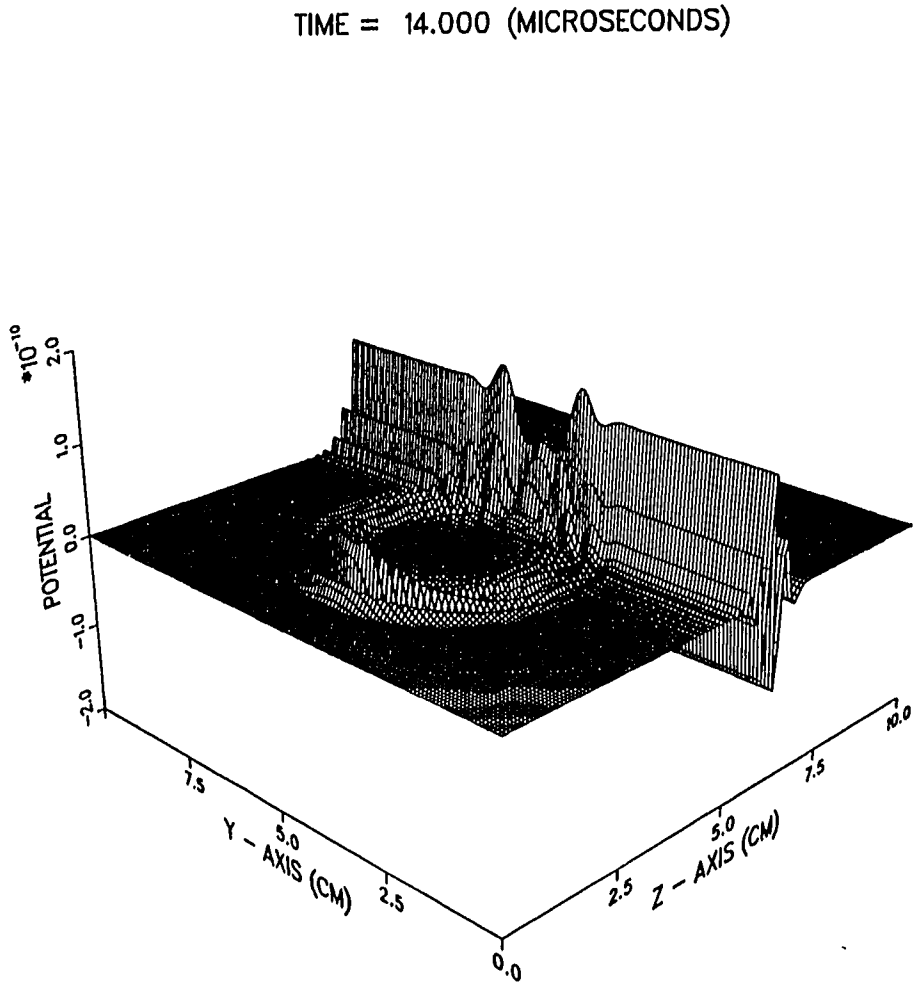

Figure 8.5: Acoustic potential scattered from a rectangular crack

giving the measured data $\Phi_M(y, z = 0, \omega)$ in the frequency domain. Further Fourier transformation of Φ_M with respect to y yields $\hat{\Phi}_M(k_y, z = 0, \omega)$ as required in Equation(7.60). This line measurement field is then back propagated into all other lines (all other z locations) in the space forming the filtered back-propagation wave field. The secondary sources are related to the back-propagated field through the Porter-Bojarski integral equation with restrictions of a planar measurement. The linearized relationship of the Born approximation then recovers the information of the object function at that frequency. Sweeping over all the frequencies in the bandwidth and inverse Fourier transforming then results in the filtered object function expressed as equations(7.60) and (7.65).

Effects of Using the Normal Displacement Component to Reconstruct the Image

When the reconstruction algorithm is derived, the primary variable is the acoustic potential. In real ultrasonic experiments, however, the transducer records the normal displacement component which is then used for reconstructing the defect images. Are there any significant effects from use of the displacement instead of the acoustical potential? To evaluate the effects of using the normal displacement component in the image reconstruction, defects in an elastic body and in an acoustic body are separately reconstructed and then compared to observe the differences. Using the same geometries, the finite element codes are used to produce both the reflected displacement for the elastic problem and the reflected potential for the acoustic case as described in the last section. Reconstructed images of these two cases are displayed in Fig. 8-6. It can be seen that the defect image from the normal component of the

displacement is about the same as the one from the acoustic potential. Therefore, it can be concluded that using the normal component of the displacement does not significantly degenerate the quality of the image reconstruction.

An attempt to use the displacement field for the reconstruction has been made by Schade[96]. The potential fields (both scalar and vector potentials representing longitudinal and shear waves, respectively) are uniquely related to the displacement vector through the Helmholtz decomposition. By defining separate longitudinal and shear propagators, the scattered field including the mode converted shear wave then can be correctly back-propagated to the full space. The advantage of the displacement vector is that both longitudinal and shear waves are utilized which function as two independent experiments. If the mode converted shear wave is neglected, as in those formulations presented in this dissertation, the reconstruction from the displacement field is just the same as that from the potential function. This observation supports the afore-mentioned conclusion.

Effect of the Weak Scatterer Assumption

It has been clearly stated in Chapter 7 that the linearized reconstruction of the object functions is based on the weak scatterer approximation. In many cases, however, we are interested in a strong scatterer such as a crack or a void in a bulk material. Does the reconstruction still give correct information about the defect? To see this effect, the reconstruction algorithm is applied to both weak and strong square scatterers simulated by 2-D finite element code. Results are shown in Fig. 8-7 indicating that the reconstruction gives the volumetric information for the weak scatterer but only the contour of the illuminated side for the strong scatterer. This

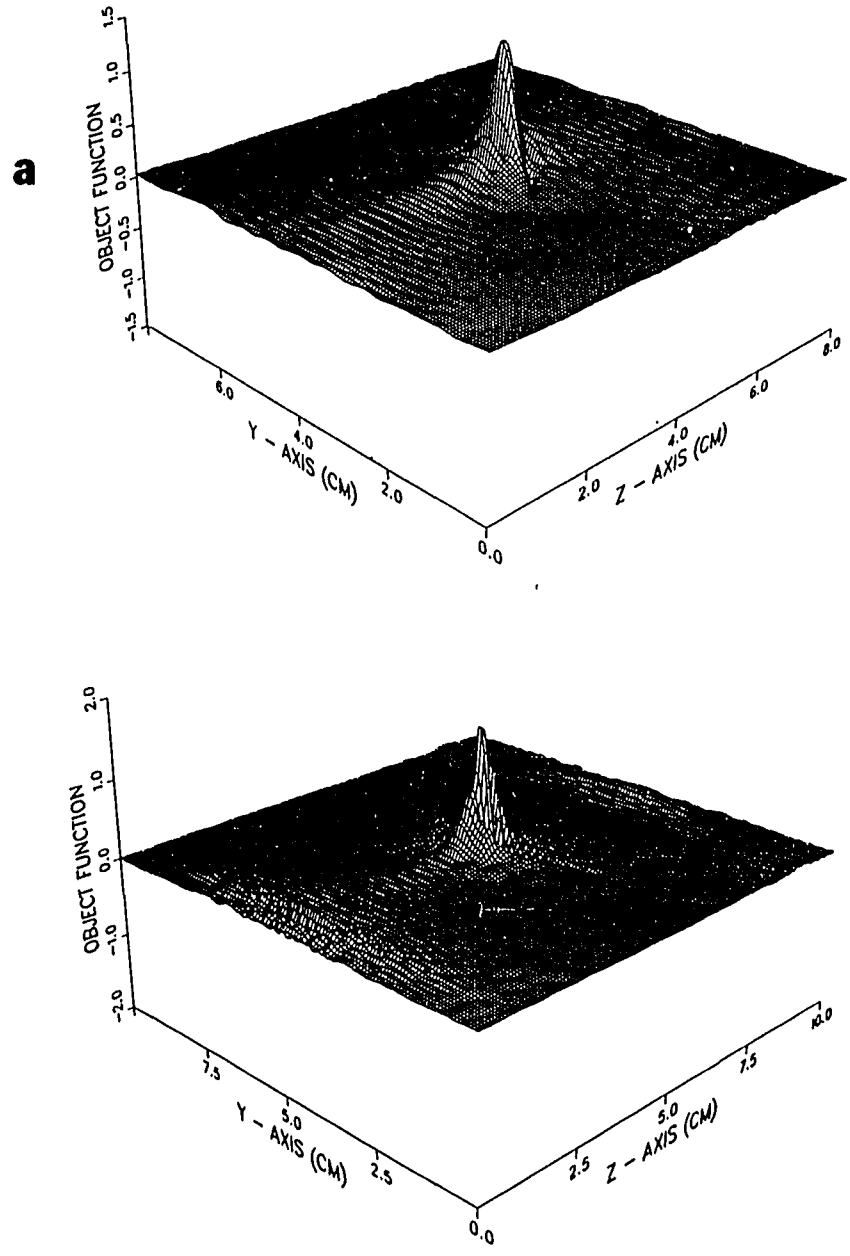

Figure 8.6: Reconstructed images from a) acoustic potentials; b) the normal component of the reflected L-wave displacement

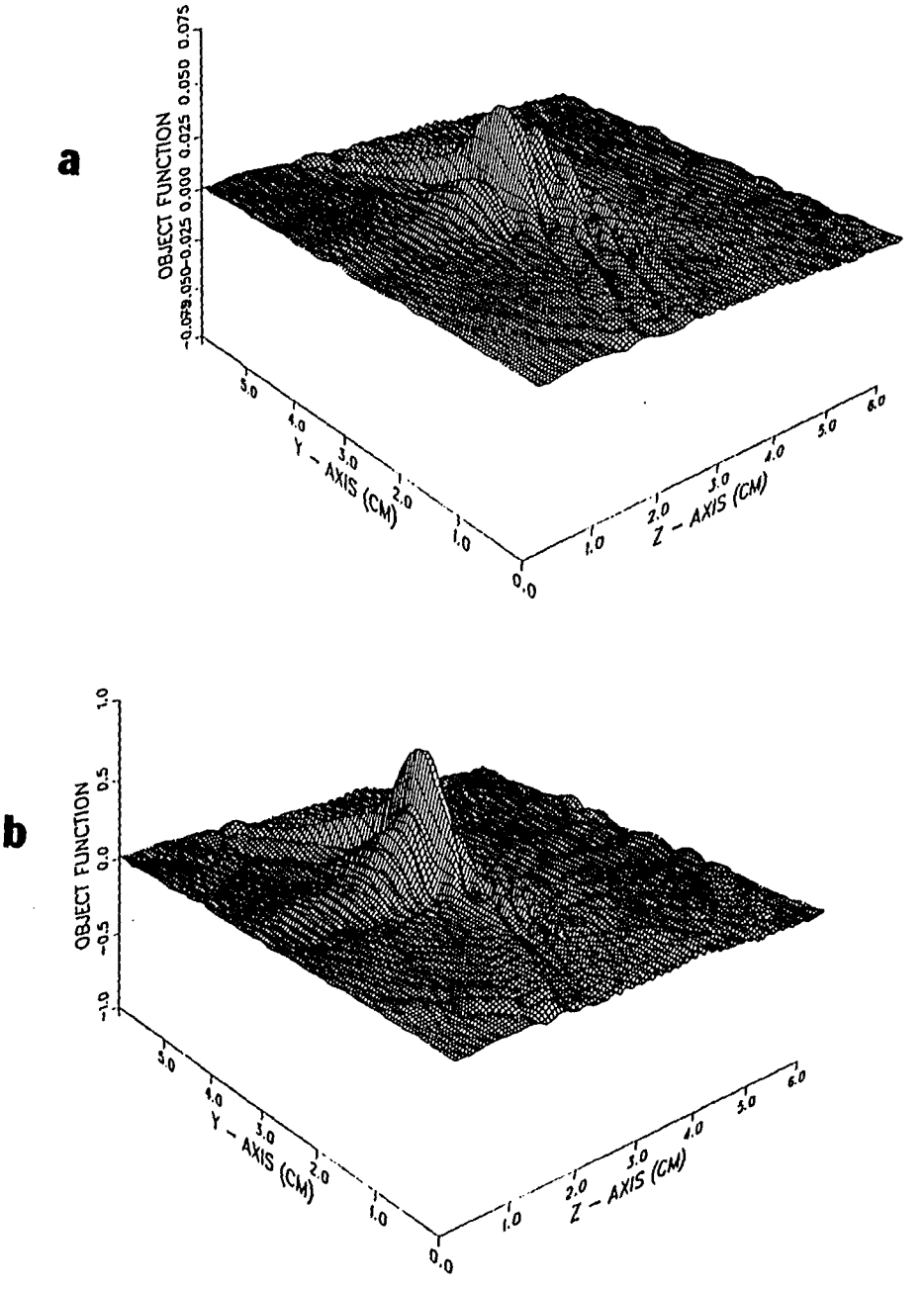

Figure 8.7: Comparison of the reconstructed images from a) a weak scatterer; b) a strong scatterer

phenomenon can be partially observed from the reflected waves plotted in Fig. 8-8. The reflection from the weak scatterer (Fig. 8-8a) has two wave fronts. One is from the front surface and the other is from the back surface of the scatterer. On the other hand, the reflection from the strong scatterer (Fig. 8-8b) is from only the front surface. The complete contour of a strong scatterer can be obtained only if all four sides are illuminated. This can also be seen from the shape of the filter in the spatial frequency domain. Illumination from four sides recovers the full object function instead of the filtered part in the frequency domain. This observation, however, is applicable to the weak scatterer also, since both cases have the same spatial filter.

Finite Aperture Effects

The derivation of the reconstruction algorithms has assumed a plane incident wave which is rarely met in practice. This section is intended to evaluate the effects of a finite aperture by varying the aperture of the transmitter, as well as the receiver. Consider again an aluminum block of dimensions 10 cm x 10 cm with a subsurface crack of dimensions 0.4 mm x 8 mm, which is illustrated in Fig. 8-1a, insonified by the incident waves from a finite aperture transducer whose aperture varies from a point to infinity (plane wave). The aperture is modeled as a uniform force input over the aperture region. The reconstructed images with incidence from different apertures are illustrated in Figs. 8-9a to 8-13a showing very little effect from aperture variations. The background noise increases due to the presence of the edge waves. A typical snapshot of the displacement field with an 1.27 cm diameter aperture is shown in Fig. 8-14 in which a strong edge wave is observed. Even though a time window is applied to eliminate this edge wave, it is difficult to obtain the pure reflection

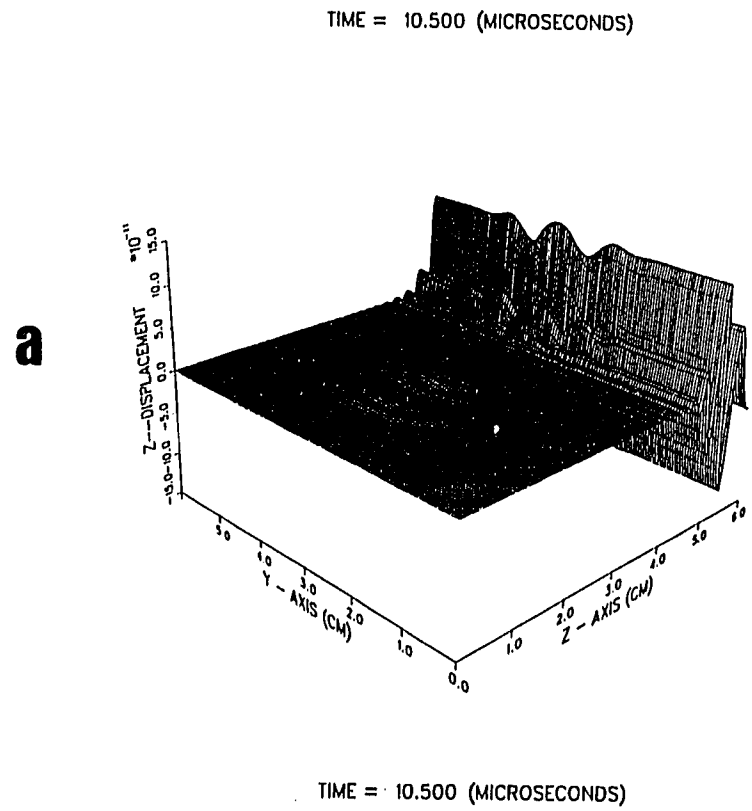

Figure 8.8: Wave reflection from a) a weak scatterer; b) a strong scatterer

for those locations where the edge wave and the reflection arrive at about the same time. The other observable effect is that the error of sizing the defect increases as the aperture of the incidence decreases. The amount, however, is so small that the assumption of plane wave incidence is reasonable in practical situations [97]. If the image output are from the half valued threshold as shown in Figs. 8-9b to 8-13b, the effect of finite aperture is basically negligible.

The receiver region now is also varied to take into account the limited angle. It is assumed that each receiver acts as a point receiver, but the accessible area is restricted which then results in the limited angle reconstructions. Two typical limited angle results are shown in Figs. 8-15 and 8-16.

Anisotropy Effects

Even though the reconstruction algorithm is derived for the assumption of isotropic materials, it is interesting to see whether it is possible to apply this algorithm to anisotropic materials. As an example, an orthorhombic block with parameters

$$C'_{22} = 11.43 \times 10^{10}\ N/m^2 \qquad C'_{33} = 28.6 \times 10^{10}\ N/m^2$$
$$C'_{44} = 13.96 \times 10^{10}\ N/m^2 \qquad C'_{23} = 3.47 \times 10^{10}\ N/m^2$$

is chosen to demonstrate the anisotropy effects. A defect of the same dimensions as that in the aluminum block is placed at the center of the block.

Repeating the same procedures as described in the previous sections with plane incidence, the defect images are reconstructed for three different grain orientations: parallel, perpendicular and 45^o to the direction of the incident wave as shown in Figs. 8-17 to 8-19. It can be seen that the material anisotropy plays an important

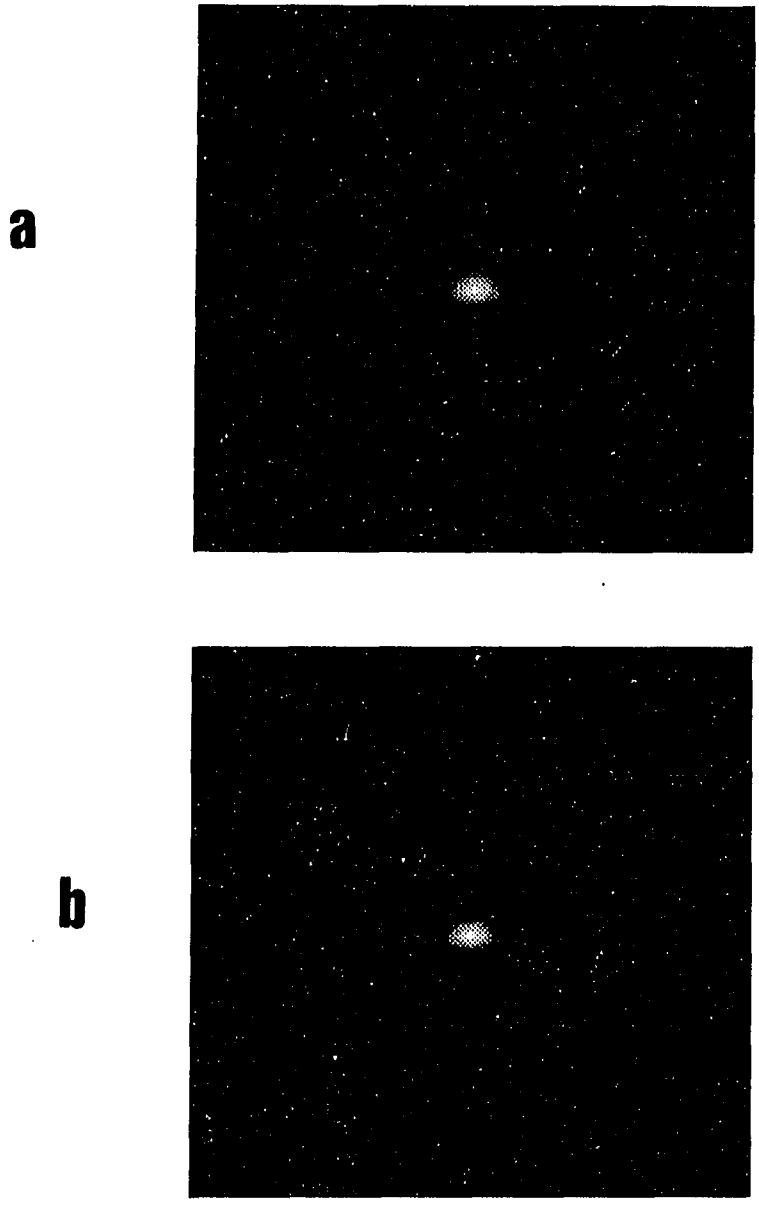

Figure 8.9: Image reconstructed from plane incident wave: a) Original image; b) With half value threshold

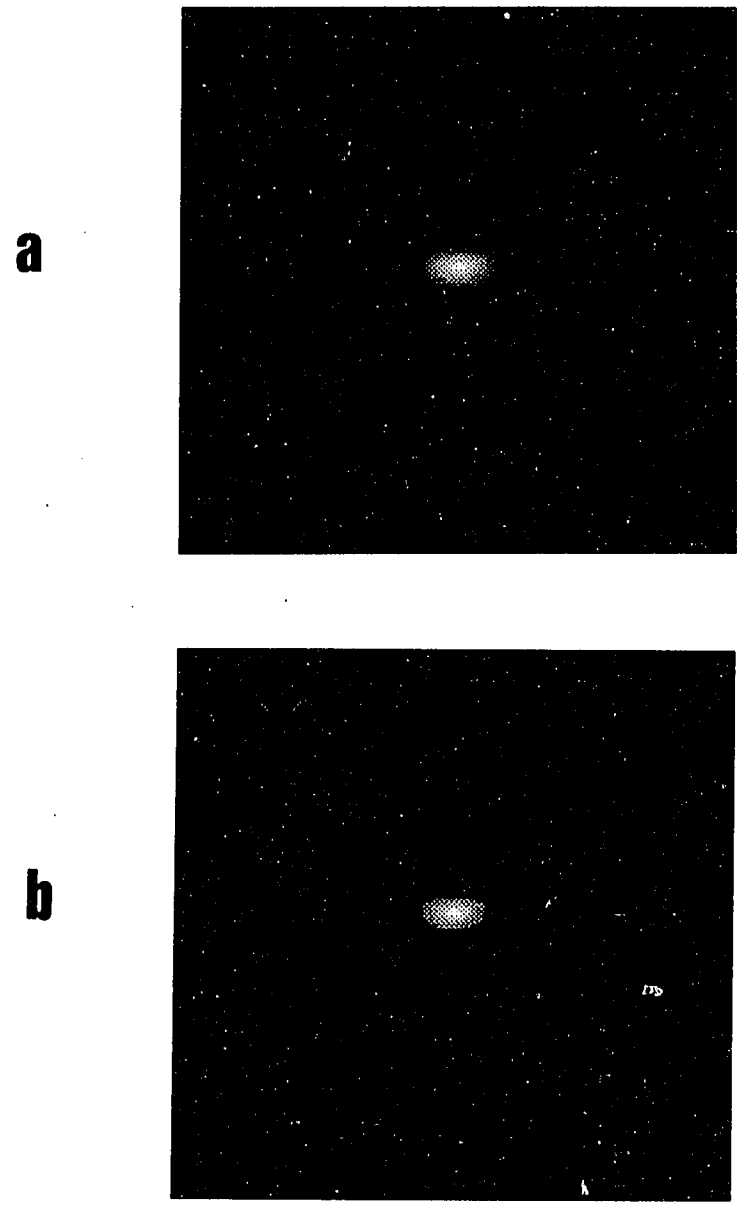

Figure 8.10: Image reconstructed from an 1" diameter aperture transmitter: a) Original image; b) With half value threshold

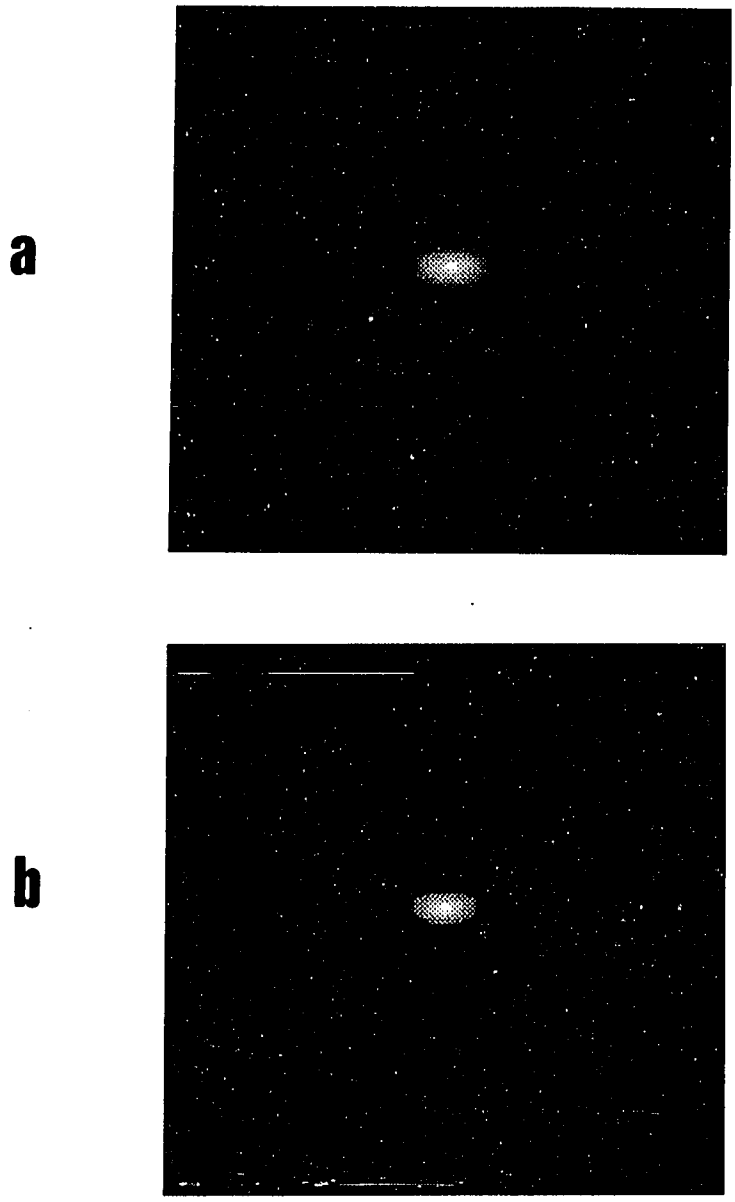

Figure 8.11: Image reconstructed from a $\frac{1}{2}$" diameter aperture transmitter: a) Original image; b) With half value threshold

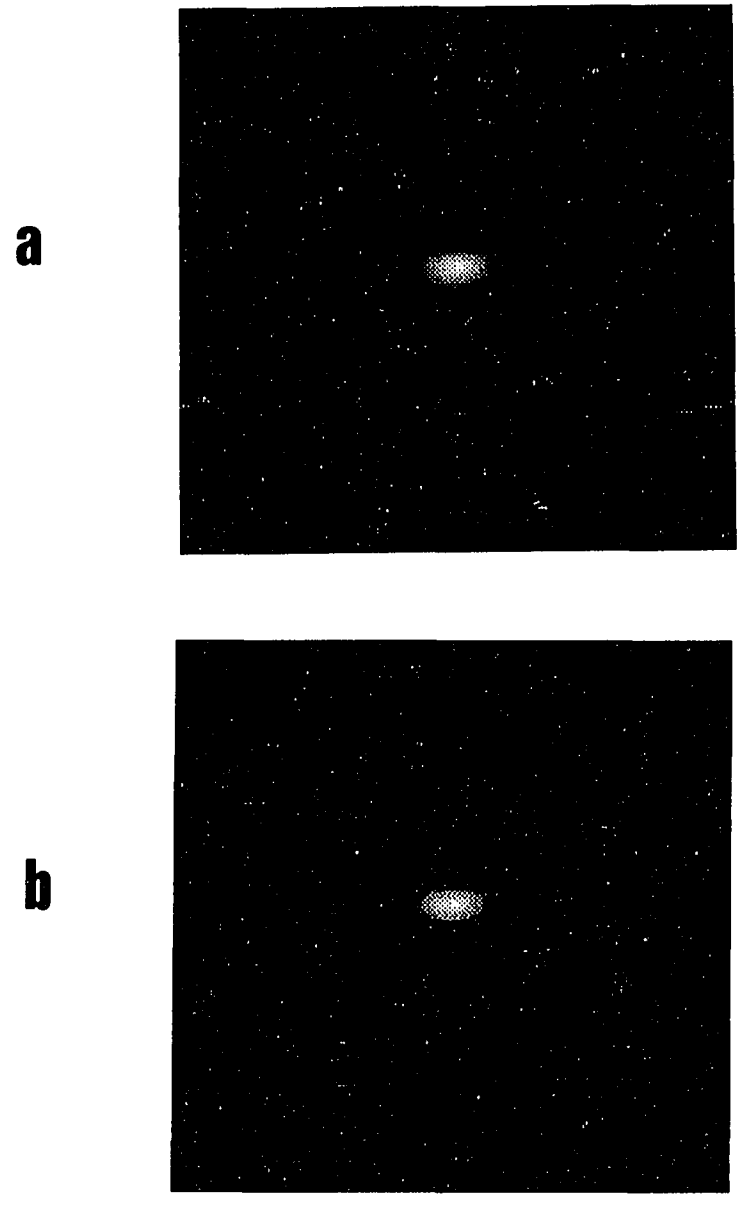

Figure 8.12: Image reconstructed from a $\frac{1}{4}$" diameter aperture transmitter: a) Original image; b) With half value threshold

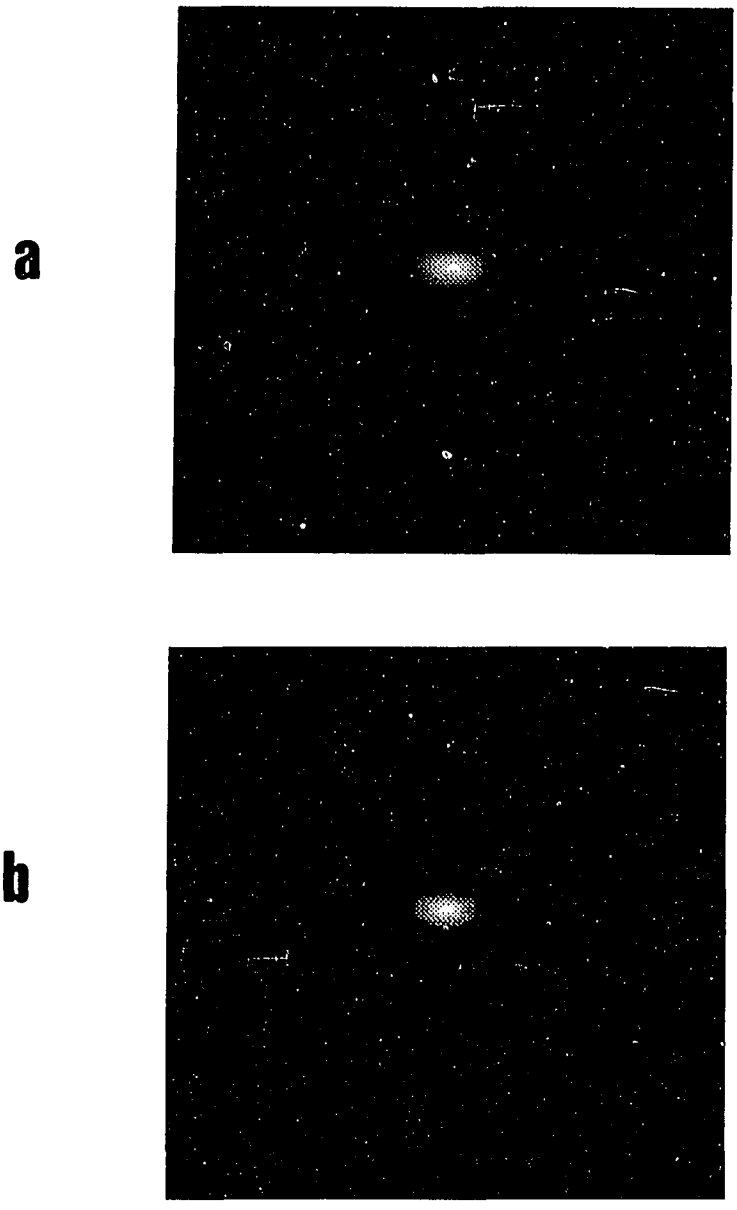

Figure 8.13: Image reconstructed from a point source incidence: a) Original image; b) With half value threshold

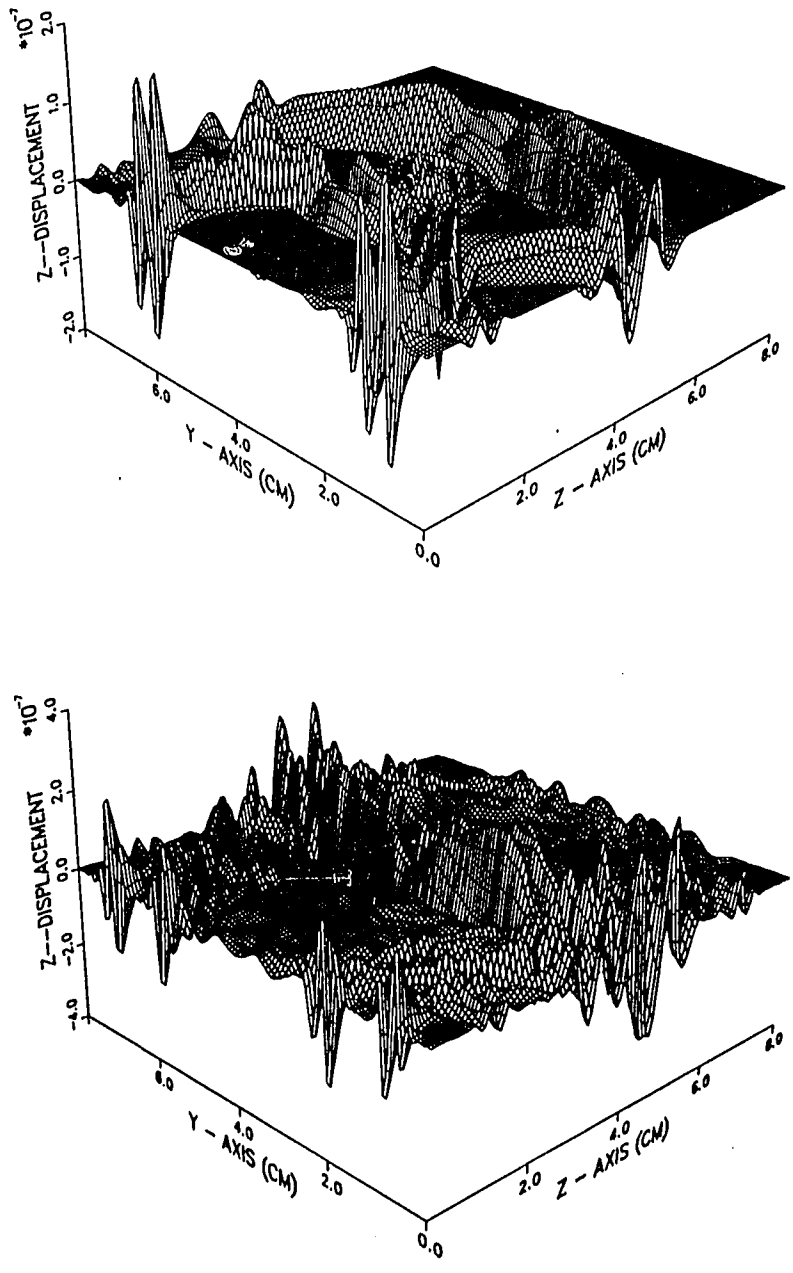

Figure 8.14: Interaction of the wave from a $\frac{1}{2}$" aperture transducer with a rectangular defect

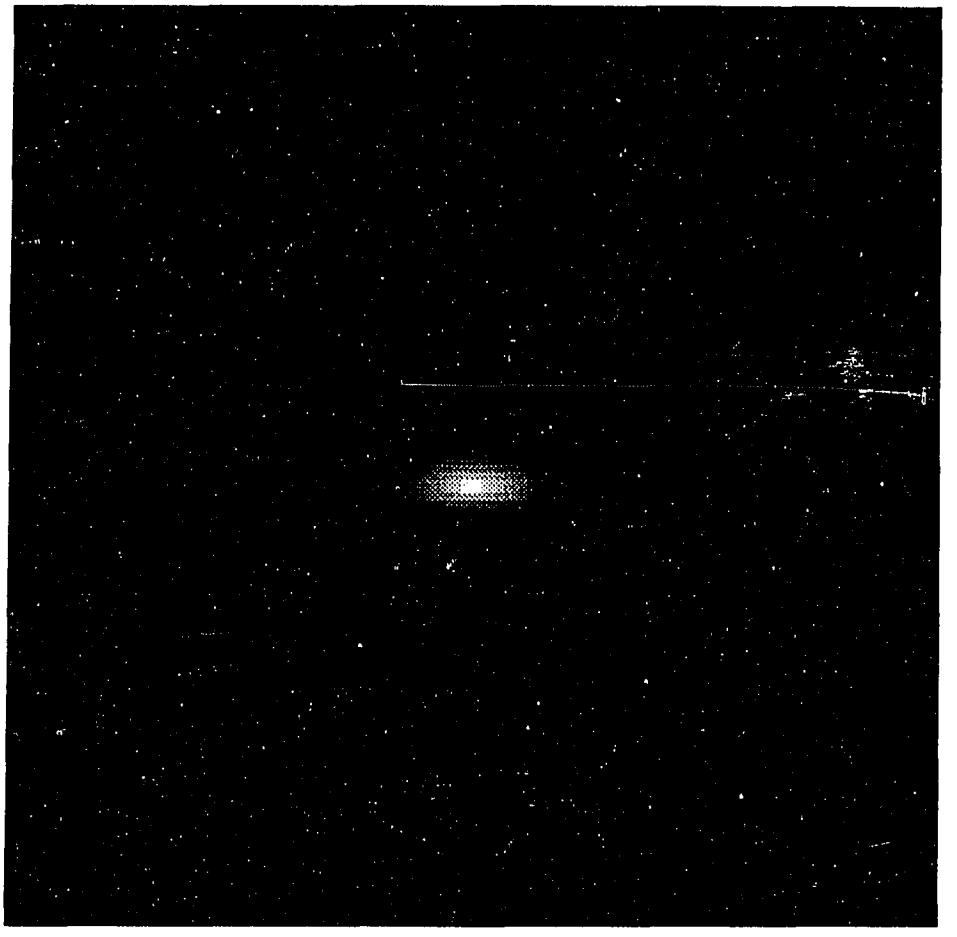

Figure 8.15: Image reconstructed from the reflections within the area of 90^o view angle

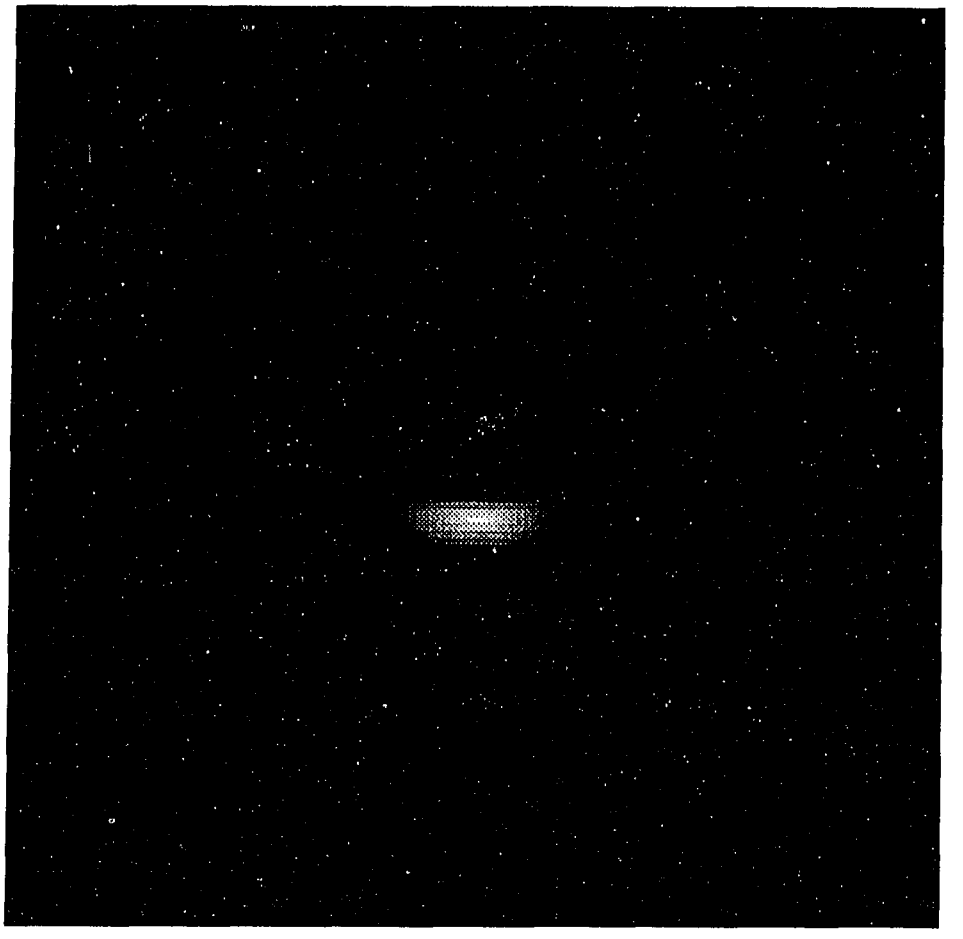

Figure 8.16: Image reconstructed from the reflections within the area of 50^o view angle

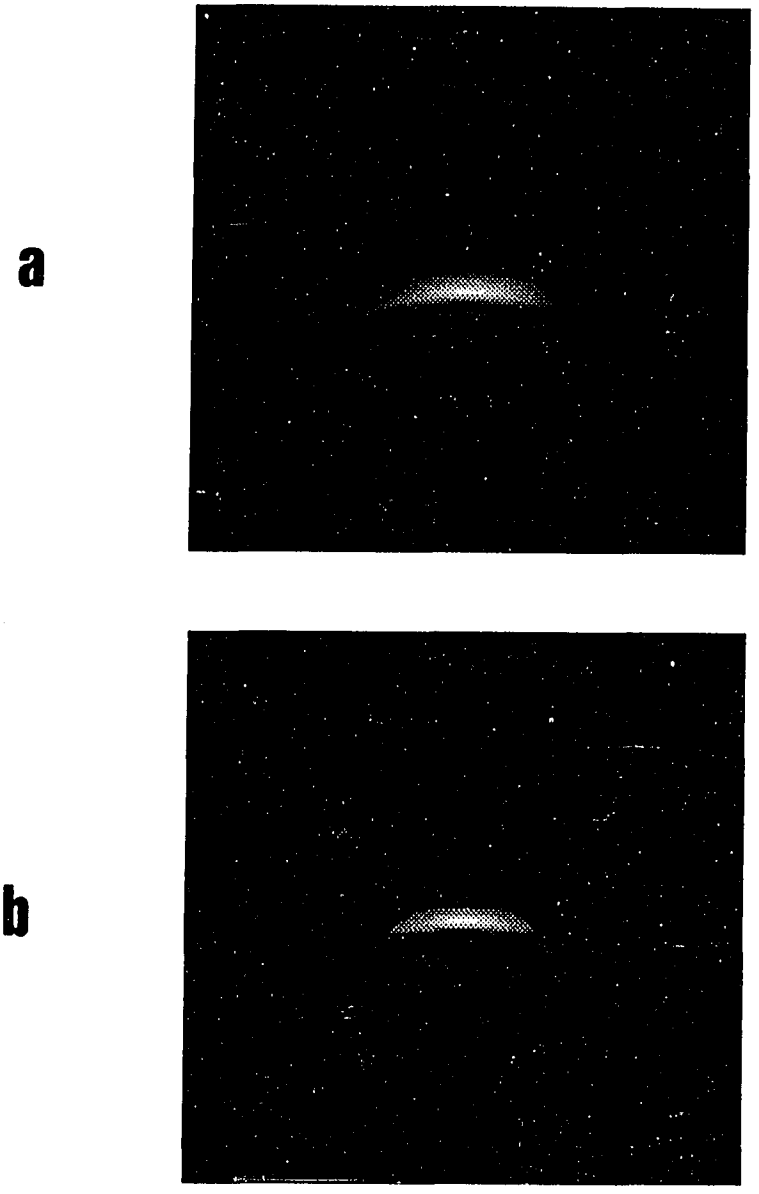

Figure 8.17: Image reconstructed from an orthorhombic material when the grain orientation is parallel to the direction of the incident wave: a) Original image; b) With half value threshold

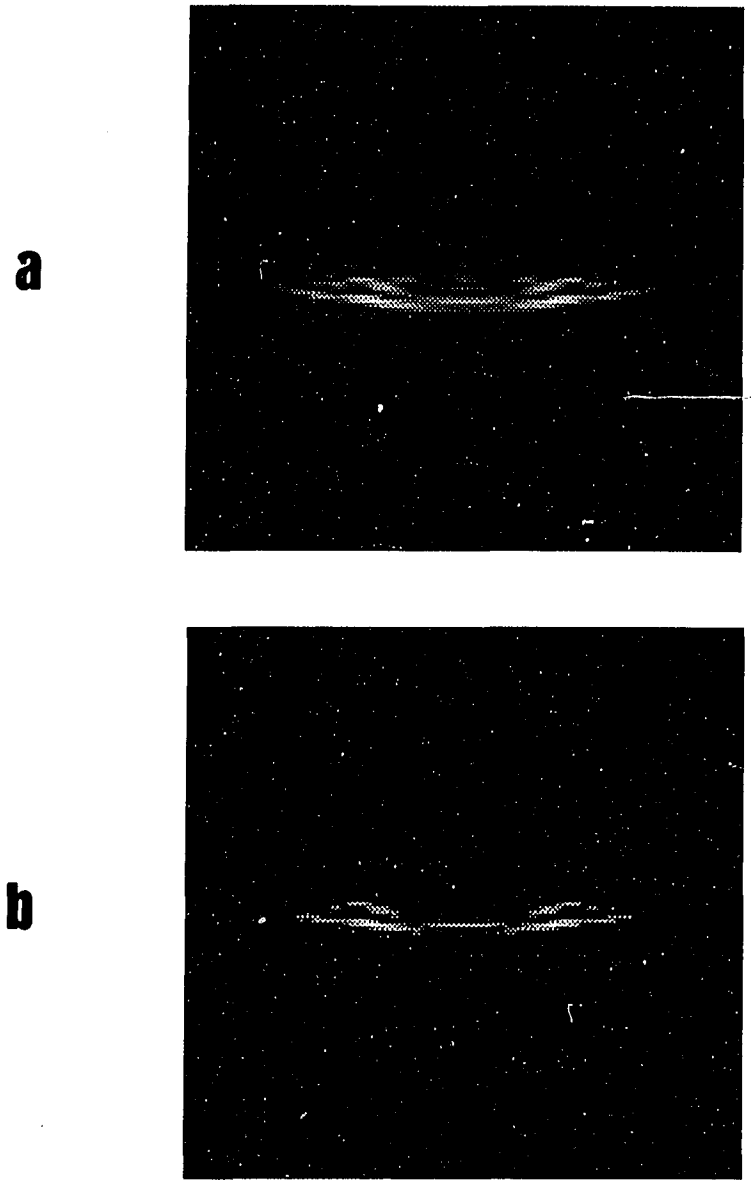

Figure 8.18: Image reconstructed from an orthorhombic material when the grain orientation is perpendicular to the direction of the incident wave: a) Original image; b) With half value threshold

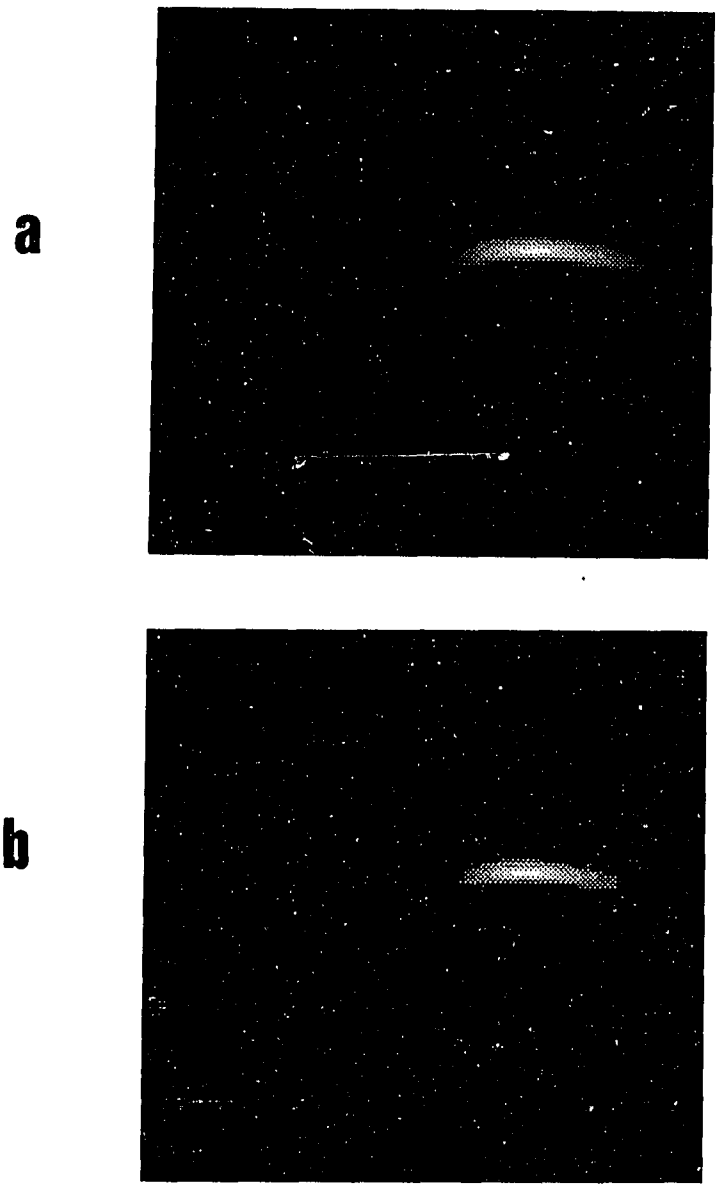

Figure 8.19: Image reconstructed from an orthorhombic material when the grain orientation is in 45^o to the direction of the incident wave: a) Original image; b) With half value threshold

role in the defect reconstruction. The convex shaped object image in Fig. 8-17 results from the velocity differences in the different directions of the traveling wave. The focusing effect does not contribute too much to the degeneration of this image. Fig. 8-18, however, shows clearly the effects of both the velocity differences and the defocusing phenomenon. Velocity differences contribute to the concave shape of the object image, while the defocusing results in the wide spread of the object function. The size of the crack in Fig. 8-18b is obviously much larger than the actual situation. Therefore, the reconstructed image does not give correct information about the defect size. In Fig. 8-19, the position of the object is shifted due to the skewing phenomenon and the convex shape results from the velocity differences. The sizing under half valued threshold does not predict the actual size in this case.

In practical situations, the skewing phenomenon usually accompanies the focusing or defocusing effect. Therefore, diffraction tomography does not apply to general anisotropic materials because the reconstructed image gives neither the correct defect position, nor the correct defect sizing.

In order to use diffraction tomographic algorithms for anisotropic materials, the raw data should be preprocessed. The basic idea of the preprocessing is to shift the relative time of flight as if the reflected waves have travelled at the *same* speed from different directions. Considering only the velocity differences at this stage, we assume a point reflector located at the center of the block. For every point on the measurement surface, the corresponding velocity can be calculated according to the directions. Choosing the direction of incident wave propagating as the reference direction which is represented as $\phi = 0$ in Fig. 20, any location on the measurement

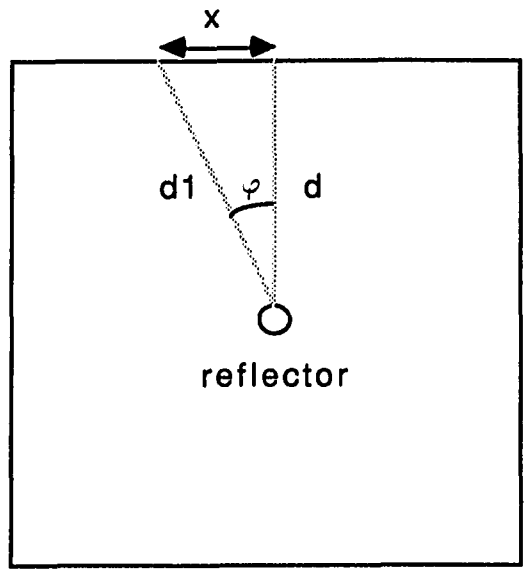

Figure 8.20: Illustration of the reference direction for the data preprocessing

surface at x has an angle of ϕ which satisfies

$$\phi = \arctan(x/d) \tag{8.1}$$

where d is the distance from the reflector to the reference point. Let V_l^0 represent the L-wave velocity in the reference direction and V_l^ϕ be the velocity from the reflector to the location x. All these velocities are group velocities and can be read from the velocity surface. Time shifting t_d is calculated by

$$t_d = \frac{d_1}{V_l^\phi} - \frac{d_1}{V_l^0} \tag{8.2}$$

where d_1 is the distance from the reflector to the location x. The originally recorded displacement A-scan data $u(x,t)$ is used as $u(x,t-t_d)$ for the reconstruction. When skewing occurs, the position should be shifted before time shifting. However, the position cannot be shifted easily because there will not be enough information available. The uncertainty of the reflector position leaves the directions of the reflected

wave unknown, which makes the determination of the skewing angle impossible. Reconstructions with preprocessing are reproduced for the cases of grain orientation parallel, and perpendicular to the phase velocity. The results are shown in Figs. 8-21 and 8-22. It can be seen that the effects of the velocity differences are removed. However, the defocusing effect still degenerates the image as shown in Fig. 8-22.

Comparisons of the Reflection Mode with the Transmission Mode

Unlike the reflection mode where the reflections on the front surface are used for the reconstruction, the transmission mode utilizes the transmitted wave on the back wall. The processing procedures are the same as the reflection mode described in previous sections. A typical reconstruction is shown in Fig. 8-23 which shows a very similar nature to the one from the reflection mode of Fig. 8-7a.

Consider now a 'multiple cracks' situation where two cracks are present in an aluminum block of the same dimensions as before. The reconstructed images are shown in Fig. 8-24 for the reflection mode and Fig. 8-25 for the transmission mode. It can be seen that the transmission mode does not give the correct information about the different depths of these two cracks. The explanation is that the transmitted data does not have the information about the depths of the cracks. The depths, are only related to the arrival time of the reflected data. This is one of the advantages of the reflection mode over the transmission mode. The reflection mode also has a better resolution than that of the transmission mode because of the better space coverage of the Λ-shaped filter than that of the $\sum$-shaped filter for a finite bandwidth source signal.

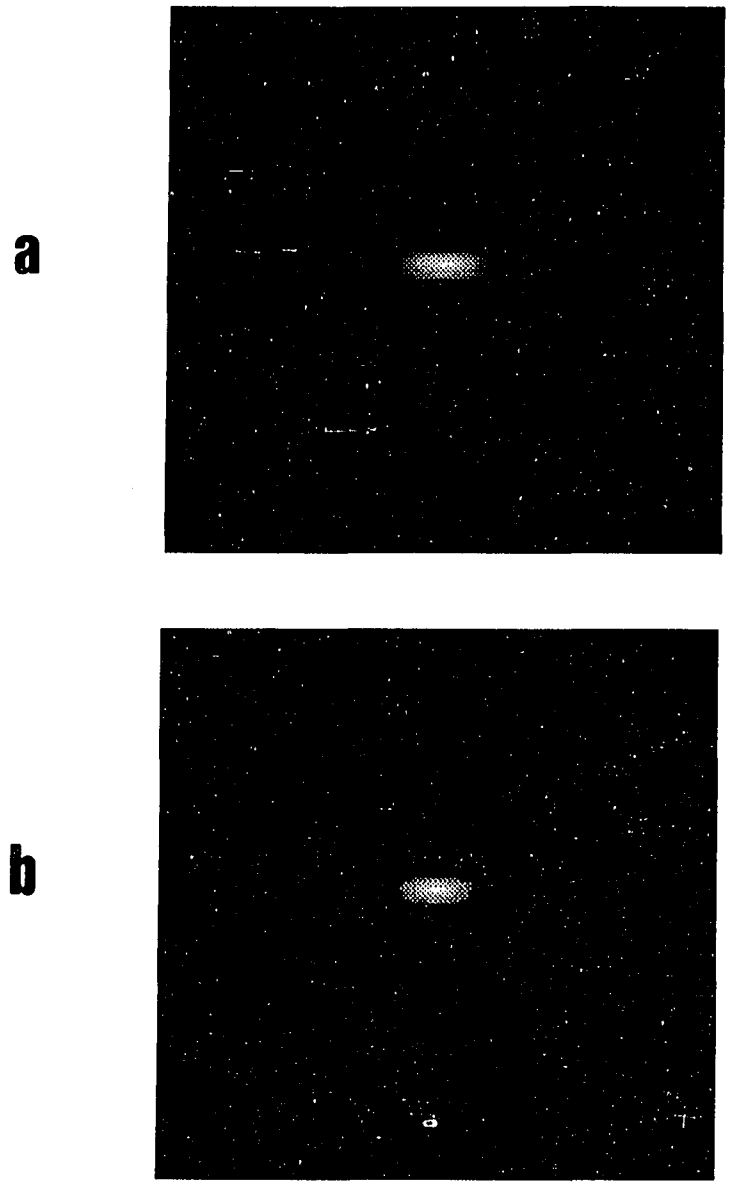

Figure 8.21: Image reconstruction with data preprocessing when the grain orientation is in parallel to the direction of the incident wave: a) Original image; b) With half value threshold

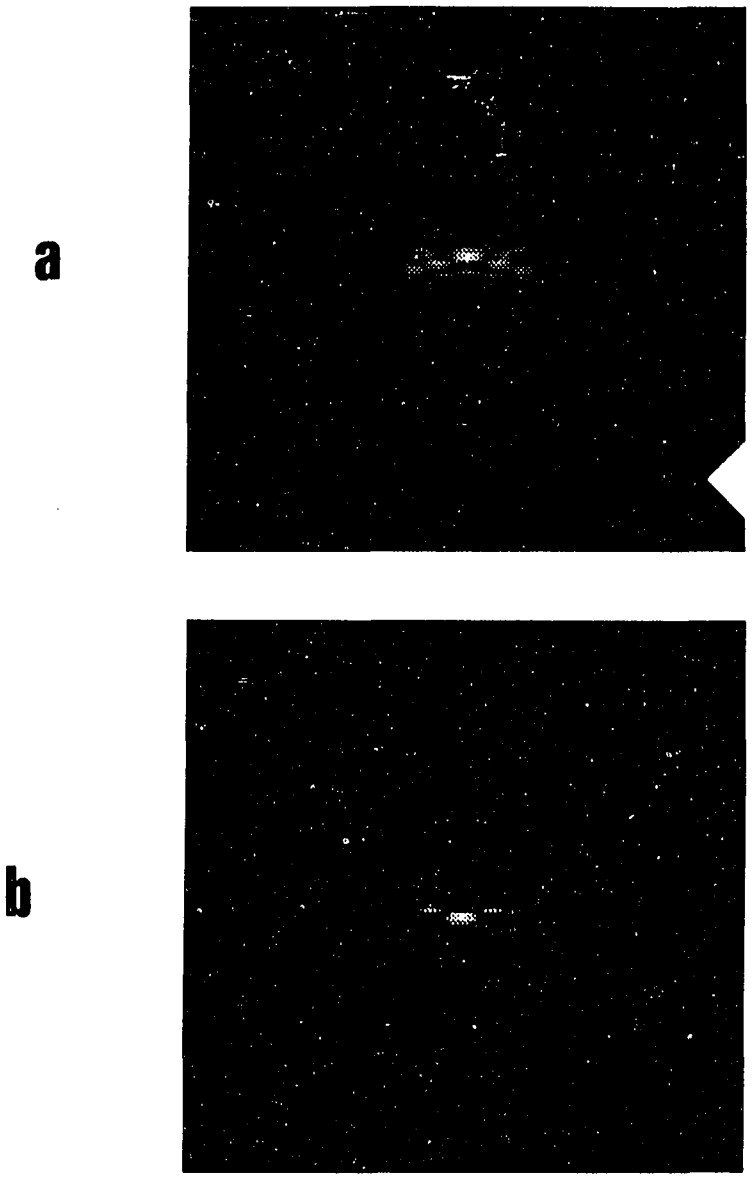

Figure 8.22: Image reconstruction with data preprocessing when the grain orientation is in perpendicular to the direction of the incident wave: a) Original image; b) With half value threshold

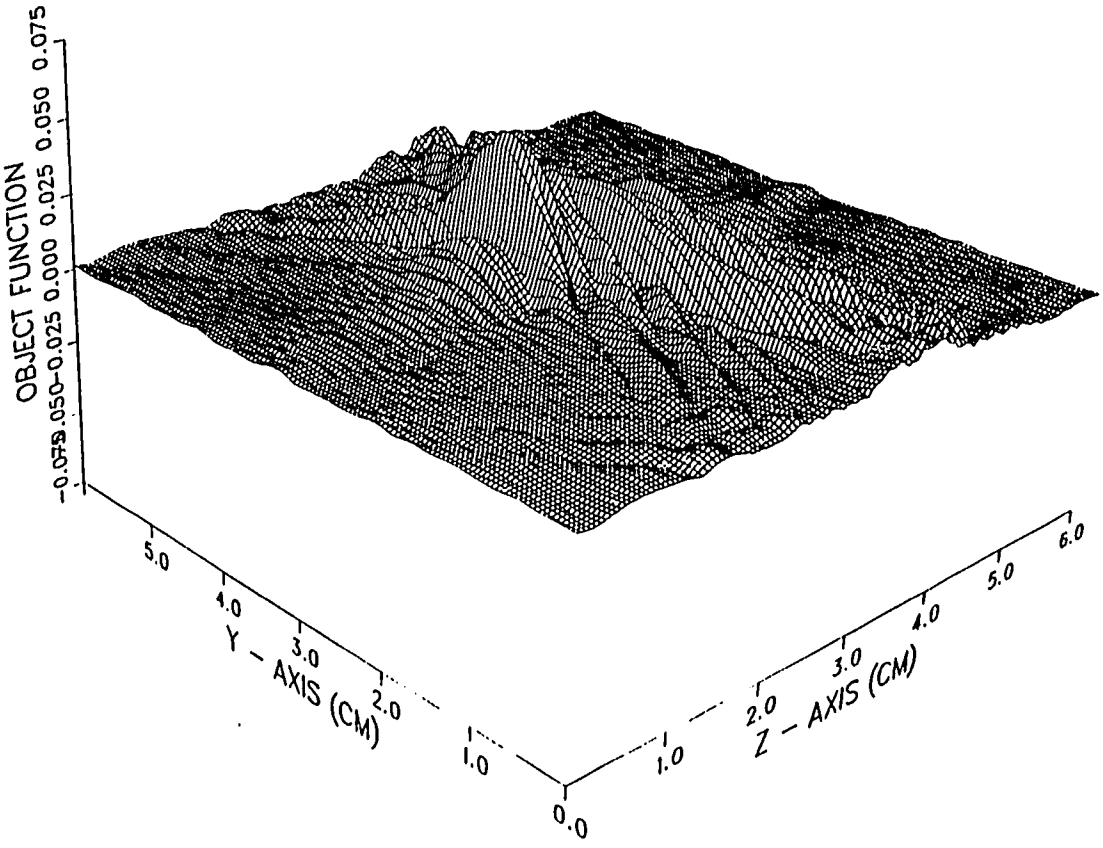

Figure 8.23: Image reconstructed by the diffraction tomography in transmission mode

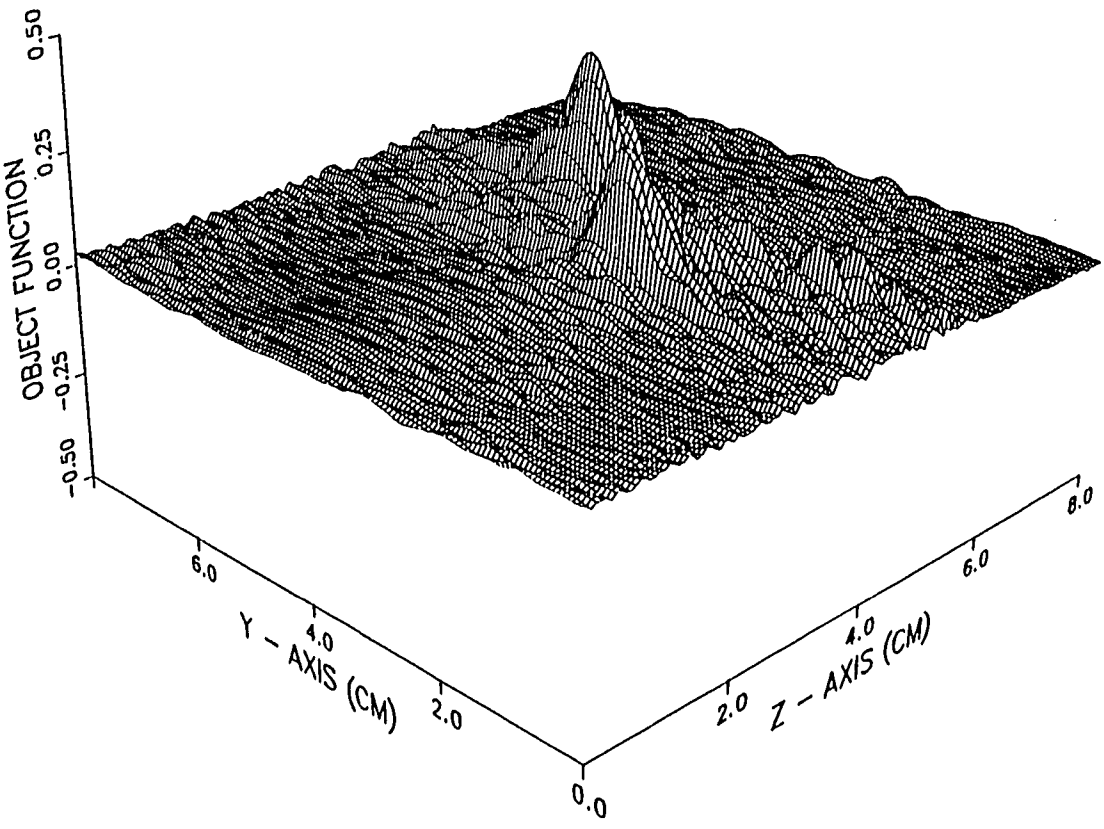

Figure 8.24: Image of two cracks reconstructed by the reflection tomography

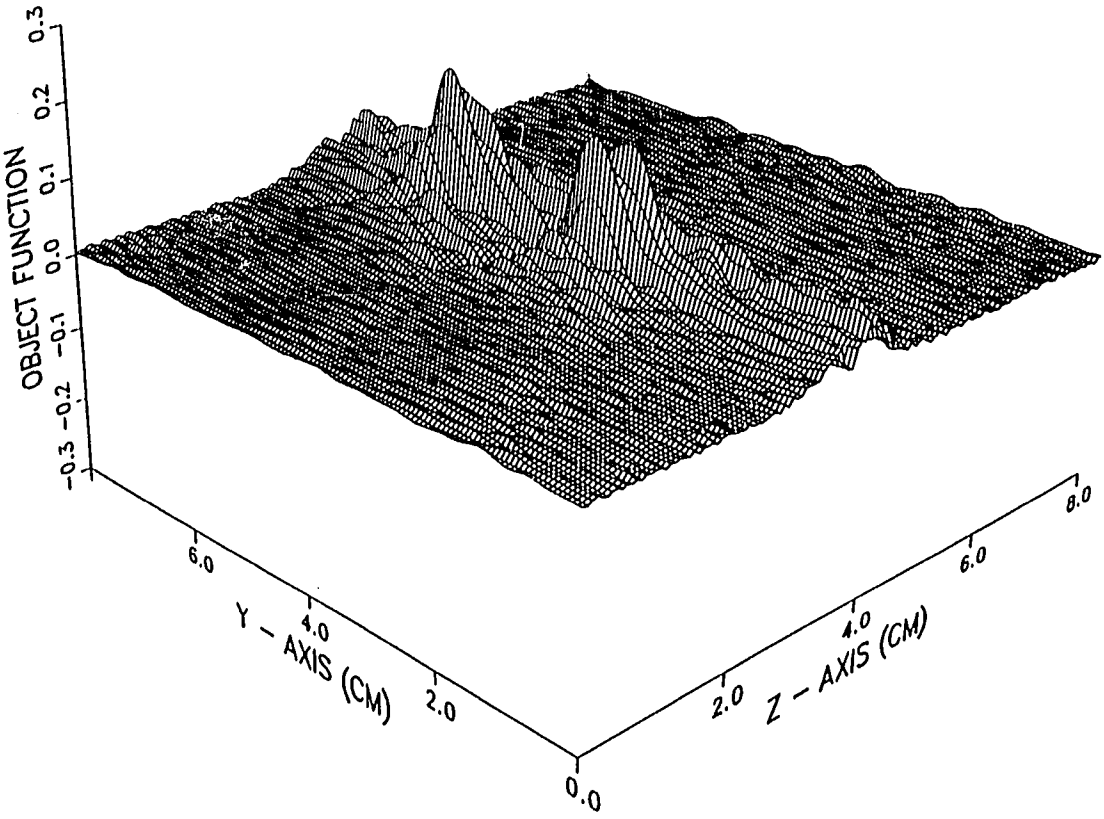

Figure 8.25: Image of two cracks reconstructed by the transmission tomography

CHAPTER 9. CONCLUSIONS AND FUTURE WORK

The main objective of this dissertation is the development of a finite element model for ultrasonic NDE and the application of this model to test diffraction tomographic algorithms for defect image reconstruction. This chapter summarizes the contributions and suggests areas of future research.

Summary of Major Achievements

This dissertation has illustrated that the finite element model is a powerful tool for studying inverse algorithms. The primary advantage of this model lies in the flexibility of modifying the material properties and the geometric configurations, which enables one to evaluate independently the various factors affecting the reconstructed images.

In order to consider all the practical factors, the finite element model should incorporate general anisotropy, inhomogeneity and complex geometries. Based on the 2-D isotropic model developed in previous research, this dissertation first introduces anisotropy into the basic formulation, thus allowing a large class of realistic materials to be modeled. In addition, an explicit integration scheme and a mass lumping technique are introduced. Geometries modeled by the original 2-D algorithm consisted of less than 8000 nodes on a Cyber 205 supercomputer due to the huge memory

requirement. On the other hand, with the new model, geometries of up to 1 million nodes can be handled on most mainframes and work stations. The development of the axisymmetric formulation extends the horizon of this research as it takes into account the 3-D nature of the problem. This allows the model to characterize a realistic transducer profile. A special formulation is introduced to model attenuation due to viscous damping. Even though this model is restricted to problems where both the geometry and sources satisfy axisymmetric conditions, it is very useful for many practical situations as computer resources limit applications of the 3-D model. The most important step in developing the finite element model is the general 3-D model which includes arbitrary anisotropy and inhomogeneity, as well as attenuation. Careful comparisons with analytic solutions have proven the validity of this model. Applications of this 3-D model will be more practical in the very near future, as parallel architecture machines are developed. Utilization of absorbing boundaries enhances the ability of the finite element model. The results in this dissertation show that a combination of viscous boundary conditions and the non-reflecting boundary is an effective approach.

Using the improved finite element model as a test bed, a careful study was made to determine the sensitivity of the diffraction tomographic reconstruction algorithm to changes in transducer aperture and material anisotropy. Aperture size of the transducer does not have much effect on the images even though the underlying reconstruction algorithm assumes a plane incident wave. Results also show that the normal component of the displacement on the measurement surface, instead of the potential, can be used as the primary variable for image reconstruction. Material anisotropy, however, severely degenerates the quality of reconstructed images. A

time shifting scheme introduced in this dissertation improves the quality of the reconstructed images. Even though it is difficult to apply diffraction tomography to general anisotropic materials, the incorporation of the finite element model as a test bed gives a valuable tool to study further more powerful preprocessing methods by which the correct defect image in an anisotropic medium of arbitrary orientation can be reconstructed.

Future Work

The work reported in this dissertation clearly shows the power of numerical techniques. Further development and refinement of the finite element model are desirable. Special algorithms for improving the quality of the reconstructed images for anisotropic materials are also very important. Suggestions for additional studies include:

1. The possible use of an array processor to speed up the computation should be considered. Due to the fact that the finite element algorithm performs most of the computation element by element, the global equation can be parallelized or distributed to all elements of an array processor. If the CPU-time is dramatically reduced, the finite element model could be used for simulating more complicated geometries.

2. It is difficult to model repeated experiments such as the SAFT data acquisition procedure as the computation is iterated for each transducer location. To avoid this long process, a beam forming[98] technique can be used. The finite element model predicts the displacement field for one particular transducer location

and records the scattered field on the surface. For all consequent transducer locations, the beam forming can be used to produce the A-scan data. Thus the finite element model can be used to study SAFT.

3. In terms of the non-reflecting boundary, it is possible to implement this scheme such that the solution need not be repeated entirely. As the wave cannot travel more than one spatial grid in one time step, the repeated solution can be restricted to a small area near the boundaries. Even though the implementation needs more sophisticated programming, the outcome is expected to be overwhelming because an accurate absorbing boundary can be achieved without additional computation effort.

4. A numerical model to handle the fluid and solid interface is of interest to the NDE community. In many test situations, a fluid is used to couple the transducer and specimen. The finite element model can be expanded to include the fluid materials if the condition $\nabla \cdot \underline{u} = 0$ can be imposed. A special interface condition is also required to count for the discontinuity of the displacement vector at the solid-fluid interface. Another possible approach is to couple the acoustic model (solving for the acoustic potential) and the elastic model (solving for the displacement) together. The advantages of this scheme are that the rotation free condition in the fluid medium is satisfied automatically and the number of unknowns is less because only one variable is involved in the fluid region.

5. Based on an understanding of the underlying physics of wave propagation in an anisotropic material, appropriate data preprocessing algorithms should be

further exploited. The objective of data preprocessing is to modify the raw data such that the effect of the anisotropy is compensated. Image reconstruction algorithms derived for isotropic materials can then be used to image the defects in an anisotropic medium.

BIBLIOGRAPHY

[1] L. Filipczynski. "Scattering of a Plane Longitudinal Wave on a Free Surface of a Disc in a Solid Medium." Proceedings of Vibration Problems 2, no. 1(6) (1961): 41-54.

[2] R. M. White. "Elastic Wave Scattering at a Cylindrical Discontinuity in a Solid." Journal of Acoustical Society of America 30 (1958): 771-785.

[3] T. S. Lewis, D. W. Kraft and N. Hom. "Scattering of Elastic Waves by a Cylindrical Cavity in a Solid." Journal of Applied Physics 47 (1976): 1795-1798.

[4] C. F. Ying and R. Truell. "Scattering of a Plane Longitudinal Wave by a Spherical Obstacle in an Isotropically Elastic Solid." Journal of Applied Physics 27 (1956): 1086.

[5] Y-H Pao and C. C. Mow. "Theory of Normal Modes and Ultrasonic Spectral Analysis of the Scattering of Waves in Solid." Journal of Acoustical Society of America 59 (1976): 1046-1056.

[6] U. Aulenbacher and K. J. Langenberg. "Transient Radiation Pattern of Ultrasonic Transducer on Elastic Half-Space." In New Procedures in Nondestructive Testing, ed. P. Holler, 81-92. Berlin: Springer Verlag, 1983.

[7] R. Ludwig, D. Moore and W. Lord. "An Analytical and Numerical Study of Transient Force Excitation on an Elastic Half-Space." IEEE Trans. on Ultrasonics, Ferroelectrics, and Frequency Control UFFC-36, no. 3 (1989): 342-350.

[8] E. A. Kraut. "Advances in the Theory of Anisotropic Elastic Wave Propagation." Reviews of Geophysics I (1963): 401.

[9] M. Lusk. "A Semi-Numerical Solution to Wave Propagation in Hexagonal Media." M.S. Thesis, Colorado State University, 1988.

[10] J. E. Gubernatis, E. Domany, J. A. Krumhansl and M. Huberman. "The Born Approximation in the Theory of the Scattering of Elastic Waves by Flaws." Journal of Applied Physics 48 (1977): 2812.

[11] J. H. Rose and J. L. Opsal. "The Inverse Born Approximation: Exact Determination of Shape of Convex Voids." In Review of Progress in Quantitative NDE, Vol. 2B, eds. D. O. Thompson and D. E. Chimenti, 949. New York: Plenum Press, 1983.

[12] C. J. Bowkamp. "Diffraction Theory." Reports on Progress in Physics 17 (1954): 35.

[13] J. M. Coffey and R. K. Chapman. "Application of Elastic Scattering Theory for Smooth Flat Cracks to the Quantitative Prediction of Ultrasonic Defect Detection and Sizing." Nuclear Energy 22 (1983): 319-333.

[14] J. B. Keller. "Diffraction by an Aperture." Journal of Applied Physics 28 (1957): 426-444.

[15] J. D. Achenbach, A. K. Gautesen and H. McMaken. Ray Methods for Waves in Elastic Solids. Boston: Pitman, 1982.

[16] P. C. Waterman. "Matrix Theory of Elastic Wave Scattering." Journal of Acoustical Society of America 60 (1976): 567.

[17] V. K. Varadan and V. V. Varadan, eds. Acoustic, Electromagnetic and Elastic Wave Scattering - Focus on the T-Matrix Approach. New York: Pergamon, 1980.

[18] C. A. Brebbia, J. C. F. Telles and L. C. Wrobel. Boundary Element Techniques - Theory and Applications in Engineering. Berlin: Springer-Verlag, 1984.

[19] F. J. Rizzo, D. J. Shippy and M. Rezayat. "A Boundary Integral Equation Method for Radiation and Scattering of Elastic Waves in Three Dimensions." International Journal of Numerical Methods in Engineering 21 (1985): 115-129.

[20] D. E. Budreck and J. D. Achenbach. "3-D Ultrasonic Scattering from Planar Cracks by the Boundary Element Method." In Review of Progress in Quantitative NDE, Vol. 7A, eds. D. O. Thompson and D. E. Chimenti, 103-111. New York: Plenum Press, 1988.

[21] P. J. Schafbach, R. B. Thompson, F. J. Rizzo and T. J. Rudolphi. "Elastic Wave Scattering by Arbitrarily Shaped Voids." In Review of Progress in Quantitative NDE Vol. 8A, eds. D. O. Thompson and D. E. Chimenti, 15-22. New York: Plenum Press, 1989.

[22] Z. Alterman. "Finite Difference Solutions to Geophysical Problems." Journal of Physics of the Earth 16 (1968): 113.

[23] L. J. Bond. "Methods for the Computer Modeling of Ultrasonic Waves in Solids." In Research Techniques in NDT, Vol. VI, ed. R. S. Sharpe, 107-150. New York: Academic Press, 1982.

[24] L. J. Bond. "Computer Modeling in Ultrasonics." Ultrasonics 18 (1980): 43.

[25] L. J. Bond, M. Punjani and N. Saffari. "Ultrasonic Wave Propagation and Scattering Using Explicit Finite Difference Methods." In Mathematical Modeling in Nondestructive Testing, eds. M. Blakemore and G. A. Geogious, 81-124. Oxford: Clarendon Press, 1988.

[26] A. H. Harker. Elastic Waves in Solids - With Applications to Nondestructive Testing of Pipelines. Bristol, England: Adam Hilger, 1988.

[27] K. Harumi. "Numerical Calculation of the Near Field of Elastic Wave in the Solid Half Space." In 7th International Conference on Nondestructive Testing, Warsaw, 1973.

[28] K. Harumi. "Computer Simulation of Ultrasonics in a Solid." Material Evaluation 44 (1986): 1086.

[29] K. Harumi, T. Saito and T. Fujimori. "Motion Picture of the Computer Simulation of Elastic Waves from Transducers." In Proc. of 10th World Conference on Nondestructive Testing, Moscow, 1982.

[30] R. Ludwig. "The Finite Element Modeling of Ultrasonic NDT Phenomena." Ph.D Dissertation, Colorado State University, 1986.

[31] T. J. R. Hughes. The Finite Element Method - Linear Static and Dynamic Finite Element Analysis. Englewood Cliffs, New Jersey: Prentice-Hall, 1987.

[32] O. C. Zienkiewcz. The Finite Element Method in Engineering Science. 2nd edition. London: McGraw-Hill, 1971.

[33] J. Lysmer and L. A. Drake. "A Finite Element for Seismology." Methods in Computational Physics 11 (1972): 181-216.

[34] W. D. Smith. "The Application of Finite Element Analysis to Body Wave Propagation Problems." Geophysical Journal of Royal Astronomy Society 42 (1975): 747-768.

[35] Z. P. Bazant, J. L. Glazik and J. D. Achenbach. "Finite Element Analysis of Wave Diffraction by a Crack." Journal of the Engineering Mechanics Division, ASCE 102 (1976): 479-496.

[36] S-J Tsao, V. V. Varadan and V. K. Varadan. "T-Matrix Approach to Scattering of Elastic(SH-) Waves by an Inclined Surface Void." Journal of Applied Mechanics 50 (1983): 143-148.

[37] S. K. Datta and A. H. Shah. "Scattering of SH Waves by Embedded Cavities." Wave Motion 4 (1982): 265-283.

[38] R. Ludwig and W. Lord. "Development in the Finite Element Modeling of Ultrasonic NDT Phenomena." In Review of Progress in Quantitative NDE, Vol. 5A, eds. D. O. Thompson and D. E. Chimenti, 73-81. New York: Plenum Press, 1986.

[39] R. Ludwig and W. Lord. "A Finite Element Formulation for the Study of Ultrasonic NDT Systems." IEEE Trans. on Ultrasonics, Ferroelectrics and Frequency Control UFFC-35, no. 6 (1988): 809-820.

[40] R. Ludwig and W. Lord. "A Finite Element Study of Ultrasonic Wave Propagation and Scattering in an Aluminum Block." Material Evaluation 46, no. 1 (1988): 108-113.

[41] W. Lord. "Application of Numerical Field Modeling to Electromagnetic Methods of Nondestructive Testing." In Electromagnetic Methods of Nondestructive Testing, ed. W. Lord, 1-20. New York: Gordon and Breach Science Publishers, 1985.

[42] A. J. Devaney and G. C. Sherman. "Nonuniqueness in Inverse Source and Scattering Problems." IEEE Trans. on Antennas and Propagation AU-30 (1982): 1034.

[43] A. J. Devaney. "Fundamental Limitations in Inverse Source and Scattering Problems in NDE." In Review of Progress in Quantitative NDE, Vol. 5A, eds. D. O. Thompson and D. E. Chimenti, 303-316. New York: Plenum Press, 1986.

[44] K. L. Langenberg. "Applied Inverse Problems for Acoustic, Electromagnetic and Elastic Wave Scattering." In Basic Methods of Tomography and Inverse Problems, ed. P. C. Sabatier, 127-470. Bristol: Adam Hilger, 1987.

[45] K. L. Langenberg. "Introduction to the Special Issue of Wave Motion on Inverse Problems." Wave Motion 11, no. 2 (1989): 99-112.

[46] K. L. Langenberg, K. Mayer, T. Kreutter and V. Schmitz. "Computed Imaging with Elastic Waves." Keynote paper in 12th World Conference on Nondestructive Testing, Amsterdam, April 1989.

[47] A. Tarantola. "Inversion of Seismic Reflection Data in the Acoustic Approximation." Geophysics 49, no. 8 (1984): 1259-1266.

[48] P. Mora. "Nonlinear Two-Dimensional Elastic Inversion of Multioffset Seismic Data." Geophysics 52, no. 9 (1987): 1211-1228.

[49] A. Tarantola. "A Strategy for Nonlinear Elastic Inversion of Seismic Reflection Data." Geophysics 51 (1986): 1893-1903.

[50] J. H. Rose and M. Cheney. "Self-Consistent Equations for Variable-Velocity Three-Dimensional Inverse Scattering." Physical Review Letters 59, no. 9 (August 1987): 954-957.

[51] M. Cheney and J. H. Rose. "Three-Dimensional Inverse Scattering for the Wave Equation: Weak Scattering Approximation with Error Estimate." Inverse Problems 4 (1988): 435.

[52] L. Udpa. "Imaging of Electromagnetic NDT Phenomena." Ph.D. dissertation, Colorado State University, 1986.

[53] L. Udpa and W. Lord. "A Search-Based Imaging System for Electromagnetic Nondestructive Testing." IEEE Expert 4, no. 4 (Winter 1989): 18-26.

[54] G. T. Herman. Image Reconstruction from Projections. New York: Academic Press, 1980.

[55] S. R. Dean. The Radon Transform and Some of Its Applications. New York: John Wiley and Sons, 1983.

[56] A. C. Kak and M. Slaney. Principles of Computerized Tomographic Imaging. New York: IEEE Press, 1988.

[57] A. C. Kak. "Tomographic Imaging with Diffraction and Non-Diffraction Sources." In Array Signal Processing, ed. S. Haykin. Englewood Cliffs: Prentice-Hall, 1985.

[58] R. P. Porter and A. J. Devaney. "Generalized Holography and Computational Solution to Inverse Source Problems." Journal on Optical Society of America 72 (1982): 1707.

[59] N. N. Bojarski. "Exact Inverse Scattering Theory." Radio Science 16 (1981): 1025.

[60] R. P. Porter. "Diffraction Limited Scalar Image Formation with Holograms of Arbitrary Shape." Journal on Optical Society of America 60 (1970): 1051.

[61] A. J. Devaney and G. Beylkin. "Diffraction Tomography Using Arbitrary Transducer and Receiver Surface." Ultrasonic Imaging 6 (1984): 81.

[62] M. Slaney, A. C. Kak and L. E. Larsen. "Limitations of Imaging with First-Order Diffraction Tomography." IEEE Trans. Microwave Theory and Techniques MTT-32 (1984): 860.

[63] A. J. Devaney. "A Filtered Backpropagation Algorithm for Diffraction Tomography." Ultrasonic Imaging 4 (1982): 336.

[64] H. Ermert and R. Karg. "Multifrequency Acoustical Holography." IEEE Trans. on Sonics and Ultrasonics SU-26 (1979): 279.

[65] C. Q. Lan, K. K. Xu and G. Wade. "Limited Angle Diffraction Tomography and Its Application to Planner Scanning Systems." IEEE Trans. on Sonics and Ultrasonics SU-32 (1985): 9.

[66] S. K. Kenue and J. F. Greenleaf. "Limited Angle Multifrequency Diffraction Tomography." IEEE Trans. on Sonics and Ultrasonics SU-29 (1982): 213-217.

[67] K. Nagai. "A New Synthetic-Aperture Focusing Method for Ultrasonic B-Scan Imaging by the Fourier Transform." IEEE Trans. on Sonics and Ultrasonics SU-32 (1985): 531-536.

[68] K. Mayer and K. J. Langenberg. "SAFT Signal Processing." Proc. of 11th International Conference on Nondestructive Testing, Las Vegas, Nevada, 1985.

[69] M. Kaveh, M. Soumekh, Z. Q. Lu, R. K. Muller and J. F. Greenleaf. "Further Results on Diffraction Tomography Using Rytov's Approximation." Acoustical Imaging 12 (1982): 598-608.

[70] M. Soumekh and M. Kaveh. "A Theoretical Study of Model Approximation Errors in Diffraction Tomography." IEEE Trans. on Ultrasonics, Ferroelectrics and Frequency Control UFFC-33, no. 1 (1986): 10-20.

[71] Z. You, M. Lusk, R. Ludwig and W. Lord. "Numerical Simulation of Ultrasonic Wave Propagation in Anisotropic and Attenuative Solid Materials." submitted to IEEE Transactions on Ultrasonics, Ferroelectrics, and Frequency Control.

[72] B. A. Auld. Acoustic Fields and Waves in Solids, Vol. I. New York: John Wiley & Sons, 1973.

[73] K. G. Graff. Wave Motion in Elastic Solids. Columbus: Ohio State University Press, 1975.

[74] W. Lord, R. Ludwig and Z. You. "Developments in Ultrasonic Modeling with Finite Element Analysis." Submitted to International Journal of NDT.

[75] N. M. Newmark. "A Method of Computation for Structural Dynamics." Journal of Engineering Mechanics Division, ASCE 85 (1959): 67.

[76] I. Fried and D. S. Malkus. "Finite Element Mass Matrix Lumping by Numerical Integration without Convergence Rate Loss." International Journal of Solids and Structures 11 (1976): 461-466.

[77] E. Hinton, T. Rock and O. C. Zienkiewicz. "A Note on Mass Lumping and Related Processes in the Finite Element Method." Earthquake Engineering and Structural Dynamics 4 (1976): 245-249.

[78] C. F. Carey and J. T. Oden. Finite Elements – Computational Aspects, Vol. III. Englewood Cliffs, New Jersey: Prentice-Hall, 1984.

[79] G. Strang and G. J. Fix. An Analysis of the Finite Element Method. Englewood Cliffs, New Jersey: Prentice-Hall, 1973.

[80] Z. You and W. Lord. "Finite Element Study of Elastic Wave Interactions with Cracks." In Review of Progress in Quantitative NDE, Vol. 8A, eds. D. O. Thompson and D. E. Chimenti, 109-116. New York: Plenum Press, 1989.

[81] D. P. Flanagan and T. Belytschko. "A Uniform Strain Hexahedron and Quadrilateral with Orthogonal Hourglass Control." International Journal for Numerical Methods in Engineering 17 (1981): 679-706.

[82] Z. You and W. Lord. "Numerical Modeling of Elastic Wave Propagation in Anisotropic materials." In Review of Progress in Quantitative NDE, Vol. 7A, eds. D. O. Thompson and D. E. Chimenti, 23-30. New York: Plenum Press, 1988.

[83] V. T. Buckwald. "Elastic Wave in Anisotropic Media." Proceedings of the Royal Society of London, Ser. A, Vol. 253 (1959): 563-580.

[84] J. Lysmer and G. Waas. "Shear Waves in Plane Infinite Structures." Journal of the Engineering Mechanics Division ASCE 98 (1972): 85-105.

[85] E. Kausel, J. M. Roësset and G. Waas. "Dynamic Analysis of Footings on Layered Media." Journal of the Engineering Mechanics Division ASCE 101 (1975): 679-693.

[86] S. Pissanetzky. "An Infinite Element and a Formula for Numerical Quadrature over an Infinite Interval." International Journal of Numerical Methods in Engineering 19 (1983): 913-928.

[87] G. Waas. "Linear Two-Dimensional Analysis of Solid Dynamics Problems in Semi-Infinite Layered Media." Ph.D. Dissertation, University of California, Berkeley, 1972.

[88] R. Clayton and B. Engquist. "Absorbing Boundary Conditions for Acoustic and Elastic Wave Equations." Bulletin of the Seismological Society of America 67, no. 6 (1977): 1529-1560.

[89] H. Ang and N. M. Newmark. "Development of a Transmitting Boundary for Numerical Wave Motion Calculations." Report to Defense Atomic Support Agency, 1972.

[90] J. Lysmer and R. L. Kuhlemeyer. "Finite Dynamic Model for Infinite Media." Journal of the Engineering Mechanics Division ASCE 95 (1969): 859-877.

[91] W. D. Smith. "A Nonreflecting Plane Boundary for Wave Propagation Problems." Journal of Computational Physics 15 (1973): 492-503.

[92] E. Kausel and J. Tassoulas. "Transmitting Boundaries: A Closed-Form Comparison." Bulletin of the Seismological Society of America 71 (1981): 143-159.

[93] W. White, S. Valliappan and I. K. Lee. "Unified Boundary for Finite Dynamic Models." Journal of the Engineering Mechanics Division ASCE 103 (1977): 949-964.

[94] V. R. Dewey, B. F. Oliver, C. A. Picard. " Finite Element Modeling of Ultrasonic Inspection of Weldments." In Review of Progress in Quantitative NDE, Vol. 2A, eds. D. O. Thompson and D. E. Chimenti, 256-263. New York: Plenum Press, 1983.

[95] Z. You and W. Lord. "A Finite Element Test Bed for Diffraction Tomography." In Review of Progress in Quantitative NDE, Vol. 9A, eds. D. O. Thompson and D. E. Chimenti, 447-454. New York: Plenum Press, 1990.

[96] M. Schade. "Elastodynamische Holographie." University of Kassel, FRG, 1988. (unpublished)

[97] Z. You and W. Lord. "Finite Aperture and Anisotropy Effects of Diffraction Tomography." In Review of Progress in Quantitative NDE, Vol. 10A, eds. D. O. Thompson and D. E. Chimenti, New York: Plenum Press, 1991.

[98] T. Shan and T. Kailath. "Adaptive Beamforming for Coherent Signals and Interference." IEEE Transactions on Acoustics, Speech and Signal Processing ASSP-33, no. 3 (1985): 527-536.